Numerical Simulation and Modeling of Shock Tube Experiments

Matthew Satchell

Department of Engineering Science

The University of Oxford

A thesis submitted for the degree of Doctor of Philosophy.

Hertford College July 2021

Acknowledgements

None of this research or the remarkable personal journey which accompanied its undertaking would have been possible without the support of Russ Cummings. Thank you also to Greg Abate for your guidance and believing in me to start along this path. My sincere gratitude is also owed to the US Air Force Academy, and the US Air Force as a whole for providing this unique opportunity.

Thank you to my advisors, Professors Luca di Mare and Matthew McGilvray, for your patient mentorship and for sharing your amazing depth of knowledge.

Thank you also to Peter Collen, Alex Glenn, Luke Doherty, and the rest of the T6 team for your help in obtaining high quality experimental data without which my work could not have existed.

I would also like to thank the Fire Marshall for a lifetime of inspiration and strength which pushed me to achieve more.

Most all, my profound gratitude to my wife Abigail, children Emma and Isaac, and my broader family who whose patience, support, encouragement, perspective, and joy have afforded me the chance to pursue my dreams and persevere through to their attainment.

Thank you so much to everybody who has helped me along the way!

Abstract

Shock tube experiments are a key method of reproducing the flow conditions encountered by hypersonic flight vehicles and are the primary source of known thermochemical reaction rates. However, because of the complex nature of hypersonic flows, and also due to the many subtle complexities of the shock facilities themselves, full characterization of the flows they produce is elusive. This work develops a numerical method for the simulation of shock tube experiments using a novel technique of shock tracking to improve the resolution and decrease the computational cost of such simulations. An axisymmetric, Navier-Stokes shock tube simulation code entitled FROSST keeps the shock and contact discontinuity each stationary in their own zone of refinement that slides along a coarse background mesh of the entire facility. Using this solver, the role of shock history in the formation of nonuniformities in shock tube test gases is investigated in the context of ideal gas simulations. Shock speed variations from -29% to +33% are found to influence temperatures in the test slug by as much as 55% in an Argon test gas with a tube-end 2100 m/s. These results give rise to the observation that nearly all nonuniformities in the test gas originate with variations in shock speed along the tube. Based upon this observation, a novel method is devised to use experimentally measured shock speed to predict test flow properties for each experiment. This method tracks the influence of waves associated with shock speed variation upon isentropic slices of shock-processed gas. By tracking a number of such slices, the entire test slug is reconstructed to a high degree of accuracy. The analytical methodology, entitled LASTA, is extensively validated against simulated ideal Argon data and also experiments performed in the Oxford T6 Stalker shock facility with both Argon and thermochemically reacting air. LASTA is found to capture the shot-to-shot nonuniformities to within 1% within minutes on a single core. Real-world application of LASTA is already leading to improved understanding of radiative emissions from shock tube experiments.

Table of contents

Chapter 1

INTRODUCTION

Many nations are pursuing the growing global interest in routine access to space for space tourism, satellite delivery, and continued exploration of other celestial bodies. Flight vehicles entering planetary atmospheres such as probes or manned vehicles returning to Earth from space, as well as the fastest military systems, travel at hypervelocity speeds. Figure 1.1 shows a range of vehicle trajectories for Earth flight at high speeds. Such trajectories produce a complex flight environment which presents unique design challenges and causes analysis of high speed vehicles to be extraordinarily challenging.

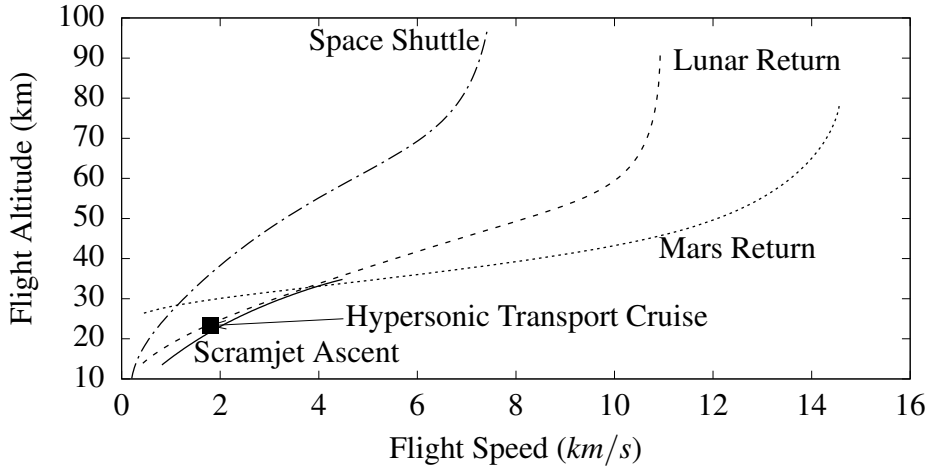

Fig. 1.1 Representative hypervelocity flight vehicle altitude-speed trajectories through Earth's atmosphere. Adapted from [37].

Because hypervelocity vehicles travel well faster than the speed of sound, a shock wave is formed around the leading edges of the craft. At the stagnation point of the vehicle, this shock is normal to the direction of flight. Shock waves convert the kinetic energy of a vehicle into internal energy of the gas, elevating its temperature and pressure. As the speed of the vehicle increases, the shock wave strengthens, and the temperature of the gas behind the shock increases.

1.0.1 SHOCK-HEATED GASES

The high post-shock temperatures excite internal energy states - the modes in which an atom or molecule may store energy - in the molecules and atoms behind the shock, and species begin to dissociate. For example, molecular nitrogen and oxygen may split into atomic species, and new species are thus introduced to the gas. As temperature continues to increase, atomic species begin to ionize, and electrons flow throughout the hottest portions of the flowfield. These electrons influence ongoing chemical reactions and contribute to the formation of still further species. Radiative emissions may be produced by collisions between species and/or electrons, quantum transitions from higher internal energy states to lower ones, or result from the absorption of a photon by a chemical species. These emissions are in turn absorbed by nearby molecules, elevating the electron states of those molecules and subsequently causing them to re-emit, and so a continuous emission may be produced. Flows with a high degree of ionisation also produce a large degree of radiative emission. This radiative emission from the shock-heated gas may also be absorbed into the flight vehicle itself. Because of the high temperatures, any material exposed to the flow may begin to deteriorate due to pyrolysis and ablation, introducing still further species to the near-wall flow such as carbon and hydrogen. This process is described in Figure 1.2 for air near a wall made of a carbon-based species.

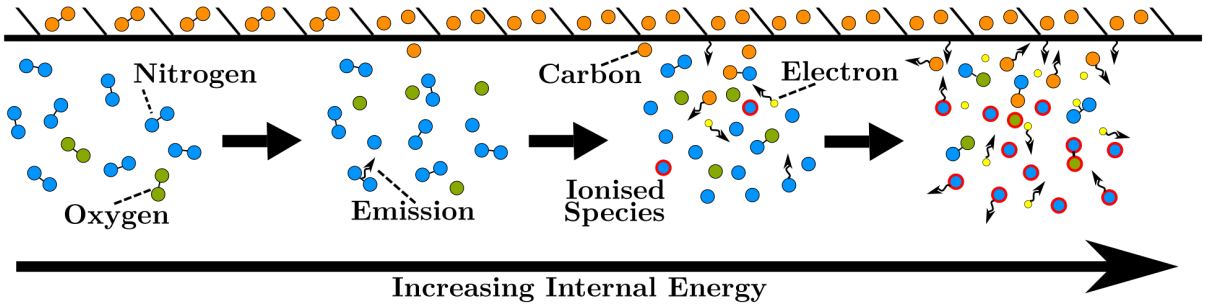

Fig. 1.2 The evolution of air near a carbon-based wall at increasing temperature.

The chemical and radiative properties of the shock-heated gas play an essential role in the aerodynamics and surface heating of a vehicle. For example, the pitching moment of a hypersonic flight vehicle is strongly dependent upon the shock standoff distance, which itself varies greatly with the thermochemical state of the gas. Thus, any prediction of flight vehicle aerodynamic performance must include an accurate assessment of the chemical properties behind leading edge shock waves. Likewise, convective and radiative heat transfer to the vehicle are determined in large part by the chemical makeup of the gas, as well as the particular chemical reactions which occur at and within the surface (catalysis, pyrolysis and ablation) [63]. Emissions from the gas reduce the gas internal energy

and can travel into the wall, reradiate, and contribute to a complex thermochemical and heat transfer environment, deviating the gas behaviour from ideal gas properties. In the design of hypersonic flight vehicles, thermochemical effects and radiative heating change both the flight dynamics of, and the heat transfer to, a vehicle [63]. As an example, radiative heating constituted for the case of the Galileo probe 95% of the total heating to the surface of the vehicle as it entered the Jovian atmosphere [2]. Furthermore, the emissions interfere with radio communications to and from the vehicle, and cause the vehicle to be easily tracked by its radiative signature, both of which processes are of concern to military users of hypersonic technology. Accordingly, design of both civilian and military high speed vehicles is critically dependent upon accurate characterisation of the chemical properties at and near the surface.

1.0.2 CHARACTERISING THE THERMOCHEMICAL STATE

After an atom or molecule has been heated to conditions wherein internal energy states have been excited, that chemical species will begin the process of relaxing down to lower energy states. Such relaxation may occur through collisions and reactions with other molecules or by the emission of radiation, but a finite amount of time is required in either case to bring the mixture to a steady state for the given temperature and pressure conditions, termed thermochemical equilibrium. The gas may be described during the time in which it is relaxing towards equilibrium as being in a state of thermochemical nonequilibrium. During this time, the internal energy states relax at different rates from one another. The formation of chemical bonds between species depends upon the internal energy states of each species at the time of collision. Thus, in order to determine the chemical composition and internal energy distribution of a gas during the relaxation process, finite rate thermochemical analyses must accurately account for each energy state of each species at any point in time.

The degree to which the gas has relaxed towards equilibrium also influences the radiative emissions of the gas. As the many species in a typical hypersonic flowfield relax towards equilibrium, many transitions between states occur, and a strong radiative intensity is produced. Even in equilibrium, chemical reactions and electron transitions are continuously occurring which average out to the equilibrium state. As a result, gases in chemical equilibrium at high internal energies will also produce a continuous radiative emission which may constitute a major portion of the radiative heat transfer to the vehicle [8].

Any analysis seeking to determine the chemical makeup or radiative properties of the gas at a given location around the vehicle flowfield must necessarily understand whether the gas is in chemical equilibrium or nonequilibrium, and if in nonequilibrium, how far along the relaxation process the gas stands. The importance of accurate characterisation of the thermochemical environment to hypersonic flight vehicle design is evident in examination of the predicted surface temperatures against which a thermal protection system must survive. Figure 1.3 shows the surface temperature as predicted by classical equilibrium conical flow analysis versus that predicted by a nonequilbrium characteristic analysis for a 45° cone flying 6640 m/s at high altitude. Predictions near the leading edge produce a radically different surface temperature between the two methodologies. Even far from the leading edge, the temperature remains off 5%, which would lead to a substantially different thermochemical and radiative environment, and consequentially different thermal protection system requirements.

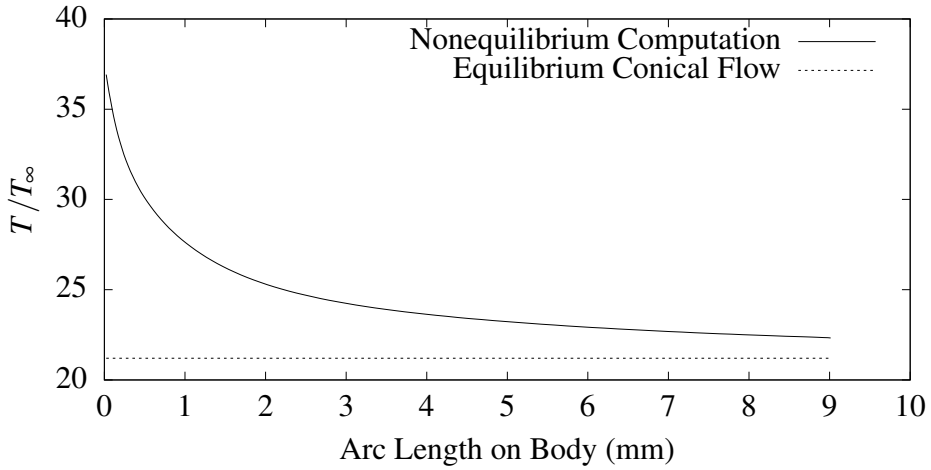

Fig. 1.3 Surface temperature for 45° cone. $T_\infty = 273\,\mathrm{K}$, $P_\infty = 0.01\,\mathrm{atm}$. Adapted from Spurk [73].

Thermochemical effects in hypervelocity flowfields may be studied in a variety of ways. At the macro level, flight tests may be performed which take measurements from the vehicle itself and also from observations made by terrestrial and airborne observation platforms. However, such tests are often prohibitively expensive, and the amount and types of obtainable data are limited by bandwidth and recoverability of the vehicle, as well as design considerations. Because of these limitations, ground-based reproduction of the hypervelocity flight environment is much more common. Such ground test facilities range broadly in size and type, including ballistic free-flight ranges, test tracks upon which vehicles are accelerated by rockets to appropriate speeds, and numerous varieties of wind tunnels.

Numerical simulations also comprise an important and growing utility to studies of thermochemistry in the hypersonic flight environment. Flight and ground tests are often limited in the types and amounts of information which can be gathered about flows, but numerical simulation provides deep insight into every aspect of the flowfield. However, the accuracy of numerical simulations of thermochemically reacting flows is strongly dependent upon accurate reference data for the chemical behaviours which are being simulated. For a flow in chemical equilibrium wherein two thermodynamic properties are known (e.g. pressure and entropy, or enthalpy and entropy), the chemical composition, remaining thermodynamic properties and transport properties may be computed from theory [53]. As a result, for relatively low speed hypersonic flows which are dominated by equilibrium chemistry, numerical simulation provides a well-established and accurate means of flight vehicle analysis. Unfortunately, a great deal of uncertainty surrounds the known chemical rates which establish the nonequilibrium environment.

Thermochemical rates associated with high speed flight can be obtained from measurements of the test gas in shock tube experiments [63]. However, such experiments have extensive uncertainties arising from as yet poorly characterised nonuniformities within the test gases [8]. The impact of the uncertainty in chemical rates upon flight vehicle design was recently quantified for the afterbody radiative heating for a blunt body undergoing atmospheric entry to earth by West *et al* [77] in 2017. Among other uncertainties, the electron excitation rates, which dominate the ionisation and photoemission processes, were assumed to have an uncertainty range of ± 1 order of magnitude based on the data of Johnston and Kleb [47]. West *et al* then found that ionisation rates in Nitrogen and Oxygen dominated the uncertainty of the radiative heating rates, which were found to possess an uncertainty between -50% and +125% of the nominally computed rate, with obvious implications for the design of the thermal protection system. These uncertainties are, perhaps, the reason that Bensassi *et al* [3] stated in their 2020 analysis of shock tube characterisation techniques that accurately measured chemical rates 'constitute the holy grail for the computational modelling tribe.'

This thesis is not concerned directly with obtaining such measurements, or even performing simulations which utilise the chemical rates thereby obtained. Rather, this work studies the flow conditions in shock tube experiments, which are the source of nearly all the compiled chemical rate coefficients [63]. As is discussed in the next sections, the greatest source of the extensive uncertainties

surrounding chemical rates originates in the limitations in understanding and diagnostics of shock tube flows.

1.1 SHOCK TUBE FACILITIES

Although shock tubes have been in use for hypersonic investigations since the 1950's, the number and type of investigations which utilize them has increased substantially in the past two decades. Chemical reaction rates which are utilised in nonequilibrium numerical simulations are obtained from shock tube experiments. Other research fields, such as astrophysics, combustion, blast wave theory, and many more also depend upon the thermochemical rates which are produced by shock tubes. Despite the large number and complexity of different shock tube facilities around the world, all share some basic characteristics.

Shock tubes operate by building up pressure on one side of a tube divided by a diaphragm until the diaphragm bursts as seen in Figure 1.4. The large pressure difference between the driver and driven gases causes a shock wave which travels into the test gas (Region 1) at a speed u_s. The contact discontinuity separating the driver and test gases follows more slowly at the local speed u. The expansion wave travels into the unexpanded driver gas (Region 4) at a speed $u-a$, causing the driver gas to undergo an unsteady expansion (Region 3) which produces constant pressure across the contact discontinuity (i.e. $u_2 = u_3$ and $p_2 = p_3$).

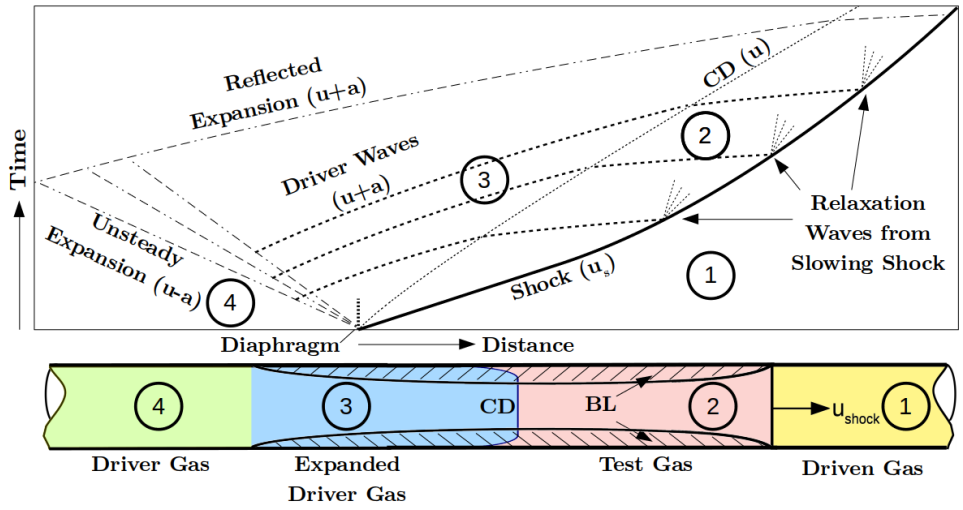

Fig. 1.4 Distance vs Time diagram of waves in a shock tube. Not to scale.

Properties of the test gas such as radiation or thermochemical composition in the test section are measured from the shock-heated gas (Region 2), often termed the 'test slug.' This gas produces an

approximate duplication of the stagnation line flowfield observed in hypervelocity flight. The arrival of the contact discontinuity and expanded driver gas (Region 3) concludes the test gas. In ideal analyses a longer tube produces a longer test time since the contact discontinuity travels more slowly than the shock. Figure 1.4 provides a schematic of the layout of these flow features.

Although this thesis concentrates on the application of shock tubes for shock layer thermochemistry and radiation experiments, shock tubes have also previously been applied to convective and heat transfer experiments as well as aerodynamic investigations. However, other impulse facilities such as reflected shock tunnels and expansion tunnels are more applicable to these types of experiments as they can produce longer test times, larger core flows and colder gas (i.e. gas is closer to ambient temperature/composition). These facilities build upon the simple shock tubes by the incorporation of additional tube sections and diaphragms. Thus the focus of this thesis and its outcomes have implications to the operation of these more complex facilities.

1.1.1 NON-IDEAL EFFECTS IN SHOCK TUBES

Although idealized shock tube flows are often depicted as simple cases against which numerical flux schemes may be tested, the actual behaviour of the primary waves is quite complex. In reality, a number of phenomena arise which cause shock tube experiments to deviate significantly from theoretical analyses. Test times reach a maximum some distance down the tube [25, 58], rather than growing with greater distance. Because of a combination of boundary layer effects, shock speed variation and influences from the non-ideal compression and bursting processes, the post-shock flow contains nonuniformities in density, internal energy and thermochemical makeup [58, 66]. Such a profile is evident in Figure 1.5.

Because of the variability in compression and bursting processes, each test at nominally identical conditions causes the shock to follow a different trajectory down the tube and produces different results. Such shot-to-shot variations are, to date, unreproduceable by numerical or analytical methods, which produce a single prediction from the single, nominal input set. As the complexity of a facility grows, e.g. by the stacking of additional diaphragms and tube sections, the nonuniformities introduced in an upstream section compound with the features created by the downstream sections. For example, it was shown by Petersen *et al* [64] that nonuniformities behind the incident shock in a reflected shock tube were amplified by the reflected shock, thus modifying the test results. Since many facilities

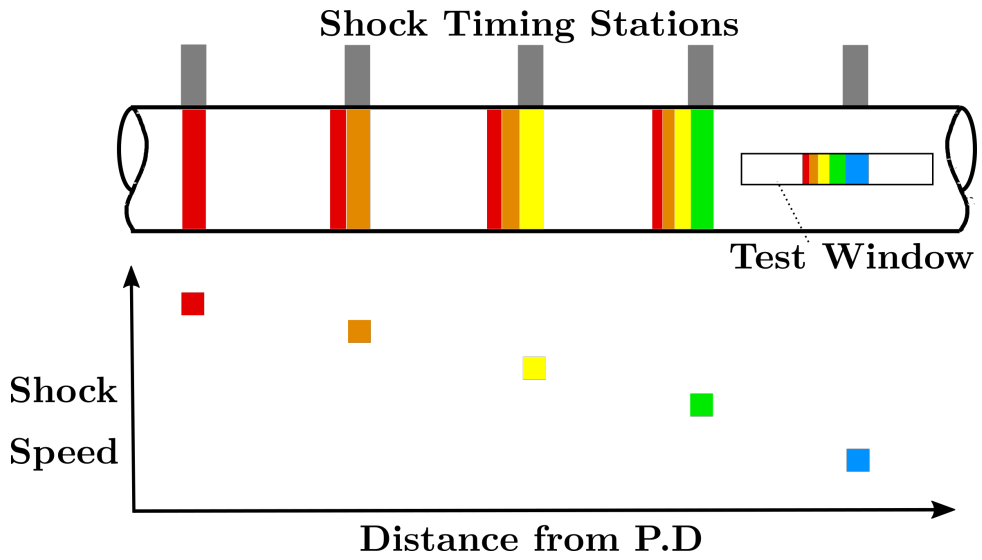

Fig. 1.5 The compression of slices of gas processed by a shock of decreasing speed.

possess multiple diaphragms and sections of tube, the accumulation and interaction of post-shock nonuniformities clearly represent a compounding uncertainty. This thesis will focus only on the basic shock tube in order to characterise the many uncertainties associated with the elemental flows which are present across the more complex facilities.

1.1.2 SHOCK TUBE THERMOCHEMICAL ANALYSIS

Thermochemical measurements are obtained at shock facilities primarily by use of spectrographic techniques measuring the flow from the tunnel sidewall. Typical outputs of emission spectrometer measurements from a shock tube experiment are seen in Figure 1.6. Observations in the changes in spectral radiance with distance from the shock may be used in order to extract information about chemical rates. The speed of the shock at the location of the spetrometer is measured, and so in an ideal shock tube with no flow nonuniformities, any variation of spectral emissions should arise from the chemical relaxation processes as the flow approaches equilibrium after its initial excitation by the shock. It is from such observations that chemical rate coefficients are obtained and the bulk of known chemical rates have been computed [63].

Any flow nonuniformities in the axial direction influence the chemical relaxation rates. It may be reasonably asked, for example, how the rear slope in radiance 4 cm from the shock, or distribution of wavelength intensities with distance from the shock are influenced by axial nonuniformities in the experiment. The importance of characterising the conditions under which measurements are taken in shock tube flows is well-summarized by Petersen *et al* [64]: ‘For an average temperature of 1500 K,

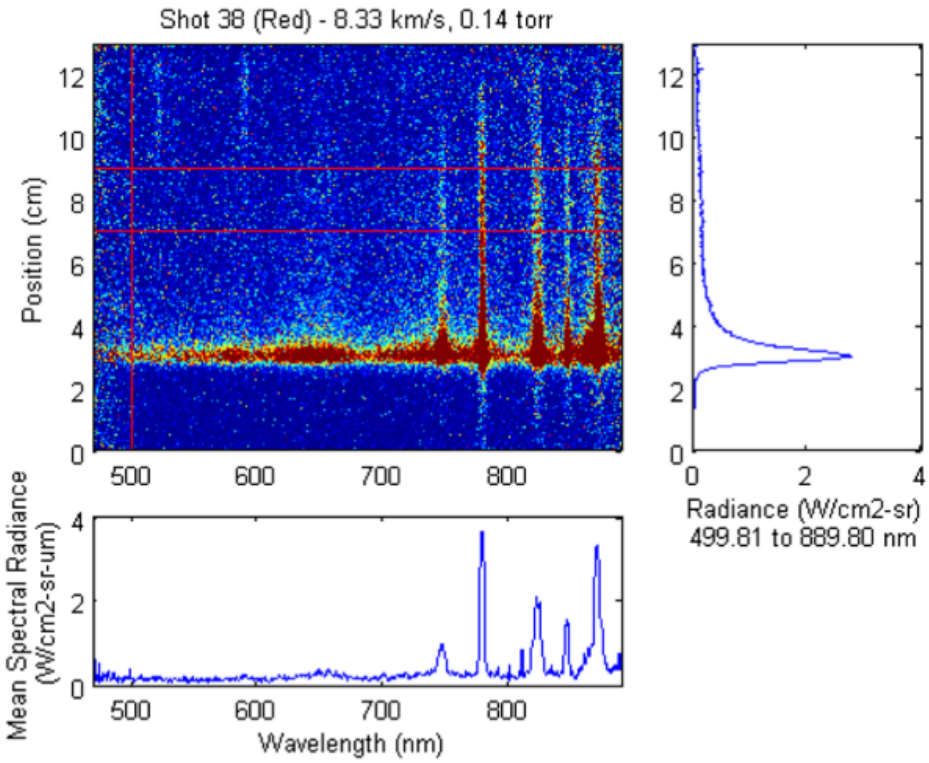

Fig. 1.6 Typical spectral measurements in a shock tube experiment from [20].

a 15 K error in temperature (i.e. only 1%) can lead to a 25% error in the measured rate coefficient.' It is thus pivotal in seeking to understand the measurements obtained in shock tubes to examine the particular flowfield which produced these measurements.

Several approaches to deconvoluting flowfield nonuniformities from measured relaxation rates have been tried, with limited success. The POst SHock relAxation (POSHAX) algorithm [32] is a one-dimensional spatial marching technique which applies a chemical relaxation scheme behind a standing normal shock based on known rates, assuming no flow nonuniformities aside from those introduced by thermochemistry. Another technique is to assume that the post-shock flow is analogous to a stagnation streamline on a blunt body, but the shortcomings of this methodology are well-documented. One- or two-dimensional simulations, or a hybrid approach which couples both types together for the sake of reducing computational cost, have been used but these simulations are highly expensive, and produce mixed results. Many simulations apply an initial thermochemistry model and tune the chemical rates until agreement is achieved with experiment, but this too yields varied results. Altogether, there is as yet no highly successful means of separating the influence of flow nonuniformities from the computation of chemical rates in shock tubes.

In addition to uncertainties introduced by the axial nonuniformities, further uncertainty is caused by the fact that spectroscopic measurements are integrated across the depth of the tunnel. As a result,

the spetrometer measures together the intensity of not just the core flow, but the boundary layer on either side of the tunnel. The use of an integrated measurement means that, although the boundary layer likely possesses significantly different radiative properties from the core flow, the spectrometer indistinguishibly includes both emissions from the core flow and the boundary layer emissions in its measurements. Furthermore, the boundary layer absorbs radiative emissions from the core flow, further complicating the determination of actual spectra from a given core flow condition [49].

Taken together, the role of flow nonuniformities in shock tube experiments are not well understood [3, 12] despite the broad use of such facilities for hypersonic and thermochemical investigations. Because shock tube experiments are used not just for study of thermochemical processes but also to investigate aerodynamic response and radiative emission - all of which phenomena which are co-dependent upon one-another - uncertainties introduced by nonuniformities in shock tube experiments are echoed in both the experimental measurements of flight vehicles and also numerical simulations seeking to represent them [3]. Since, paradoxically, simulations seeking to characterise shock tube experiments also rely upon the thermochemical data produced by the experiments, this interplay of theory, experiment and analysis thus produces a complex array of uncertainties in hypersonic investigations. In pursuit of reducing these uncertainties, developing an affordable and complete means of extricating the influence of flow nonuniformities from shock tube experimental results is the main subject of this thesis.

1.2 THESIS OBJECTIVES

Targeting the important gaps in knowledge of uncertainties shock tube experiments, the purpose of this effort is to answer the scientific question: ‘What are the primary sources of nonuniformities in the test gases of shock tube experiments, and how can they be efficiently modelled to enable a complete characterisation of experimental test gases?’ In order to answer this question, three primary objectives are addressed:

1. Characterise the origins and extents of flow nonuniformities in the test gas
2. Develop a means of characterising test gas flow properties directly from experimental data
3. Produce a means of efficient full-shock tube simulation including non-ideal facility effects

1.3 THESIS STRUCTURE

The remainder of this thesis is divided into four technical chapters and a chapter containing concluding remarks. The technical chapters are structured as first-author journal papers. The paper in Chapter 3 has been published in AIAA Journal. The paper in Chapter 4 has been recommended for publication at AIAA Journal pending minor revisions, while the two papers which constitute Chapter 5 have been submitted to AIAA Journal for peer review.

Chapter 2: Literature Review

This chapter reviews the literature pertinent to the current state of the art in terms of understanding and characterising shock tube flows. The discussion first examines the current knowledge around the types and sources of nonuniformities present in the test gas, and then examines the methods by which attempts have thus far been made to characterise them.

Chapter 3: A Novel Navier-Stokes Solver for Shock Tube Simulations

A novel numerical method is developed and validated against a range of experimental data. This code contains two primary contributions: 1) the use of an overset formulation using multiple moving domains to capture the primary discontinuities, and 2) the development of an efficient means to keep the shockwave stationary in its moving frame of reference even in the presence of substantial shock speed variation.

Chapter 4: The Influence of Non-Constant Shock Speed

The influence of variations in shock speed down the tube are investigated in the context of an ideal gas. The major findings of this section are that: 1) the variation of entropy behind a shock of changing speed leaves an enduring temperature gradient in the test gas; 2) pressure waves associated with the variation of shock speed work to shift the gradients established by the entropy variation by a process of relaxation; 3) the test gas which is measured in the test section is composed of gas from some sublength of the tube as limited by boundary layer mass balance and also the presence of the contact discontinuity 4) contamination by driver gas caused by the variation of shock speed dramatically shortens the test time in the form of jets formed along the wall and centreline of the tube.

Chapter 5: An Analytical Methodology for Rebuilding Shock Tube Experiments

A quasi-one dimensional analytical model entitled the LAgrange Shock Tube Analysis (LASTA) code is developed which predicts post-shock property variations based exclusively on the history of the shock speed, tube geometry and fill conditions. This model is then validated against a range of numerical and experimental data for both ideal and equilibrium gases. The major contributions of this section are to: 1) demonstrate that nearly all post-shock nonuniformities are predictable from shock history alone; 2) produce a computationally inexpensive method of predicting test gas nonuniformities; 3) validate the methodology; 4) show that characterisation of the test gas demands a reasonably accurate capture of shock experimental trajectory.

Chapter 6: Conclusions and Future Work

The conclusion highlights the major findings and broader significance of the technical work performed herein. Recommendations are made for future work which would further extend the results thus presented and enable broader application of the developed numerical codes.

Chapter 2

LITERATURE REVIEW

2.0.1 A HISTORICAL NOTE

Some historical context is relevant prior to framing the present state of the technical literature around shock tube experiments. The field of hypersonics has a well-established reputation for a boom-bust cyclical pattern of funding and interest [39]. As with the funding cycles, so the investment in and knowledge of hypersonic test facilities likewise oscillated. The result of these cycles, as applies to shock tubes, may be observed in the historical citations to Mirels' landmark work, 'Test-Time in Low Pressure Shock Tubes' [58]. This paper is almost necessarily cited in any discussion of the mechanics of shock tube flows because it first explained the source of fundamental limitations in shock tube experiments. These limitations and the importance of Mirels' findings are described in-depth later in this section. Figure 2.1 clearly shows that the period of 1980-2000 contained comparatively little interest in predicting or explaining shock tube test times by analytical methods. It is for this reason that a careful examination of the references listed herein may appear to generally skip two decades of scientific advancement; theoretical research into the nature of shock tube flows was simply highly limited during this period.

2.1 NON-IDEAL EFFECTS IN SHOCK TUBES

The fundamental mechanisms that cause the nonuniformities which arise in shock tube experiments are now discussed. Such nonuniformities arise both axially and radially due to the interaction of complex factors, including: boundary layer effects, unsteady effects associated with the opening of

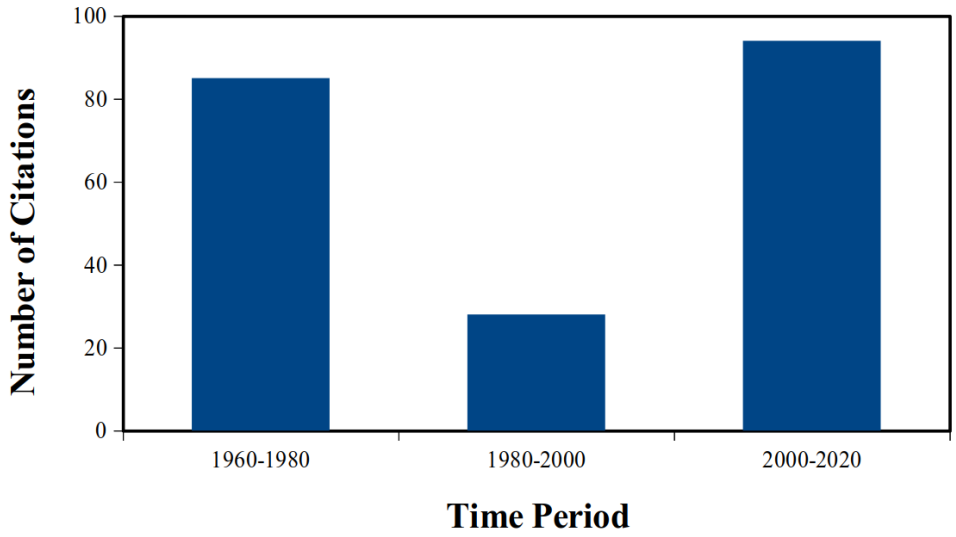

Fig. 2.1 Number of citations of Mirels' 'Test-Time in Low Pressure Shock Tubes' [58] by date of citation. Data obtained from aip.scitation.org.

the diaphragm and driver pressurisation, thermochemistry, and variations in shock speed. A focus is placed upon those aspects of the literature which discuss the initial development of the shock and its travel down the tube, since that is the challenge which is most clearly not met by the literature and is explicitly addressed by this work.

2.1.1 BOUNDARY LAYER EFFECTS

As the shock travels, the motion of the fluid behind it causes the formation of a hydrodynamic boundary layer. Duff first reported that the formation of the boundary layer appeared to influence the test time [25]. Thereafter, Hooker [41] and Roshko [68] developed models which demonstrated that mass flow consumption of the boundary layer from the core flow caused gas upstream to be pulled forward to replace the gas consumed by the boundary layer, as seen in Figure 2.2. Since the contact discontinuity travels at the local convection speed, it accelerates and, if the tube is of sufficient length, eventually achieves parity of speed with the shock. This shortens the test time from ideal estimations, particularly in narrow tubes [25], observed by Mirels to extend to a reduction of 60% in some cases [57]. Mirels performed extensive boundary layer analysis and improved upon the models of Roshko and Hooker to produce a reliable method of predicting the test time in shock tube experiments [58]. This methodology remains today a standard for predicting test time in experimental design [46].

The accelerating core flow has the additional effect of causing property nonuniformities in the test slug. The faster upstream flow colliding with the slower post-shock flow causes an increase

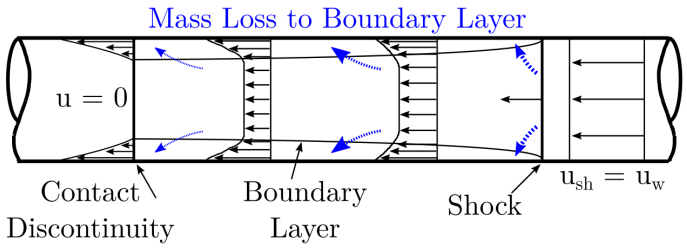

Fig. 2.2 Schematic of core flow acceleration due to mass loss to the boundary layer. Adapted from Mirels [58].

in temperature, pressure and density in the test slug moving from the shock towards the contact discontinuity [60]. Viewed from the frame of reference in which the moving shock is stationary, the post-shock flow appears to be moving away from the shock, but slowing the closer it gets to the contact discontinuity until it 'stagnates.' As a result, the nonuniformities produced by boundary layer effects are sometimes analogued to that of a subsonic diffuser, which allows prediction of such nonuniformities to acceptable accuracy for many conditions where shock speed does not vary substantially and the tube is of such an aspect ratio as to allow achievement of the the maximum test time [60]. The shortening of test time and nonuniformities arising from the boundary layer mass consumption are often referred to as Mirels' effects. A representation of the variation of test slug properties due to Mirels' effects alone is seen in Figure 2.3. The subscripts $_e$ and $_1$ refer to the test gas and pre-shock properties, respectively.

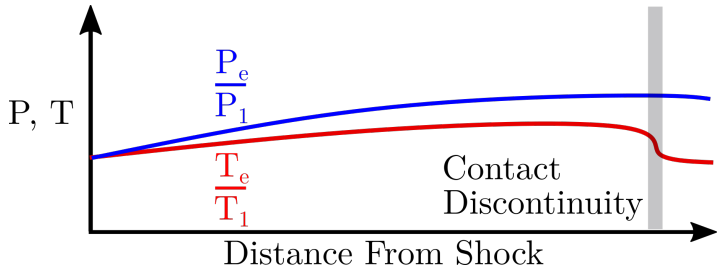

Fig. 2.3 The variation of test gas temperature and pressure due to Mirels' effects.

Zeitoun [82] performed a more complex simulation coupling a solution of the boundary layer equations with a separate solution of the Euler equations behind a moving shock, arriving at similar results as Mirels but using a model which enabled more detailed analysis of the flow phenomena involved. In particular, Zeitoun improved upon predictions near the rear of the test slug, finding that properties change rapidly near the contact discontinuity, and that velocity profiles follow a linear trend after the initial 30% of the test slug length, as opposed to the parabolic change that Mirels predicted.

A final influence of the boundary layer may be observed in the shock speed. Glass [31] showed that mass loss into the boundary layer produced expansion waves which slowed the shock. These

waves travel downstream to reach the shock, and cause it to attenuate. Mirels also investigated this phenonenon [57]. However, many studies such as those of Mirels and Zeitoun assume that the shock attenuation reaches a steady state when the maximum test time is reached, and so the effect is explicitly neglected or considered as small.

A turbulent boundary layer increases the boundary layer thickness and accompanying mass flow into it as compared to a laminar boundary layer, thereby worsening the Mirels' effects. This increased influence extends to the shortening of the test slug, strengthened nonuniformities, and greater shock attenuation [59]. The test gas boundary layer can transition in several ways. The most direct process is for the shock-processed gas in the test slug boundary layer to transition naturally prior to reaching the contact discontinuity, thus producing a portion of test gas affected by turbulent flow. This typically occurs with relatively high fill pressures, and the flow has been observed to become increasingly stable with higher Mach numbers. The source of this stability is speculated to arise with the strong favorable pressure gradient caused by boundary layer and shock deceleration nonuniformities [38]. Another source of test gas turbulence is that the driver gas behind the contact discontinuity may transition to turbulence, and the transition front can propagate downstream to ultimately reach the test slug [76]. A third source of transition is the contact discontinuity itself because of vorticies associated with a variety of causes, leading to a growing turbulent boundary layer at the rear of the test slug [41]. Most of the analysis in this thesis will assume a laminar flow, but some additional detail of the transition process is described in a later section.

2.1.2 DIAPHRAGM EFFECTS

In ideal analyses of shock tube flows, the diaphragm is assumed to instantaneously disappear across the whole section of the tube, thus allowing the waves to form immediately. In reality, the diaphragm bursts over a finite time and also spatially deforms, causing the formation of the shock wave to be an extended, unsteady process. White [78] first reported that the finite opening of the diaphragm influenced the strength and trajectory of the primary shock. White stated that a series of compression waves are generated which overtake the primary shock wave and influence its trajectory due to the widening constriction of the bursting diaphragm. Simpson et al [71], followed later by Rothkopf and Low [69], investigated the effects of producing 'scored' diaphragms, where a series of lines are deeply

inscribed upon the diaphragm to weaken it in those areas, allowing the diaphragm to open in a more even manner. A comparison of a scored and an unscored diaphragm after burst is seen in Figure 2.4.

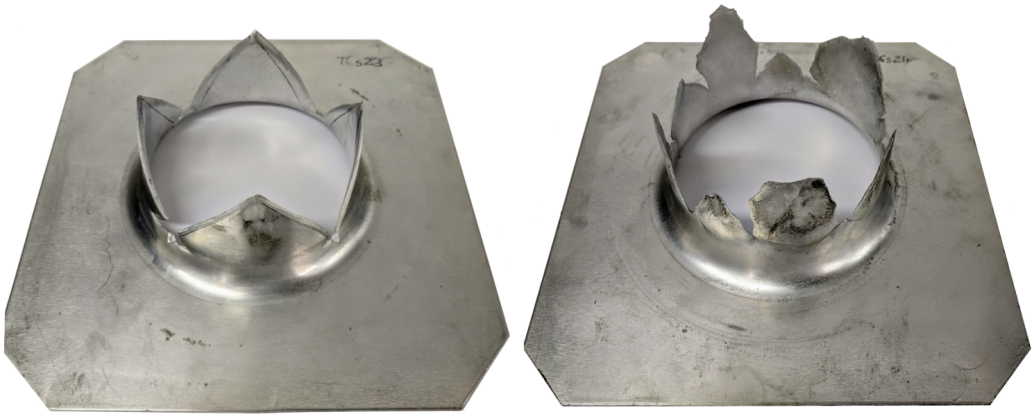

Fig. 2.4 Comparison of scored and unscored diaphragms after burst. Image from [17].

Although the flow is substantially improved by the scoring, the slower opening causes the shock to take several meters to accelerate to its full speed and may reach faster speeds than those predicted by ideal shock theory [18, 69, 71], yielding still further uncertainties in test slug characteristics. If the diaphragm is not scored, it bursts unevenly in a roughly circular shape, and can send shrapnel along behind the main discontinuities [18]. In such a case, the discontinuities form more quickly, but cause non-uniformities in the test gas, alter the shock trajectory, and scatter debris into the flowfield, all of which can rapidly combine with thermochemical effects to produce significant uncertainties in the measured qualities of the test slug [69, 18].

White [78] also reported that the finite opening of the diaphragm should lead to a radial disparity of flow speeds around the contact discontinuity, transforming it into a mixing region rather than an actual discontinuity. Rothkopf [69] added to this depiction of a deformed contact discontinuity by noting that the unsteady bursting of the diaphragm and development of the discontinuities cause transverse waves which further contaminate the test slug with driver gas. Petrie-Repar [65] performed axisymmetric, inviscid simulations of the opening process and showed that a spherical shock initially forms. The resulting post-shock flow combines with the various waves and radial velocities emerging from the constricted diaphragm to cause substantial and enduring unsteadiness in the initial shock formation, and also a highly distorted contact discontinuity. Because of minor manufacturing variations in diaphragm thickness and scoring, the bursting process for each nominally identical diaphragm under nominally identical test conditions will be slightly different. Thus, repeat tests for the same conditions produce variations in shock speed and test results from test to test [28]. Altogether, the finite opening of the

diaphragm leads to substantial variations in shock speed, test slug properties, and test time as the deformed contact discontinuity contaminates the test gas.

2.1.3 DRIVER EFFECTS

In order to produce high strength shockwaves, a high sound speed ratio across the diaphragm is desired [67]. Thus, in addition to the high pressures which cause diaphragm burst, high temperatures in the driver section are also desired in order to maximise shock tube performance. In order to attain both, many different processes have been devised. Some examples include the free piston driver [56], electric arc heated drivers [19], detonations [61], and others. Each of these methods of compression and heating produce spatial and temporal nonuniformities of both pressure and temperature in the driver gas, and heat transfer into the cold wall produces additional radial nonuniformities. The high temperatures also cause appreciable thermochemical effects under many conditions, which couple with the pressure, temperature and temporal nonuniformities. Resler [67] proposed, and Alpher [1] experimentally confirmed and more fully explained that use of a driver section wider than the driven tube produces a stronger shock due to isentropic effects, and so an area convergence between the driver and driven sections is also common in experimental facilities.

While the shock and contact discontinuity travel downstream, the expansion wave propagates upstream into the driver gas at a speed of $u-a$. The expansion wave causes the driver gas to expand into the lower pressure tube, sending compression waves ahead of it at a speed $u+a$. Although ideal shock tube analysis assumes initially uniform properties upstream of the diaphragm, actual shock tube experiments rarely produce such a condition because of the many nonuniformities in the driver gas. Driver gas temperature and thermochemical nonuniformities cause variations in the speed of of sound and thereby expansion wave speed and strength. Multidimensional effects such as the formation of a boundary layer and flow formation through the driver/driven area constriction are coupled with the opening diaphragm, further complicating the flow through it. Simultaneously, the process driving initial compression does not stop with the bursting of the diaphragm. For example, a free piston will continue to move, producing additional compression waves. Thus, additional nonuniformities and waves are introduced to the expanding flow as the expansion wave works upstream through the driver. Eventually, the expansion wave will reach the rear surface of the driver section, reflect from the wall, and travel downstream at a speed of $u+a$.

Jacobs [45] showed that strong transient waves are produced by the compression process in a free-piston shock tube, and must be accounted for in the modeling of reflected shock tunnels in order to accurately capture variations in the final test slug. McGilvray, Dann and Jacobs [55] demonstrated the necessity of including driver gas effects in characterising the test gas. If the reflected expansion wave reaches the test slug, it will also influence conditions in the test gas.

While driver waves directly influence the content of the test slug, shock speed is also affected by the waves produced by driver gas expanding into the low pressure tube. Although area convergence and compression processes such as piston motion may help to attenuate the reflected expansion wave, under many circumstances the wave will ultimately catch up to the shock, causing the shock to attenuate rapidly. In a similar manner, the variations in driver expansion due to nonuniformities in the driver section produce waves which also influence the shock speed. Kendall [48] demonstrated that entropy distribution in the driver gas influences the shock speed, and recommended a variety of methods to uniformly heat the driver gas prior to pressurization. Taken together, it is clear that waves emerging from the driver section exert a potent influence upon shock tube performance.

2.1.4 THERMOCHEMICAL NONUNIFORMITIES IN SHOCK TUBES

Because thermochemical relaxation takes a finite amount of time after initial excitation of gas by the shock, some portion of gas in the test slug is always in nonequilibrium, and at least some small degree of thermochemical nonuniformity must be present behind the shock. If a given packet of shock-processed gas is tracked, the amount of gas pressed in front of the packet compounds rapidly, and the packet may be pushed deep into the test slug before the relaxation has reached equilibrium values, thus yielding a strong spatial chemical gradient. In characterising the nonuniformities within a region of test gas, its location within this relaxation process must be accounted for, as seen in Figure 2.5.

Spence [72] demonstrated that the relaxation of species behind the shock causes shock attenuation. Given enough time and absent other disturbances, the shock will attenuate until it reaches a state where the flow behind it is almost entirely equilibrium. Thus chemical nonequilibrium introduces additional nonuniformities into the flow by virtue of influencing shock speed.

It is clear that, even under analyses disregarding other sources of test slug nonuniformities such as boundary layer effects, the region of chemical nonequilibrium associated with high speed shock

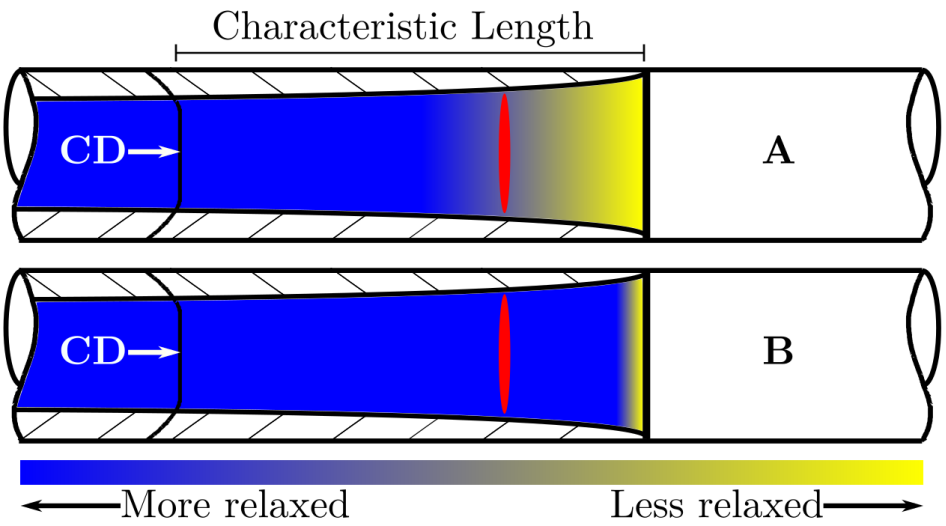

Fig. 2.5 A slice of gas located in a nonequilibrium (A) and an equilibrium (B) section of the test slug.

tube tests introduces a substantial nonuniformity behind strong shocks, which is observable in the measured outputs (e.g. radiative emission). However, Light [52] in his analysis indicates that the nonuniformities arising from other sources, such as boundary layer effects or variations in shock speed should contribute an associated nonuniformity in chemical species throughout the test slug, in addition to the relaxation process. Thus the nonuniformities introduced by thermochemical relaxation will both interact with and be exacerbated by those flow nonuniformities produced by nonideal shock tubes, producing a sort of chicken-and-egg problem.

As temperature and pressure vary through the test slug, the equilibrium conditions which are eventually reached by the relaxing gas will likewise be variable, causing an observable chemical gradient. Distinguishing between a spatially variable equilibrium condition and nonequilibrium relaxation based on radiative measurements becomes challenging. Put differently, the question becomes: "where does nonequilibrium end, and equilibrium begin?" The challenge of this question is highlighted by Figure 2.6, which is taken from Collen et al 2019 [18]. Figure 2.6 compares the post-shock radiance as measured under nominally identical conditions at the Oxford T6 Stalker free piston facility and the NASA EAST arc-driven shock facility. The dotted lines represent an analytical prediction for each, with different magnitudes because of difference in tube diameters leads to the T6 tests being optically more thin. Also, the initial rising slopes are different because of measurement technique [18]. However, radiance in both the nonequilibrium and equilibrium portions of the test slug are seen to follow entirely different trends, and there is no clear indication of where nonequilibrium is occurring. The portion thus labeled as equilibrium was identified for the brief period of constant radiance in the

EAST dataset. Equilibrium radiance constitutes the bulk of radiative heat transfer to the vehicle under many flight conditions such as Earth entry from a Lunar return. Thus, challenges in identification of the equilibrium region are a major source of uncertainty to prediction of radiative heat transfer [21], in addition to those uncertainties such challenges introduce into the analysis of chemical rates.

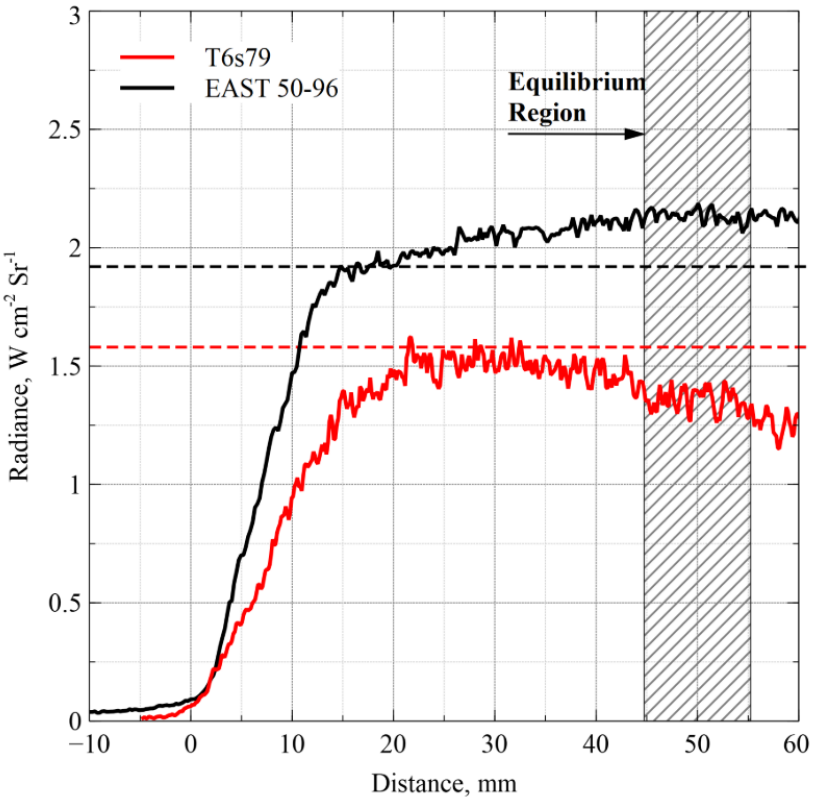

Fig. 2.6 Comparison of radiance measured at nominally identical test conditions between Oxford T6 Stalker facility and the NASA EAST facility. Source: Peter Collen et al 2019 [18].

In addition to the challenge of deconvoluting flow nonuniformities from thermochemical relaxation, the relaxation rates themselves are highly sensitive to pressure and internal energy variations. As a result, the nonequilibrium region will itself be influenced by nonideal effects. Since the chemical gradients are themselves often the desired outputs of experimentation, characterization of the interaction of thermochemical relaxation with flow nonuniformities in the test slug is of crucial importance. This situation is aptly summed by Brandis *et al* [6] when they state: 'the idea of "measuring" the level of equilibrium is very difficult, if not impossible.'

2.1.5 SHOCK SPEED VARIATION

The strength of the shock varies substantially as a result of the many nonuniformities discussed above compounding and interacting. This variation causes the test gas at different locations to be

processed by different strength shocks [61]. The test gas thus processed is retained within the test slug, and so different portions of the test slug possess different levels of entropy, leading to a variation of internal energy and pressure throughout the test slug which do not have time to relax via thermal conduction. Mirels [58] first remarked that entropy variations in the test slug due to nonuniform shock motion might contribute to nonuniformities in the test slug, but otherwise neglected to comment further. Mirels later mentioned [60] that this influence existed, but his analysis was focused around a limiting case wherein shock speed has ceased to vary, and so explicitly disregarded it in his estimations of nonuniformities in test slug properties.

Holbeche first proposed that variations in shock speed produce non-negligible entropy variations through the test slug [40], but assumed only minor variations, thus limiting the findings. In 1973, Light [52] also proposed a model involving entropy variations, but did not investigate the influence of expansion waves produced by pressure reduction behind a decelerating shock. These models and their respective shortcomings are addressed in a later section. It is clear from these sources, however, that the conditions in the test slug are directly affected by the various unsteady waves, and are further indirectly affected by them via the variations in shock speed in response to those waves. Interestingly, although a variety of sources explicitly suggest that shock speed variation may be the cause of much uncertainty in shock tube experimental results, no recent work has rigorously attempted to accommodate this influence into analytical characterisations of the flow. Since the studies of Holbeche and Light were limited in their application and generality, it is also clear that further investigation into the influence of shock speed upon test gas nonuniformities is required.

2.2 CHARACTERISING SHOCK TUBE EXPERIMENTS

Considering the many established nonuniformities in shock tube experiments, accurate understanding of the conditions under which radiative measurements are made is essential. Cruden [23] stated, ‘there can be no substitute for well-characterized experimental measurement of radiance in relevant conditions.’ Extending consideration to the application of shock tube experimental results, characterization of the experimental conditions which are used to understand the thermochemical and radiative environment are ultimately critical in flight vehicle design and numerical simulations of flight vehicles.

2.2.1 EXPERIMENTAL CHARACTERISATION

Despite the simplicity of concept in running a shock down a tube and measuring the flow behind it, actually obtaining accurate measurements of any aspect of the flow presents a daunting challenge. The primary barriers to accurate measurement are: test times on the order of a few hundred microseconds or less, a need to shield sensors from shrapnel originating with the bursting diaphragm, extreme pressures and temperatures which tend to destroy delicate and costly sensors, and the physical limitations of what may be directly measured in a supersonic flow. The most common experimental diagnostics for flow analysis are measurement of:

1. Shock speed by use of:
    - Shock timing pressure transducers along tube wall
    - Photomultiplier tubes
    - High speed video
2. Wall and stagnation heat flux
3. Wall static pressure
4. Pitot pressure
5. Emission and absorption spectroscopy

Reviewing this list, it is clear that the only post-shock flowfield variable which is directly obtainable is static pressure, possible only under the generally reasonable assumption that wall static pressure is the same as the core static pressure. Each of the other measurements involves the inseparable influences of thermochemistry, flow speed, and even transport property variations, and so obtaining information about the flowfield itself is challenging. Knowledge of the shock speed, however, provides the basis for numerical and analytical characterisations.

2.2.2 MODELLING AND SIMULATION OF SHOCK TUBE FLOWS

A summary of relevant numerical efforts regarding the modelling and simulation of high enthalpy shock tubes to date is now given. Numerical characterisations of shock tube flows may be divided into three broad categories: 1) *a priori* based upon initial conditions 2) *a posteriori* informed by experimental shock speed measurements and 3) systems of combining the results of multiple methods. Within each of these categories, a number of different types of approaches may be applied:

1. *a priori* based upon initial conditions
    - Zeroth-Dimensional models
    - One-dimensional simulations
    - Multidimensional simulations
2. *a posteriori* informed by experimental data
    - End-tube shock speed only
    - Variable shock speed
3. Hybrid methods

The published efforts relating to each of these categories are now reviewed.

2.2.2.a *A PRIORI* CHARACTERISATIONS

A priori characterisations use given fill and burst conditions with tube geometry to predict conditions in the test section. Such simulations can only produce a single output for a single input. In other words, the shot-to-shot variations which are caused by non-ideal effects are not possible to capture by such methods. However, such simulations are helpful in experimental designs, and for studying the general behaviour of different flow phenomena.

James *et al* [46] recently published the PITOT code, which is an example of a multitude of locally utilised zeroeth-order simulation techniques. Such methods use closed-form thermodynamic relations and models to predict the state of the gas at the end of the tube from theory. Non-ideal effects such as the boundary layer effects can only be accounted for indirectly, e.g. by setting the post-shock gas speed equal to the shock speed in accordance with the predictions of Mirels under the limiting condition. Other effects such as the influence of a variable shock speed cannot be accounted for at all, and so the accuracy is highly limited. These codes are helpful in selecting experimental run conditions by anticipating upper and lower bounds for the resulting flow conditions. They can also construct 'state-to-state' analyses of complex facilities with multiple sections and diaphragms, such as expansion tubes.

A variety of one-dimensional codes which solve the Navier-Stokes equations with varying degrees of limitations have been developed to predict shock tube flows. Jacobs [44] developed a one-dimensional Lagrangian solver, L1d, which accounted for finite-rate chemistry and driver waves, including from piston compression. L1d includes shear stress and heat transfer models based on fully developed pipe flow to account for boundary layer effects. More complex boundary layer effects

are included by an attempt to models Mirels' effects, but this application has been shown to be of limited accuracy [29]. The quasi-one-dimensional code has a number of useful features such as: models for the effects of unsteady diaphragm opening; area changes such as those encountered moving between the driver and driven section of many facilities; and spatially and temporally variable driver conditions. L1d allows a computationally affordable full-facility simulation, including the ability to capture multiple tube sections and diaphragms in a complex facility configuration.

Recently, Sharma [66] developed a quasi one-dimensional solution of chemically reacting governing equations which incorporated the burst conditions, mass loss to the boundary layer and the influence of stream tube area changes due to the displacement thickness. The boundary layer was modeled with an arbitrary scaling law to allow for parametric study of the influence of boundary layer effects on shock speed. The parametric nature of the boundary layer, coupled with the lack of consideration of upstream waves led to substantial deviation from the compared experimental results. Nevertheless, the study obtained a quantitative characterization of the role that viscous effects play upon influencing shock speed and post-shock non-uniformities.

In pursuit of accurate multidimensional simulation of shock tube flows, a number of investigational strategies have been employed. These may be divided into two categories: high resolution simulation of some final component of the tunnel such as the unsteady stagnating flow in a reflected tunnel, and simulation of some or all of the actual facility. A multitude of studies utilizing the former strategy may be found in the literature, depending upon the feature of interest. A small sample of different strategies in this regard may be observed in works by Weber [75], Chue [14] and Daru [24] which all investigated, via different starting conditions and limitations in the context of developing computational methods and capabilities, the reflection of the shock off a secondary diaphragm and its resultant flow. A great diversity of strategies and studies of particular phenomenon involved in such flows may be found in the references contained therein. However, by reducing the multidimensional computational domain to only the region of specific interest, non-ideal facility effects are generally captured using one-dimensional or empirical tools when captured at all.

Wilson, *et al* [80] investigated an all-Nitrogen experiment at the NASA HYPULSE expansion tube facility via numerical simulation from a shock-stationary frame of reference. They were able to accurately capture boundary layer effects, and demonstrated the role of transition to turbulence in the growth of the boundary layer. Their major finding was that the thicker boundary layer caused by

transition increased the boundary-layer driven acceleration of the contact discontinuity, consistent with the theory of Mirels [58]. Given the computational limitations of the time, this study was unable to afford a grid of sufficient resolution as to reach grid-convergence, and so the strength of the shock was found substantially different from experimental values.

Goozée, Jacobs and Buttsworth [36] utilized a two-dimensional code developed by Jacobs [44] to perform full-facility two-dimensional simulation of the Drummond free-piston reflected shock tube at the University of Queensland (UQ), Australia with excellent agreement to experimental data. The code used was *mbcns2*, which was the predecessor to the popular Eilmer code [35] of today, and incorporated an 'iris-based' model of the diaphragm which allowed a simplified simulation of the finite diaphragm opening and its effects upon the experiment. Although the paper was largely focused on the post-reflection flow, the simulation achieved good agreement with experiment and concluded that such full-facility simulations may provide 'useful information on the relevant mechanisms' of the flows [36]. For example, the simulations showed that the contact discontinuity deforms significantly under the influence of unsteady diaphragm effects, contaminating the test gas.

Gollan *et al* [34] used L1d to simulate the piston dynamics of the X2 facility, and *mbcns2* (later, Eilmer) to simulate the remainder of the facility. This work applied the methodology established by Jacobs *et al* [43], which used L1d to simulate the piston dynamics in order to produce an unsteady input to the axisymmetric *mbcns2* code for a higher fidelity simulation of the downstream tube sections. The final shock speed was then fed into the POSHAX space marching technique and the results of the two methodologies compared. Gollan *et al* concluded that a hybrid approach which used the unsteady outputs of an L1d simulation in combination with a POSHAX would be potentially 'more useful than the large-scale axisymmetric simulations' [34].

McGilvray *et al* [55] also used L1d and Eilmer to simulate the UQ T^2 tunnel, with excellent experimental agreement for a low enthalpy condition. These efforts showed the importance of upstream wave effects on shock speed. The authors specifically highlighted the elevated expense of full-facility simulation of high enthalpy shock tubes and recommended that such simulations be used primarily to investigate particular features of the flow so as to evaluate the degree of influence which those features exert upon experimental conditions in different facilities [55].

Given the computational expense of full-tube simulations, it may be tempting to reduce the diameter of the simulated tunnel and thereby reduce the cell count. However, Brouillette showed that, at small

scales, 'flow is governed by frictional and isothermal effects'[9]. Mirels' boundary layer effects also scale inversely with tube diameter, making wider tubes less susceptible to viscosity-driven effects [58]. Brouillette also showed that shock speed is directly and dramatically affected by scale, making the capture of multidimensional features such as viscosity all the more critical. Given the strong influence of tube diameter, and also the generally short length of micro-channel tubes (e.g. syringes) as compared to shock tubes used as hypersonic test facilities, the extensive literature surrounding the simulation of shocks in syringes and micro-channels is not further reviewed here.

Kotov *et al* [49] highlighted the grid dependence of discontinuity propagation speed and strength in the context of simulations of the NASA Electric Arc Shock Tube (EAST). Continuing their work, Yee [81] and Kotov in 2014 [49] further linked numerical instability and additional discontinuity inaccuracies with grid convergence in the specific context of chemically reacting flows. Kotov demonstrated that insufficient resolution of the discontinuities leads to an incorrect computation of discontinuity speed, and the problem is greatly exacerbated by the role of chemistry. However, these works were concerned with comparatively short simulations, and so did not attempt to include effects from the driver gas or the longer-term impact of viscosity on discontinuity location. These studies specifically highlighted the prohibitive computational expense of full-tube simulation at sufficient grid resolutions to capture the time-dependent evolution of shock structure and speed.

Chandel *et al* [13] performed simulations of the same NASA EAST conditions as Kotov and Yee in a single domain from frame of reference which moved with the shock in order to reduce the computational load of performing a full-facility simulation. These simulations, performed using the US3D code [10], accounted for thermochemistry and viscous effects over the whole length of the facility for the first time, but computed only the area immediately surrounding the shock and contact discontinuity. Since no non-ideal facility effects were included, the only shock speed variation was due to viscous effects, and as a result the simulation was unable to even qualitatively match the profile of the shock speed. The study concluded that the CFD simulations were predicting very different thermochemical excitation and relaxation processes as compared to the experimental study. The authors suggest to explain the discrepancy that the considerable deceleration exhibited in the experiment and not seen in the simulation is responsible for the differences in thermochemical processes. Figure 2.7 shows the discrepancy between simulated and experimental shock speeds, and the associated divergence in trend and magnitude of post-shock electron number density.

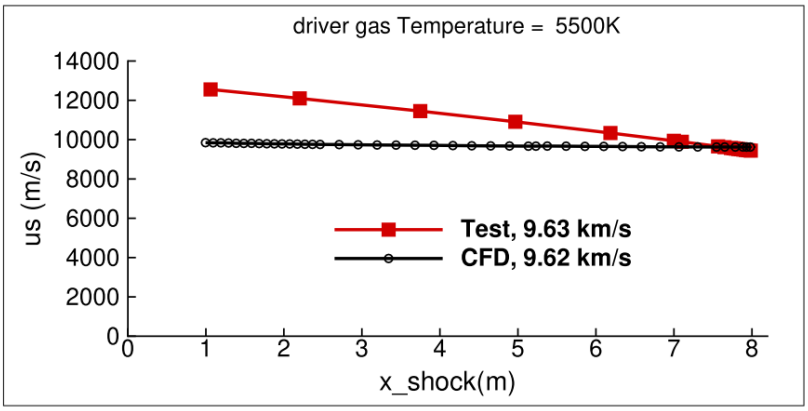

(a) Shock speed profiles.

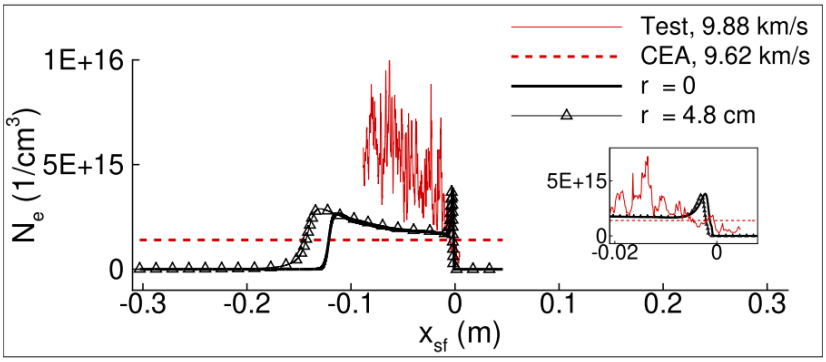

(b) Electron number density profiles at 8 m from the primary diaphragm.

Fig. 2.7 Comparison of simulated and experimental data from Chandel *et al* [13].

Bensassi recently performed a full-facility, time-accurate, axisymmetric, nonequilibrium, Navier-Stokes simulation of a shot through air in the NASA EAST tube [3]. Although the conference paper does not describe the computational expense, an accompanying presentation describes the simulation as requiring 120 days of continuous run and seven months of monitoring the simulation on 1000 cores, producing 12 TB of data; a considerable financial and computational investment [5]. The authors describe a suspected error in the axisymmetric source term as producing a disturbance along the axis, warping the shock and severely disrupting the flowfield. Although the primary results thus contained a number of consequential uncertainties, the scale of the computational costs of the simulation, coupled with the failure of stability which ultimately undermined the investment, works to highlight the present state of numerical simulations of shock tube flows. Such simulations are expensive, challenging, and potentially of limited reliability.

2.2.2.b *A POSTERIORI* CHARACTERISATIONS

Given the limited accuracy of zero- and one-dimensional simulations, and the prohibitive expense of multidimensional simulations, alternative approaches offering computationally cheaper characterisations which incorporate non-ideal effects have been devised. Such methods use experimental data - generally the shock speed - as the basis for analytical assessment of the post-shock flow. The simplest methodology is to treat the post-shock flow as uniform and inviscid, neglecting all nonuniformities not caused by thermochemistry. The POSHAX method is described by Gollan [33] and solves the flow under these assumptions behind a shock of a given speed, obtaining the nonequilibrium distribution of thermochemical species and flow field variables to some desired distance behind the shock. This methodology is used by Lemal *et al* [51, 50] of the Japan Aerospace Exploration Agency, and compared against the data of EAST, obtaining good agreement in the nonequilibrium flow immediately behind the shock, but departing substantially from the experimentally obtained radiance data farther from the shock.

Other models have attempted to accommodate nonuniformities as produced by actual shock tubes. Mirels [60] developed a model for property variations behind a shock of constant speed based upon isentropic deceleration of a subsonic flow, as the test gas may be viewed from a frame of reference in which the shock is held stationary. This was an extension of Mirels' previous work on acceleration of the core flow due to boundary layer mass consumption, and as such accounts only for nonuniformities originating in that phenomenon. Mirels published no attempt to validate the findings against experimental data, but Warshay in 1968 applied the methodology to obtained improved chemical rate constants in a Bromine-Argon mixture [74].

Fujii [26] derived a boundary layer model based on a simplified solution of the boundary layer equations, rather than an approximation derived from exact integrations, and then applied Mirels' model for thermodynamic nonuniformities caused by boundary layer effects to the results. Fujii then extended the analysis to include the influence of such nonuniformities upon the chemical kinetics. He compared the results against particle tracing in an Argon flow. The results were mixed but qualitatively validated the premise of Mirels' method, and uncertainties arose around whether the flow had transitioned to turbulence. Fujii questioned whether the effect of shock speed attenuation was influential upon the nonuniformities, and marked answering the question for future work which did not materialise.

In an extension of Mirels' analysis, a common modern methodology called the 'stagnation-line method' is the simulation of a sphere flying at the steady end-tube shock Mach number. The stganation line properties are then convolved to a spatial distribution equal in length to that of the shock facility test slug. Bensassi in 2020 [4] described this method as 'the standard' approach for flow characterisation, and this is certainly the case in literature by the NASA EAST group with Cruden's 2013 paper [22], and Brandis' 2010 [6] and 2018 [7] papers as representative samples. Palmer *et al* [62] also used this methodology to characterise the flow in the X2 facility. All of these cited papers show significant disagreement between the experimental data and results predicted by this method citing shock history, measurement error, and the fundamental inability of this method to account for free stream nonuniformities as reasons for this disagreement.

Holbeche and Spence performed an analysis which analyzed the variation of enthalpy and entropy at points fixed at some constant distance behind the moving shock [40]. The variation of entropy due to shock speed differences was accounted for under the assumption of only small variations in shock speed such that variations in post-shock pressure, density and velocity were negligible. Variations due to boundary layer effects were also neglected, as this work was completed around the same time that Mirels' landmark work on boundary layer effects was still in production. As a result, this analysis produced only the enthalpy variations due explicitly due to a gradient of entropy within the test slug under highly limited conditions, but again qualitatively showed that entropy changes due even to small variations in shock speed may substantially influence test gas properties.

Light performed an analysis of nonuniformities which included variations introduced by shock speed [52]. Tracking individual slices of gas and determining their velocity and location as determined by mass balance between the shock-processed gas and boundary layer, the entropy of each slice was preserved and its variable thermodynamic properties were solved accounting for variations due to boundary layer effects. However, Light's analysis assumed only small variations in shock speed, and thus makes use of a constant post-shock pressure assumption. The author also acknowledged the significant inaccuracies potentially introduced by not considering relaxation waves produced by the slowing shock or expansion waves arriving from upstream. The results attained only qualitative agreement with experiment, but nevertheless demonstrated the value of including entropy variations due to shock trajectory in analyses. Cruden *et al* [22] performed a somewhat informal investigation

built upon this methodology, noting that it obtained close agreement in one experiment and substantially erroneous results for others and so drew no further conclusions about the method.

Petersen [64] developed a time marching technique which input conditions to a selected initial post-shock state and evolved them isentropically with a variable shock speed. Petersen's approach focused only on the variable entropy and boundary layer effects from the variable shock speed, neglecting the relaxation effects. Furthermore, the study was severely limited by accounting only for small shock speed variations towards the end of the tube, assuming a constant shock velocity for the first 80% of the tube. Nevertheless, Petersen showed in a qualitative sense that entropy gradients caused by shock attenuation meaningfully influence the experimental outcomes. Another key result of Petersen's investigation was its alignment with the results of Rudinger [70] that showed amplification of nonuniformities behind the incident shock in the flows of the reflected shock behind a secondary diaphragm. Thus the work highlighted the criticality of properly characterising the basic shock tube flow in order to understand the flows in more complex facilities.

2.2.2.c HYBRID APPROACHES

Several methodologies apply the benefits of *a posteriori* analysis to the application of *a priori* techniques in order to obtained improved characterisation of experimentally obtained flowfields. A simple version of this is seen in McGilvray *et al* [54], who used L1d and *mbcns2* together to characterise flow in a Hypervelocity Expansion Tube facility. The work was able to obtain improved agreement with experiment by tuning against experimental data the amount of contaminating driver gas present in the initial test gas for the axisymmetric simulations. A more evolved version of such tuning was reported by Gildfind *et al* [29, 30], who simulated the entire 65 m X3 expansion facility using L1d except the final 15 m. Gildfind *et al* tuned the driver temperature in L1d to achieve agreement in shock trajectory with experiment prior to feeding the tuned, unsteady L1d outputs as an input to the axisymmetric Eilmer simulations. This mixture of *a priori* and *a posteriori* methodologies was shown to achieve acceptable agreement with experimental data for both studies.

Gildfind later notes in [28] that the practice of tuning L1d to achieve agreement for input to multidimensional simulation is still a highly expensive technique which is likely to yield discrepancies with experiments that cannot be closed. In order to address these discrepancies, Gildfind then proposes a novel methodology for scaling the final, CFD-computed flow properties based upon experimental

measurements. By using the final experimental data as a scaling guide, the shot-to-shot variations may be accounted for. This scaling is performed by determining the sensitivity of each flowfield variable to changes in the final shock speed, and then adjusting the simulated flowfield variables according to the discrepancy in final shock speed between experiment and CFD. A shortcoming of this methodology is that it cannot account for shot-to-shot variations test gas property profiles, i.e. the shape of the curve; it merely translates the final property profile. Different shock trajectories produce different test gas property profiles (e.g. entropy distribution), and so scaling the results according to the final shock speed is insufficient to fully close the discrepancies between CFD and experiment. The work is also in an early stage of development, and so has yet to be extended to thermochemically reacting cases.

The premise of using only the conditions at the end of the tube for input to a multidimensional simulation is related to a similar approach is used by Bensassi *et al* [4]. The final shock speed obtained from experiment is used to obtain post-shock conditions. These conditions are then used as inputs to simulate only the last 0.3 m of the tube in a steady-state Navier-Stokes simulation, a sufficient distance to cover the test slug. This approach simulates the boundary layer and nonequilibrium thermochemical relaxation effects behind a steady shock, and was shown to obtain improved agreement over the stagnation-line methodology described above, but still notes that substantial disagreements potentially arise from the absence of shock history effects.

2.2.3 Summary

In summary, the literature shows that various means of simulating shock tube physics have been attempted, to lesser and greater degrees of success. In spite of the broad array of developed characterisation methodologies, there are still large degrees of uncertainty in the characterisation of shock tube flows, translating into uncertainties in radiative heat transfer and chemical rates derived from shock tube experiments. The state of this uncertainty may be summed up by McGilvray [55] in his observation that, ‘Experimenters cannot make true assessments where free stream conditions are critical.’ The remainder of this thesis is focused upon developing numerical tools to more efficiently study the nonuniformities in question, and then develop improved analytical techniques with which the nonuniformities may be characterised.

Chapter 3

A NOVEL NAVIER-STOKES SOLVER FOR SHOCK TUBE SIMULATIONS

The present cost of multidimensional simulation of shock tubes is prohibitively expensive. In order to parametrically study the interaction of multidimensional non-ideal effects, a cheaper, yet accurate method of simulation is desired. A methodology is proposed in the next section which solves the Navier-Stokes equations in a shock-stationary frame of reference.

One of the struggles identified with this approach by Chandel [11] was that of choosing a speed for the moving frame of reference. Since the speed of the shock may change substantially, and rapidly, the process must necessarily be automated. Furthermore, if the shock moves between cells, numerical error is accumlated due to the approximate nature of gradient computations [3]. Finally, small errors in frame speed lead to a large degree of travel of the shock within the frame, thus necessitating a larger grid to accommodate the motion while keeping the shock in a fully resolved mesh. For all of these reasons, the automated method of selecting frame speed is desired to keep the shock essentially stationary in the moving frame regardless of the shock acceleration profile.

The test gas between the shock and contact discontinuity is also typically absent discontinuities or other strong gradients such as those associated with turbulence. As a result, fine axial resolution is not required between the shock and contact discontinuity. However, relatively fine resolution is required in order to resolve the contact discontinuity, particularly in the presence of vorticity and mixing as described by Hooker [41] and clearly simulated by Petrie-Repar [65]. Finally, the flow behind the contact discontinuity, although frequently turbulent in nature [76], is not considered to be necessary to capture in full resolution. Some potential limitations of this estimation are examined in

the following paper, but the immediate consequence is that a coarse resolution is desired behind the primary discontinuities. Since the goal of producing the subject numerical method is to maximise efficiency, it is desired that the moving frame contains a highly refined grid only around the shock and contact discontinuity, which are at all times moving with respect to one-another, and both moving ever-farther away from the diaphragm. It is for this reason that each discontinuity is given its own moving frame in which to move along a coarse background grid.

Although the implementation of multiple overset grids moving with respect to one-another is not new to the literature in and of itself, the application of such a methodology to shock tubes certainly is. Likewise, the methods by which this work determines the speeds of the independently moving frames are also new to the literature. Also of note is the automated and flexible construction of nearly any shock facility geometry, including sections of different cross-sectional areas. This automated process makes the simulation of any given flow problem as easy as inputting the tube geometric properties and fill conditions, along with desired grid resolution in each domain, while the automated meshing and domain tracking manage the rest. Thus, although only small parts of the numerical method itself are strictly novel, the particular uses and configuration of the code makes it a uniquely efficient numerical method custom-built for the well-documented challenges of shock tube simulations.

The next section contains a published AIAA Journal paper outlining the mathematical formulation of this methodology as well as the results of a series of simulations validating the methodology against experimental data. One of the experimental datasets is examined indepth because the solver was able to identify the source of as yet unexplained behaviour in a dataset of historical significance. A more detailed mathematical derivation of the formulation is present in Appendix A. The results of the resulting analysis point to the importance of understanding the role of shock speed in test gas nonuniformities. The FROSST code is then used in the following papers as the vehicle by which shock tube phenomena are studied. The findings thereby obtained and described in the subsequent paper then form the basis for an analytical methodology to characterise the nonuniformities in shock tube flows. Additional validation of FROSST against experiments conducted in T6 is then given. DPhil candidate Peter Collen performed the T6 experiments, which were originally intended to be included in the paper itself, and he is acknowledged as a co-author for his general contributions to the discussion.

Numerical Simulation of Shock Tubes Using Shock Tracking in an Overset Formulation

Matthew Satchell *, Peter Collen*, Matthew McGilvray †, and Luca Di Mare†
The University of Oxford, UK

An axisymmetric viscous shock tube simulation code is developed which keeps the shock and the contact discontinuity stationary in suitably constructed moving frames of reference. The flow field around the discontinuities is represented on fine grids which move with the frames attached to the waves. These moving grids are overset upon a coarse background grid of the entire facility, allowing efficient computation of the main discontinuities as they traverse the tube. Focus is placed upon accurate capture of the influence of wave speeds and viscous effects upon the shock and contact discontinuity as they traverse the tube. The code is extensively validated against experiments ranging from Mach 1.6-2.7 in a 26.8 mm diameter shock tube with Argon driver/driven gases and an initial pressure of 66.66 Pa. Agreement within 2% is seen in velocity throughout the tube's length. Test times are predicted to within 6% across a broad range of test conditions. Unsteady diaphragm opening effects as well as turbulent transition are demonstrated to substantially influence experimental results of the well-known experiments of Duff (1959).‖

I. Nomenclature

$\mathbf{U}$	=	Vector of Conserved Quantities
p	=	Pressure, Pa
ρ	=	Density, kg/m^3
T	=	Temperature, K
u, v	=	Axial, Radial Velocities, m/s
E	=	Energy, J
ϑ	=	Cell Volume per Radian, m^3/rad
$\mathbf{F}_c, \mathbf{F}_v$	=	Vectors of Convective and Viscous Fluxes
r	=	Radial Distance from Axis, m
$\mathbf{Q}$	=	Axisymmetric Source Term

*DPhil Candidate, Department of Engineering Science, Oxford Thermofluids Institute, Department of Engineering Science, University of Oxford.
†Associate Professor, Oxford Thermofluids Institute, Department of Engineering Science, University of Oxford.
‖Presented at AIAA AVIATION, 13 June 2020, Reno, NV

S = Cell Face Area, m^3

$\tau_{\theta\theta}$ = Radial Viscous Normal Stress, N/m^2

$\bar{\mathbf{J}}$ = Viscous Variable Jacobian Tensor

$\mathbf{W}$ = Vector of Viscous Variables

k = Velocity Magnitude, m/s

μ = Viscosity, kg/ms

γ = Ratio of Specific Heats

σ = Courant-Friedrichs-Lewey Number

Λ_c = Spectral Radius, m/s

$\mathscr{F}$ = Flux Function

f = Arbitrary Quantity

v_s = Shock Speed, m/s

a = Speed of Sound, m/s

M = Mach Number

i,j = Indices

$\vec{V_S}$ = Reference Frame Velocity Vector

$\hat{n}$ = Unit Normal

λ_* = Primary Wave Eigenvalue, m/s

t_{open} = Diaphragm Opening Time, μs

II. Introduction

Research into hypersonic flows is driven by the needs of planetary exploration and by increasing interest in both access to space and also high speed flight. One aspect of space travel that presents substantial scientific and technological challenges is the entry of space vehicles into planetary atmospheres. Ground-based shock tube facilities are commonly used to reproduce the flow conditions encountered during hypersonic flight, and are uniquely suited to allow the study of, among other phenomena, thermochemical and radiative effects present in hypersonic flowfields.

A shock tube experiment is conducted by holding gas at high pressure and temperature - the driver - at one end of the tube behind a diaphragm separating it from gas at lower pressure occupying the rest of the shock tube - the driven test gas. When the diaphragm ruptures, a shock wave is sent through the driven gas, impulsively raising its temperature and pressure. The shock-heated test gas is followed by the driver gas exhausting through the ruptured diaphragm and by a complex pattern of waves.

In an ideal experiment, the steady, constant-speed shock thus created would process all of the test gas. However,

many non-ideal effects exist which cause variation in the shock speed and thereby the properties of the test slug. Some of the most significant of these disturbances include the wave patterns generated at the start of the experiment, growth of boundary layers in the gas moving behind the shock wave [A1], the finite opening time of the diaphragm, and waves in and caused by the finite driver gas. These effects are collectively known as facility effects, and together perturb the length and properties of the test slug well away from the predictions of ideal theory.

One important type of facility effect is the shock formation distance, or the distance the shock takes to reach its maximum velocity, caused by the opening of the diaphragm. Shock formation distance scales with diaphragm pressure ratio [A2], and is sensitive to diaphragm opening time. This sensitivity increases with greater diaphragm pressure ratios [A2–4]. The analysis of White [A2] shows that the area contraction caused by the presence of the diaphragm acts as a nozzle, causing an unsteady expansion fan through which driver gas is isentropically expanded. The accelerating driver gas produces compression waves which pursue and eventually catch the shock, accelerating it even as viscous effects work to slow it. These waves may continue to drive the shock to higher velocity than ideal shock tube theory predicts [A2, 5]. This fan and its effects last until the diaphragm is sufficiently ruptured to produce a steady expansion which then moves downstream. A diaphragm which opens quickly releases these compression waves in a shorter period of time than a diaphragm which opens slowly. The more rapid delivery gives less time for viscosity to erode the speed and thereby further increases shock velocity when compared with that produced by a slower-opening diaphragm. However, the more rapid compression does ultimately produce greater entropy losses and thus a slightly slower shock if the tube is long enough to accommodate the full formation distance of the shock. Scored grooves upon the diaphragm or the absence thereof also change the nature and extent of the profile by which the diaphragm opens, which also influences shock trajectory [A6].

In the ultimate goal of understanding of the chemical rates and radiation observed in the test slug, accurate characterization of the properties of the test slug itself, as influenced by facility effects, is critical [A7, 8]. However, limited diagnostic capabilities exist to capture the temperature in the core flow at the point where chemical rates are being measured. Furthermore, spectroscopic emission and absorption measurements are volume-integrated across the line of sight of the optical system. As a result, if the measurement is made through the side-wall of the tunnel, radiation emission and absorbtion from the boundary layer cannot be readily distinguished from those originating in the core flow. Likewise, optical arrangement pointed axially along the tube's centreline is unable to distinguish between radiation emitted at the front of the test slug versus that emitted at the rear. In theory, CFD enables calculation of the variations of temperature field and chemistry throughout the test slug, and so for a given experiment the far-field radiative contamination might be quantified by simulation. In practice, however, affordable and accurate multidimensional simulation of shock tube flows has proven elusive [A9–11].

A. Simulation of Shock Tubes

Estimates of facility wave phenomena, piston trajectory and shock behaviour can be obtained by specialized one-dimensional tools, such as University of Queensland's Lagrangian quasi one-dimensional shock tube solver L1d3 [A12]. Studies of the gas slugs in portions of a facility have also been performed using general multidimensional-capable CFD codes applied in a one-dimensional fashion, such as NASA's ADPDIS3D code [A10]. Although these tools are frequently used for parametric studies in the planning of shock tube experiments, they are fundamentally unable to fully characterize the test slug for detailed comparison [A8, 11–14]. The main reasons for this shortcoming are interactions between the contact discontinuity and shock caused by the viscous boundary layer [A13], and multidimensional phenomena, such as the opening of the diaphragm or area changes in the tube. Furthermore, the multidimensionality introduced by area changes influences shock trajectory, which in turn influences the characteristics of the test slug [A15]. All these factors lead to substantial differences between test slug sizes and locations [A5, 16, 17] predicted from one-dimensional methods and experimental observations.

Two- and three-dimensional unsteady numerical methods overcome some of the limitations of one-dimensional methods in predicting the properties of the test slug, but at the price of vastly increased computational cost. In fact, the full multi-dimensional characterization of the test slug in a shock tube using a stationary frame of reference is prohibitively expensive because of the contrasting requirements of resolution - needed to accurately compute the rates of travel of discontinuities, and domain size - needed to capture upstream wave effects on those discontinuities. The considerable expense of multidimensional hypersonic shock tube simulations is the main obstacle to the numerical computation of a full shock tube experiment, even in the context of modern supercomputing resources [A11, 14, 18].

One effective method of simulating the multidimensional flow is to move the computational domain into a frame of reference which moves with the shock, as implemented by Wilson in 1995 [A9] and proposed for use with modern computational tools by Adams in 2016 [A19]. The motion of the computational domain, however, brings still further challenges, among which is determination of an appropriate frame speed [A11]. If the frame speed is constant while the shock speed actually varies, the mesh must be refined as the shock moves within it or else the refined zone must be relatively large. In a Lagrangian frame of reference, finite mass formulations cause substantial mesh deformation as viscous effects and shock/contact discontinuity speeds vary, leading to expensive remeshing operations [A20]. Because of these and other challenges, relatively little literature has focused on the high resolution simulation of the shock as it travels the undisturbed tube, leaving an uncertainty gap in experimental methods as to the sources and magnitude of variations in the test slug.

This paper presents an axisymmetric, explicit, structured finite volume solution of the Navier-Stokes equations for the ideal gas simulation of shock tube flows. The solver, known as the FRamework for Overset Simulation of Shock Tubes (FROSST) is written using an overset formulation that enables different highly refined grids to track the contact discontinuity and shockwave separately. The moving computational domains are overset upon a coarse solution

of the Navier-Stokes equations for the whole tube, allowing for modeling of the expansion and compression waves which propagate through the tube from the driver pressurization and diaphragm bursting processes while reducing the computational cost of doing so dramatically.

The FROSST formulation enables detailed, full-facility investigation into fundamental, yet poorly understood, effects influencing shock tube experiments such as waves from the driver section and the diaphragm opening process. Furthermore, by focusing on ideal-gas conditions, uncertainties introduced by real-gas effects may be avoided and the accurate function and efficiency of the algorithm may be assessed prior to introduction of thermochemistry. Although the present effort examines comparatively low-speed cases, the facility effects studied herein are present at higher speeds as well. This paper establishes a novel method of improving understanding of these effects, and in validation of this capability, explains the hitherto unidentified causes of the deviation of the experiments of Duff [A21] from both theory and the results of nominally comparable data sets.

III. Numerical Formulation

FROSST solves the unsteady Navier-Stokes equations for an ideal gas using a viscous variable formulation, the details of which will now be outlaid where implementations are not directly derived from literature. The use of an overset formulation on shock tube simulations in order to capture facility effects is a new development in viscous shock tube simulation. Furthermore, a new method of domain speed determination is described in order to overcome the challenges of applying a moving domain to shock tube simulations described in the recent works of Chandel [A11], which resulted in excessively large zones of refinement in order to accommodate motion of the shock within the frame. Let U be the vector of conserved quantities at cell centres in two dimensions:

$$\mathbf{U} = \begin{bmatrix} \rho \\ \rho u \\ \rho v \\ \rho E \end{bmatrix} \tag{1}$$

The Navier-Stokes equation can be expressed in a finite volume formulation as:

$$\frac{\partial}{\partial t}\int_{\vartheta} \mathbf{U} d\vartheta + \int_{\partial\vartheta} r(\mathbf{F}_c + \mathbf{F}_\mu) dS = \int_{\vartheta} \mathbf{Q} \partial\vartheta \tag{2}$$

Here, $\mathbf{F}_c$ and $\mathbf{F}_\mu$ are the convective and viscous fluxes of the conserved quantities, respectively, and S is the area of the face between each cell, with the volume per radian given as ϑ. $\mathbf{Q}$ is the axisymmetric source term, given in terms of the cell center pressure p and radial viscous stress $\tau_{\theta\theta}$ as:

$$\mathbf{Q} = \begin{bmatrix} 0 \\ 0 \\ p - \tau_{\theta\theta} \\ 0 \end{bmatrix} \tag{3}$$

Transforming the updated variables to viscous variables $\mathbf{W} = [u, v, P, T]^T$, noting that cell volumes are held constant at all times, Equation 2 becomes:

$$\bar{\mathbf{J}} \frac{\partial \mathbf{W}}{\partial t} \vartheta + \int_{\partial\vartheta} r(\mathbf{F}_c + \mathbf{F}_\mu) dS = \int_{\vartheta} \mathbf{Q} \partial\vartheta \tag{4}$$

where

$$\bar{\mathbf{J}} = \frac{\partial \mathbf{U}}{\partial \mathbf{W}} = \begin{bmatrix} 0 & 0 & \frac{\rho}{P} & -\frac{\rho}{T} \\ \rho & 0 & \frac{\rho u}{p} & -\frac{\rho u}{T} \\ 0 & \rho & \frac{\rho v}{p} & -\frac{\rho v}{T} \\ \rho u & \rho v & \frac{\rho k}{p} + \frac{1}{b} & -\frac{\rho k}{T} \end{bmatrix} \tag{5}$$

Convective fluxes $\mathbf{F}_c$ are evaluated at cell faces using an Advection Upstream Splitting Method (AUSMPW+) flux vector splitting formulation [A22]. Hemker & Koren's limiter [A23] is placed upon a second-order MUSCL extrapolation and is implemented as detailed by Blazek [A24]. AUSMPW+ is a modification of the AUSM+ scheme designed for stability in the region of shockwaves and boundary layers at high Mach numbers, and has been shown by Kitamura and Roe [A25] to avoid the carbuncle phenomenon in hypersonic flows more reliably than most other fluxes. The details of the flux implementation may be found in Kim et al 2001 [A22]. For the purpose of flux evaluation in a frame moving at speed v_s, the left and right Mach numbers in the AUSMPW+ flux are modified as follows:

$$M_{l,r} = \frac{u_{l,r} - v_s}{a_{l,r}} \tag{6}$$

where $a_{L,R}$ is the speed of sound and $v_s = \vec{V}_S \cdot \hat{n}$ is the component of the frame velocity normal to the cell's face.

The spectral radius of the flux Jacobian at each face is also computed for use in computation of the local Courant number, and is likewise modified by the frame speed. The maximum eigenvalue is found as:

$$\lambda_M = max(a_l, a_r) + max(|u - v_s|, |u + v_s|) \tag{7}$$

The vector of viscous fluxes F_μ is discretized using central differences on a 6-cell stencil shown in Figure 1. Gradients $\frac{\partial f}{\partial x}$ at the face $i + \frac{1}{2}$ are constructed by a central difference from the cell centers at level j. Derived quantities, such as density and viscosity, are computed for the left and right states prior to averaging.

$$\frac{\partial f}{\partial \mathbf{x}} = \left(\frac{\partial \mathbf{x}}{\partial \xi}\right)^{-1} \frac{\partial f}{\partial \xi} \tag{8}$$

with

$$\frac{\partial f}{\partial \xi} = \begin{bmatrix} \frac{\partial f}{\partial \xi} \\ \frac{\partial f}{\partial \eta} \end{bmatrix} = \begin{bmatrix} f_{i,j} - f_{i-1,j} \\ \frac{1}{2}\left(f_{i,j+1} + f_{i-1,j+1} - f_{i,j-1} - f_{i-1,j-1}\right) \end{bmatrix} \tag{9}$$

For the viscous j-fluxes, the same stencil planform is used, but rotated 90°. Using gradients thus computed, assuming Stokes' hypothesis for the bulk viscosity, and assuming a Newtonian fluid in 2-dimensional flow, the viscous stresses are then constructed as given by Blazek [A24].

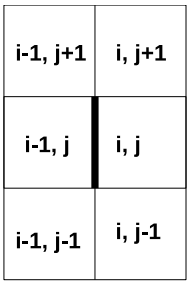

Fig. 1 i-Face Stencil for Viscous Fluxes

Time stepping is achieved by use of a second-order accurate Heun's method. Starting with a forward Euler prediction W_1, a corrector stage W_2 is applied and then the resulting solutions are averaged for the solution update:

$$\mathbf{W}_1 = \mathbf{W}^n + \bar{\mathbf{J}}^{-1} \frac{\Delta t}{\vartheta} \mathscr{F}(\mathbf{W}^n) \tag{10}$$

$$\mathbf{W}_2 = \mathbf{W}^n + \bar{\mathbf{J}}^{-1} \frac{\Delta t}{\vartheta} \mathscr{F}(\mathbf{W}_1) \tag{11}$$

$$\mathbf{W}^{n+1} = \frac{1}{2}(\mathbf{W}_1 + \mathbf{W}_2) \tag{12}$$

The inverse of transformation Jacobian $\bar{\mathbf{J}}^{-1}$ is:

$$\bar{\mathbf{J}}^{-1} = \begin{bmatrix} -\frac{u}{\rho} & \frac{1}{\rho} & 0 & 0 \\ -\frac{v}{\rho} & 0 & \frac{1}{\rho} & 0 \\ kb & -ub & -vb & b \\ kb\frac{T}{P} - \frac{T}{\rho} & -ub\frac{T}{P} & -vb\frac{T}{P}v & -b\frac{T}{P} \end{bmatrix} \tag{13}$$

and

$$\mathscr{F} = \int_{\vartheta} \mathbf{Q}\partial\vartheta - \int_{\partial\vartheta} r(\mathbf{F}_c + \mathbf{F}_\mu)dS \tag{14}$$

The explicit timestep is computed from the CFL σ by the definition:

$$\Delta t = \sigma \frac{\Delta x}{\Lambda_c} \tag{15}$$

Here, Λ_c is estimated conservatively from the sum of the maximum eigenvalues of the convective flux Jacobian across each face in a cell, as computed previously, and the constant $b = \gamma - 1$ and $k = \frac{1}{2}(u^2 + v^2)$.

All velocities variables are absolute, i.e. referred to the laboratory frame of reference. Fluxes and spectral radii of flux Jacobians are modified as shown in equations 6 and 7 in the blocks with moving grids. In this way the velocities computed in each domain are kept from coming into conflict at each zone of interpolation, and the addition of an acceleration term to the time derivatives is avoided. In other words, the state in each cell is not directly adjusted for the moving frame; only the fluxes are adjusted to account for the motion. Because the cells are not deforming but merely translating, the geometric conservation law is automatically satisfied [A24]. Running the solver for a uniform flow in an accelerating frame as formulated above was shown to preserve the uniform state.

IV. Mechanics of the Moving Frames

Before developing the algorithms used for computation of frame speeds, some background on the uses of moving frames in FROSST is necessary. The primary stationary grid, Domain 0, extends the length of the whole tube and exists primarily to propagate the waves produced by the driver section. The moving grids 1 and 2 may be set independently to the speeds of the shock and contact discontinuity, respectively, or set so that Domain 2 moves with Domain 1 and effectively acts as an extension of Domain 1, growing coarse away from the shock. Fine resolution of uniform spacing is used in the immediate vicinity of the discontinuities, while the grids are allowed to grow at a rate of 10% in the axial-direction as they move away from the refined zones. All domains use an isothermal no-slip wall condition at temperature T=300 K.

All grids are Cartesian and produced automatically at the outset of each run based on the desired layout of the tube. Presently, the stationary background grid consists of four blocks which constitute the zones separating spatial variations

as seen in Figure 2. In keeping with a desire to keep the code computationally lightweight, and made possible by the simplicity of the facility's geometry, all area changes are treated as spatially instantaneous. Thus the diaphragm is represented by a wall boundary condition at the shared ends of Domains 3 and 4, with direct-injection interpolation from the adjacent domain feeding the ghost cells of those portions of the boundary beyond the top of the obstruction, which are not against a wall. The diaphragm opens as an iris, the implementation of which is discussed later. Because of the overset formulation, each background domain is able to have its own level of grid refinement as required for stability and accuracy. Domains 3 and 4 form the initial zones of the driven and driver sections, respectively, and may be refined sufficiently to resolve the shock formation as necessary.

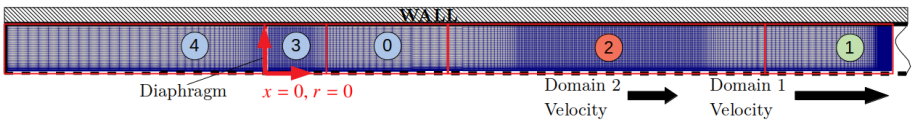

Fig. 2 Layout of the Computational Domains

Interpolation from and to moving domains is done via a Cartesian product of a minimum-gradient limited interpolation in the axial and radial directions from the donor grid. As Domains 1 and 2 move, the range of updated values in each is selected to overlap by 3 cells, where two ghost cells in each overlap with updated cells in the counterpart grid, as seen in Figure 3. Algorithm 1 shows the pseudocode method of computing the Cartesian product of the minimal gradient at the desired cell in the context of destination cells located at the end of a domain (nominally Domain 2) overlapping with the start of another domain (Domain 1). Gradients across either side of the source cell are computed, and the least of the two gradients is selected for extrapolation to the destination cell's center from the source's center. This algorithm is repeated in the radial direction based on the extrapolated values computed first in the axial direction. Each iteration, the interpolated cells first obtain values by this minimum gradient method, and then the fluxes are computed through all domain cells and integrated in time. It is thus clear that the ghost cells i_{end+1} and i_{end+2} are only updated by action of the interpolation, whereas the final domain cell i_{end} receives an interpolated value, and is then updated by the resulting fluxes and time integration. This updated value is then available on the next iteration for any cell which references i_{end} as a source for interpolation.

This methodology of interpolation was shown not to produce spurious waves in the presence of weak discontinuities or a boundary layer under a broad variety of conditions. It is important to observe that the interpolation scheme is applied only to the moving domains after they have begun moving; all domains are stationary at the outset of the simulation, with cell centres aligned exactly so as to allow direct injection of source cell values into the destination cells across domain boundaries. Since each moving domain keeps a primary discontinuity centred within it, far from the domain edges after motion has started, use of this non-conservative interpolation scheme is carefully restricted to use in regions with only weak or no discontinuities.

A number of studies were performed explicitly seeking artificial discontinuities in flow variables across interpolation zones, using grids of various sizes and under many conditions, and showed this scheme to produce negligible errors. These results are not presented herein. However, a more rigorous validation should be performed in a future study in order to quantify the order of discretisation error thereby produced. Such a study might be performed by initialising a flow with a known gradient across a boundary, and comparing the computed conserved quantities against those of the known solution. By repeating this exercise across a number of gradient orientations (e.g. radially aligned, axially aligned, or mixed), and across a number of grid sizes, the performance of the scheme under different conditions may be determined.

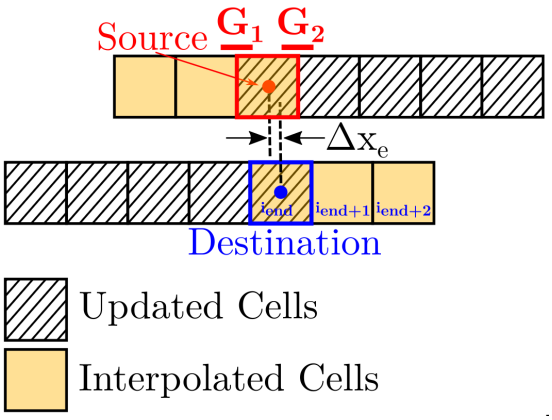

Fig. 3 Minimum Gradient Interpolation Stencil

Algorithm 1 Minimum Gradient Interpolation

1: **for** i_{end} to i_{end+2} **do**
2: find source cell containing destination cell center
3: compute Δx_e
4: compute gradients G_1 and G_2
5: $G_e = min(|G_1|, |G_2|)$
6: $Q(i) = G_e \Delta x_e$
7: **end for**

No interpolation is necessary between grids 1 and 0, since the state ahead of the shock is uniform in the present formulation and Domain 0 is not updated ahead of Domain 1. Thus the solution is updated on the background grids from the left wall to the start of Domain 2, on the moving domains from the start of Domain 2 to the selected point between 2 and 1, and then that same point on Domain 1 to its end, just past the shock. This layout ensures that none of the primary discontinuities cross between the grids at any point after startup, as each of the moving domains is designed to keep its respective discontinuity within it. This method of solution also avoids the reproduction of computations at a given spatial location across multiple grids; the background Domain 0 is never updated in the regions covered by the moving domains, but rather has cells in those regions deactivated. Those cells are thus only activated and updated after

the moving domains have passed by.

All domains begin the simulation stationary, and begin moving only when the shock has reached the desired location within Domain 1. This location is defined by the user, and for this work was typically set near the centre of the refined zone. Domain 1's frame speed is computed in such a manner as to limit the shock's movement to within one cell of the initial position in the domain. Doing so allows extremely fine resolution of the shock while keeping the extent of fine mesh resolution limited only to the region immediately surrounding the shock. The refinement zone is constructed sufficiently large to accommodate shock curvature and deformation, which is often substantial during the few meters of shock travel [A5]. An example of a curved shock, stationary in its refined zone, is seen in Figure 4. Since the degree of shock curvature or deformation for a given case is not typically known a-priori, a conservative estimate based on experience with the conditions being simulated was used to size the refined shock zone. However, after performing simulations across a broad variety of conditions, it was found that a width of 100 cells was sufficient to ensure a wide enough refinement zone to encompass the shock during all observed deformations. This was routinely checked for new cases by running a simulation until the desired starting motion of the domains and checking a visualisation. By this time, shock deformation due to unsteady opening effects, which typically exceeds curvature due to viscosity, was in the process of settling out. Given the small computational expense of the code, such a check was not considered prohibitively expensive.

In order to keep the shock stationary in its moving domain, two steps are completed. First, the discontinuity is identified, and then the speed of propagation of the discontinuity is determined. Identification of the shock is performed by seeking the strongest pressure gradient along the symmetry boundary of the domain. Having identified the shock, its speed may then be calculated and the domain speed thereby set. Since the shock may be substantially deformed, the calculation of shock speed is repeated across the shock at each radial location in the inner 75% of the tube radius, and the fastest shock speed thus computed is taken as the domain speed. Aside from a short initial period during the initial diaphragm opening if a finite diaphragm model is used, the centreline is typically the radial location which determines the shock speed.

The right-going acoustic wave speed λ_4 in the Riemann problem is the speed of the propagation of information to the right across a right-going discontinuity, as seen in Figure 5. In the case of a shock, λ_4 is therefore also the speed of the shock for an inviscid, perfect gas flow. Thus, if the states to the left and right of the shock are treated as inputs to a Riemann problem, Roe's characteristic analysis enables computation of the wave speeds across the discontinuity, from which the frame speeds may be set. The right-going acoustic wave speed is an eigenvalue of the Roe Jacobian [A26]:

$$\vec{V}_s = \lambda_4 = \tilde{u} + \tilde{a} \tag{16}$$

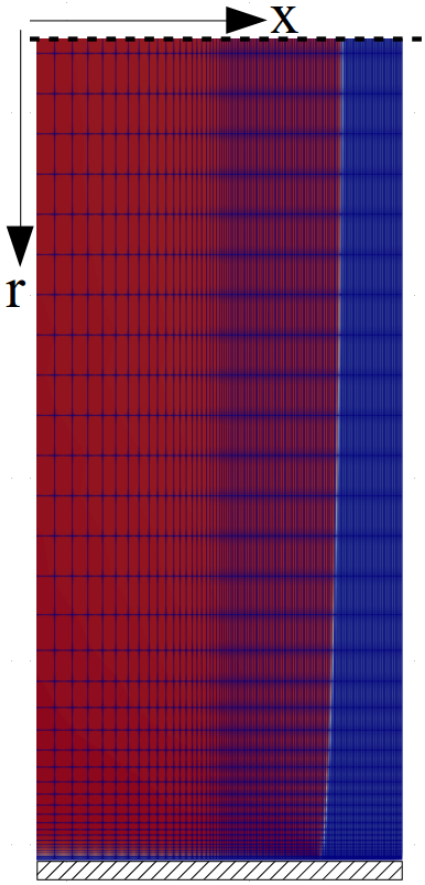

Fig. 4 A curved shock fit within its refined grid. Contours of velocity magnitude.

The Roe variables in one dimension are computed as:

$$\tilde{u} = \frac{u_L\sqrt{\rho_L} + u_R\sqrt{\rho_R}}{\sqrt{\rho_L} + \sqrt{\rho_R}} \tag{17}$$

$$\tilde{a} = \sqrt{(\gamma - 1)(\tilde{H} - \frac{1}{2}\tilde{u}^2)} \tag{18}$$

$$\tilde{H} = \frac{H_L\sqrt{\rho_L} + H_R\sqrt{\rho_R}}{\sqrt{\rho_L} + \sqrt{\rho_R}} \tag{19}$$

Each of the moving domains' frame speeds is computed every iteration, with Domain 1 using equation 16 and Domain 2 using the local convective velocity at the location of the CD. Since viscosity and numerical dispersion error tend to smear the shock across several cells, in practice the pressure gradient search tends to select a left state part-way through the shock, producing a slower speed than desired, and so the shock slowly slides to the right. To prevent this sliding, a condition is placed which temporarily sets the frame speed 5% faster than the computed speed if it detects that the shock location has slipped forward. This tends to slide the shock backwards immediately, with the result that

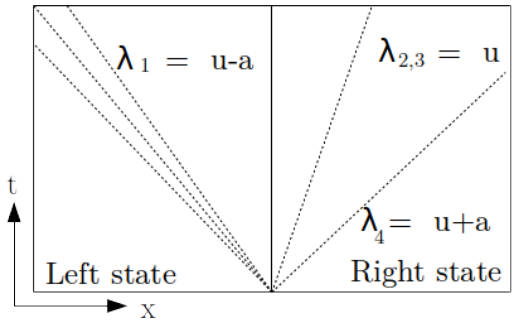

Fig. 5 Wave Speeds Across a Discontinuity

the shock remains fixed between the same two cells for the duration of the simulation, even as the frame speed varies substantially because of wave interactions with the shock. Since pressure and velocity do not experience strong gradients across the interface, entropy gradients are selected to identify the CD, and the velocity at the location of the highest gradient is selected as Domain 2's velocity. This formulation of wave speed for the CD is consistent with the classical observation that the CD moves with wave speed equal to the local velocity [A27]. The movement of the CD within the domain is then restricted in the same manner as in Domain 1. For computational efficiency, Domain 0 is updated only in the range exposed between Domains 2 and 3, since Domains 1 and 2 cover the distance to the shock, and Domain 0 is uniform prior to arrival of the shock. In terms of the fluxes, absolute velocities are actually stored and used for interpolation, while the conservation laws are written in an arbitrary moving frame.

A. Finite Opening of the Diaphragm

FROSST has the capability of modifying diaphragm opening times and profiles by using a two-dimensional iris-opening akin to that used in Jacobs et al 1994 [A28]. Simpson [A6] showed that, regardless of material or opening time, the angle through which the diaphragm is opened with time follows a nearly parabolic profile. However, Rothkopf [A4] later showed that bulging of the diaphragm prior to burst at higher pressures may significantly influence the definition of 'opening angle' under such circumstances. FROSST uses an exponential opening profile whose exponent may be set to very closely approximate a parabolic profile, but which may also be set to dramatically alter the profile, as seen in Equation 20.

$$r(t) = \frac{h}{2}\left(1 - \frac{e^{\frac{tk}{t_{open}}} - 1}{e^{\frac{t}{t_{open}}} - 1}\right) \tag{20}$$

Here, r is the height of the remaining diaphragm surface, h is the diameter of the tube, t is the time from burst and k is a constant which may be set as desired. Figure 6 shows the effect of varying k upon the opening profile. Depending upon the case of interest, different profiles and opening times may be used as appropriate.

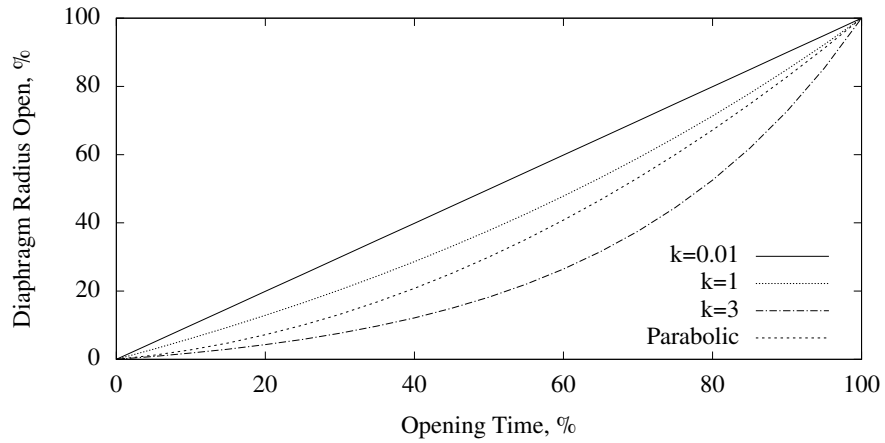

Fig. 6 Diaphragm opening profiles used by FROSST, with $k = 1$ as nominal.

V. Validation

Before seeking to apply the code to shock tube experiments, several test cases were run in order to validate the basic functionality of the code, as well as its ability to accurately represent key features of shock tube flows. For the following canonical validation cases which were designed to test the numerics of the solver, stationary grids in a single domain were utilised. Sod's problem [A29] is commonly used to investigate the accuracy of numerical schemes, and is used here in order to assess the convective fluxes and time integration of FROSST. Using a pressure ratio of 10 and density ratio of 8 in air, a diaphragm separating the two regions is instantaneously removed, and the strengths and speeds of the resulting discontinuities is tracked for comparison against the known exact solution. Seen in Figure 7, agreement between Sod's predictions and the calculated locations of discontinuities is well within 1%. Properties are seen to be monotonic around the shock, indicating that the limiter is functioning correctly. Using the flux eigenvalue method of computing shock speed, the predicted shock speed was 619.2 m/s, and the Sod shock speed was 619.1 m/s. This numerical error, arising from numerical dissipation, is considered acceptable, particularly considering that the code automatically adjusts frame speed to re-center the shock if it begins to move within the frame. The grid consisted of 100 points distributed streamwise with spacing 10 mm.

A laminar shock-boundary layer interaction study was used in order to validate the viscous fluxes, with experimental data obtained from Degrez et al 1987 [A30]. This case is for a freestream Mach number of 2.2 at a stagnation pressure of 10.7 KPa and a stagnation temperature of 293 K with a 2.75° compression angle. The shock formed from the compression ramp impinges upon the flat plate and the laminar boundary layer which has formed over it, causing the flow to temporarily separate from the wall, as seen in Figure 8. Accurate simulation of this case requires production of the correct strength oblique shock and, more challenging, appropriate growth of a compressible laminar boundary layer and the complex viscous phenomena associated with shock-induced separation.

Simulated wall pressure is compared against the experimental data of Degrez in Figure 9, showing that the extent

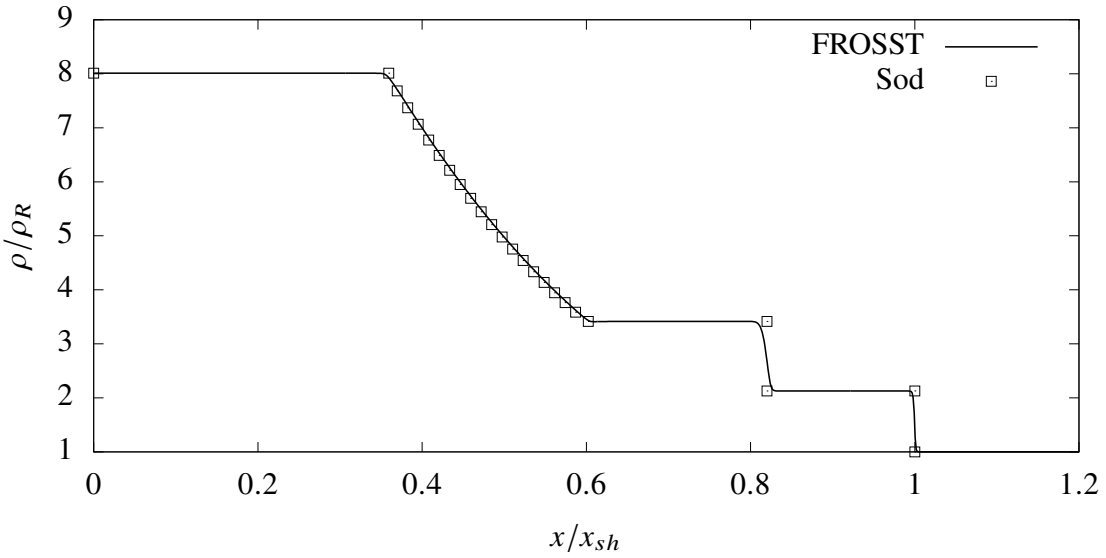

Fig. 7 Sod's Problem, Density: $t = 4e^{-5}$ **s**

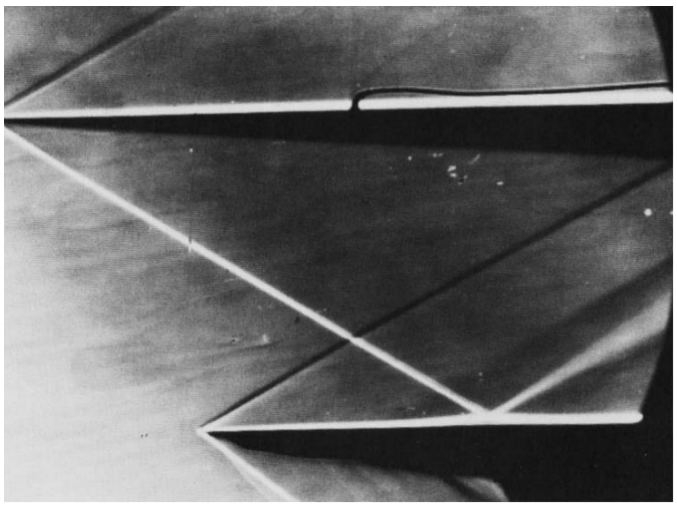

Fig. 8 Schlieren photograph of shock-boundary layer interaction from Degrez 1987 [A 30]

and strength of the separation bubble are computed accurately, confirming accurate simulation of the shock, laminar boundary layer and separation. Several grids were run in order to demonstrate grid independence, shown in Figure 1. All cases were run time-accurate until the maximum residual had dropped at least 9 orders of magnitude. The baseline grid consisted of 222 cells evenly distributed in the streamwise direction with clustering around the location of shock formation. 59 cells were distributed in the normal direction and clustered around the lower wall. Baseline wall spacing was 0.08 mm with a geometric growth rate of 9%, and the entire separation bubble was contained within the growth region.

In Figure 9, P_0 is the lowest pressure reached prior to the separation bubble, consistent with Degrez's presentation. $x_{sh} = 0.8$ m in this case as well, consistent with the Degrez setup and indicating a correct boundary layer height at the appropriate Reynolds number. The shock impingement was located at a Reynolds number of 2.96x10^5, (0.08 m). Blasius velocity profiles were also run for incompressible cases on a flat plate (not shown here), likewise showing excellent agreement and, together with the more challenging laminar shock/boundary layer interaction case, indicating correct formulation of the viscous fluxes and wall boundary conditions.

Table 1 Laminar shock/boundary layer interaction case grid spacings.

Case	Δx (mm)	Wall Δy (mm)
A	2	0.04
B	4	0.08
C	2	0.08
D	1	0.08
E	2	0.16

A test case was required in order to assess the correct implementation of the additional terms and metric coefficients needed to handle axisymmetric configurations, and also to establish the code's ability to correctly model a shock diffracting around a sharp corner such as from the opening diaphragm. Jiang et al [A31] performed an inviscid numerical study of a shock traversing a tube which encounters a sudden change in cross section, and the results were validated using data from the Shock Wave Research Center, Tohoku University, Japan. A Mach 1.5 shock ran into sea-level standard air in a test section with a ratio of 2 between the inner and outer radii. The code used therein was an axisymmetric code, allowing direct comparison against experimental results. Figure 10 compares density contours from FROSST (top) against Jiang et al (bottom) for the case which was validated experimentally as accurate, both using the same grid resolution on a uniform grid, spaced such that there are 200 radial points of spacing 0.1 mm in the shock tube section, and 600 in the streamwise direction with spacing of 0.1 mm. Close reproduction of features may be observed by FROSST, with the vortices in FROSST showing as slightly sharper owing to the less dissipative scheme, with a secondary vortex behind the primary slightly more clearly established by the more modern code.

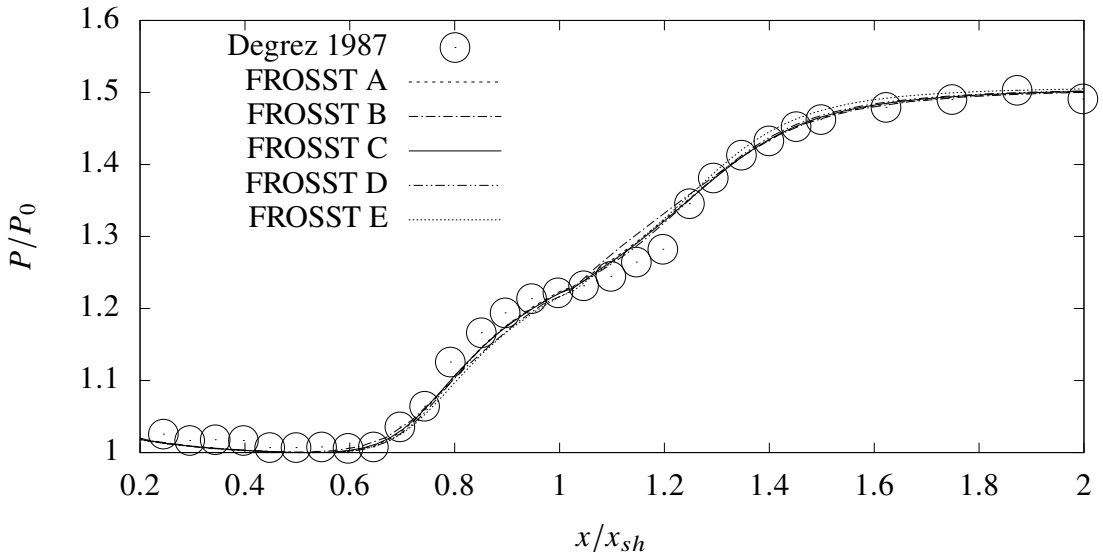

Fig. 9 Wall pressure distribution in laminar shock/BL interaction with different grids (see Table 1).

The above validation cases have shown that FROSST is able to accurately capture the primary flow features of interest to shock tube experiments: 1.) wave phenomena and speeds of travel 2.) appropriate boundary layer growth 3.) shock-boundary layer interactions and 4.) shock diffraction and reflection from a wall. Additionally, each aspect of the numerical formulation has been vetted against established experimental and theoretical data as a result of these investigations. The convective fluxes and time integration were shown to be accurate by Sod and the shock diffraction to be accurate, whilst the viscous fluxes were shown by Blasius and the laminar shock-boundary layer interaction to produce the appropriate flow features. The axisymmetric formulation was also seen to be accurate by reproduction of the shock diffraction case.

VI. Simulation of the Duff Shock Tube Experiments

Accurate and efficient capture of wave and viscous phenomena in a shock tube by FROSST was tested against the well-documented shock tube experiments of Duff [A21]. The experiments of Duff utilised an Argon driver and Argon driven condition at comparatively low speeds, providing a unique data set highlighting facility effects and free of contamination from multi-species or chemically reacting gasses. Duff studied the attenuation of shocks in a 26.8 mm internal diameter shock tube with instrumentation placed at the end of the tube in order to capture the shock's final speed and flow properties. Because measurements were made only at the end of the tube, in order to examine shock attenuation at different distances from the diaphragm a number of runs were conducted, each with a different length tube. The longest of these terminated 7.47 m from the primary diaphragm. The driver section was 0.8636 m in length, sufficient to ensure that the reflected expansion wave did not affect the experiments [A21]. Both the driver and driven gases were

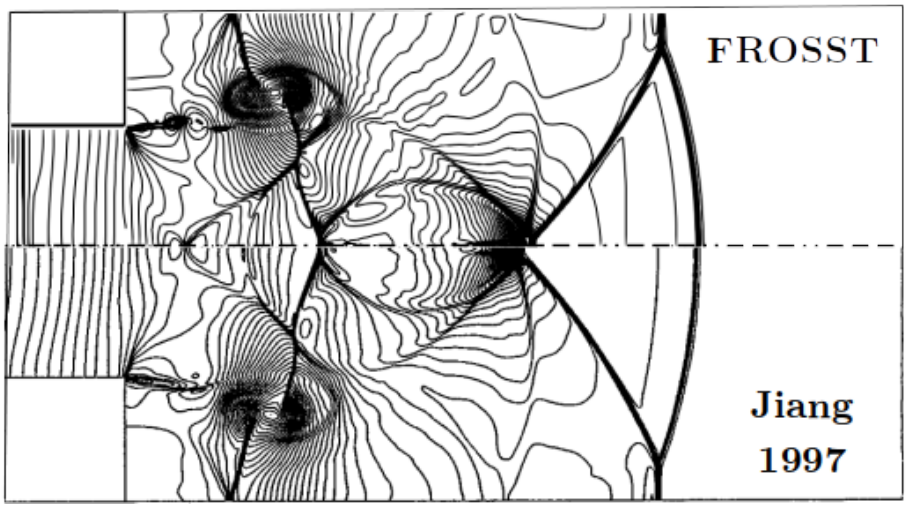

Fig. 10 Shock traversing sudden cross-sectional change Contours of Density

Argon at an unspecified ambient temperature, assumed here to be 297 K, and the driven tube was filled to 66.66 Pa.

These tests were found to be an ideal test of FROSST's present formulation, owing to their inclusion of a full shock trajectory in conditions which approximate an ideal and thermally perfect gas. They also benefit from the absence of substantial waves emanating from the driver section as might be found in more complex facilities. Domains in FROSST were arranged as seen in Figure 2. The diaphragm separates Domains 3 and 4 and, when the "burst" began, the resulting shock propagated through domains until appropriately situated within Domain 1's refined zone. At this point, Domains 1 and 2 began to slide along stationary Domain 0. In these runs, Domain 2 lacked a refined zone, allowing the CD to remain in coarse background cells because it was found that its refinement was unnecessary for the present study. The minimum axial grid spacings for each domain are listed in Table 2. All domains used the same radial distribution of cells, with a spacing along the wall of 0.5 mm, and a maximum of 2 mm. Outside of refined zones, the axial spacing in each domain grew to the same maximum value of 10 mm. Each case required 20-30 minutes of wall clock time running on 16 Intel® Xeon® W-2155 CPU cores at 3.30 GHz on a machine with 31 Gb memory.

Table 2 Minimum axial grid spacings for all domains. Refer to Figure 2.

Domain	Min Δx (mm)
0	10
1	0.8
2	10
3	0.5
4	0.5

A grid convergence study was performed where the spacings for each portion of the tube were halved and the

Table 3 Grid convergence spacing changes for cases in Figure 11.

Case Title	Domain of Concern	Spacing Direction	Test Spacing (mm)	Baseline Spacing (mm)	Flow Feature
A	All	Min Δy	0.1	0.2	Boundary Layer
B	All	Max Δy	1.0	2.0	CD, Background
C	All	Max Δx	5.0	10.0	Background
D	3,4	Min Δx	0.2	0.5	Initial Shock Formation
E	1	Min Δx	0.4	0.8	Shock

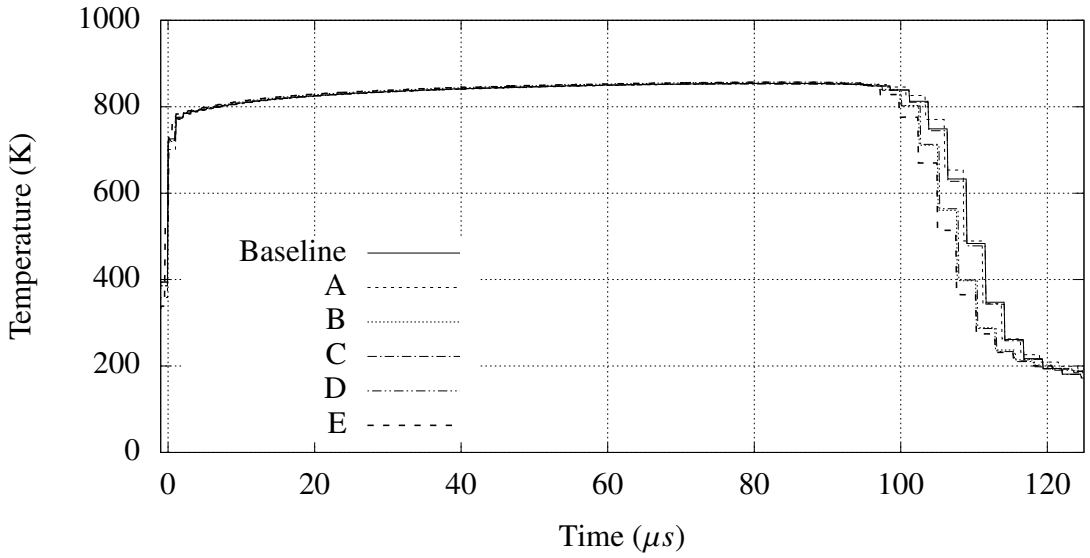

Fig. 11 Temperature profile through the test slug for different grids (see Table 3). Diaphgram pressure ratio of 5120, t_{open} = 1250 μs. Timings adjusted to align at t = 0.

resulting test times and shock strengths were compared, shown in Table 3. The maximum diaphragm pressure ratio tested herein was 5120, which produces the strongest gradients and thus a grid sufficient to capture this case may be considered sufficient for the lower speed cases. The maximum diaphragm opening time of 1250 μs, which most extends the unsteady finite opening effects, was used for this case. Figure 11 shows that the baseline grid is sufficient, with identical temperature profiles resulting from refinement. The negligible changes in slug length were limited to a single cell-width, being caused by variable smearing of the CD rather than shifts in its actual travel.

In the following discussion, the diaphragm opening profile k = 1 was used with a diaphragm opening time t_{open} = 200 μs unless otherwise specified. A cold-wall temperature of 297 K was used for the wall boundaries.

A. The Variation of Shock Speed as it Travels the Tube

By varying the length of the shock tube and extracting shock velocity at the end of each, Duff was able to reconstruct the shock velocity history as it traversed a 7.47 m tube at a single pressure ratio of 125. This history, along with FROSST's calculated velocity are shown in Figure 12. Agreement within 3% can be seen until the shock reaches 6 m. Experimental measurement error was documented as 2%.

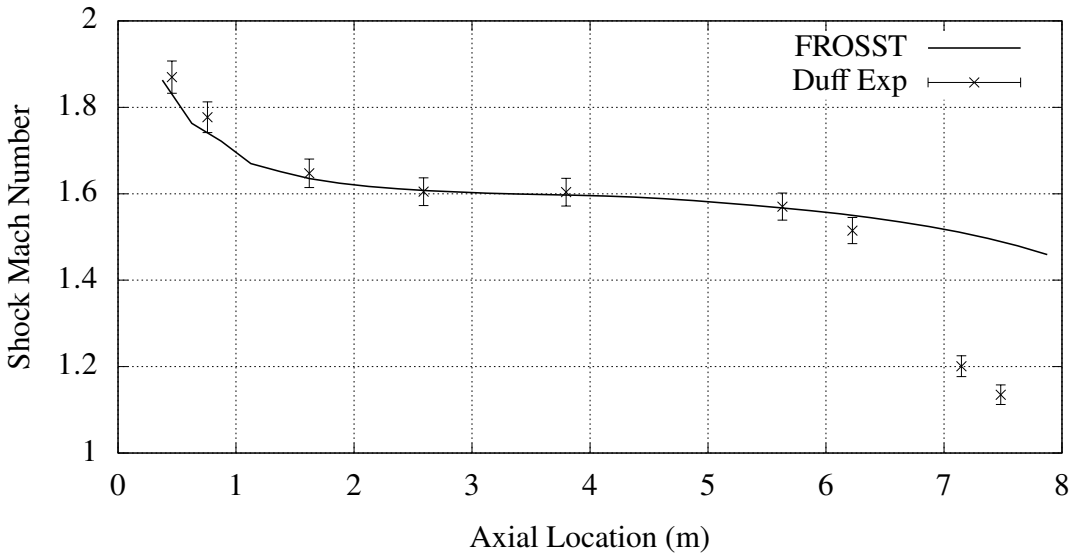

Fig. 12 Shock trajectory at a diaphragm pressure ratio of 125. Diaphragm opening time t_{open} = 200 μs.

The initial deceleration is explained by the growth of the boundary layer and heat transfer at the wall [A21] [A32], as well as losses due to mixing around the interface between driver and driven gases caused by the finite opening of the diaphragm [A2]. Once the boundary layer has fully developed and the speed of the contact discontinuity has reached parity with that of the shock, a quasi-equilibrium is formed for a time and the shock's velocity levels out. Eventually, growth of the boundary layer in the driver gas grows to dominate the radius of the tube, overcoming this equilibrium [A21] as waves from the cold-flow boundary layer are permitted to reach the shock by the weakening contact discontinuity. While the contact discontinuity remains strong and intact, such waves would be partially reflected from the discontinuity [A33]. However, as the contact discontinuity weakens with distance [A21], the growing influence of these waves is able to increasingly affect the shock. As the shock slows, the boundary layer in the test slug thickens, exacerbating the cold-flow boundary layer influence, and these phenomena combine to cause the second rapid deceleration. Figure 13 visually demonstrates the growing thickness of the boundary layer and the weakening of the contact discontinuity.

Turbulent transition of the expanded driver gas is suspected to reach the contact discontinuity in the experimental data around an axial location of 5.5 m, thickening the boundary layer in the test slug and causing the sharper deceleration observed in the experiment. As a result of the two-dimensional formulation of FROSST, the code does not predict this

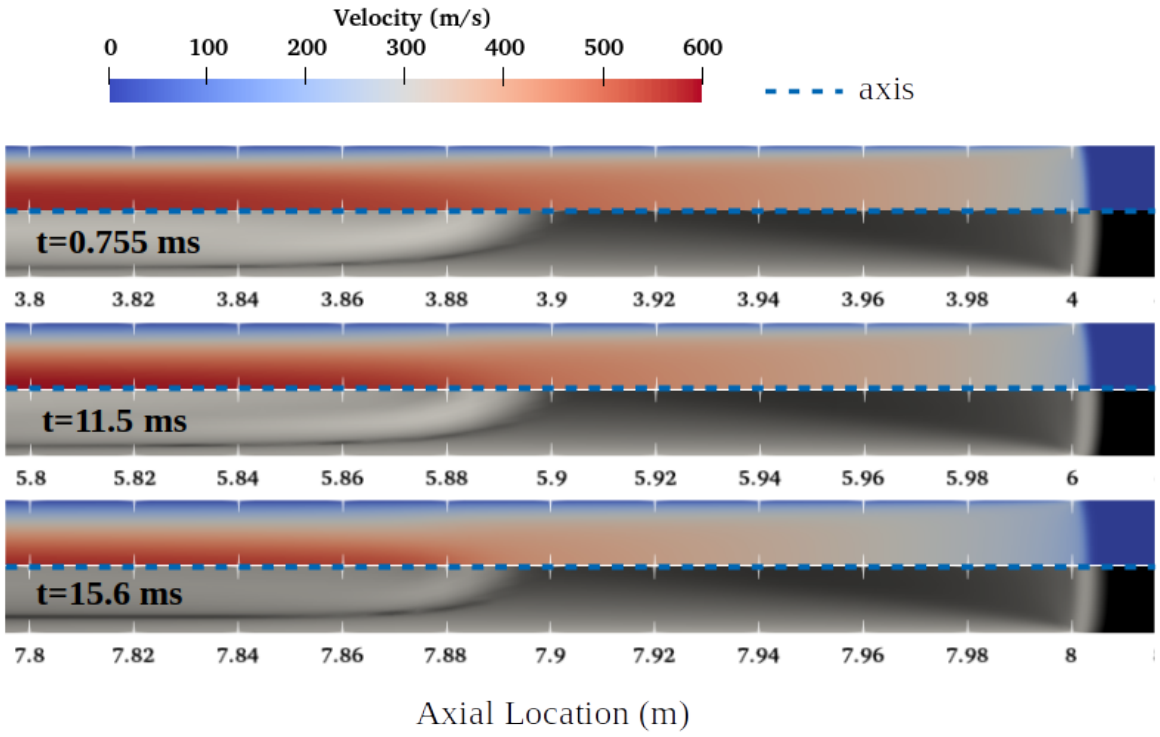

Fig. 13 Plot of velocity and density gradient magnitudes at different times for pressure ratio of 125, diaphragm opening time t_{open} = 200 μs.

transition, and therefore does not capture the second phase of rapid deceleration. Evidence to support this assertion is presented in a later section.

B. The Effects of Diaphragm Pressure Ratio upon Shock Trajectory and Test Time

In addition to accurately capturing shock velocity in the context of strong viscous forces, the case that the solver is accurately capturing boundary layer effects may therefore be strengthened by examining the test time. Test slug length is known to be dominated by interactions between the boundary layer, shock and contact discontinuity, and changes as the shock propagates along the tube [A32]. These effects are exacerbated by the narrow tube, in which the boundary layer consumes most of the internal diameter the tube [A21]. Duff examined test time across a range of diaphragm pressure ratios using otherwise the same setup as described previously. Having the ability to reconfigure the tube into a number of different lengths, diaphragm pressure ratio was varied in order to obtain to obtain a shock Mach number of 1.6 at the end of each length of tube, and the test time was measured for a Mach 1.6 shock at different distances from the diaphragm. These results provide a convenient additional means of testing both the accuracy of FROSST's shock trajectories across a number of conditions and its ability to reproduce the viscous effects that integrate into the test time at a given location.

Figure 14 shows the direct comparison between Duff's experiments and FROSST's results, yielding agreement

to within 6% until the effects of turbulent transition reach the test slug at an axial distance of 5.5 m. Duff cites the reproducibility uncertainty of the values in Figure 14 to be 5%, and so the level of error in FROSST is considered acceptable. The diaphragm pressure ratios required to produce these test times, as well as the actual Mach number predicted by FROSST at these locations are given in Table 4. No uncertainty is provided by Duff on the accuracy of the Mach 1.6 annotated speed at each tube length, but Mach numbers at each location were within 2% of the reported Mach of 1.6 up to an axial distance of 5.5 m.

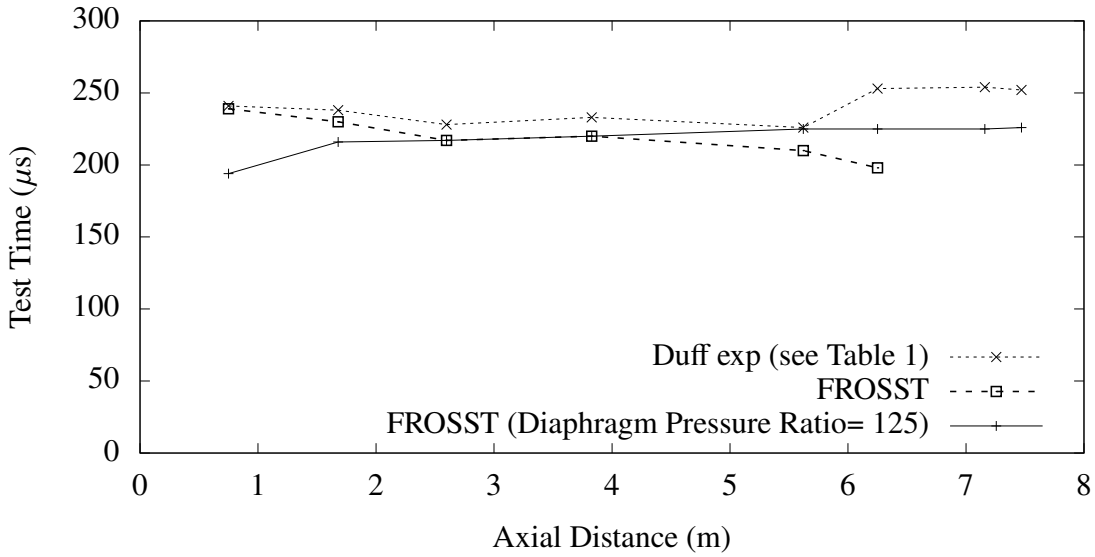

Fig. 14 Test time for a shock traveling Mach 1.6 at different axial locations. Diaphragm pressure ratios used are in Table 4. Simulated test times for a single diaphragm pressure ratio of 125 are also presented for comparison. Diaphragm opening time t_{open} = 200 μs

Table 4 Diaphragm pressure ratios used to produce a Mach 1.6 shock at each axial distance, as used in Fig 14. Mach numbers are computed by FROSST, whereas Duff reported all Mach numbers as 1.6.

Axial Distance (m)	Diaphragm Pressure Ratio	FROSST Mach	Mach % Error
0.75	61	1.57	1.88
1.68	106	1.59	0.63
2.60	125	1.59	0.63
3.83	125	1.59	0.63
5.62	152	1.62	1.25
6.25	196	1.67	4.38
7.16	426	N/A	N/A
7.47	488	N/A	N/A

In the experiments, an electron-gun densitometer was used to detect the arrival of the shock and contact discontinuity

and thereby determine the test time. In order to representatively compare test time, the simulation used the line-averaged density across the radius of the tube, ρ_* as given in Equation 21. Here, h is the tube radius and n_y is the number of radial cells across which the density is being integrated. The resulting trace of density is seen in Figure 15.

$$\rho_* = \frac{\Sigma_{j=1}^{j=n_y} \rho_j \Delta y_j}{h} \tag{21}$$

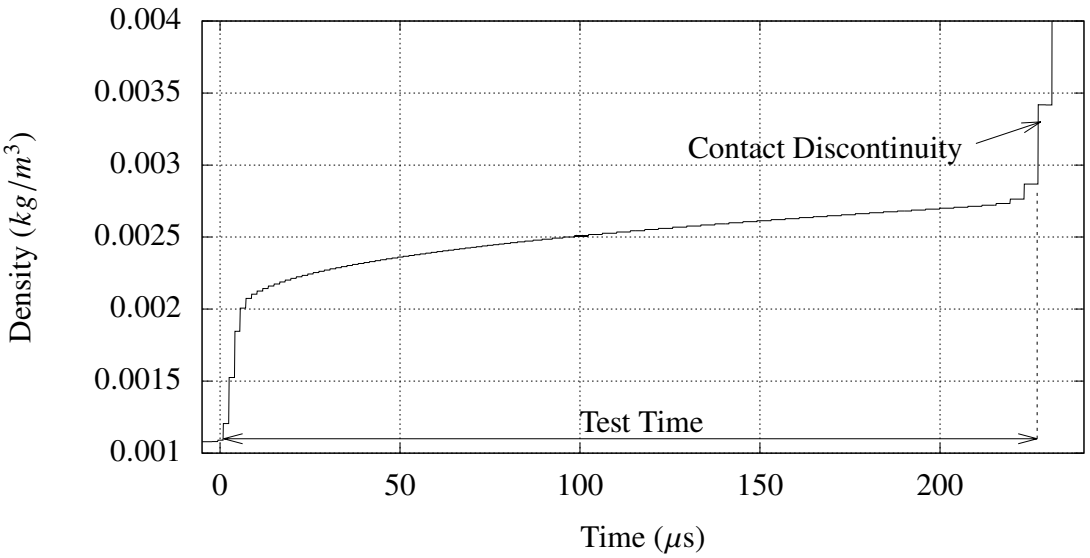

Fig. 15 Measurement of simulated test time by use of line-averaged density, time-shifted for alignment with the axis. Diaphragm pressure ratio of 125, diaphragm opening time t_{open} = 200 μs

In the simulations, test time is measured from the arrival of the shock to arrival of the contact discontinuity along the centreline. Although it is to be noted that the experimental test times were measured using an optical densitometer and thus represent an integrated measurement of density across the tube's section, the difference in measurement techniques in FROSST is estimated to produce a difference of less than 1% and so the simpler centreline measurement was considered sufficient.

Duff varied the diaphragm pressure ratios across the diaphragm from 44 to over 5,000 in order to achieve shock Mach numbers ranging from 1.2 to 3.0. However, Duff's publication did not specify any information regarding the diaphragms used, as his work predated the bulk of research showing these sensitivities. Given the range of diaphragm pressure ratios examined, it is likely that he switched materials at least once as pressures increased and thereby changed the diaphragm opening times and profiles. To accommodate this uncertainty, a variety of opening times were simulated at many of the test conditions in order to evaluate the dependency of Duff's results upon diaphragm opening time at the higher diaphragm pressure ratios, as seen in Figure 16. For reference, White 1958 [A2] examined diaphragm opening dynamics across a range of diaphragm pressure ratios starting at 1000 in a square-section shock tube. White indicated

that the diaphragm opening times were "about 600 μs" but opening time may vary by as much as 40% if aluminium is used instead of bronze. 50 μs runs were also included as a shorter reference point to highlight the resulting variation. In light of these variations, it is interesting to note that an instantaneous, as opposed to a merely very rapid diaphragm opening, results in a significantly lower shock speed for all conditions consistent with the findings of Petrie-Repar [A5]. Agreement within 10% of the experimental measurements of shock speed is obtained for all diaphragm pressure ratios, with the higher speed cases demonstrating the necessity of a comparatively long opening time in the simulation. Given the uncertainties associated with the experiments of Duff, such as actual temperatures of driver/driven gasses or diaphragms used, this is agreement is considered to be strong.

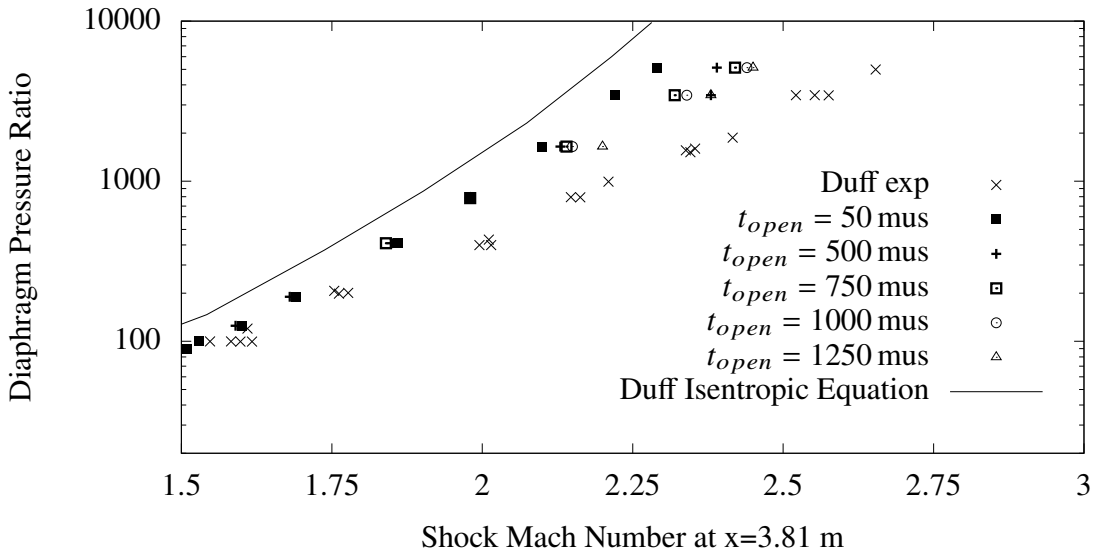

Fig. 16 Shock Mach number at axial distance 3.81 m vs Diaphragm Pressure Ratio with different diaphragm opening times. Experimental data and isentropic minimum-Mach relation taken from Duff 1959 [A 21].

C. The Variation of Diaphragm Opening Time

The dependence of shock Mach number on diaphragm opening time at higher diaphragm pressure ratios is primarily caused by the extended formation distance of the shock at high speed, a phenomenon which is elaborated at length by White [A2] and Rothkopf [A4]. Figure 17 shows that, for a given measurement location, some nominal diaphragm opening time will yield a maximum shock speed for a given measurement location. Faster openings push the location of peak velocity upstream. This pattern is evident in Figure 16 in the higher speed cases as the opening time which leads to the highest speed observed shifts with increasing diaphragm pressure ratio. Better agreement with experiment is obtained at lower diaphragm pressure ratios by using a longer opening time, and at higher pressure ratios better agreement is obtained by using faster opening times. These observations, coupled with the results of Rothkopf [A4] and White [A2] that lower diaphragm pressure ratios cause longer opening times, gives some indication of the likely

diaphragm opening times encountered in the experiments of Duff.

At higher shock strengths, the shock has yet by the location of measurement to settle into the temporarily steady speed which all profiles asymptotically approach as seen in Figure 17c. A maximum shock speed for the 5120 diaphragm pressure ratio occurs between the 1000 μs and 1250 μs opening times, providing an upper limit for the opening time at this condition. With lower diaphragm pressure ratios, both the formation distance and losses to entropy are reduced, and so the role of the diaphragm opening time on shock speed is likewise diminished. The early jaggedness of the higher opening times is caused by the finite opening profile used by FROSST as each additional cell is converted from a wall boundary condition to an open flow condition. Figure 17a shows the variation of diaphragm opening time in the lower speed case of diaphragm pressure ratio 125, where it can be seen that, although the shock takes longer to accelerate, it ultimately approaches the same steady speed except variations within 0.8% due to entropy.

Despite the strong influence of diaphragm opening effects on the observed shock trajectory, the length of the test slug and thus test time is almost entirely unaffected by the delayed shock development. Figure 18 shows the variation of test time as produced by the shocks of Figure 16. Test time at the diaphragm pressure ratio 125 condition changed by only 0.9% with the variations shown in Figure 17a. The very close agreement between the simulation and experimental data demonstrates that boundary layer growth, and the waves which it produces to influence the primary discontinuities, are accurately captured by FROSST. It may be noted that longer diaphragm opening times were not explored for this case because of the marked departure from the experimental data at the 500 μs opening time.

Given the role of diaphragm opening time in determination of the Mach number encountered at a given location in a narrow shock tube, the influence of diaphragm opening profile must also be examined. All runs discussed thus far have used an opening profile of $k = 1$, but by changing the exponent k in Equation 20, the opening profile in FROSST was adjusted. Given the increased sensitivity to diaphragm opening time at higher Mach numbers, the highest diaphragm pressure ratio, 5120, was selected, with an opening time of 500 μs with the results seen in Figure 19.

As the initial opening is slowed, the rate of energy deposition into the test slug is likewise slowed, and so just as with a longer opening time, a slower opening time results in a delayed buildup of the shock. However, it is evident that each profile ultimately yields the same shock speed farther down the tube. In the longer diaphragm opening times where the shock is still developing by the time of measurement, clearly the two effects would compound to further influence Mach number, further elevating the top speed and potentially increasing the speed observed at a set observation point such as in the experiments of Duff. Considering together the opening time, profile, and pre-burst deformation of the diaphragm, the influence of unsteadiness arising from the diaphragm clearly plays a pivotal role in the measured properties of shock tube experiments, especially in shorter tubes where the shock may not have fully developed prior to measurement. This observation may be further extended to conclude that tubes utilizing secondary diaphragms may also be severely perturbed by diaphragm opening effects from the primary diaphragm.

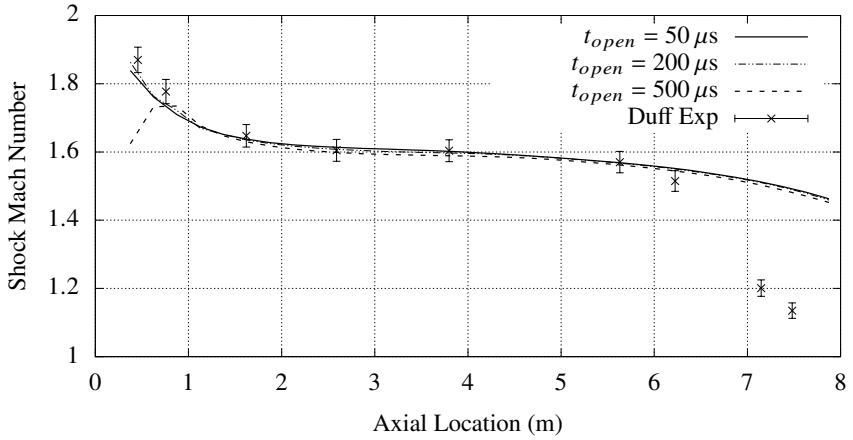

(a) Shock trajectories for diaphragm pressure ratio of 125.

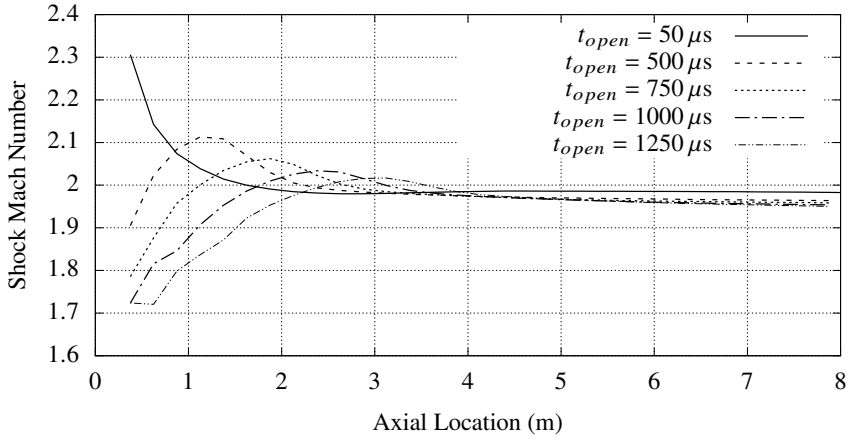

(b) Shock trajectories for diaphragm pressure ratio of 748.

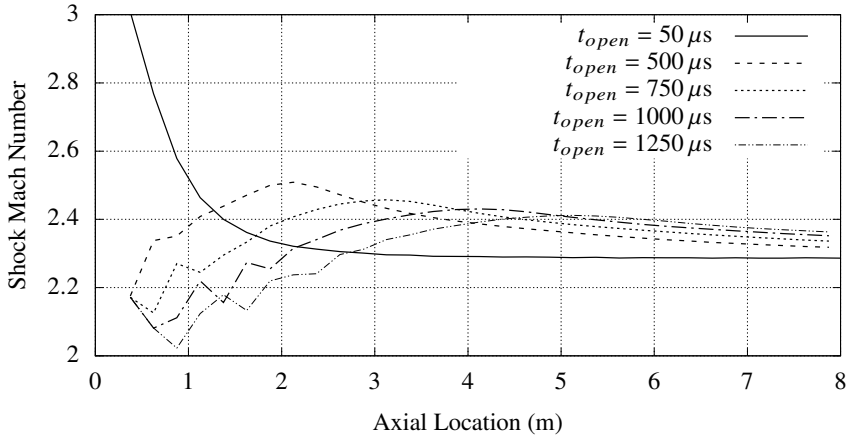

(c) Shock trajectories for diaphragm pressure ratio of 5120.

Fig. 17 The influence of diaphragm opening times upon shock trajectory at diaphragm different pressure ratios.

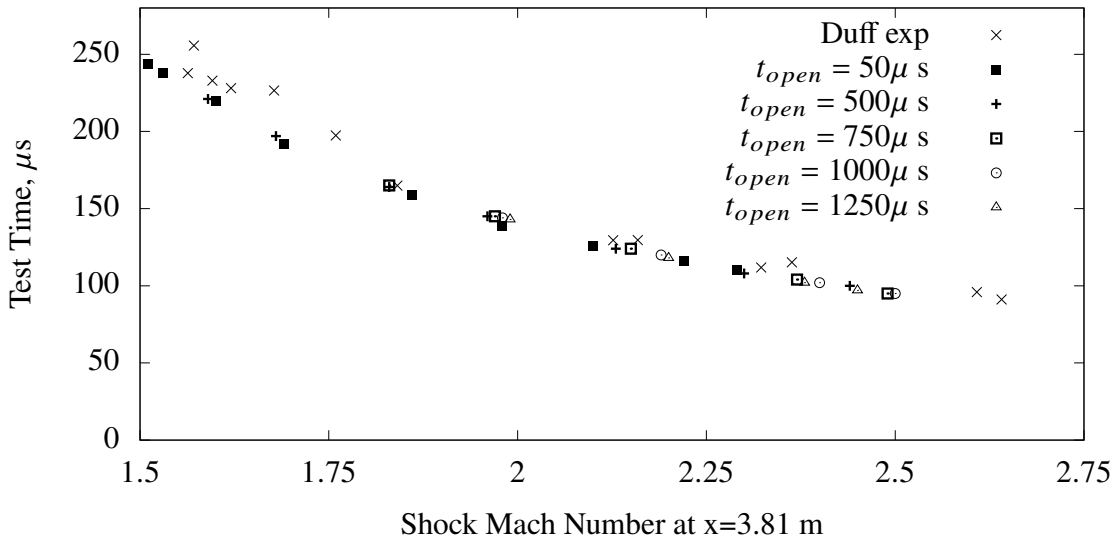

Fig. 18 Test time at axial distance of 3.81 m for different shock Mach numbers produced by varying diaphragm pressure ratios (see Figure 16).

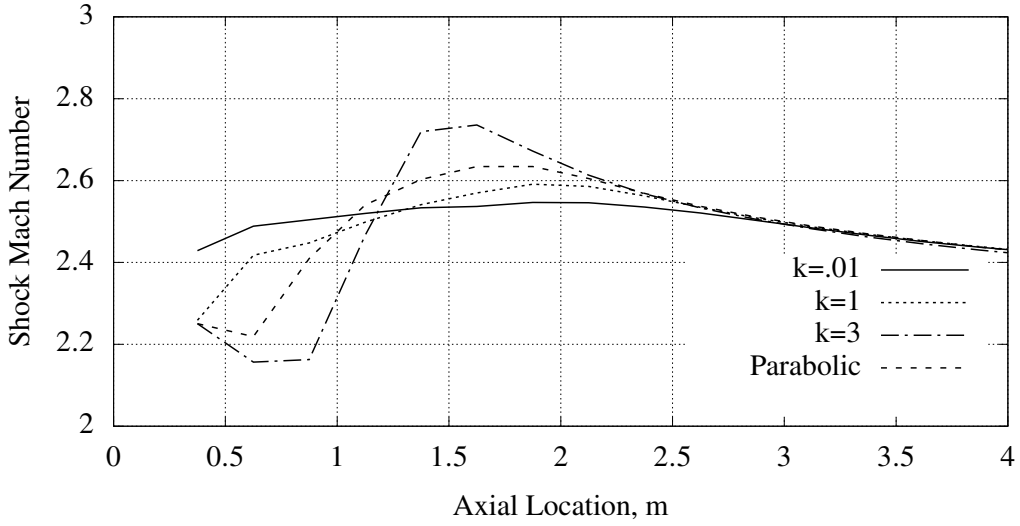

Fig. 19 Trajectories for diaphragm pressure ratio 5120 with different diaphragm opening profiles k and t_{open} = 500 μs.

D. Transition to Turbulence in the Experiments of Duff

Transition to turbulence is believed to have occurred in the experiments at a diaphragm pressure ratio of 125. This effects all measurements beyond an axial distance of 5.5 m, where the start of a precipitous drop in shock trajectory may be observed. However, FROSST is two dimensional in its nature and therefore unable to capture the influence of this transition, causing the solver to predict shorter test times and faster shock velocities in the longest tubes used by Duff. This transition is in part due to the laminar growth of the cold-flow boundary layer behind the CD as noted by Duff [A21] and Badcock [A34], and as such is also weakly reflected in the FROSST results. Transition in the driver gas would increase boundary layer thickness in the cold flow and thereby reduce the speed of the shock.

Hartunian et al 1960 [A35] developed, and Weilmuenster 1974 [A36] elaborated on the concept of the integrated Reynolds number encountered by a packet of gas as a way to to predict transition in a shock tube in a way analogous to that used for a flat plate. From the extensive data compiled by Hartunian, it may be observed that Argon should transition in a shock tube at an integrated Reynolds number of $2e6 - 3e6$. In FROSST, the integrated Reynolds of infinitesimal particles distributed along the centreline was computed by allowing the particles to convect at the local velocity, with their location updated each iteration.

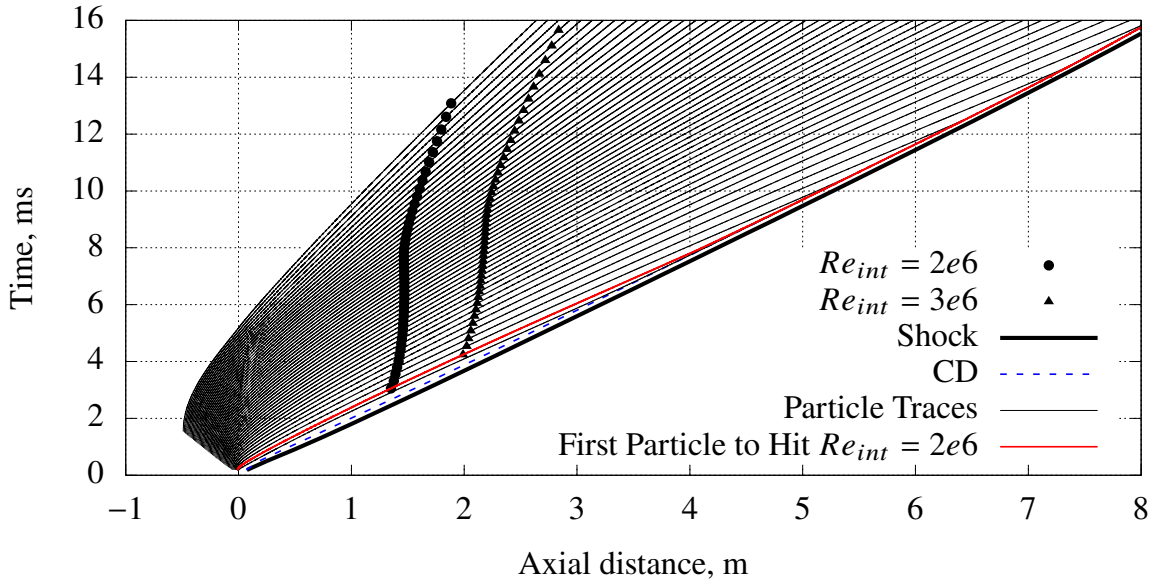

Fig. 20 Trajectories of infinitesimal particles along the centreline with the locations and times of their accumulating integrated Reynolds numbers approaching turbulent transition. Diaphragm pressure ratio=125.

Figure 20 shows the trajectories in an $x - t$ plane of these particles, along with the shock and CD. When each particle reached an integrated Reynolds number of $2e6$ or $3e6$, that location was denoted, confirming that much of the driver gas reached transition when the shock was at around an axial distance of 2 m. Although waves from the rapid growth of the boundary layer in this region would have reached the shock following a characteristic of $u + a$ within one metre, Paull

and Stalker 1992 [A33] showed that the CD would at least partially reflect such waves, diminishing their influence upon the shockwave. However, the trajectories of the driver gas can be seen accelerating and catching the CD, continually feeding it fresh driver gas of increasing integrated Reynolds as driver gas from deeper in the compression chamber reaches it. The consumption of core flow gas by the boundary layer causes this replenishment by accelerating gas from upstream to replace the core gas. This is the same phenomenon that accelerates the CD and slows the shock to cause parity of speeds between the two discontinuities as discussed by Mirels [A32]. Thus, the visualization in Figure 20 lends some additional clarity, if any is needed, to the mechanisms at work in so-called Mirels' effects.

The first transitioned particle, which now represents the leading edge of the turbulent driver gas can be seen to impact the CD at around an axial distance of 4.5 m and turbulence would thereby enter the boundary layer of the test slug. At this point, the test slug boundary layer would thicken, and the waves produced by this thickening would reach the shock without any mitigating interference by the CD, and therefore rapidly slow the shock. Analysis again shows that the $u + a$ characteristic from the impact of the turbulent gas with the CD would reach the shock at an axial distance of 5.5 m, which is just prior to the large drop in velocity observed in the experimental data. The presence of a growing turbulence upstream, and its dragging effect upon the CD, may also explain why the test time suddenly grows in the experiments of Duff beyond a length of 6 m as observed in Figure 14.

VII. Conclusions

An overset CFD methodology, entitled FROSST, was introduced which utilizes a novel method of shock tracking in order to study shock waves traversing shock tube facilities. Basic functionality of the code was validated against a number of historical and canonical cases, and a series of full-facility ideal-gas simulations were performed against the extensive catalogue of experiments performed by Duff [A21]. Excellent agreement was observed between the Duff experimental data, and the code was shown to be capable of accurately and efficiently simulating multidimensional shock tube flows. Using the code's ability to vary diaphragm opening profiles and via the use of Lagrangian particle tracking, the experiments of Duff were shown to be substantially influenced by the presence of turbulence in the driver gas, and experiments performed at higher shock speeds were seen to be heavily affected by the unsteady opening of the diaphragm.

The end goal of the code is support of shock tube experiments at a higher degree of fidelity than produced by the current one-dimensional tools but with far less computational expense than legacy axisymmetric and 3D codes. The present effort focused on validation of the basic components of the code and introduction of the shock tracking technique prior to introducing the full complexity of thermochemistry. Future efforts will focus on utilizing FROSST to examine the driving mechanisms which lead to variations in test slug properties. Some of these mechanisms include driver-section waves produced by compression, mixing of the driver and driven gasses in the vicinity of a contact discontinuity, and the role of shock trajectory on development of the test slug. Although the introduction of thermochemistry is also planned,

the mechanisms discussed above exist even in the absence of thermochemistry, and so shall be investigated prior to its addition. The final form of the code will include both thermochemistry and an ability to examine radiative effects within the flow.

VIII. Acknowledgements

The authors would like to thank the US Air Force for their support of this effort.

References

[A1] Davis, H., and Curchack, H., "Shock Tube Techniques and Instrumentation," *DTIC*, Vol. 10, No. 9, 1967, pp. 1894–1896. https://doi.org/10.1063/1.1762384.

[A2] White, D. R., "Influence of Diaphragm Opening Time on Shock-Tube Flows," *Journal of Fluid Mechanics*, Vol. 4, No. 6, 1958, p. 585–599. https://doi.org/10.1017/S0022112058000677.

[A3] Ikui, T., and Matsuo, K., "Investigations of the Aerodynamic Characteristics of the Shock Tubes : (Part 1, The Effects of Tube Diameter on the Tube Performance)," *Bulletin of JSME*, Vol. 12, No. 52, 1969, pp. 774–782. https://doi.org/10.1299/jsme1958.12.774.

[A4] Rothkopf, E. M., and Low, W., "Diaphragm Opening Process in Shock Tubes," *The Physics of Fluids*, Vol. 17, No. 6, 1974, pp. 1169–1173. https://doi.org/10.1063/1.1694860.

[A5] Petrie-Repar, P., and Jacobs, P., "A Computational Study of Shock Speeds in High-Performance Shock Tubes," *Shock Waves*, Vol. 8, No. 2, 1998, pp. 79–91. https://doi.org/10.1007/s001930050101.

[A6] Simpson, C. J. S. M., Chandler, T. R. D., and Bridgman, K. B., "Effect on Shock Trajectory of the Opening Time of Diaphragms in a Shock Tube," *The Physics of Fluids*, Vol. 10, No. 9, 1967, pp. 1894–1896. https://doi.org/10.1063/1.1762384.

[A7] Bensassi, K., and Brandis, A. M., "Time Accurate Simulation of Nonequilibrium Flow Inside the NASA Ames Electric Arc Shock Tube," *AIAA Scitech 2019 Forum*, American Institute of Aeronautics and Astronautics, 2019. https://doi.org/10.2514/6.2019-0798.

[A8] McGilvray, M., Austin, J. M., Sharma, M., Jacobs, P. A., and Morgan, R. G., "Diagnostic Modelling of an Expansion Tube Operating Condition," *Shock Waves*, Vol. 19, No. 1, 2009, pp. 59–66. https://doi.org/10.1007/s00193-009-0187-9.

[A9] Wilson, G. J., Sussman, M. A., and Bakos, R. J., "Numerical Simulations of the Flow in the HYPULSE Expansion Tube," *NASA Technical Report NASA-TM-110357*, 1995.

[A10] Kotov, D. V., Yee, H., Panesi, M., Prabhu, D. K., and Wray, A. A., "Computational challenges for simulations related to the NASA electric arc shock tube (EAST) experiments," *Journal of Computational Physics*, Vol. 269, 2014, pp. 215–233. https://doi.org/10.1016/j.jcp.2014.03.021.

[A11] Chandel, D., Nompelis, I., and Candler, G. V., "Computations of High Enthalpy Shock-waves in Electric Arc Shock-Tube (EAST) at NASA Ames," *2018 AIAA Aerospace Sciences Meeting*, American Institute of Aeronautics and Astronautics, 2018. https://doi.org/10.2514/6.2018-1722.

[A12] Jacobs, P. A., "Quasi-One-Dimensional Modeling of a Free-Piston Shock Tunnel," *AIAA Journal*, Vol. 32, No. 1, 1994, pp. 137–145. https://doi.org/10.2514/3.11961.

[A13] Mirels, H., "Test Time in Low-Pressure Shock Tubes," *The Physics of Fluids*, Vol. 6, No. 9, 1963, pp. 1201–1214. https://doi.org/10.1063/1.1706887.

[A14] James, C. M., Gildfind, D. E., Lewis, S. W., Morgan, R. G., and Zander, F., "Implementation of a State-to-State Analytical Framework for the Calculation of Expansion Tube Flow Properties," *Shock Waves*, Vol. 28, No. 2, 2018, pp. 349–377. https://doi.org/10.1007/s00193-017-0763-3.

[A15] "Detonation-Driven Shock Tubes and Tunnels," *Advanced Hypersonic Test Facilities*, American Institute of Aeronautics and Astronautics, 2002, pp. 135–203. https://doi.org/10.2514/5.9781600866678.0135.0203.

[A16] Cambier, J., Tokarcik, S., and Prabhu, D., "Numerical Simulation of Unsteady Flow in a Hypersonic Shock Tunnel Facility," *17th Aerospace Ground Testing Conference*, American Institute of Aeronautics and Astronautics, 1992. https://doi.org/10.2514/6.1992-4029.

[A17] Gaetani, P., Guardone, A., and Persico, G., "Shock Tube Flows Past Partially Opened Diaphragms," *Journal of Fluid Mechanics*, Vol. 602, 2008, p. 267–286. https://doi.org/10.1017/S0022112008000815.

[A18] Gildfind, D. E., James, C. M., and Morgan, R. G., "Free-Piston Driver Performance Characterisation Using Experimental Shock Speeds Through Helium," *Shock Waves*, Vol. 25, No. 2, 2015, pp. 169–176. https://doi.org/10.1007/s00193-015-0553-8.

[A19] Adams-Cairns, A., *Preliminary Shock Layer Radiation for Mars Entry in a Non-Reflected Shock Tube*, The University of Oxford, 2016.

[A20] Farhat, C., Geuzaine, P., and Grandmont, C., "The Discrete Geometric Conservation Law and the Nonlinear Stability of ALE Schemes for the Solution of Flow Problems on Moving Grids," *Journal of Computational Physics*, Vol. 174, No. 2, 2001, pp. 669 – 694. https://doi.org/10.1006/jcph.2001.6932.

[A21] Duff, R. E., "Shock-Tube Performance at Low Initial Pressure," *Physics of Fluids*, Vol. 2, No. 2, 1959, p. 207. https://doi.org/10.1063/1.1705910.

[A22] Kim, K. H., Kim, C., and Rho, O.-H., "Methods for the Accurate Computations of Hypersonic Flows: I. AUSMPW+ Scheme," *Journal of Computational Physics*, Vol. 174, No. 1, 2001, pp. 38 – 80. https://doi.org/10.1006/jcph.2001.6873.

[A23] Hemker, P., and Koren, B., "Multigrid, Defect Correction and Upwind Schemes for the Steady Navier–Stokes Equations," *Numerical Methods for Fluid Dynamics*, Vol. III, 1988, pp. 153–170.

[A24] Blazek, J., *Computational Fluid Dynamics: Principles and Applications*, Elsevier, 2015. https://doi.org/10.1016/c2013-0-19038-1.

[A25] Kitamura, K., Roe, P., and Ismail, F., "Evaluation of Euler Fluxes for Hypersonic Flow Computations," *AIAA Journal*, Vol. 47, No. 1, 2009, pp. 44–53. https://doi.org/10.2514/1.33735.

[A26] Roe, P., "Approximate Riemann solvers, Parameter Vectors, and Difference Schemes," *Journal of Computational Physics*, Vol. 43, No. 2, 1981, pp. 357 – 372. https://doi.org/10.1016/0021-9991(81)90128-5.

[A27] Anderson, J., *Modern Compressible Flow, With Historical Perspective*, McGraw Hill House, Berks, SL6 2QL, UK, 1982.

[A28] Jacobs, P. A., "Quasi-one-dimensional modeling of a free-piston shock tunnel," *AIAA Journal*, Vol. 32, No. 1, 1994, pp. 137–145. https://doi.org/10.2514/3.11961.

[A29] Sod, G. A., "A Survey of Several Finite Difference Methods for Systems of Nonlinear Hyperbolic Conservation Laws," *Journal of Computational Physics*, Vol. 27, No. 1, 1978, pp. 1 – 31. https://doi.org/10.1016/0021-9991(78)90023-2.

[A30] Degrez, G., Boccadoro, C. H., and Wendt, J. F., "The Interaction of an Oblique Shock Wave with a Laminar Boundary Layer Revisited. An Experimental and Numerical Study." *Journal of Fluid Mechanics*, Vol. 177, 1987, p. 247–263. https://doi.org/10.1017/S0022112087000946.

[A31] Jiang, Z., Takayama, K., Babinsky, H., and Meguro, T., "Transient shock wave flows in tubes with a sudden change in cross section," *Shock Waves*, Vol. 7, No. 3, 1997, pp. 151–162. https://doi.org/10.1007/s001930050072.

[A32] Mirels, H., "Attenuation in a Shock Tube Due to Unsteady-Boundary-Layer Action," *NACA Report 1333*, 1957.

[A33] Paull, A., and Stalker, R. J., "Test flow disturbances in an expansion tube," *Journal of Fluid Mechanics*, Vol. 245, 1992, p. 493–521. https://doi.org/10.1017/S0022112092000569.

[A34] Badcock, K. J., "A Numerical Simulation of Boundary Layer Effects in a Shock Tube," *International Journal for Numerical Methods in Fluids*, Vol. 14, No. 10, 1992, pp. 1151–1171. https://doi.org/10.1002/fld.1650141003.

[A35] Hartunian, R. A., Russo, A. L., and Marrone, P. V., "Boundary-Layer Transition and Heat Transfer in Shock Tubes," *Journal of the Aerospace Sciences*, Vol. 27, No. 8, 1960, pp. 587–594. https://doi.org/10.2514/8.8656.

[A36] Weilmuenster, K., "An Experimental Investigation of Wall Boundary Layer Transition Reynolds Numbers in an Expansion Tube," *NASA Technical Report NASA-NASA-TN-D-7541, L-9337*, 1974.

3.3 COMPARISON TO T6 EXPERIMENTS

In addition to the validation points addressed in the previous paper, additional comparisons to experiment cases were completed using data obtained from the T6 Stalker facility. A comparison of shock speed profile from the T6 Stalker Tunnel and results from FROSST for a 200 Pa Argon test condition at 3 km/s were performed.

3.3.1 THE T6 STALKER FACILITY

The T6 Stalker Tunnel is a multi-mode hypersonic impulse facility located at the Osney Thermofluids Institute. Recently commissioned [18], it utilizes a free-piston driver and can operate in shock-tube, expansion or reflected shock tunnel modes by exchanging the sections prior to the test section. The present tests were performed in Steel Shock Tube mode, pictured in Figure 3.1. PCB113A piezoelectric pressure transducers are used for shock-timing measurements along the tube and also for measurement of Pitot pressure in the test section. Diamond heat transfer gauges may also be installed at the locations indicated [27].

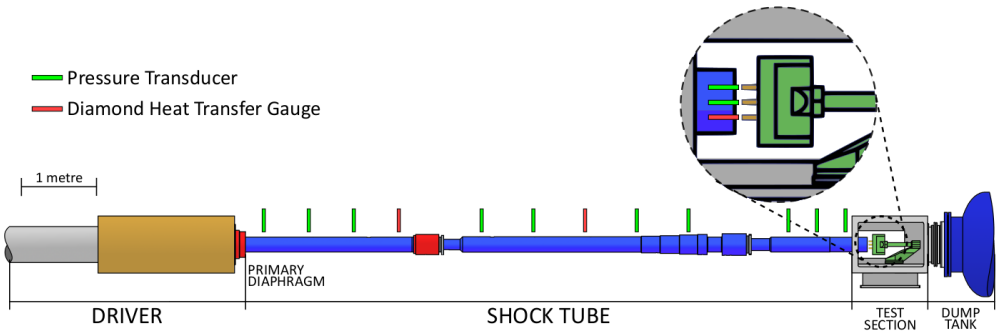

Fig. 3.1 T6 Facility Schematic. Reproduced from Collen et al 2019 [18].

T6 features an area change from 300 mm in the driver section to 96 mm in the driven section, which substantially improves its performance [56]. In addition, it also utilizes an orifice plate just downstream of the primary diaphragm to ensure a soft landing condition for the piston, creating a throat in the driven section. The dimensions of the facility are seen in Table 3.1.

Table 3.1 Conditions at burst and simulation initialization

Compression Tube	6 m length	300 mm dia
Oriface Plate	12 mm thickness	76.2 mm dia
Driven Tube	7.1 m length	96.3 mm dia

As a result of the several area changes, the shockwave which emerges from the primary diaphragm encounters a significant blockage, yielding choked flow through this throat. The area changes combine with the choked flow to substantially slow the development of the shockwave, and also change the characteristics of the waves emerging from the driven section.

3.3.2 TEST CONDITIONS AND FROSST SETUP

In keeping with the cautions of Kotov et al. [49], cases were selected which could be easily reproduced in T6 for validation within the limitations of the code. In order to avoid chemical reactions, Argon was selected as both the test gas and the driver. In order to keep ionization effects from entering the results, conditions were selected which were estimated to produce less than 1% ionization. In this way uncertainties related to real-gas effects or boundary layer transition were avoided and the elements of the code as included to date could be directly validated. Namely, the wave speeds, effects of viscosity and driver wave effects are left as the primary flow phenomenon, all of which fall within the purview of the present state of the code. T6 was run at the conditions shown in Table 3.2 to provide relevant validation data for the case at hand.

Table 3.2 Conditions at burst and simulation initialization

CFD (Const Area)	**Driver**	**Driven**
Pressure	15.6 MPa	200 Pa
Temperature	5442 K	300 K
Gas	Argon	Argon
Experiment (Area Change)		
Pressure	10 MPa	200 Pa
Temperature (K)	4492 K	300 K
Gas	Argon	Argon

Although the wider diameter of the piston tube plays a significant role in the development of the standoff distance between shock and CD, this area change was not modeled at this stage in development. As a result, the solver was unable to account for the substantial effects of waves from the driver section due to the compression process and area changes. However, since the area change brings with it an increase in experimental shock speed, direct use of experimental burst conditions as inputs to the simulation produces a shock which is substantially slower than that seen in the experiment. In order to account for this, the UQ Pitot code [46] was run in order to determine the burst pressure which would be required in a tube of uniform diameter to produce the same strength and speed shock as seen in

the experiment. The left-state conditions thus computed were then used as inputs to FROSST. The simulation utilised an infinite driver. Two simulations were performed: the first used an instantaneously opened diaphragm, while the second used the iris-opening model described previously. A finite diaphragm opening time of 300 μs on a parabolic opening profile was used with otherwise identical setup to the instantaneous case. The relation used to determine the parabolic profile was:

$$r_D = h\frac{1}{2}\left(1-(0.8\tau^2+0.2\tau)\right) \tag{3.1}$$

Here, $\tau = \frac{t}{t_{open}}$, where t is the global simulation time, and $t_{open} = 300\,\mu$s is the prescribed diaphragm opening time.

3.3.3 GRID CONVERGENCE

A grid convergence study was performed to ensure sufficient resolution of the discontinuities. The study focused on capturing three main metrics: speed of the shock, strength of the shock, and speed of the contact discontinuity. Care was taken to ensure that the refined zone contained the entirety of the shock, which curved significantly near the wall. Runs were conducted to a time of $13\mu s$, with the shock covering a distance of $48mm$ in that span. Noting Kotov's observation [49] that "*the major contribution to the error in shock location obtained on the coarse grid is due to the first* 5 μs", this time was estimated to be sufficient to discern meaningful differences in shock error. The final grid spacings are seen in Table 3.3. Doubling was performed for both grids, and the locations and strengths of the discontinuities changed on the order of 0.1%, indicating that the coarser spacing was sufficient. CFL was set to 0.8 and the resulting timestep averaged 7.7×10^{-10} s. The 8.5 m simulation took 12 hours using 16 Intel ® Xeon® W-2155 CPU cores at 3.30 GHz on a machine with 31 Gb memory.

Table 3.3 Final Grid Spacings

Domain	**0**	**1**	**2**
Min x (mm)	10	.04	.08
Min y (mm)	4E-02	.01	.01
Max x (mm)	10	0.01	0.01
Max y (mm)	2	2	2

A comparison is presented in Figure 3.2 between the FROSST simulations and the results of the T6 tests. FROSST can be seen match the test section velocity against experiment s64 to within 1.4% for both simulations, whereas s62 arrived at a 2.5% slower speed, with the clear result of a

lower Pitot pressure visible in Figure 3.2b. The disagreement between the two experimental shots highlights one of the major challenges of matching simulations against experimental shock tube data; the experiments themselves have substantial variation from shot to shot even for nominally identical burst conditions, whereas numerical simulations will always produce a single result. Observing the shock speed measurements, it is clear that inclusion of the finite diaphragm opening greatly improves agreement with experiment. Although the early trajectory qualitatively agrees with experiment, it is evident that not all flow phenomena have been captured by the simulation. One explanation for this disagreement is that the interaction of the unsteady diaphragm opening with the orifice plate which resides just downstream of the diaphragm produces variations which are inaccurately captured by the iris-opening model used by FROSST. While the iris-opening model opens a hole in a planar surface, the actual diaphragm bends outwards towards the orifice plate into 'petals', producing a complex three-dimensional flowfield which would interact differently with the orifice plate downstream of it than is possible with the two-dimensional model.

Examining the Pitot pressures, FROSST is able to closely match s64 after the initial sensor rise time. The rear of both experimental test slugs exhibit substantial trend changes which are not captured by FROSST. At 110 μs, s64 shows a subtle slope rise followed at 190 μs by more obvious variations, whereas the effect is more pronounced at 150 μs for s62. Two sources for these disagreements are proposed. The first source is contamination of the driver gas due to variations in shock speed, the mechanisms for which are detailed in the next paper. The second source is thought to be the 5% ionisation which is expected in Argon under these stagnation conditions. Ionisation would limit the temperature rise and associated density variation, thereby directly impacting the Pitot measurement. The ideal gas computations of FROSST cannot account for this ionisation, which should cause an increase in density relative to the FROSST results by limiting the experimental temperature rise. Predicted test slug length is also overestimated by FROSST. This is thought to be in part due to contamination introduced by the unsteady diaphragm opening and interaction with the orifice plate. Another possible source of disagreement is the absence in simulation of the area change from the driver section, which would introduce variations in shock speed which would in turn influence test time.

Examining Figures 3.2b and 3.2c, the different diaphragm openings resulted in differing test gas property profiles. A 6.8% difference in maximum temperature is observed. Additional investigations, as well as consideration of the works of Mirels [60], Holbeche [40] and Light [52] suggested that these

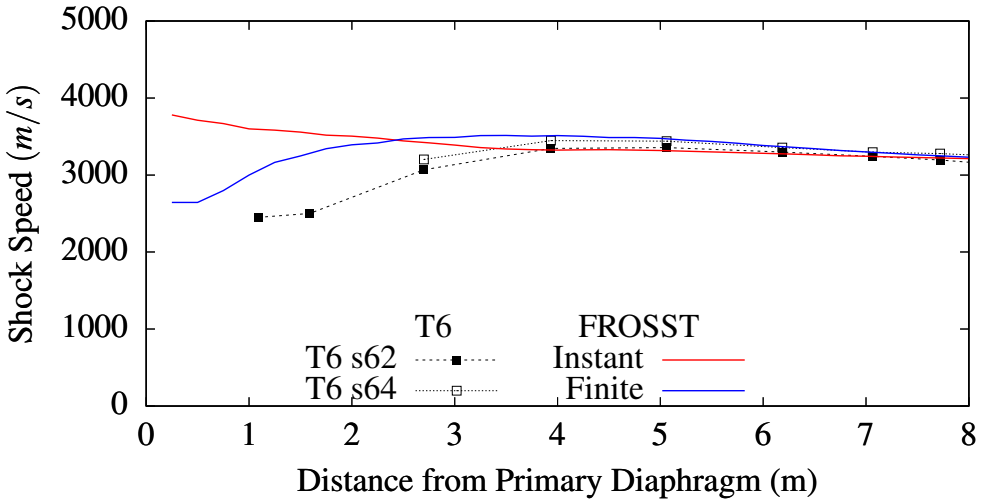

(a) Shock speed profiles.

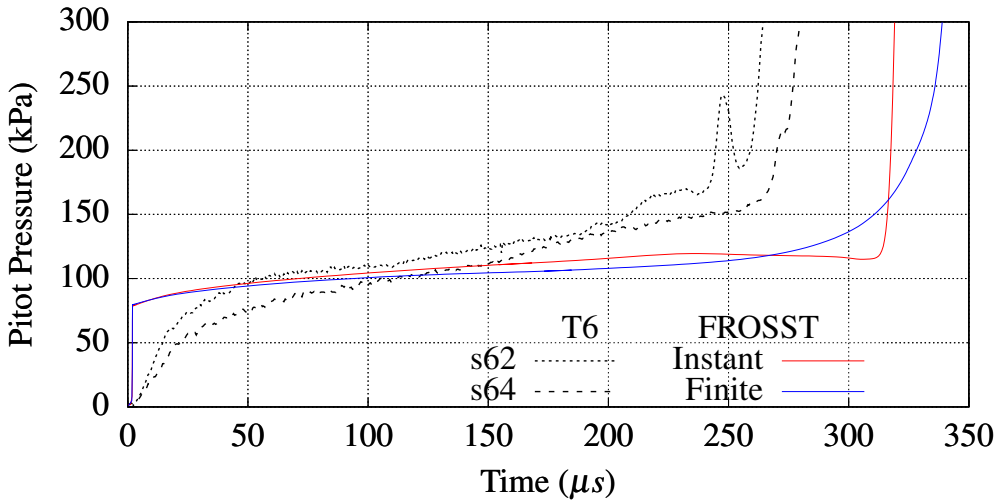

(b) Pressure profiles at 8 m from the primary diaphragm.

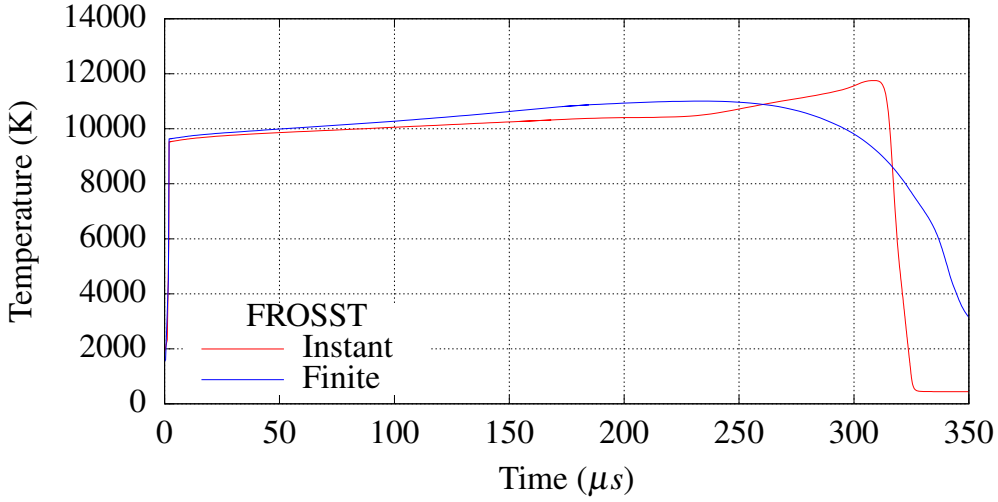

(c) Temperature profiles for the FROSST cases.

Fig. 3.2 Comparison of FROSST against experimental data from T6. FROSST data shows an instantaneously opened diaphragm and one which opens over 300 μs.

differences may have arisen primarily from the different shock trajectories. The proposal that shock speed history was the source of disagreement between the two simulated cases pointed the direction of proceeding investigations towards application of the code to cases which could more explicitly identify the role of shock speed variations in producing test gas nonuniformities.

Chapter 4

THE INFLUENCE OF NON-CONSTANT SHOCK SPEED

As shown in Chapter 3, it is difficult to reproduce experimental shock speeds by use of *a priori* methods. This is due, in part, to the shot-to-shot variations in experimental tests at nominally the same conditions. Bearing in mind this challenge, one of the primary findings of the literature review was a broad lack of rigorous investigation into the role of shock speed variation in the development of nonuniformities in the test slug. Furthermore, the potential significance this influence has been alluded to repeatedly in the literature, clearly stating the need for such an investigation. The next section contains a paper which specifically examines whether the trajectory of a shock down the tube plays a vital role in the final thermodynamic properties of the test slug.

The study centres around simulations from the FROSST solver which produce multiple shock trajectories for the same test gas fill conditions, and enter the test section at the same speed. Massless Lagrangian particles are tracked in the solver, allowing examination of the history of any given portion of the final, multidimensional test gas. The most significant contribution of this effort is identification of shock speed as the primary driver of substantial test gas nonuniformities. Results indicated that each of the Lagrangian particles remained essentially isentropic while in the test slug. This observation, along with the general methodology of tracking massless gas packets, is used as the basis for the analytical method in Chapter 5.

Flow Nonuniformities Behind Accelerating and Decelerating Shockwaves in Shock Tubes

Matthew Satchell *, Luca Di Mare †, and Matthew McGilvray ‡
The University of Oxford, UK

Shock tubes are used to investigate the chemical kinetics and radiative properties of gasses. Analyses of the flow conditions produced in shock tubes typically assume a single, constant shock speed even though the shock speed varies due to driver effects, boundary layer growth and diaphragm rupture effects. This paper will investigate the dependence of flow properties upon the entire shock speed history for a 100 mm diameter, 8 m long shock tube using the FROSST axisymmetric shock tube Navier-Stokes code. A perfect gas is applied to remove the complexity of thermochemistry and allow a focus upon the flow details. Shock speed profiles ranging from accelerating to decelerating are simulated to qualitatively represent different experimental conditions, and the resulting test slugs compared. All shocks reach the test section at the same final shock Mach number of 6.53. Pressure variations caused by the accelerating shock are found to combine with entropy gradients introduced by the changing shock strength, yielding differences in maximum temperature of the test slug by as much as 56%, and differences in maximum pressure as high as 22% despite the shared tube-end Mach number. Local temperature and pressure around gas packets in the test slug are found to relax significantly through time in response to changing post-shock conditions. Test slug variations due to boundary layer effects are found to be present, but overwhelmed by the relaxation processes under many conditions.

I. Introduction

Sustained interest in access to space and planetary exploration drives the pursuit of better understanding of the flight environment which spacecraft encounter as they fly at high speeds through planetary atmospheres. Flight vehicle airspeeds can exceed Mach 30, presenting extreme challenges to the design of survivable flight structures. Beyond Mach 5, the flight regime is said to be hypersonic, and is characterised by the excitation of thermochemical effects in the air which ultimately produce dissociation, ionization and radiative emission & heat transfer to the vehicle [B1]. Shock tube test facilities enable ground tests of this challenging flight environment and offer a means of studying the otherwise

*DPhil Candidate, Department of Engineering Science, Oxford Thermofluids Institute, University of Oxford.
†Associate Professor, Oxford Thermofluids Institute, Department of Engineering Science, University of Oxford.
‡Associate Professor, Oxford Thermofluids Institute, Department of Engineering Science, University of Oxford.

elusive associated radiative and thermochemical phenomena.

Shock tubes commonly operate by building up pressure in the driver tube until it bursts a diaphragm, sending a shockwave through the lower-pressure test gas in the driven tube. This shockwave impulsively elevates the velocity, temperature and pressure of the test gas which it processes, reproducing the thermochemical environment encountered in hypersonic flight. A contact discontinuity (CD) separates the test gas processed by the shock from the driver gas emerging from the high pressure side of the punctured diaphragm. A shock tube test ends with the arrival of the driver gas at the test section.

Because of the extreme pressures produced and short test times on the order of a few hundred microseconds, diagnostic tools available to analyze the test gas are limited [B2]. Furthermore, multidimensional numerical simulation of these tubes has historically proven challenging due to the computational expense of sufficiently resolving boundary and shock layers over the length of shock tube facilities extending upwards of 10 m in length [B3–6]. Flow complexities arising from the driver and finite opening of the diaphragm also present substantial challenges to representative simulation of shock tubes [B7]. Thus, typical analyses of shock tube experiments assume a constant shock speed.

The challenges facing analyses of shock tube flows are exacerbated by the complexity of factors which combine to dramatically diverge actual shock tube performance and flow state within the test slug from that predicted by ideal analysis. The primary established sources of test slug variations include boundary layer effects [B8–10], variations in shock history [B10–15], and contamination of the test slug volume by driver gas [B7, 16, 17]. Additionally, disturbances arising from waves produced by the pressurization of driver gas and its subsequent release through the bursting diaphragm cause pressure disturbances centered around the CD in addition to altering the shock trajectory [B18]. Since the boundary layer and flow disturbances arising from its formation play a central role in the variation of shock speed, these disturbances are discussed first.

Studies of test slug disturbances have historically focused upon variations arising from the presence of a hydrodynamic boundary layer formed behind the propagating shockwave. As the gas convects away from the shock, mass from the core flow is lost to the boundary layer, causing the core flow to accelerate, ultimately shortening the test time as the CD accelerates with the local gas [B19]. This acceleration is illustrated in Figure 1a. When viewed from the shock frame of reference, as in Figure 1b the test gas is brought towards rest as it approaches the CD, causing the pressure, temperature and density to increase through the test slug [B10, 20]. This increase occurs even behind a shock of constant speed [B10]. In addition to accelerating the CD, mass loss into the boundary layer produces pressure waves which reduce the shock speed, leading to significant attenuation over sufficiently long tubes [B10].

In addition to attenuation due to the boundary layer [B19, 21], shock velocity may also change substantially due to the influence of a number of other sources as it propagates along a shock tube. These include: mixing of the driver and test gas at the interface [B17, 22], unsteady effects caused by flow area constriction during diaphragm opening [B17, 23], thermochemistry [B**?**]kotov2014, Chandel2018, and waves from a finite, non-uniform driver [B24]. The combined

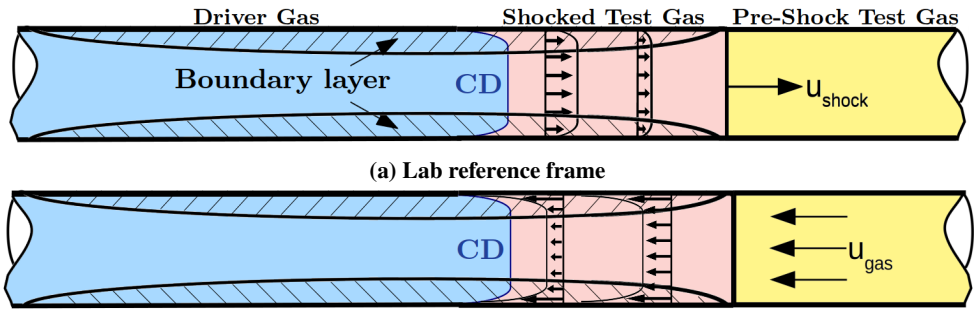

(a) Lab reference frame

(b) Shock-stationary reference frame

Fig. 1 Shock tube flow in different reference frames.

effect of these phenomena causes the shock to change its speed by as much as 50% throughout a single experiment [B25]. Petersen *et al* [B26] perform a thorough review of the relevant literature and experimental investigations.

Holbeche and Spence [B13] investigated the influence upon test slug properties of the variable entropy produced by a shock of varying speed, but neglected boundary layer effects, and also assumed only a small degree of attenuation as caused by boundary layer effects. Mirels investigated non-uniformities behind a shock due to the boundary layer effects, but neglected the influence of a variable shock speed, predicting but not confirming that such influences would be aspirated into the boundary layer [B12]. Light investigated the role of shock history in the test slug as well, but achieved only qualitative agreement. Light speculated that agreement was limited because the study assumed small perturbations and neglected the role of expansion waves produced by the slowing shockwave [B27]. Beyond these studies limited by applicable range and assumptions, no rigorous investigation of the full influence of the variation of shock speed in a shock tunnel has been performed.

This paper will evaluate the effects of shock speed variation on test gas properties with the purpose of informing the importance of the entire shock history in evaluating experiments in impulse facilities, including expansion tubes and reflected shock tubes. A series of perfect gas Navier-Stokes simulations are performed absent the complicating presence of thermochemistry effects. Shocks of different speeds are produced by varying the temperature distribution in the driver gas at rupture, with constant gas fill conditions.

II. Axisymmetric Simulations of a Shock Tube by FROSST

Simulations were performed in the FROSST solver for a 100 mm diameter, 10 m long shock tube with the test section located 8 m from the diaphragm. These dimensions are representative of typical shock tubes [B14, 28, 29]. The driver section had a diameter of 100 mm and also a length of 10 m. This was to ensure the driver was effectively infinitely long and did not influence results. Argon was used for both the driver and the test gases. All simulations used a test gas fill pressure of 66.67 Pa and a fill temperature of 300 K. Initial pressure profiles through the driver gas were constant at 667 kPa, for a diaphragm pressure ratio of 10,000. All cases were run using an instantaneous diaphragm opening.

Five shock profile cases are explored, each with different initial shock speeds at 1 m (u_i), resulting in a shock speed of 2100 m/s at the test section. To achieve this, different axial temperature profiles in the driver gas were used in order to influence the speed of the primary shockwave down the tube and thereby produce different shock trajectories. As the unsteady expansion wave processes gas of different temperatures, its speed is modified. Thus, the driver gas which is expelled through the diaphragm influences the shock speed variably as the expansion wave driving the gas evolves. The applied temperature profiles are detailed in Table 1 and visualized in Figure 2. Each temperature profile begins with a constant temperature for a distance of 10 mm in order to allow the shock to form before being influenced by the temperature gradient.

The use of driver temperature profiles to influence shock trajectory may be justified by examination of the non-ideal effects encountered in physical shock tubes. Experimentally, myriad mechanisms exist by which the pressure and temperature are elevated behind the diaphragm of a shock tube. Some examples of methods by which the initial driver section is pressurized are: getting pumped to high pressures, compressed by the motion of a piston, detonated, or by the action of an electric arc. The many methods of pressurization each produce unique distributions of nonuniform temperature and pressure through the driver section. A characterisation of pressure nonuniformities in free-piston facilities is given, for example, by Mcgilvray *et al* [B30]. Paull and Stalker [B18] showed that nonuniformities in the driver section could influence conditions in the test slug. The Rankine-Hugoniot relations dictate that conditions on either side of a shockwave determine its speed, and so it is clear that if driver section nonuniformities can influence test slug conditions, then the speed of the shock may be likewise influenced by such nonuniformities.

Table 1 Conditions at diaphragm rupture and tube-end shock Mach numbers. All used a diaphragm pressure ratio of 10,000 with a test gas fill pressure of 66.7 Pa. x **is the distance from the diaphragm in metres.**

(u_i), Shock Speed at x = 1 m (m/s)	Driver Temperature Profile (K)	Max/Min Driver Temperature (K)
2800	$5000(1.05 - 2.85x)^2$	2900
2400	3275	3275
2100	$2200(1.05 + 4.5x)^{1.001}$	3550
1800	$1500(1.05 + 3.065x)^{1.65}$	5100
1500	$1000(1.05 + 6.96x)^{1.2}$	9000

A baseline case was developed wherein the shock did not diverge by more than 2% from a speed of 2100 m/s throughout the length of the tube. The properties of the resulting test slug were then compared against four cases wherein the same driven fill conditions were used, but the driver temperature profile was adjusted so as to produce shocks of initially higher or lower speeds which accelerated or decelerated monotonically to reach the same shock speed of 2100 m/s, Mach 6.53, at 8 m from the diaphragm. The resulting shock speed profiles are shown in Figure 3. The maximum deviation from the desired Mach number at an axial distance of 8 m from the diaphragm was 0.4%. The cases

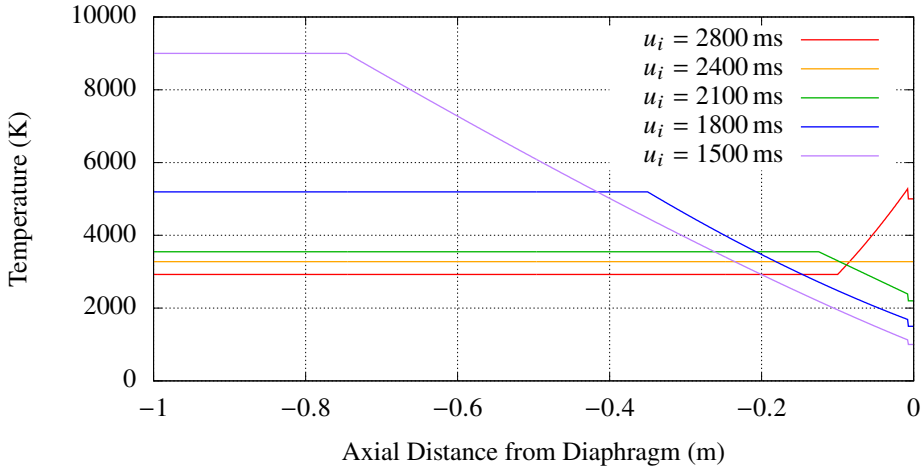

Fig. 2 Driver gas temperature profiles to produce the shock trajectories in Figure 3. Driver section extends 10 m in length, with properties held constant after the initial temperature profile.

are hereafter referred to by their approximate speed when the shock reached 1 m from the diaphragm. The first 0.5-0.75 metres for all cases experienced a small degree of deceleration due to the formation of the boundary layer.

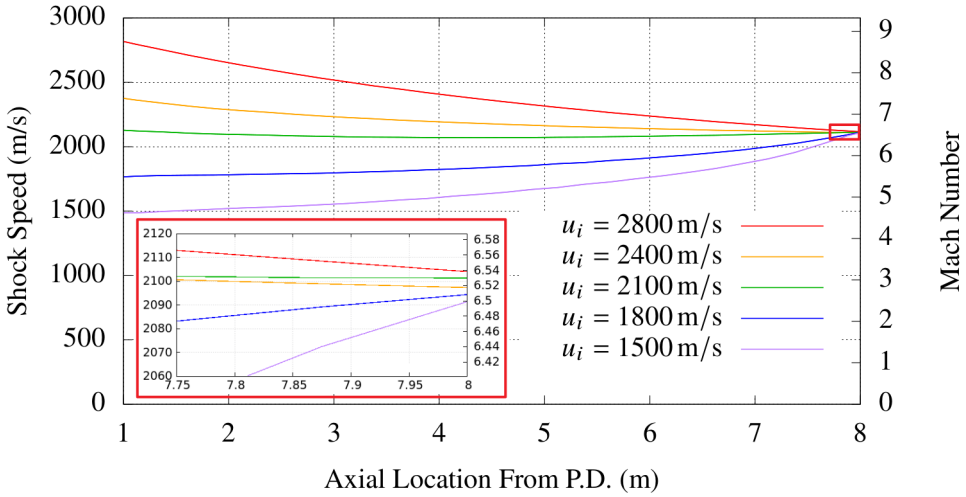

Fig. 3 Five shock trajectories, arriving at the same end-tube shock Mach number of 6.5.

Using Argon under the selected conditions, neither thermochemical effects nor transition to turbulence in the test slug should occur, and so a laminar perfect gas may be assumed. Use of the same, constant profile driver fill pressure limited the influence of different waves from the driver section upon the CD. Combined with the use of an instantaneous diaphragm opening, the selected conditions limit potential influences upon the final test gas properties to boundary layer and shock history effects. In the less ideal conditions encountered in experiments, the effects produced here will still be present, but compounded upon by the presence of the other influences.

A. Computational Domain

The layout of computational domains used in FROSST to produce these shocks may be seen in Figure 4. Domain 1 holds the zone of refinement around the shock, while Domain 2 holds the zone of refinement surrounding the CD. Each of these domains move along the stationary background Domain 0 at the speed of their respective discontinuities as computed each time step in order to keep the discontinuities stationary with regard to their zones of refinement. Stationary Domains 3 and 4 are prepended to the front of Domain 0 in order to provide adequate refinement around the initial shock formation. Domains 1 and 2 begin their motion when the shock travels into the appropriate location within Domain 1. Domain 2 at first moves at the same speed as Domain 1, and begins its independent speed tracking when the CD has travelled into its appropriate location within Domain 2. All grids used a maximum axial spacing of 10 mm, wall radial spacing of 0.1 mm, and a maximum radial spacing of 1 mm, but the minimum axial spacing was varied in order to accommodate the appropriate discontinuity. The minimum axial spacings for each domain are outlined in Table 2.

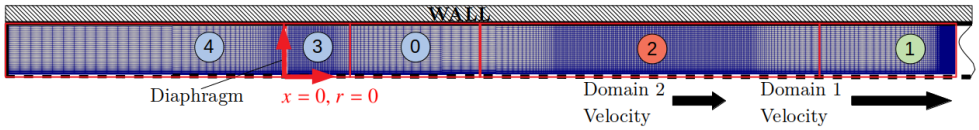

Fig. 4 Schematic of Computational Domains in FROSST.

Table 2 Minimum axial grid spacings for the baseline grid. All grew to a maximum of 10 mm. Refer to Figure 4.

Domain	Min Δx (mm)
0	1.0
1	0.2
2	2.0
3	1.0
4	1.0

B. Grid Convergence

A grid convergence study was performed upon the high deceleration ($u_i = 2800\,\mathrm{m/s}$) case, since it encountered the strongest shock and therefore the sharpest gradients both in the shock layer and the boundary layer. All cases used the same grid thereafter. Convergence was assessed upon test slug length and temperature distribution at 8 m. Shock speed history was also examined, but the trajectory ceased to change significantly on far coarser grids than were required to approach convergence of the test slug properties. The plots here are only the last level of refinement in order to demonstrate the sufficiency of the grid described above, as each zone underwent several coarser variations prior to arrival at the "baseline" given here. Grid refinement studies were found to require a whole-tube simulation, as opposed

to some sublength, because of the accumulating nature of nonuniformities upon the shock and test slug.

Table 3 Grid convergence spacing changes for baseline case.

Case Title	Domain of Concern	Spacing Direction	Spacing (mm)	Baseline Spacing (mm)	Flow Feature
A	1	Min Δx	0.1	0.2	Shock
B	All	Min Δy	0.005	0.01	Boundary Layer
C	2	Min Δx	1.0	2.0	CD
D	All	Max Δx	5.0	10.0	Background
E	3,4	Min Δx	0.5	1.0	Initial Shock Formation

Figure 5 demonstrates the sufficiency of the grid to accurately determine test time and maximum temperature in the test slug. The cases used therein are shown in Table 3. The first 250 μs can be seen to be identical for all runs. The maximum difference in test time is 1.5%, and the maximum difference in temperature is 0.8%. Given the broad range of uncertainties at the rear of the test slug encountered in actual experiments, additional uncertainties to be discussed in later sections of this paper, and considering also that further refinements all stay within this range, this convergence level was considered acceptable.

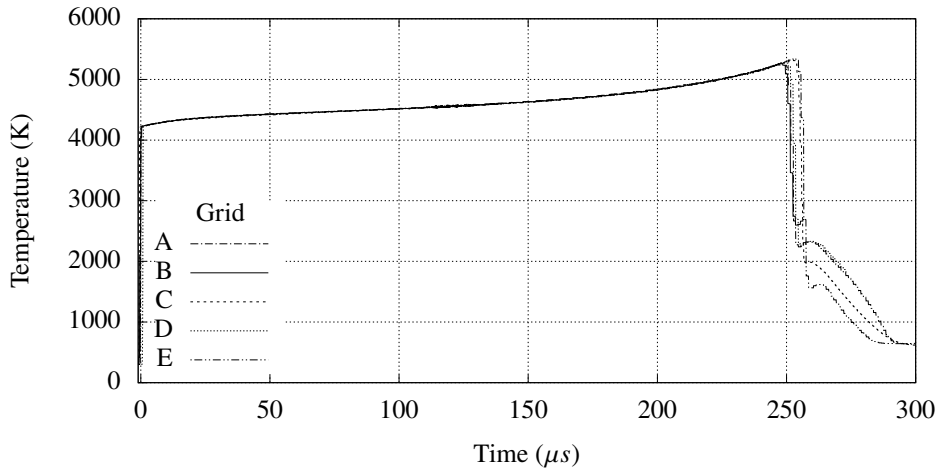

Fig. 5 Centreline temperature histories in the test slug of the u_i = 2800 m/s for different grids at x = 8 m.

III. Results

A. The Variation of Properties Through the Test Slug

Centreline test slug properties from each of the five cases are compared in Figure 6, with $t = 0$ representing the time of arrival of the shock at 8 m. Agreement of immediate post-shock properties for each profile is observed, confirming that each shock has reached 8 m at the same Mach number. The post-shock properties continue to agree with one-another

for a duration of 20 μs, with properties rising in a trend akin to Mirels' prediction of isentropic temperature rise for a steady-speed shock. However, the influence of shock history is evident for each beyond this initial phase.

The near-constant shock speed baseline case produces a test slug of nearly constant entropy and slightly rising temperature. However, temperature increases through the test gas for a decelerating case and decreases for an accelerating case. The maximum difference in temperature in the test gas is 56%. This large difference is caused by the retention of test gas processed by shocks of different strengths and the resulting changing entropy of that gas as supported by Figure 6b. As the shock changes strength, the difference in thermodynamic processes undergone by each test slug is evident, and it is also shown in Figure 6b that the entropy levels in the rear of each test slug match the entropy produced by ideal shocks of the Mach number encountered by each simulated shock near $x = 3m$. Test gas originating before this location is largely lost to the boundary layer for the present conditions. It therefore follows that the temperature variations in the test slug of each shock are a direct result of the entropy levels introduced by variations in shock speed, and are limited by the loss of test gas to the boundary layer.

Pressure increases monotonically through all observed test slugs, as seen in Figure 6c. However, perhaps counterintuitively, the magnitude of the rise follows an opposite trend to that of temperature and entropy, with the highest initial speed case producing the lowest average test slug pressure. The difference at the rear of the test slug between the initially fastest and slowest shock is 21%. The monotonic increase is consistent with the predictions of Mirels [B12], caused by the compression of test gas molecules pushed by the accelerating driver gas and CD. However, the decreasing average pressure with increasing initial shock speed is believed to be due to the relaxation waves produced by the variation in pressure behind the strengthening/weakening shockwave. These waves then partially reflect, and partially transmit through the CD due to the large change in sound speed across it, causing their influence to linger. Alongside variations in test slug thermodynamic properties, the test time may also be seen to vary as much as 19% between the different cases.

B. Comparison of Test Slug Variations Versus Theory

The mechanisms by which shock history causes variations in the test gas are explained in this section. Influences upon these trends originating from boundary layer effects must be differentiated and quantified against those produced by variations in post-shock properties. As a first look, a comparison may be made between the variations produced explicitly by boundary layer effects, the predicted properties behind ideal shockwaves, and the actual FROSST outputs. Figures 7 and 8 compare each of the centreline pressure traces seen in Figure 6 against the property variations as predicted by Mirels [B12] for a shock at the end-tube speed of 2100 m/s, and also against a test slug predicted by ideal shock theory. The ideal shock theory curves are computed by converting the Mach plot of Figure 3 into post-shock properties computed for the Mach number at each time, and then normalizing the time axis by the total time taken for the shock to reach $x = 8$ m. In reality, the compression of the gas to the rear of the test slug would bias the trends observed

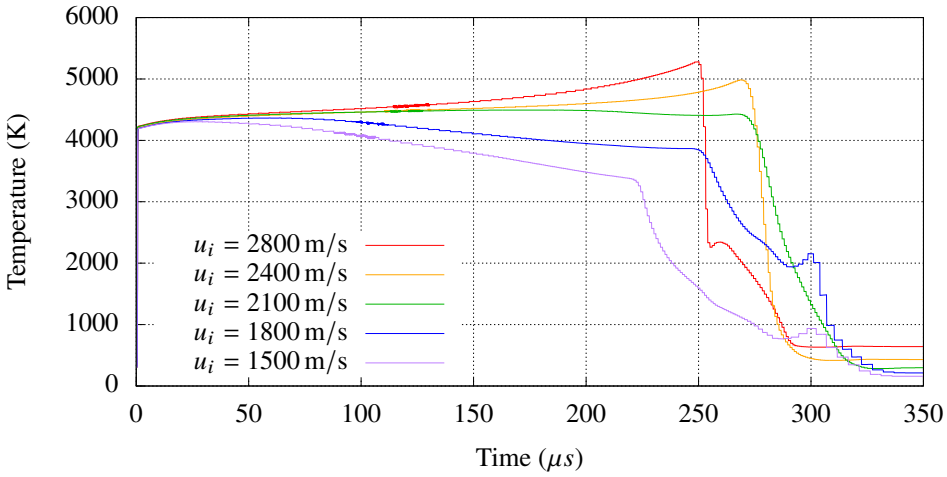

(a) Temperature profiles

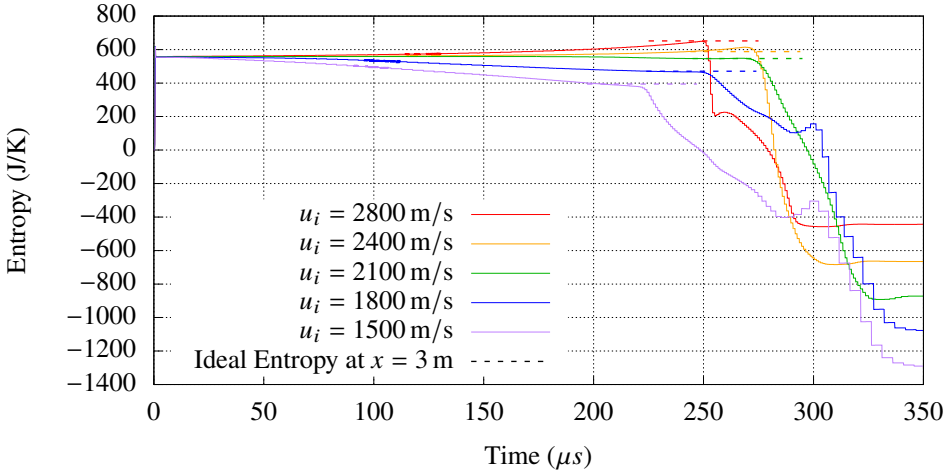

(b) Entropy profiles and ideal post-shock entropy at x = 3 m.

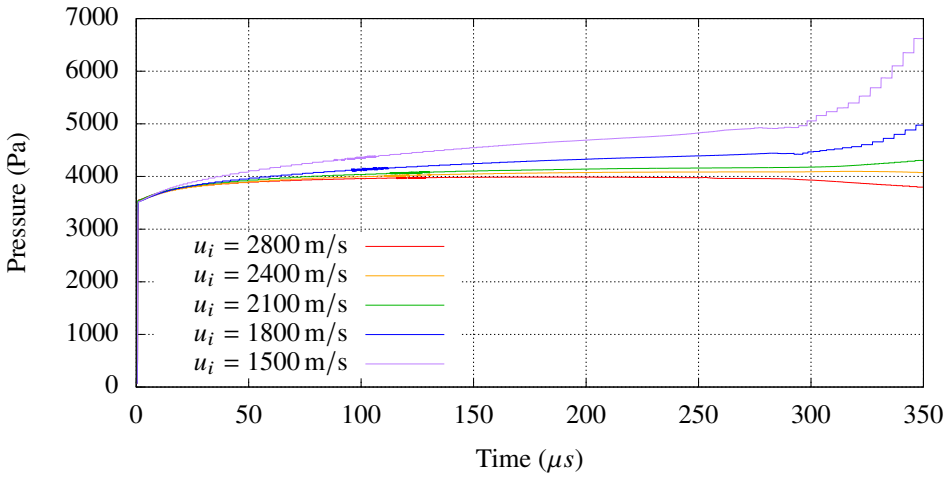

(c) Pressure profiles

Fig. 6 Temperature, entropy and pressure histories through the test slug at x = 8 m, r = 0 m.

in Figures 7-8 towards the right, but the values hereby produced enable a qualitative comparison. The FROSST test slug length was constructed by normalizing the traces of Figure 6 by the test time for each case, obtained as the time of arrival of cold gas in Figure 6a.

Starting with the baseline case of nearly constant 2100 m/s shock velocity, the trajectory reproduced Mirels' predictions to within 1.3% at all points, and 0.25% towards the rear of the test slug. The minor trend difference is due to Mirels' assumption, for the computation of property variations, of a quadratic boundary layer shape as opposed to the more complex shape which his underlying works derive [B10, 19, 31]. This very close agreement indicates that, in the absence of shock acceleration, the test slug is dominated by the well-known viscous effects of Mirels.

Pressure also initially agrees well with Mirels for both the accelerating $u_i = 1500$ m/s and decelerating $u_i = 2800$ m/s cases. However, pressure in the accelerating case continues to rise well above the predictions of Mirels and opposite the trend predicted by ideal shock theory. The decelerating case is seen to stay within 5% of the Mirels prediction, and shows no agreement with the trend predicted by ideal shock theory. These trends may be partially explained by the generation of relaxation waves as pressure changes post-shock, which travel rapidly through the test slug to equilibriate the pressure closer to the new post-shock pressure.

More substantial differences appear in temperature when the shock undergoes significant variation in speed. In the decelerating case, ideal shock theory predicts a maximum temperature of 8000 K, much hotter than the 5267 K maximum temperature shown by FROSST. Conversely, the accelerating case predicts a minimum temperature of 2230 K, whereas FROSST produces a minimum temperature of 3340 K. The accelerating case also shows a temperature trend opposite to that predicted by Mirels [B19], with the test slug temperature dropping by 22% from its maximum level behind the shock in the $u_i = 1500$ m/s case, instead of monotonically rising. Clearly, although shock history strongly influences the test slug properties, a mechanism exists to relax the temperatures away from their original post-shock levels. The source of this variation is discussed in the next section.

C. Sources of Variation in the Test Slug

1. Tracking Gas Packets in FROSST

The gas in the each test slug appears to have undergone a relaxation process by which its temperature was shifted away from both the predictions of Mirels and also ideal shock theory. In order to determine the nature of this process, the evolution of nonuniformities within the test slug as they develop throughout the run is now investigated. To study the evolution of each constituent portion of the test slug, massless gas packets were seeded in FROSST which moved at the local velocity and whose locations and associated gas properties were thereby updated each iteration. The properties of each packet were estimated using a second order central scheme at their current location. 16 packets were distributed evenly across the radius of the tube every 50 mm in the driven section, and every 5 mm in the driver section from $x = 0.0$ mm to $x = -200.0$ mm upstream of the diaphragm as visualized in Figure 9.

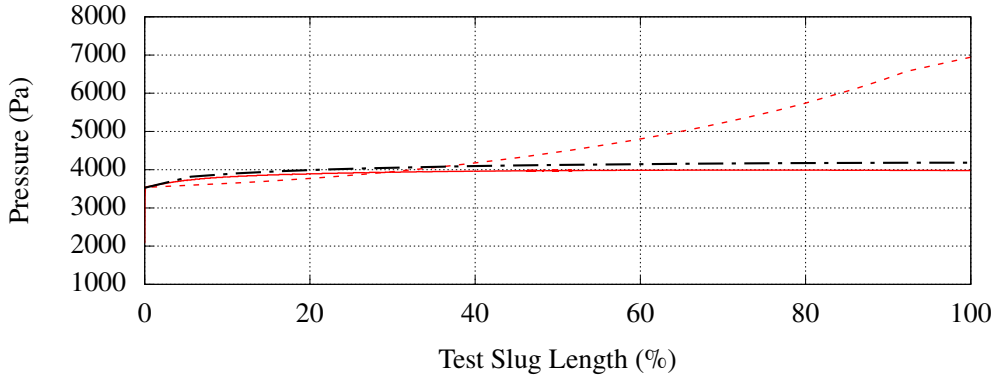

(a) Pressure, u_i = 2800 m/s, t_{test} = 250 μs

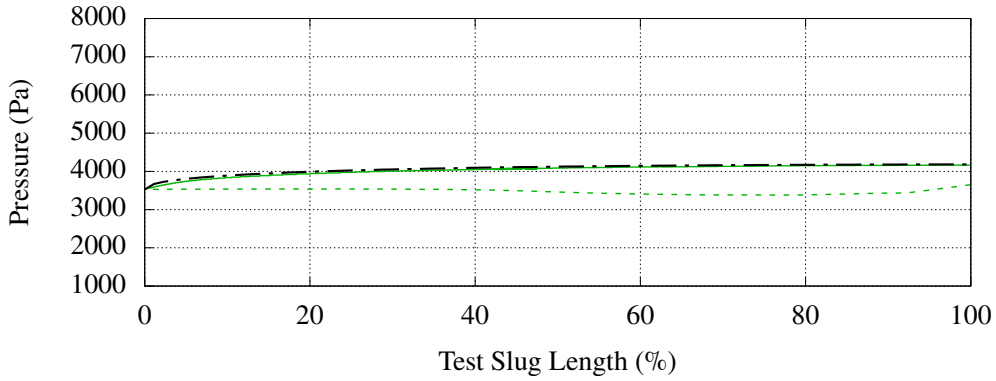

(b) Pressure, u_i = 2100 m/s, t_{test} = 267 μs

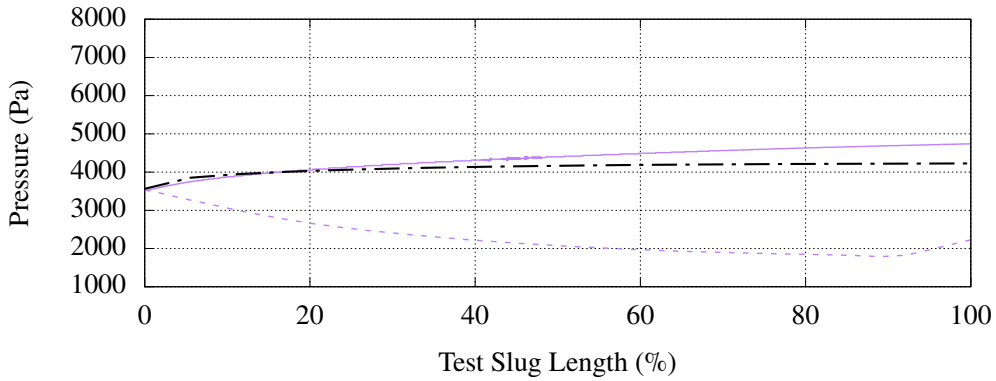

(c) Pressure, u_i = 1500 m/s, t_{test} = 220 μs

Fig. 7 Comparison of pressure profiles through the test gas at x = 8 m, r = 0 m as calculated by Mirels' theory [B 10] at u_{shock} = 2100 m/s, ideal shock theory and FROSST. t_{test} is the FROSST test time.

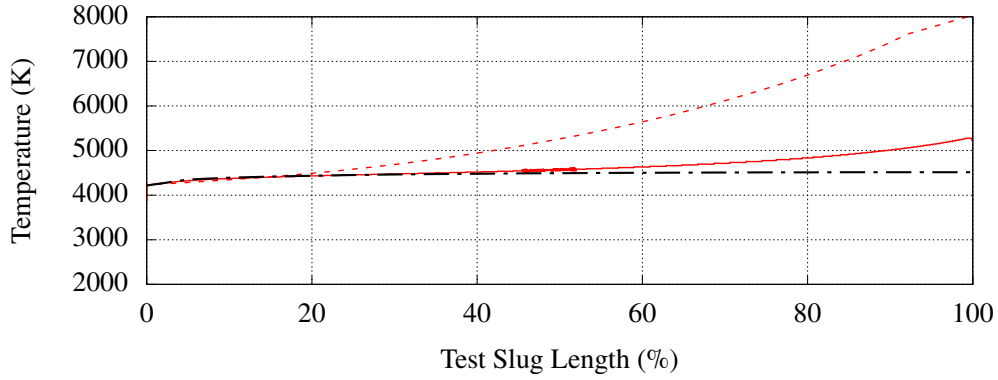

(a) Temperature, u_i = 2800 m/s, t_{test} = 250 μs

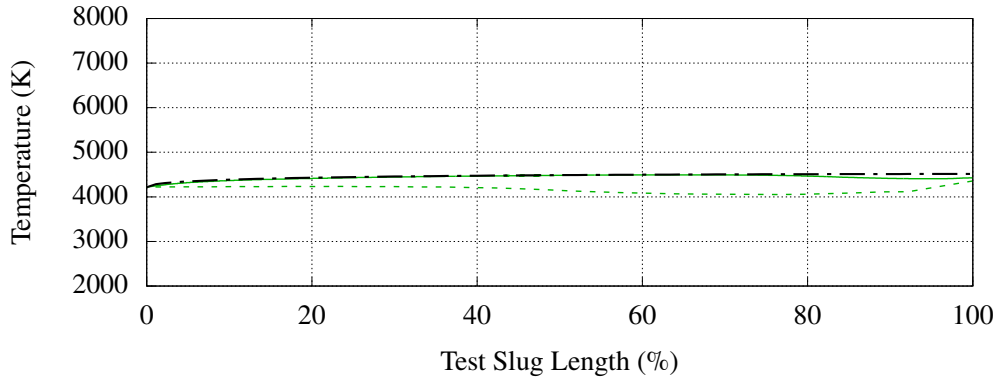

(b) Temperature, u_i = 2100 m/s, t_{test} = 267 μs

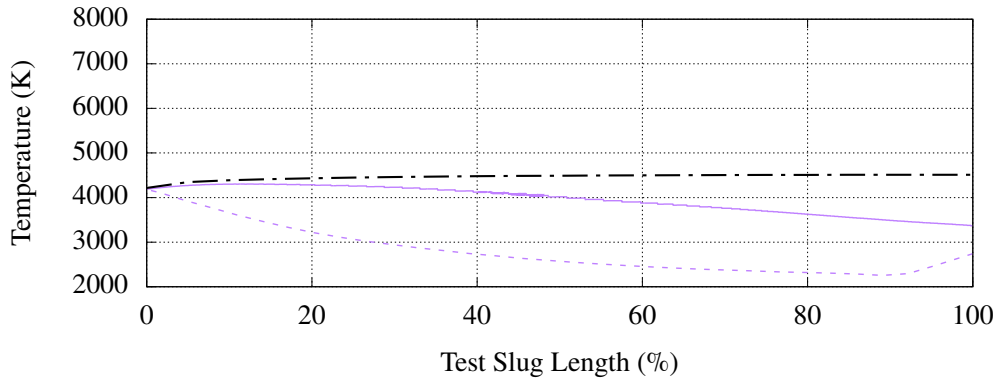

(c) Temperature, u_i = 1500 m/s, t_{test} = 220 μs

Fig. 8 Comparison of temperature profiles through the test gas at x = 8 m, r = 0 m as calculated by Mirels' theory [B 10] at u_{shock} = 2100 m/s, ideal shock theory and FROSST. t_{test} is the FROSST test time.

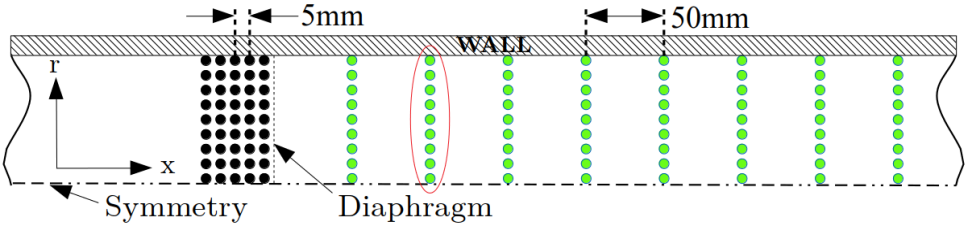

Fig. 9 Schematic of seeding points for the gas tracking with representative spacing distances (not to scale). Black denotes driver gas & green is test gas.

Location traces of the packets which initialized with passage of the shock at $x = 1$ m are pictured in Figure 10, which was produced when the shock was at $x = 8$ m for the $u_i = 2800$ m/s case. For clarity, the starting arrangement and position of these packets is circled in Figure 9. Figure 10 shows the trajectory of each of the gas packets, coloured by the time at which it passed each location. The growth of the boundary layer and the curvature of the shock both induce a radial velocity which pushes the gas slowly towards the wall. Eventually, packets originating closer to the wall are pulled into the boundary layer and slow dramatically in the laboratory frame of reference. Packets close to the centreline are only slightly influenced by the boundary layer, but are ultimately pushed towards the wall by the arrival of the driver gas.

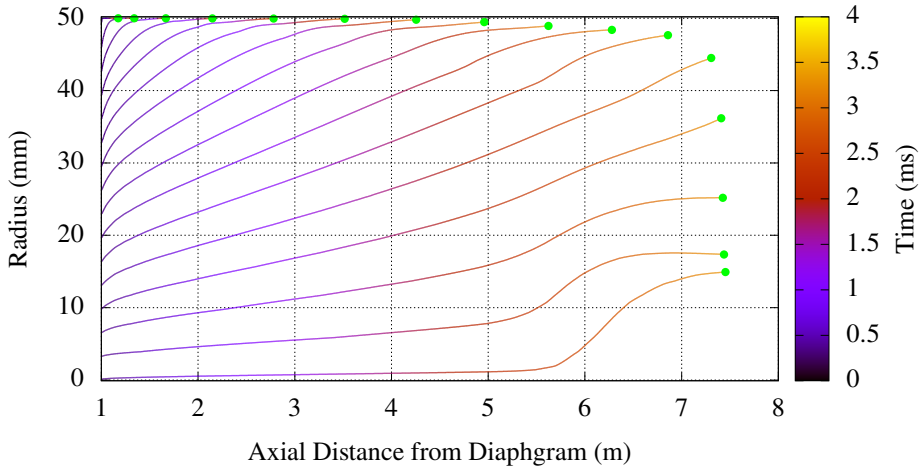

Fig. 10 Gas packet trajectories originating at axial distance of 1 m, coloured by time. Final positions marked in green. $u_i = 2800$ m/s case.

By examining the final locations of all tracked packets when the shock reaches $x = 8$ m, and colouring each packet by its starting axial location, the final arrangement of all gas processed by the shock may be determined, as seen in Figure 11. Several trends are immediately apparent. Most importantly, gas on the centreline may be seen to be composed of gas originating exclusively after $x = 3$ m. Packets originating earlier than this may be seen migrating towards the boundary layer and, upon reaching it, their influence upon variations in the test slug is thereafter lost. This shows that the test slug nonuniformities depend upon the state of gas processed far behind the final location of measurement, and

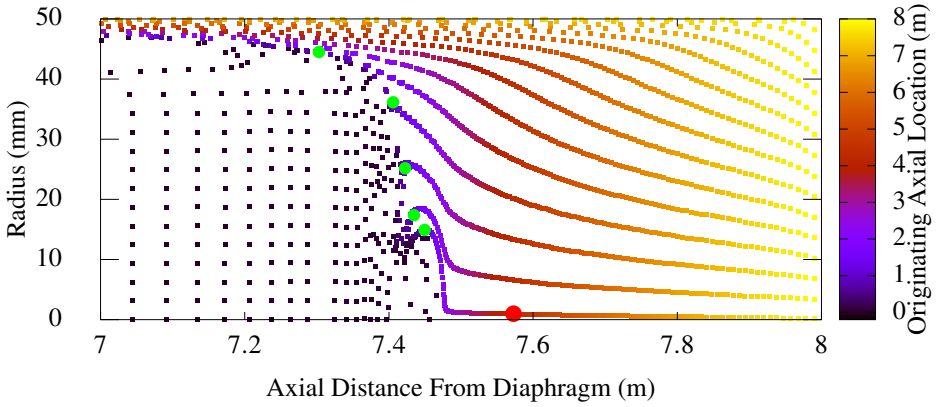

Fig. 11 Final gas packet positions colored by the original axial location of each packet, shock located at 8 m. Final positions of the packets in Figure 10 originating at $x = 1$ m are shown in green. $u_i = 2800$ m/s case.

that this dependence may be mitigated to an extent by boundary layer consumption. The effect is also exacerbated by thicker boundary layers associated with lower fill pressures, and so the maximum lifespan of gas in the test slug is dependent upon the particular conditions of a given test. Similar figures are produced for the flat $u_i = 2100$ m/s and accelerating $u_i = 1500$ m/s cases in Appendix A.

Other interesting trends are also visible. As Mirels predicted, the density increases moving upstream through the test slug from the shock, as is observable from the clustering of gas packets near the CD. The deformed shape of the contact discontinuity is also readily apparent. Finally, it may also be seen that the driver gas is very strongly pulled into the boundary layer, clearly demonstrating the source of acceleration of newer driver gas towards the CD as described by Satchell *et al* [B6].

2. Tracking the Evolution of a Single Gas Packet in FROSST

By examining the evolution of a single centreline gas packet, the process by which its final location in the test slug arrives at its given temperature may also be evaluated. The following discussion will center around a packet originating at 4 m along the centreline. The packet in question is shown in red in Figure 11. By 8 m, the packet has moved its way to the rear of the test slug but has not yet reached the CD jet. The history of this packet therefore represents the history of gas located in the rear of the test slug along the centreline, as its close neighbours will have undergone similar development processes.

Figures 12-13 show the evolution of the gas packet beginning with its arrival past the shock in the highly decelerating $u_i = 2800$ m/s case in 12a and 13a, and highly accelerating $u_i = 1500$ m/s case in 12c and 13c. Referring back to Figure 6a, and focusing first on the $u_i = 2800$ m/s case, the temperature of the test slug increases moving away from the shock and towards the CD. However, the packet can be seen to heat up briefly but then monotonically decrease

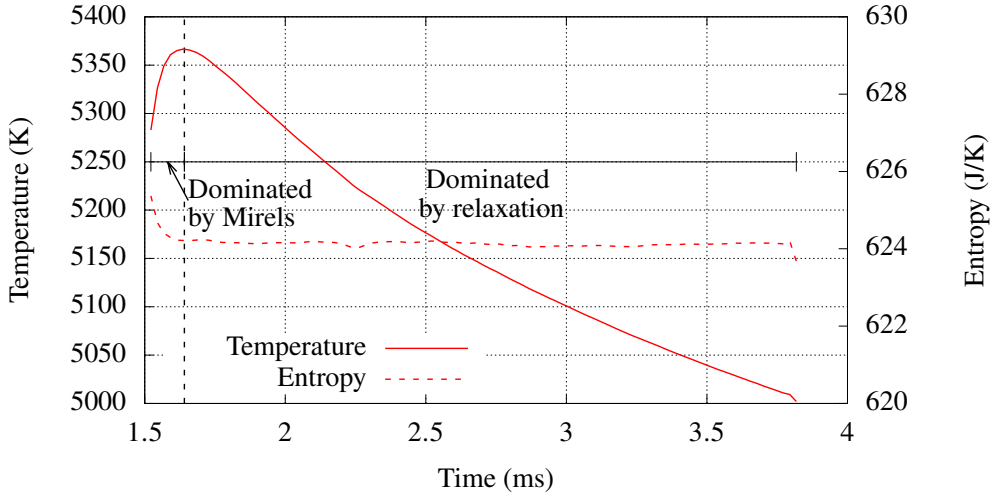

(a) u_i **= 2800 m/s Case**

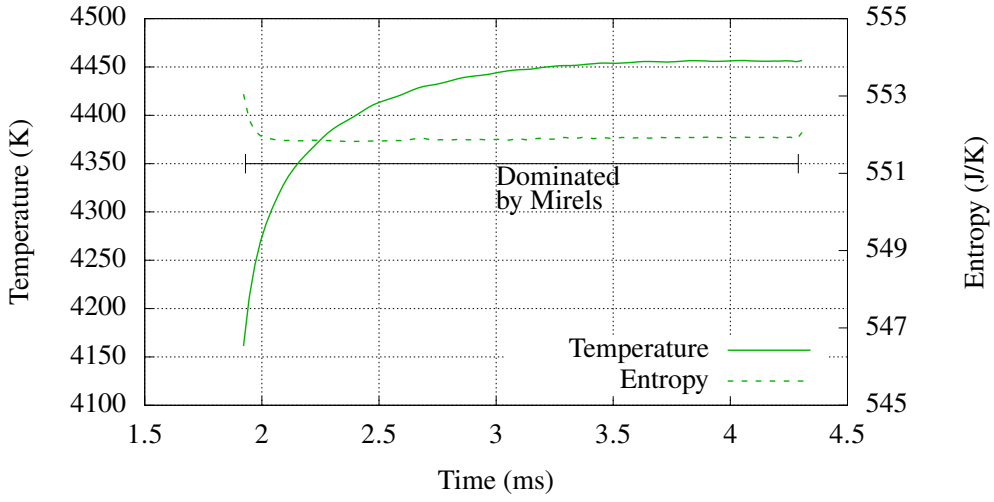

(b) u_i **= 2100 m/s**

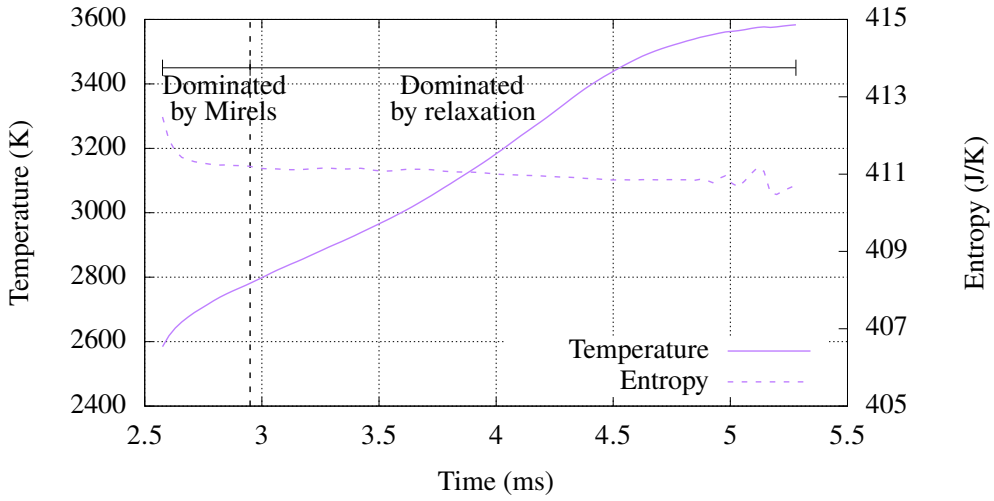

(c) u_i **= 1500 m/s**

Fig. 12 Evolution of centreline gas packet temperature and entropy, originating at x **= 4 m.**

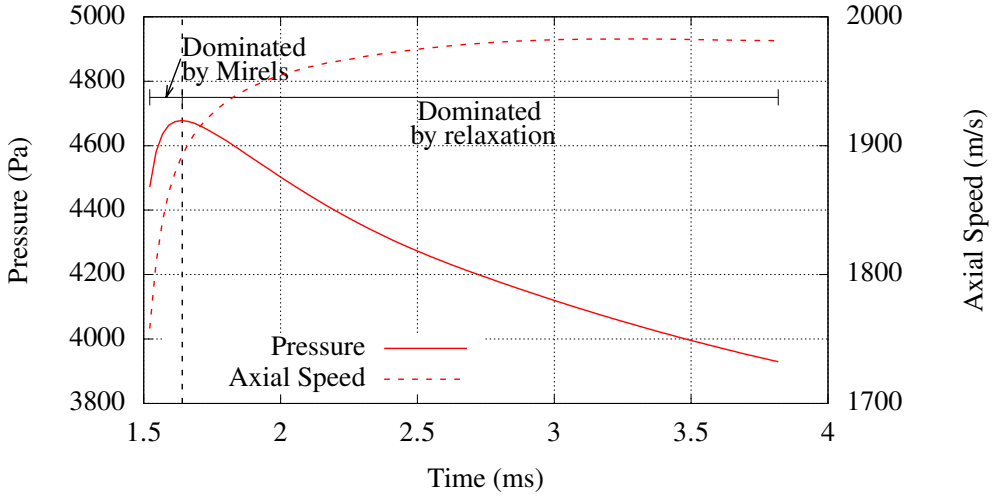

(a) u_i **= 2800 m/s Case**

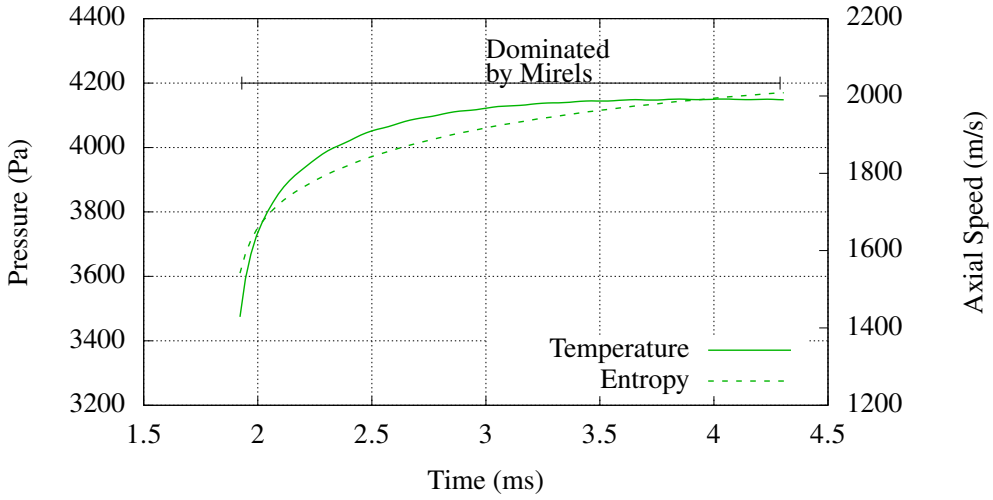

(b) u_i **= 2100 m/s**

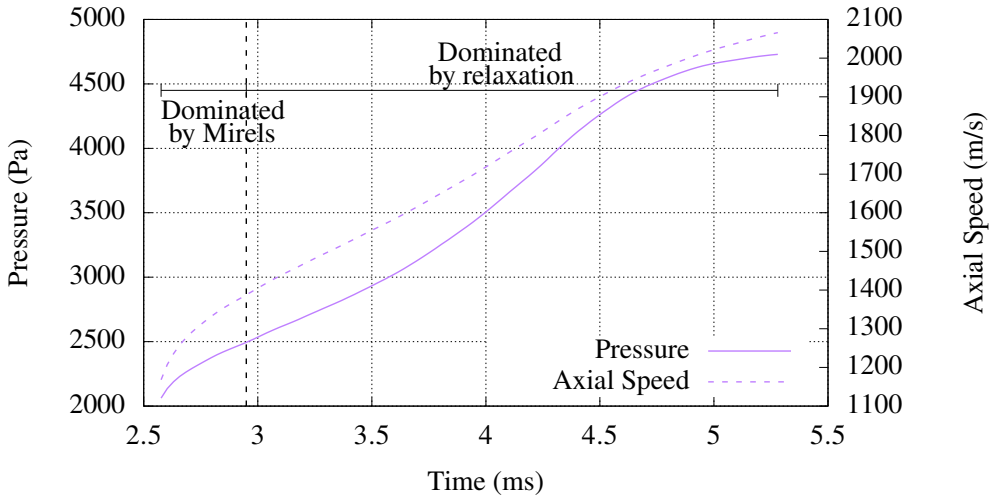

(c) u_i **= 1500 m/s**

Fig. 13 Evolution of centreline gas packet pressure and axial speed in the laboratory frame of reference, originating at x **= 4 m.**

nearly 350 K in a trend opposite to that observed in the overall test slug. The initial temperature and pressure rises are the result of the so-called 'Mirels effects.' Here, the acceleration of the gas packet due to boundary layer effects resembles, in a frame of reference travelling at the speed of the shock, a stagnation of the gas and is accompanied by an appropriate rise in temperature and pressure. The reason for the subsequent drop in temperature of the gas packet as it travels may be inferred by examination of the associated entropy and pressure histories. The process can be observed to be essentially isentropic, causing the temperature to reduce in a trend directly proportional to that of the pressure as it lowers behind the slowing shock. Thus source of temperature variation in the slice is the drop in pressure caused by the relaxation of pressure waves emitted by the slowing shock.

Examining now the strongly accelerating case of $u_i = 1500\,\mathrm{m/s}$ in Figure 12c and 13c, the same centreline $x = 4\,\mathrm{m}$ packet is examined in Figure 12c and 13c. Temperature and pressure trends are exactly opposite to those observed for the decelerating case. The temperature is seen to isentropically rise with the post-shock pressure, also in a trend opposite to that of the overall test slug for the case. In addition to shifting the temperature in the test slug, the relaxation of pressure waves from a shock of variable speed also significantly influences the test time by deforming the CD as seen in Figure 14a. Pressure waves are not able to completely penetrate the CD, partially reflecting and partially transmitting [B18]. When the relaxation waves reach the CD, these waves cause a pressure disturbance around the CD which results in its deformation.

D. Deformation of the Contact Discontinuity

The pressure difference across the CD sets the conditions to form a Rayleigh-Taylor instability across it [B32]. Although the instability is only beginning to form in the flat $u_i = 2100\,\mathrm{m/s}$, visible as small waves in Figure A4 in Appendix A, the increasing local pressure from an accelerating shock pushes upon the CD, whilst decreasing pressure pulls on it, ultimately triggering the instability. Additionally, curvature of the CD, as well as the presence of the boundary layer itself, causes these pressure waves to act upon the CD in a non-uniform manner, such that the waves exert more influence upon the CD towards the core of the flow. The result is that in the accelerating shock case the higher pressure pushes on the CD towards the center but not as much towards the wall. The instability thus forms near the wall and thereby contaminates the test slug, as can be seen in Figure 14a. Likewise, lowering pressure behind the decelerating shock pulls on the CD towards the center, causing a more coherent structure of driver gas to be pulled into the test gas along the axis. The resulting contamination of the test slug causes, in both accelerating and decelerating cases, the test time to be shortened by 16% as compared to the flat trajectory wherein the CD remains largely undeformed. The slight smearing of the CD for the flat case is due to the minor levels of acceleration and deceleration encountered in that trajectory. These observations confirm the predictions of Hooker that the CD should become a zone of "considerable mixing" under many conditions [B9]. These findings also suggest that the contamination of the test gas caused by CD deformation may be expected to worsen with increased variations in shock speed.

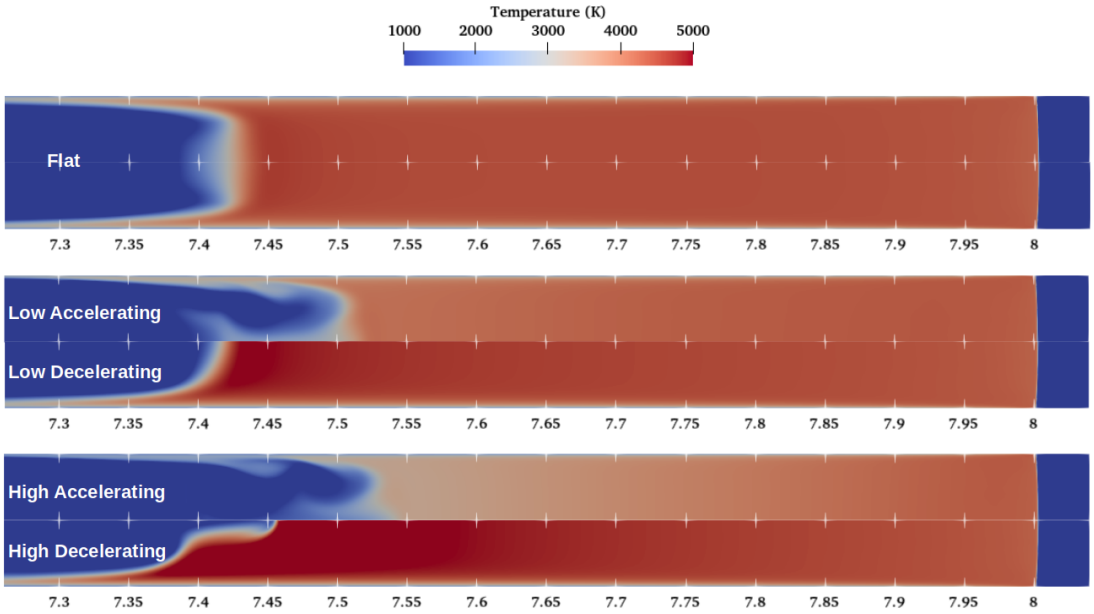

(a) FROSST surface plots of temperature showing CD deformation due to variations in shock speed.

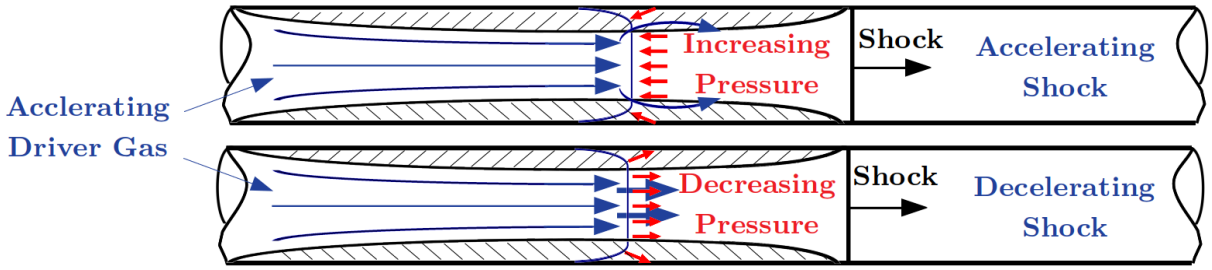

(b) Schematic of pressures affecting CD deformation.

Fig. 14 CD deformations caused by pressurization or depressurization of the test slug due to shock speed variations.

IV. Discussion

Macroscopic nonuniformities in the test slug caused by a changing shock velocity have been shown here to arise from a combination of processes: gas leaving the test slug, Mirels' effects, post-shock entropy variations and relaxation of the pressure field produced by variations in post-shock pressure. The resulting nonuniformities in temperature, pressure and entropy through the slug yielded substantial divergence from the predictions of the theories of Mirels. It was further shown in the more localized view that a packet of gas, having been processed by the shock, undergoes a relaxation process due to the changing shock speed. This relaxation process is driven by the changing post-shock pressure equilibrating throughout the test slug, isentropically shifting the temperature with it.

This study was performed in the context of a perfect, inert gas absent any thermochemical processes, indicating that the flow features discussed herein are fundamentally products of fluid dynamics. As such, it is clear that these influences will remain present and interfere with the thermochemical complexities which are of primary interest to

most shock tube studies. The time of flight of a given particle in the test slug and the thermodynamic processes which influence it are key factors in determining the chemical state of that particle [B12, 13]. The demonstrated evolution of the particles as they travel the test slug indicates that any effort to determine the chemical state of a given portion of the test slug must consider the history of the shock which processed that gas. In other words, in the presence of thermochemistry, an evaluation of test results which considers the thermodynamic processes discussed herein would result in a substantially different chemical makeup within the test slug than an evaluation which did not consider shock history. As the test Mach number increases and thermochemical nonequilibrium begins to dominate the test slug, the significance of the unsteady particle relaxation history also increases.

It is further proposed that, in comparing the radiative or thermochemical results of two different impulse facilities, the shock history produced by each facility must be accounted for in the comparison. Several studies have indicated that shock history effects are suspected in several of their thermochemical studies, for example in [B15, 33]. Collen *et al* [B29], in comparing radiative emissions of nominally identical test conditions in the test results of the Oxford T6 Stalker facility [B34] and the NASA EAST facility [B35] identified significantly different trends in radiative intensity through the test slug. The authors' supposition that part of this difference may originate in the different shock trajectories which each facility characteristically produces is supported by the findings of this work.

A. Conclusion

This paper has demonstrated that variations in shock speed produce nonuniformities in the test gas which follow them. The macroscopic test slug variations are shown to be opposite from the variations encountered by the particles which traverse and comprise the test gas. Although an accelerating shockwave may produce a test slug whose temperature lowers moving away from the shock, the particles which migrate to the rear of the test slug in fact heat up as they travel, and the opposite observations apply to decelerating shocks. Therefore, as a chemically reacting and/or radiating gas travels through the test slug, its pressure and temperature will be substantially influenced not just by the products of its reactivity, but also by the isentropic shock history effects detailed herein. Although these results were investigated in the absence of thermochemical phenomena, it is clear that consideration of shock history in the analysis of radiative and thermochemical processes investigated in shock tubes is important. Accordingly, models seeking to predict or interpret shock tube experimental results, compare results between facilities, or to establish the conditions at a secondary diaphragm in expansion or reflected shock tubes, must account for these effects in order to provide accurate results. These findings may also help to explain some of the well-documented uncertainties in thermochemical rate data and radiative heating of hypersonic vehicles.

Appendix A - Gas packet tracking for $u_i = 1500\,\mathrm{m/s}$ and $u_i = 2100\,\mathrm{m/s}$ cases

Gas packet tracking profiles are shown for the accelerating $u_i = 1500\,\mathrm{m/s}$ and flat $u_i = 2100\,\mathrm{m/s}$ cases in Figures A1-A2 and A3-A4, respectively. Significant mixing, caused by the wall jet may readily be observed in the accelerating case. The flat case shows no such mixing, since the slug and the interface are both smooth flows exhibiting none of the instabilities associated with unsteady shock speed.

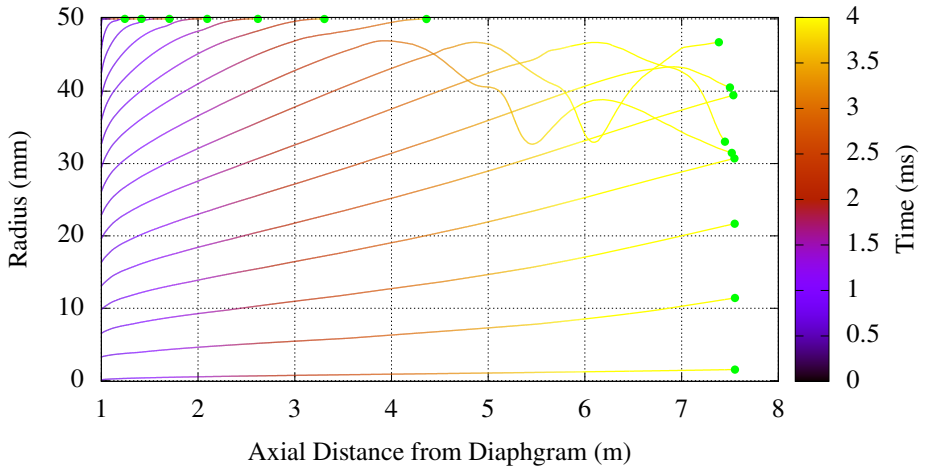

Fig. A1 Gas packet trajectories originating at axial distance of $x = 1\,\mathrm{m}$, colored by time. Final positions marked in green. $u_i = 1500\,\mathrm{m/s}$ case.

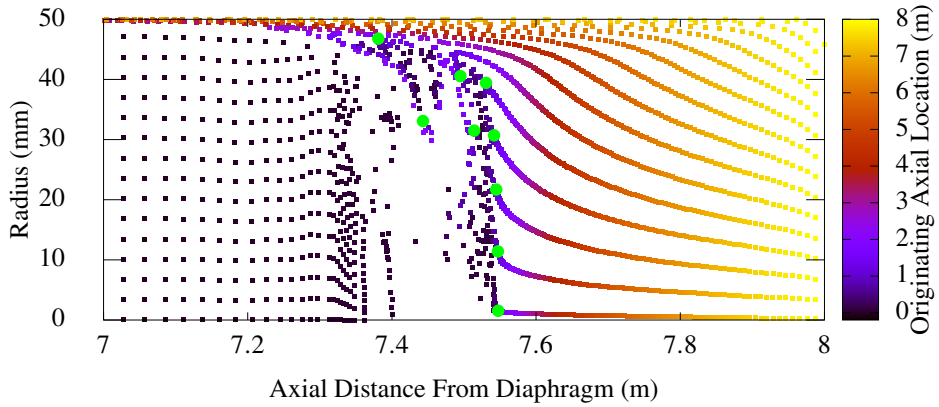

Fig. A2 Final gas packet positions coloured by the original axial location of each packet, shock located at 8 m. Final positions of the packets in Figure A1 originating at $x = 1\,\mathrm{m}$ are shown in green. $u_i = 1500\,\mathrm{m/s}$ case.

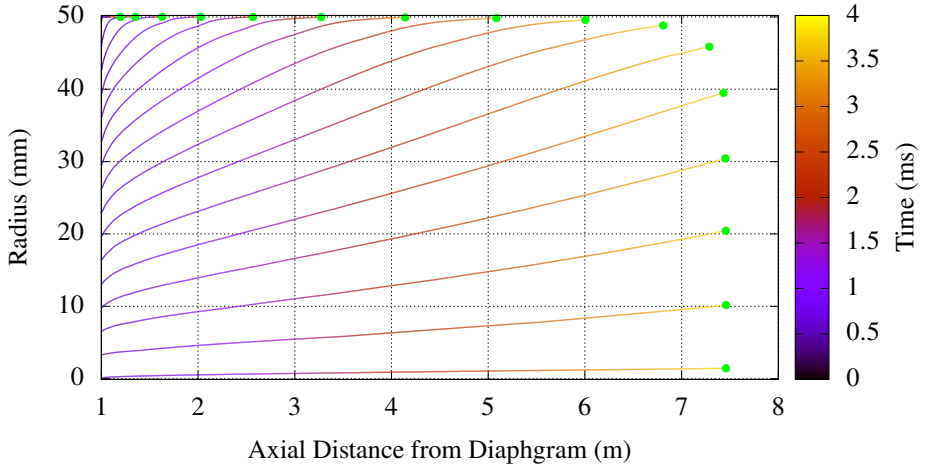

Fig. A3 Gas packet trajectories originating at axial distance of $x = 1$ m, colored by time. Final positions marked in green. $u_i = 2100$ m/s case.

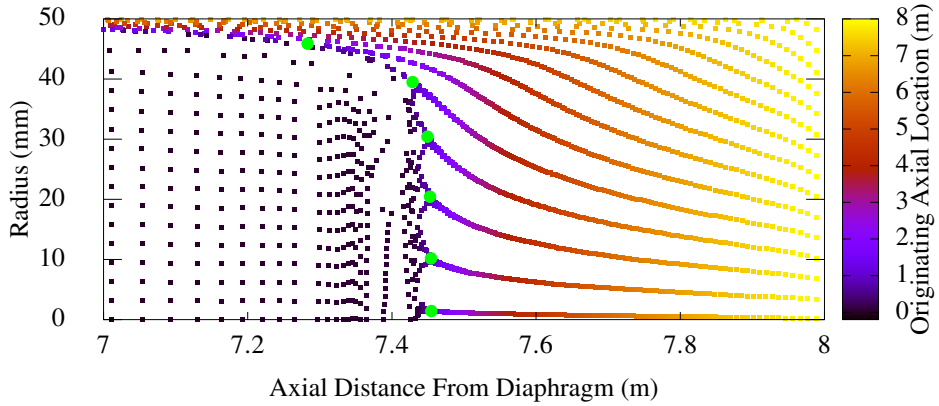

Fig. A4 Final gas packet positions coloured by the original axial location of each packet, shock located at 8 m. Final positions of the packets in Figure A3 originating at $x = 1$ m are shown in green. $u_i = 2100$ m/s case.

A. Acknowledgements

The authors would like to thank the US Air Force for their support of this effort.

References

[B1] Anderson, J., *Hypersonic and High Temperature Gas Dynamics*, American Institute of Aeronautics and Astronautics, Reston, VA, 2000.

[B2] McGilvray, M., Austin, J. M., Sharma, M., Jacobs, P. A., and Morgan, R. G., "Diagnostic modelling of an expansion tube operating condition," *Shock Waves*, Vol. 19, No. 1, 2009, pp. 59–66. https://doi.org/10.1007/s00193-009-0187-9, URL https://doi.org/10.1007/s00193-009-0187-9.

[B3] Kotov, D. V., Yee, H., Panesi, M., Prabhu, D. K., and Wray, A. A., "Computational Challenges for Simulations Related to the NASA Electric Arc Shock Tube (EAST) Experiments," *Journal of Computational Physics*, Vol. 269, 2014, pp. 215 – 233.

[B4] Chandel, D., Nompelis, I., and Candler, G., "Computations of High Enthalpy Shock-waves in Electric Arc Shock-Tube (EAST) at NASA Ames," *2018 AIAA Aerospace Sciences Meeting*, American Institute of Aeronautics and Astronautics, 2018. https://doi.org/10.2514/6.2018-1722.

[B5] James, C. M., Gildfind, D. E., Lewis, S. W., Morgan, R. G., and Zander, F., "Implementation of a State-to-State Analytical Framework for the Calculation of Expansion Tube Flow Properties," *Shock Waves*, Vol. 28, No. 2, 2018, pp. 349–377. https://doi.org/10.1007/s00193-017-0763-3.

[B6] Satchell, M., Collen, P., McGilvray, M., and Mare, L. D., "Numerical Simulation of Shock Tubes Using Shock Tracking in an Overset Formulation," *AIAA Journal*, 2021, pp. 1–11. https://doi.org/10.2514/1.j059829.

[B7] Petrie-Repar, P., and Jacobs, P., "A Computational Study of Shock Speeds in High-Performance Shock Tubes," *Shock Waves*, Vol. 8, No. 2, 1998, pp. 79–91. https://doi.org/10.1007/s001930050101.

[B8] Rothkopf, E. M., and Low, W., "Diaphragm Opening Process in Shock Tubes," *The Physics of Fluids*, Vol. 17, No. 6, 1974, pp. 1169–1173. https://doi.org/10.1063/1.1694860.

[B9] Hooker, W. J., "Testing Time and Contact-Zone Phenomena in Shock-Tube Flows," *Physics of Fluids*, Vol. 4, No. 12, 1961, p. 1451. https://doi.org/10.1063/1.1706243, URL https://doi.org/10.1063/1.1706243.

[B10] Mirels, H., "Test Time in Low-Pressure Shock Tubes," *Physics of Fluids*, Vol. 6, No. 9, 1963, pp. 1201–1214. https://doi.org/10.1063/1.1706887.

[B11] Mirels, H., "Shock Tube Test Time Limitation Due to Turbulent Wall Boundary Layer," *AIAA Journal*, Vol. 2, No. 1, 1964, pp. 84–93. https://doi.org/10.2514/3.2218.

[B12] Mirels, H., "Flow Nonuniformity in Shock Tubes Operating at Maximum Test Times," *Physics of Fluids*, Vol. 9, No. 10, 1966, p. 1907. https://doi.org/10.1063/1.1761542.

[B13] Holbeche, T. A., and Spence, D. A., "A Theoretical and Experimental Investigation of Temperature Variation Behind Attenuating Shock Waves," *Proceedings of the Royal Society of London. Series A, Mathematical and Physical Sciences*, Vol. 279, No. 1376, 1964, pp. 111–128. URL http://www.jstor.org/stable/2414836.

[B14] Brandis, A., Cruden, B., Prabhu, D., Bose, D., McGilvray, M., Morgan, R., and Morgan, R., "Analysis of Air Radiation Measurements Obtained in the EAST and X2 Shocktube Facilities," *10th AIAA/ASME Joint Thermophysics and Heat Transfer Conference*, American Institute of Aeronautics and Astronautics, 2010. https://doi.org/10.2514/6.2010-4510.

[B15] Cruden, B. A., Brandis, A. M., and Prabhu, D. K., "Compositional Dependence of Radiance in CO2/N2/Ar Systems," *44th AIAA Thermophysics Conference*, American Institute of Aeronautics and Astronautics, 2013. https://doi.org/10.2514/6.2013-2502.

[B16] Vasil'ev, E. I., and Danil'chuk, E. V., "Numerical solution of the problem of shock tube flow development with transverse diaphragm withdrawal," *Fluid Dynamics*, Vol. 29, No. 2, 1994, pp. 270–276. https://doi.org/10.1007/bf02324319.

[B17] White, D. R., "Influence of Diaphragm Opening Time on Shock-Tube Flows," *Journal of Fluid Mechanics*, Vol. 4, No. 6, 1958, p. 585–599. https://doi.org/10.1017/S0022112058000677.

[B18] Paull, A., and Stalker, R. J., "Test flow disturbances in an expansion tube," *Journal of Fluid Mechanics*, Vol. 245, 1992, p. 493–521. https://doi.org/10.1017/S0022112092000569.

[B19] Mirels, H., "Attenuation in a Shock Tube Due to Unsteady-Boundary-Layer Action," *NACA Report 1333*, 1957.

[B20] Duff, R. E., "Shock-Tube Performance at Low Initial Pressure," *Physics of Fluids*, Vol. 2, No. 2, 1959, p. 207. https://doi.org/10.1063/1.1705910.

[B21] Glass, and patterson, "A Theoretical and Experimental Study of Shock-Tube Flows," *Journal of the Aeronautical Sciences*, Vol. 22, No. 2, 1955, pp. 73–100. https://doi.org/10.2514/8.3282.

[B22] Spence, D. A., and Woods, B. A., "A review of theoretical treatments of shock-tube attenuation," *Journal of Fluid Mechanics*, Vol. 19, No. 02, 1964, p. 161. https://doi.org/10.1017/s0022112064000623.

[B23] Ikui, T., and Matsuo, K., "Investigations of the Aerodynamic Characteristics of the Shock Tubes : (Part 1, The Effects of Tube Diameter on the Tube Performance)," *Bulletin of JSME*, Vol. 12, No. 52, 1969, pp. 774–782. https://doi.org/10.1299/jsme1958.12.774.

[B24] III, C. G. M., and Jones, J. J., "Incident Shock-Wave Characteristics in Air, Argon, Carbon Dioxide, and Helium in a Shock Tube with Unheated Helium Driver," *Technical Report TN D-8099*, 1975.

[B25] Brandis, A. M., and Cruden, B. A., "Shock Tube Radiation Measurements in Nitrogen," *2018 Joint Thermophysics and Heat Transfer Conference*, American Institute of Aeronautics and Astronautics, 2018. https://doi.org/10.2514/6.2018-3437, URL https://doi.org/10.2514/6.2018-3437.

[B26] Petersen, E. L., and Hanson, R. K., "Nonideal Effects Behind Reflected Shock Waves in a High-Pressure Shock Tube," *Shock Waves*, Vol. 10, No. 6, 2001, pp. 405–420.

[B27] Light, G. C., "Test Gas Properties Behind a Decelerating Shock Wave in a Shock Tube," *Physics of Fluids*, Vol. 16, No. 5, 1973, p. 624. https://doi.org/10.1063/1.1694397.

[B28] Jacobs, P. A., "Quasi-One-Dimensional Modeling of a Free-Piston Shock Tunnel," *AIAA Journal*, Vol. 32, No. 1, 1994, pp. 137–145. https://doi.org/10.2514/3.11961.

[B29] Collen, P. L., Doherty, L., McGilvray, M., Naved, I., Geraets, R. T. P., Hermann, T. A., Morgan, R. G., and Gildfind, D., "Computations of High Enthalpy Shock-waves in Electric Arc Shock-Tube (EAST) at NASA Ames," *57th AIAA Aerospace Sciences Meeting*, American Institute of Aeronautics and Astronautics, 2019. https://doi.org/10.2514/6.2019-1941.

[B30] McGilvray, M., Dann, A. G., and Jacobs, P. A., "Modelling the complete operation of a free-piston shock tunnel for a low enthalpy condition," *Shock Waves*, Vol. 23, No. 4, 2013, pp. 399–406. https://doi.org/10.1007/s00193-013-0437-8, URL https://doi.org/10.1007/s00193-013-0437-8.

[B31] Mirels, H., "Boundary Layer Behind Shock or Thin Expansion Wave Moving Into Stationary Fluid," *NACA TN-3712*, 1956.

[B32] Youngs, D. L., "Numerical simulation of turbulent mixing by Rayleigh-Taylor instability," *Physica D: Nonlinear Phenomena*, Vol. 12, No. 1-3, 1984, pp. 32–44. https://doi.org/10.1016/0167-2789(84)90512-8.

[B33] Cruden, B. A., and Brandis, A. M., "Measurement of Radiative Nonequilibrium for Air Shocks Between 7 and 9 km/s," *Journal of Thermophysics and Heat Transfer*, Vol. 34, No. 1, 2020, pp. 154–180. https://doi.org/10.2514/1.t5735.

[B34] Collen, P. L., Doherty, L., and McGilvray, M., "Measurements of radiating hypervelocity air shock layers in the T6 free-piston driven shock tube," *International Conference on Flight vehicles, Aerothermodynamics and Re-entry Missions and Engineering (FAR 2019)*, 2019.

[B35] Brandis, A. M., and Cruden, B. A., "Benchmark Shock Tube Experiments of Radiative Heating Relevant to Earth Re-entry," *55th AIAA Aerospace Sciences Meeting*, American Institute of Aeronautics and Astronautics, 2017. https://doi.org/10.2514/6.2017-1145.

Chapter 5

AN ANALYTICAL METHODOLOGY FOR REBUILDING SHOCK TUBE EXPERIMENTS

As observed in Chapter 4, the entropy of a gas packet far from the boundary layer remains essentially constant once processed by the shock. The LAgrange Shock Tube Analysis (LASTA) code is now developed around tracking isentropic 'slices' of shock-processed gas as their total enthalpy is influenced by wave processes and boundary layer effects. It is perhaps noteable that the formulation of Light [52] is premised upon a similar concept. However, where Light tried to produce a system of equations relating the many slices to one-another through a series of boundary conditions, this present work treats each slice as an entirely independent entity which is uninfluenced by its neighbouring slices. Light's analysis was limited by his assumption that deviations in post-shock properties would be small, and so Light noted that the methodology was unable to capture the relaxation effect of continuous expansion behind the decelerating shock. Light also highlighted that the absence of waves originating upstream, such as from the driver gas, introduced additional errors into the calculation. In the present methodology, accurate capture of the relaxation effects comprises the majority of the theoretical development.

LASTA is able to account for thermochemical equilibrium effects by using an in-house tool entitled the Osney Chemical Equilibrium ANalysis (OCEAN) code [15]. The code has been validated against CEA and is presently being further developed to accommodate chemical nonequilibrium solutions. The code in its present state obtains the chemical state by use of a Helmholtz free energy minimization

based on the general methodology developed by Zeleznik and Gordon [83]. It is able to solve a variety of problems which perform the minimisation while holding different properties constant, such as pressure and entropy, temperature and pressure, or enthalpy and entropy, and also a normal shock problem provided a shock speed and pre-shock conditions.

LASTA is shown to allow full characterisation of equilibrium experimental shock tube test gases with virtually no computational expense. This characterisation is enabled by the basic premise that the shock trajectory contains all information required to determine the state of the gas behind it. The information is contained in the form of upstream waves which determine the trajectory, the entropy gradients produced by the changing shock speed, and the relaxation waves which are produced accompanying the entropy gradients. By extracting from the shock trajectory the influences of each of these effects upon the post-shock flow, and a performing mass balance to account for losses to the boundary layer, the entire test slug may be reconstructed with a high degree of confidence.

The validation of the LASTA code against experiments performed in T6 demonstrates the accuracy and versatility of the methodology against the full complexity encountered in actual experimental test conditions. The code, once validated, was supplied to DPhil candidate Peter Collen in order to use the thermochemical variations in the test slug predicted by LASTA to study the radiative intensity from a broad variety of production data from T6 and also NASA EAST. These tests included substantial shock deceleration as is typical with EAST shots, and were sufficiently high speed that most contained significant zones of thermochemical nonequilibrium. The results of these investigations were highly accurate reproductions of the experimental radiative data to within 5%-10% for most cases outside of the initial zone of nonequilibrium. This development represents a major step forward in the present state of the field, and will allow a far more accurate analysis of radiative emissions and the underlying thermochemistry studied in shock tubes than has previously been possible.

Both of the following papers have been submitted together as a series to AIAA Journal for peer review. Co-authors on the second paper, DPhil candidates Alex Glenn and Peter Collen operated T6 for the experiments, and Rowland Penty-Geraets performed the experimental heat transfer analysis.

An Analytical Method of Evaluating Nonuniformities in Shock Tube Flows. Part 1: Theory and Development.

Matthew Satchell *, Matthew McGilvray †, and Luca Di Mare ‡
Osney Thermofluids Institute, University of Oxford, United Kingdom

Shock tube experiments are a cornerstone of investigations into the hypersonic flight environment. However, the actual flow through the basic shock tube has not been well characterised in the literature, and nonuniformities arising in the test gases are not well understood. This work produces a quasi-one-dimensional analytical methodology for predicting the nonuniformities in shock tube experimental test gases based exclusively on the experimentally measured history of shock speed down the tube. Wave effects extracted from shock speed variations are shown to provide all information necessary in order to reconstruct the test slug from any particular experiment. Accurate representation of flow dynamics is initially checked against ideal gas cases following accelerating and decelerating shock trajectories, each with a tube-end Mach number of 6.5 and a fill pressure of 66.66 Pa. Agreement between the method and results from a viscous, axisymmetric Navier-Stokes solution is found to within 1% in pressure and temperature.

I. Nomenclature

Variables

U	=	Gas State Variables
P	=	Pressure, Pa
ρ	=	Density, kg/m^3
T	=	Temperature, K
h	=	Static Enthalpy, J/Kg
H	=	Total Enthalpy, J/Kg
u	=	Axial Velocity, m/s
c	=	Sound Speed, m/s
S	=	Flow Area, m^2
r	=	Radius, m

*DPhil Candidate, Department of Engineering Science, Oxford Thermofluids Institute, University of Oxford.
†Associate Professor, Oxford Thermofluids Institute, Department of Engineering Science, University of Oxford.
‡Associate Professor, Oxford Thermofluids Institute, Department of Engineering Science, University of Oxford.

t = Current Time Level, s

t^+ = Future Time Level, s

t^- = Earlier Time Level, s

t^0 = Slice Starting Time Level, s

λ = Wave Speed, m/s

s = Entropy, $J/(KgK)$

l = Distance Between Slice and Shock, m

ω = Characteristics

M = Mach Number

$a_{L/R}$ = Wave Amplification Factor

β = Boundary Layer Shape Factor

C_M^α = Mirels Shape Adjustment Factor

δ = Arbitrary Change in Time or Space

Δ = Change Between Discrete States

Subscripts

$1, 2$ = Pre/Post-Shock States

a, b, c = Post-Shock Time States

sh = Post-Shock Properties

E = Slice Properties

L, R = Riemann Problem States

w = Wall Properties

$\tilde{}$ = Roe-Averaged Property

II. Introduction

Shock tube experiments are vital to the study of the hypersonic environment and provide a unique ground testing source of "clean" thermochemical and radiative data about the flows which are encountered during high speed atmospheric flight. The shock speed is typically set to represent the flight speed of the vehicles and the fill density and composition to that seen at a particular planetary body's altitude point. This experimental methodology allows for the non-equilibrium thermochemistry and radiative absorption/emission behind a shock to be studied as a function of distance/time. As shown schematically in Figure 1, shock tubes operate by building up pressure in the driver gas (4) behind a diaphragm until it bursts, sending a shock wave through the low pressure test gas at ambient temperature

(1). This shock impulsively elevates the temperature, pressure and velocity of the test gas behind it (2), producing conditions representative of those found on the stagnation line of a hypersonic vehicle. The shocked test gas is limited in length/time to the arrival of the expanded driver gas (3), separated by the contact surface.

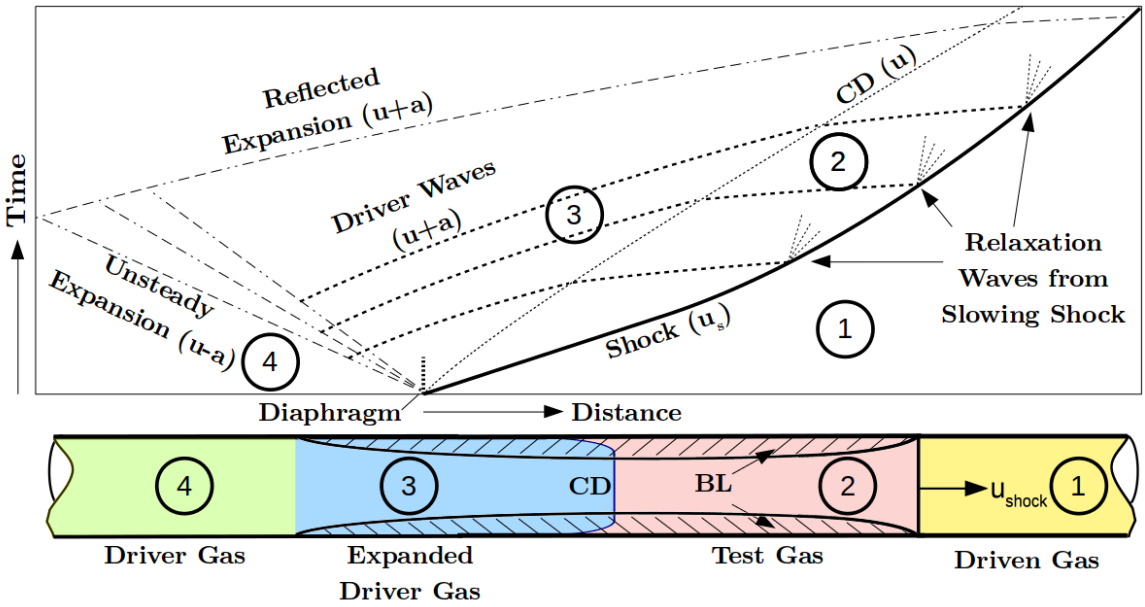

Fig. 1 Distance-time diagram of the primary waves produced by a shock tube (not to scale).

Although shock tubes are seen to have a relatively simple operation, complexity is inherent experimentally which alters the shocks speed down the tube. Several sources produce compression and expansion waves which can reach and alter the speed of the shock wave. Boundary layer growth along the entire length of the tube, including within the driver gas, produces waves which cause shock attenuation [C1]. The driver also causes further waves to reach the shock. This is due to having a finite length, change in volume if a free piston driver is used or transient heating processes if a deflagration, detonation or arc heating driver are used [C2]. Additionally, the diaphragm rupture is not an instantaneous process and can introduce a rapid acceleration of the shock and subsequent deceleration, substantially influencing shock tube performance [C3, 4]. Thermochemistry also plays a role in the variation of shock speed [C5, 6].

Shock speed variation down the tube has a direct effect on the measured test gas behind the shock, as the compressed slices of gas behind the shock will have been processed by different shock speeds [C7]. The properties (speed, pressure temperature, thermochemical state) of any slice of shocked test gas alters as it convects down the tube will be influenced by the shock speed profile. Additionally, there are other effects caused by boundary layer growth in the shocked test gas, namely “Mirels effects” [C8]. Behind a shock of constant speed, the mass lost to the boundary layer causes the gas behind the shock to accelerate in the lab frame of reference towards the shock speed, as seen in Figure 2. This means that as the shocked test gas slices convect downstream that they will cluster towards the contact surface. This effect was shown in Satchell *et al.* [C9] to be present also behind shocks undergoing acceleration or deceleration. It should also be

noted that gas within the boundary layer will influence any absorption or emission measurements as these are integrated across the diameter of the tube.

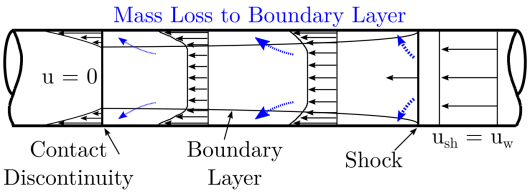

Fig. 2 Core flow acceleration due to mass loss to the boundary layer in the shock frame of reference, adapted from Mirels [C 1].

Most analysis of the non-equilibrium experimental data from shock tubes simply use the shock speed at the test section or measurement location and the fill conditions. A common analysis is to numerically model a one-dimensional steady state behind a shock of constant velocity using non-equilibrium thermochemistry models [C10, 11]. A similar method may be performed to characterize the stagnation-line flow on a large blunt body as an analogy to the post-shock flow, which is a method currently employed by the group at NASA Ames [C12]. Many researchers have performed full facility simulations of the shock tube to try to incorporate the more complex effects of driver and boundary layer growth, the simplest being one-dimensional models, such as L1d by Jacobs et al. [C13, 14] and Sharma et al. [C15], which have simplified models of the boundary layer growth that alter the shock speed and gas slice locations. Simulation complexity may be expanded up to fully two-dimensional simulations of the entire facility, incorporating numerical models of the transient driver and diaphragm opening, which account for the larger proportion of shock speed variation effects [C16, 17]. These have the benefit of also calculating the properties within the boundary layer and other multidimensional phenomena. Improved accuracy has been recently introduced by using formulations in the shock frame of reference and overset meshing [C4, 5] to ease mesh requirements. These struggle to match the shock speed profiles observed in the physical machine due to simplifications in the numerical models for the drivers and diaphragm ruptures. Additionally, none of the methods described above account for the large test to test variations seen in the shock speed profile and therefore cannot match the shock speed profile which is the largest proportion of uncertainty.

Mirels [C1] and Holbeche [C18] sought to develop analytical models of the test gas. Mirels assumed a steady shock speed and used boundary layer theory to develop a simple model to predict the change in gas properties with due to the loss of mass flow. Holbeche observed that the relaxation of pressure waves behind a shock of variable strength influences the temperature of the gasses in the test slug, and developed a more complex model which accommodated a variable shock speed, but the method was limited in numerous ways by the assumption of only small variations in shock speed. Holbeche noted that, due to the short test times, entropy-producing processes such as viscous loss or conduction are insignificant for any element of gas. Light [C19] later described the test slug behind a decelerating shock as a series of gas elements processed at different shock strengths which were gradually consumed by boundary

layer mass consumption. He then composed a method of obtaining variations in element density and speed based on continuity in a shock-steady frame of reference. However, Light's method assumed small perturbations both in shock speed and properties behind the shock, applying the method only to a small range of conditions, and Light himself acknowledged the limited extent of the application. Importantly, Light comments on how the gas behind a decelerating shock is undergoing constant expansion due to the diminishing shock strength, specifically highlighting the importance of accounting for this effect in future studies.

This paper, the first in a series of two, proposes a new methodology to reconstruct the resulting non-uniform test slug directly taking the experimentally measured shock passing times at several axial positions and the tube fill conditions. The methodology assumes the gas is either a perfect gas or at thermochemical equilibrium. Results from an implementation of this methodology are then verified by comparison to the perfect gas simulations of Satchell *et al.* [C9]. The second paper in the series [C20] shows the application of the methodology to experiments from the Oxford T6 Stalker shock tube facility [C21] in order to demonstrate the generality of the method.

III. Development of a Quasi One-Dimensional Model

Knowledge of the spatial variation of flow velocity, enthalpy and pressure behind the shock is crucial in understanding shock tube experiments. These can vary from test to test due to non-ideal effects. The following methodology characterises the core flow of the shocked test gas in an individual shock tube experiment, by calculating the entropy in each portion of the test gas and then determining its enthalpy. This calculation takes the shock speed trajectory and initial test gas fill conditions as inputs. and from that efficiently predicts the thermodynamic properties of the entire test slug. It accounts for the Mirels effects (*i.e.* boundary layer mass loss) within the calculation, though does not directly calculate the properties within the boundary layer. Overall, this gives a quasi one-dimensional representation of the experiment.

For a perfect gas, Satchell *et al.* [C9], showed the only influence on the entropy of an individual gas packet is the shock speed that processed it. This observation should hold for a gas in thermochemical equilibrium. Assuming that gas outside the boundary layer at a given axial distance from the shock may be treated as radially homogeneous, the observation of isentropic gas packets may be applied to the slices described above, and obtaining the enthalpy becomes a matter of performing an energy balance. This observation constitutes the basis of the following analysis.

The test slug of a shock tube experiment is comprised of initially stationary gas which is processed by the shock and then moves at a slower rate than the shock, causing the gases to propagate away from the shock, with the interstitial space continuously filled by gas processed by the shock further downstream. As a result, the test slug may be viewed as the sum of a number of infinitesimal slices of gas originating along the length of the shock tube which each undergo compression and acceleration by the shock, and are stacked consecutively to form the entire slug, as seen in Figure 3. The entropy of each slice is set by the shock speed that processed it, and its axial position is determined by the boundary layer mass loss.

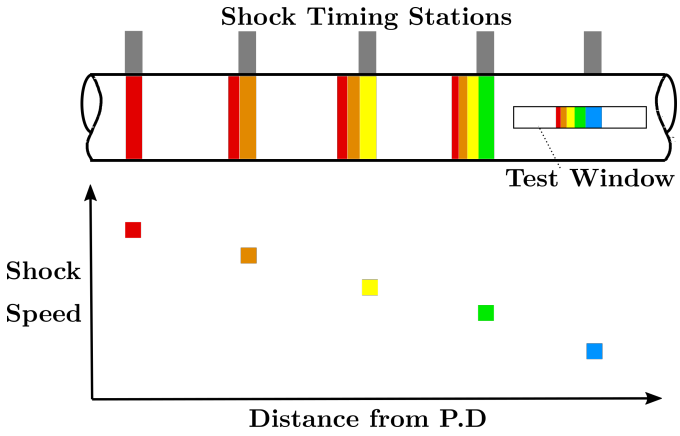

Fig. 3 Individual slices constituting a test slug, coloured by the variable entropy caused by a slowing shock as measured by shock timing stations.

The present methodology is built upon tracking the location and properties of discrete slices initially distributed along the tube length. A shock is marched along its trajectory, as recorded by experiment. When the shock reaches the location of each slice, that slice is processed to the post-shock entropy level and an initial total enthalpy. Slice speed is then determined at each point in the remaining shock trajectory by performing a mass balance against the boundary layer. Having determined the slice distance from the shock and its speed, the variation in total enthalpy is computed at each point in the trajectory due both to its variation in speed and also from work performed by isentropic waves. This process is repeated for all the discrete slices, and the final locations and properties of each slice then comprise the extents and properties of the test slug. The entire process is conceptually summarized in the flow diagram of Figure 4. In practice, switching the inner and outer loops is more computationally efficient.

In the following mathematical descriptions, properties referring to the original post-shock state of a slice will be denoted using the superscript t^0, and do not change with time. The original post-shock state is important, since the entropy is held constant from this point, and the total enthalpy at later steps is referenced as changes to this original state. At some later time, the slice is farther from the shock and at the same entropy level, but with a variable total enthalpy as waves from the accelerating shock affect it. The properties of a slice are influenced by the properties behind the shock, and so properties at the slice shall be referenced with subscript E, and post-shock properties shall be denoted by subscript $_{sh}$. However, waves require a finite time to travel between slice and shock. A time level t^+ refers to conditions at the point in the future when an upstream wave co-located with the slice at the current time level t will reach the shock to influence its trajectory. Time level t^- refers to conditions at the point in the past when the relaxation wave co-located with the slice at time level t was emitted by the shock. Each of these points in time, along with the waves which define them, are shown in Figure 5a, as well as the property locations referenced in each subscript in 5b.

The following formulation assumes a laminar boundary layer. However, under many circumstances the boundary layer within the test slug will transition to turbulence. The boundary layer in the present methodology may be computed

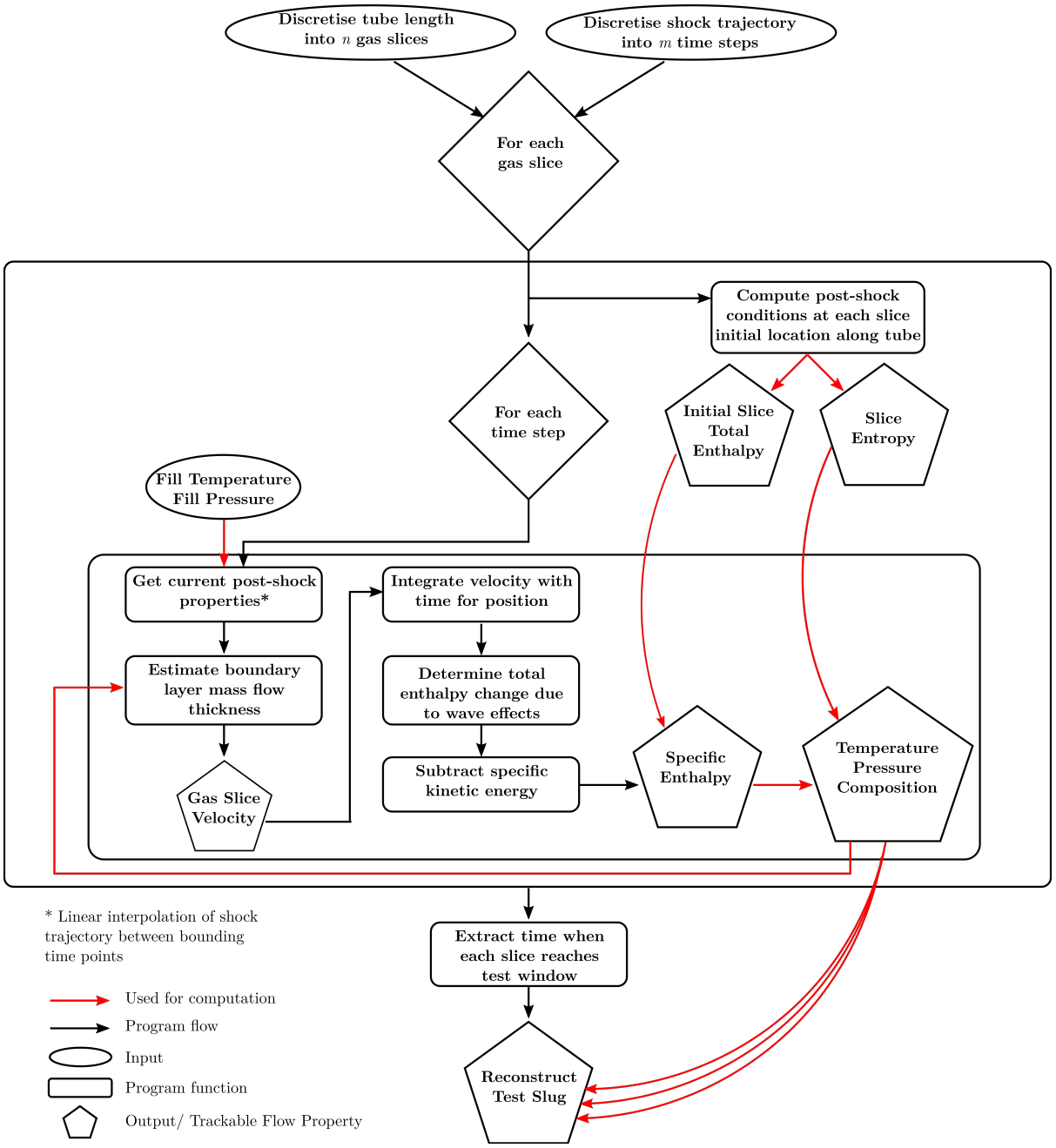

Fig. 4 Flow diagram for the LASTA program.

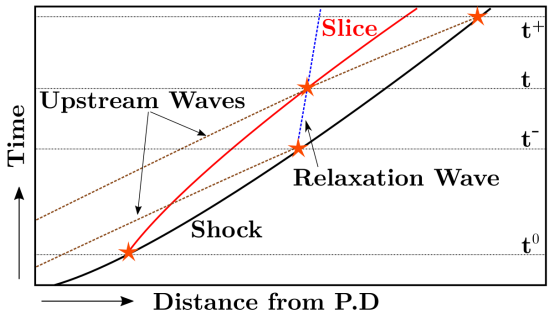

(a) Time levels. Stars denote wave intersections which define each time level.

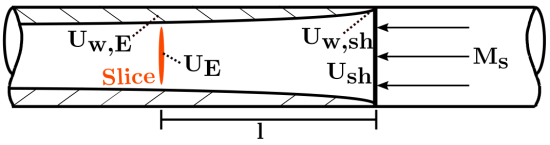

(b) Gas property locations, where U is any flow variable, in the shock frame of reference.

Fig. 5 Schematics annotating the time levels (superscripts) and spatial locations (subscripts) associated with each slice.

using the laminar relations described herein until the transition point, after which location the turbulent relations may be used instead as described in Appendix A.

A. Determination of Slice Speed and Location

After each slice is processed by the shock, it is accelerated impulsively to a post-shock velocity, as well as entropy and enthalpy, which may be obtained for the known shock Mach number. The motion of the gas produces a boundary layer along the wall, consuming mass from the inviscid core flow. This in turn causes the core flow to accelerate in the laboratory frame, or decelerate towards stagnation in the shock-stationary frame [C1]. Thus, the acceleration of the slice due to mass loss from the core may be found by using a mass balance. Knowing the slice velocity at each point in the trajectory, the slice location may also be integrated. The first step of the formulation is to determine the slice velocity and location. This process is now explained, as well as the means to find the resulting stream tube area, which influences the waves which affect the slice enthalpy.

At the slice location, the total mass flow must be the sum of the mass flow in the boundary layer $\dot{m}_{BL}$ and the mass flow in the inviscid core flow $\dot{m}_{core}$, which together must equal the mass flow processed by the shock, $\dot{m}_{sh}$:

$$\dot{m}_{sh} = \dot{m}_{BL} + \dot{m}_{core} \tag{1}$$

The boundary layer and core mass flows are given as:

$$\dot{m}_{core} = \rho_E u_E \pi (r_{tunnel} - \delta_m)^2 \tag{2}$$

$$\dot{m}_{BL} = \rho_{w,sh} u_w \pi \left\{ r_{tunnel}^2 - (r_{tunnel} - \delta_m)^2 \right\} \tag{3}$$

δ_m is the mass flow thickness as defined by Hooker [C22] and improved upon by Mirels [C1]. $u_w = u_s$ is the wall speed, which equals the speed of the reference frame (shock speed), and $\rho_w = P_E/(RT_w)$ is the density along the wall, which assumes a cold wall of temperature equal to the pre-shock gas temperature. Plugging in Equations 2 and 3 into 1, the slice velocity in the shock frame of reference u_E may be obtained as:

$$u_E = \frac{\dot{m}_{sh} - \dot{m}_{BL}}{\rho_E \pi (r_{tunnel} - \delta_m)^2} \tag{4}$$

From Hooker [C22], the mass flow thickness δ_m for a laminar boundary layer may be calculated by Equation 5 using conditions at the wall and packet distance l from the shock, where $u_{abs} = u_{shock} - u_E$:

$$\delta_m = \beta \left(\frac{\mu_w l}{\rho_{w,E} u_{abs}} \right)^{\frac{1}{2}} \tag{5}$$

Mirels' extensive analysis provided estimates of shape factor β behind a moving shockwave [C1], with the result seen in Equation 6.

$$\beta = C_M^{\alpha} 1.59 \left(1 + \frac{1.796 + 0.802W}{WZ - 1} \right) \tag{6}$$

where

$$C_M = \frac{\rho_{sh} \mu_{sh}}{\rho_{w,sh} \mu_w} \tag{7}$$

Here, $W = u_w/u_{sh}$ comprises a measurement of shock strength, where u_{sh} is the post-shock velocity in the current time steps shock's frame of reference, and $Z = \frac{\gamma+1}{\gamma-1}$. The coefficient C_M^{α} accounts for changes to the boundary layer shape due to variations in the freestream. The value of α used herein is 0.48. Note that in Mirels' analysis [C1], C_M is based upon the the ratio of freestream properties to those at the wall at time t^0. In order to couple the unsteady shock speed into the boundary layer shape, the current post-shock freestream values (A) were used to compute C_M, implying an instantaneous reshaping of the entire boundary layer with changes in shock speed. In the mass balance, post-shock mass flow m_{sh}^t at the current time step must be used, coupling the mass flow of each slice to the changing shock speed. This forces the slice to, for example, slow with the shock, but results in a loss of momentum conservation. This loss is accounted for later.

All parameters have now been defined to find the slice speed in Equation 4 for u_E. By integrating the speed of each slice with time, its location may be obtained as well as its distance from the shock.

B. Determination of Displacement Thickness

Prior to returning to discussion of the slice thermodynamic properties, the correlations of Mirels may be further utilised to find the stream tube area for Equation 19. Mirels [C23] gives a laminar boundary layer thickness as:

$$\delta = C_M^{\alpha} \left[\eta_\delta - I(\infty)\right] \frac{\rho_{w,sh}}{\rho_{e,sh}} \sqrt{\frac{2l\nu_w}{u_{e,sh}}} \tag{8}$$

Here, subscript $_e$ signifies the core flow value. In keeping with the present formulation of boundary layer shape to accommodate the changing shock speed, the values with subscript $_e$ are taken at the current time t post-shock location. The terms η_∞ and $I(\infty)$ are approximate parameters obtained by numerical integration of the boundary layer equations as performed by Mirels. Since the present study falls within the shock strength ranges established by Mirels in [C23], their accuracy was considered acceptable for the demonstrative purposes of this work. In these relations:

$$\eta_\delta = \frac{3.20}{\sqrt{1 + 0.543w}} \tag{9}$$

$$I(\infty) = \frac{1.134}{\sqrt{1 + 1.022w}} \frac{\frac{h_r}{he} - \frac{h_w}{he}}{\sigma^{0.47+0.029w}} - \frac{1.569}{1 + 0.993w} \frac{(w-1)^2 \frac{u_e^2}{2h_e}}{\sigma^{0.045(w-1)}} \tag{10}$$

Finally, the displacement thickness may be given as:

$$\delta^* = \delta - \delta_m \tag{11}$$

Here, σ is the Prandtl number, and h_r signifies the recovery enthalpy. Equation 11 shall be referenced later in Equation 20 in order to obtain stream tube areas. The coefficients in the Mirels boundary layer equations are obtained from interpolation fits for exact integrations of the compressible boundary layer equations as obtained by Mirels in [C24]. These coefficients do not change with different gas species, but do have a weak dependence on Prandtl number which Mirels reports should be negligible for most gases encoutered in shock tubes [C1].

C. Variation in Total Enthalpy

At each time in the trajectory, the present conditions of each processed slice are updated by performing an energy balance on it in a shock-stationary frame of reference. Since the slice remains isentropic, all thermodynamic changes originate in variations in total enthalpy and exchange between kinetic and internal energy:

$$\boxed{H_E^t = H_E^{t^0} + \Delta H = H_E^{t^0} + \Delta h_E^t + \int_{us_1}^{us_2} u_E \partial u_s} \tag{12}$$

Δ is used herein to denote a finite change between discrete states in the slice of gas. The total enthalpy of a given

slice is not constant as it travels because of the accelerating frame of reference and pressure waves emerging from a variety of sources, which are accounted for by $\int_{us_1}^{us_2} u_E \partial u_s$ and Δh_E^t, respectively. Both terms are thus computed as the change from time t^0 to time t, as opposed to between consecutive times t. In the inviscid and chemically inert core flow, the only source or sink of total enthalpy must arise from pressure waves, and act directly upon the static enthalpy of the slice. This indicates that the decelerating shock sends waves which reduce the static enthalpy of the gas behind it, while the accelerating shock is associated with waves which elevate the static enthalpy behind it. Expressing the static enthalpy as a function of pressure, then, the change in static enthalpy from t^0 to time t may be written as:

$$\Delta h_E = \frac{\partial h_E}{\partial p_E} \Delta p_E \tag{13}$$

$\frac{\partial h_E}{\partial p_E}$ may be estimated in the case of a chemically reacting gas by solution of a classic entropy/pressure equilibrium problem from, for example, repeated calls to the NASA CEA code [C25] in order to produce a local derivative. The computation of the change in pressure at the slice, Δp_E is discussed next.

D. Influences Upon the Slice Pressure p_E

The slice pressure p_E is subject to waves emitted by a number of influences, enumerated in order of diminishing magnitude:

1) Relaxation waves from changing post-shock conditions
2) Waves travelling from upstream which also cause shock acceleration
3) Waves from mass flow absorption by the boundary layer
4) Waves from mixing and reflections at the contact discontinuity

The local pressure was also shown by Mirels [C8] to rise as the core flow ‘stagnates’ in the shock frame of reference, accelerated in the stationary frame of reference by mass loss to the boundary layer and exchanging kinetic energy for internal energy, which effect is accounted for later. Since the shock Mach number versus time is provided as an input, the sum of waves which influence shock acceleration such as items 2) – 4) may be treated together as a single wave which will impact the shock and cause it to accelerate at some future time. This approximation is enabled by the domination of waves travelling from upstream in shock speed determination. For conciseness, the sum of the waves which combine to affect shock speed are hereafter referred to as ‘upstream’ waves.

Considering the above, the pressure of an isentropic slice of gas is subject to the influence of one family of waves which travel upstream, and another family of waves travelling downstream, as seen in Figure 6. In the shock frame of reference, all flow in the test slug is subsonic, and so waves are free to propagate both to the shock from any given slice, and also back from the shock to that slice. As a result, the effect of a series of waves upon an isentropic slice with

uniform radial properties may be treated by the principle of superposition. In other words, the contribution of each wave upon the pressure may be added to each other for a sum total influence of the waves upon the particle at any instant in time.

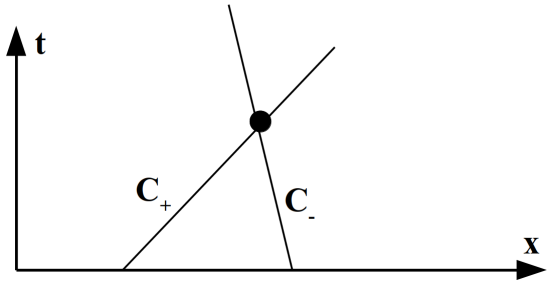

Fig. 6 Propagation of two families of pressure waves across an infinitesimal point in a subsonic flow.

In the test gas behind a moving shock, the Mach number is subsonic in the shock frame of reference throughout the flowfield, and so all slices encounter up- and down-stream oriented families of waves in a non-simple region. Put mathematically, this means that the pressure at a given point in a one-dimensional flow is subject to waves which travel with the left- and right-going characteristics C_- and C_+:

$$\Delta p = \Delta p_{C_+} + \Delta p_{C_-} \tag{14}$$

The left-going waves are the relaxation waves emitted by the shock itself, which travel on the characteristic C_-. The right-going upstream waves travel towards the shock on the characteristic C_+. The change in slice pressure due to relaxation and upstream waves may thus be given by:

$$\Delta P_E^t = \underbrace{\frac{\partial p_E^t}{\partial p_{sh}^t}\Delta p_{sh}}_{\text{Relaxation}} + \underbrace{\frac{\partial p_E^t}{\partial p_{sh}^t}\frac{\partial p_{sh}^{t^+}}{\partial M_s^{t^+}}\Delta M_s}_{\text{Upstream}} \tag{15}$$

In Equation 15, the first term is the influence of relaxation waves as produced by the changing shock Mach number M_s, and the second term is the strength of upstream wave which will reach the shock at some future time, but which is currently passing the location of the slice. Each of the derivatives in Equation 15 are now examined in the following sections,.

1. Amplification and Attenuation of Pressure Waves Due to Travel Through the Test Slug

It is helpful to visualize the core flow as a subsonic nozzle, wherein the walls of the nozzle are formed by the boundary layer and its entrance is at the shock. The relaxation and upstream waves are subject to variations in magnitude as they traverse the nozzle of varying local densities and sound speeds, as well as a changing cross-sectional area as the

boundary layer thickens along the slug. Both the shape of the nozzle, and the variation in properties are easily seen in Figure 2. A pressure wave produced at the post-shock location will be amplified or attenuated both by the gas between the shock and the isentropic slice, and also the nozzle shape as it moves rearward. A wave travelling from the slice towards the shock will likewise be attenuated or amplified in an opposite manner. The term $\frac{\partial p'_E}{\partial p'_{sh}}$ accounts for this change, and is derived from the characteristic formulation of the Euler equations next.

The quasi one-dimensional Euler Equations in characteristic form may be written as:

$$\frac{\delta}{\delta t}\begin{bmatrix} w_1 \\ w_2 \\ w_3 \end{bmatrix} + \begin{bmatrix} u & \cdot & \cdot \\ \cdot & (u+c) & \cdot \\ \cdot & \cdot & (u-c) \end{bmatrix} \frac{\delta}{\delta x}\begin{bmatrix} w_1 \\ w_2 \\ w_3 \end{bmatrix} = \begin{bmatrix} 0 \\ -uc \\ uc \end{bmatrix} \frac{1}{S}\frac{\delta S}{\delta x} \tag{16}$$

Here, S is the area of the stream tube, u is the local velocity and c is the local speed of sound. Along a characteristic, the following equation relates the pressure change δp to the characteristics as:

$$\delta w_2 - \delta w_3 = \frac{2}{\rho c}\delta p \tag{17}$$

The use of δ signifies that the change applies equally to gradients in time or in space. Assuming a quasi-steady state, Equation 16 may be plugged into Equation 17 in order to obtain:

$$\delta p = -\frac{\rho c}{2S}\frac{\delta S}{\delta x}\left(\frac{uc}{u+c} + \frac{uc}{u-c}\right) \tag{18}$$

Equation 18 describes the general variation of pressure associated with a variation in Riemann variables along a characteristic as influenced by the changing area of the streamtube. Pressure fluctuations at one end of the streamtube will be communicated to the other end of the tube under the same variation. As a result of this similarity, a given pressure wave of amplitude Δp_{sh} which originates with some density ρ_{sh}, speed of sound c_{sh} and stream tube area S_{sh} and travels into a gas with density ρ_E, speed of sound c_E and stream tube area S_E will emerge from its travel at strength δP_E. Assuming a linear area change $\frac{\delta S}{\delta x}$ =constant, the change in pressure at location B from a wave originating at location A then becomes:

$$\frac{\partial p_E}{\partial p_{sh}} = \frac{\delta P_E}{\delta P_{sh}} = \frac{S_{sh}}{S_E}\frac{a_E}{a_{sh}} \quad \text{where} \quad a_* = \rho_* c_* \left(\frac{u_* c_*}{u_* + c_*} + \frac{u_* c_*}{u_* - c_*}\right) \tag{19}$$

S_{sh} is the full tube area, and the area of the stream tube, S_E, is the area of the tube minus the area of the boundary layer displacement thickness:

$$S_E = \pi(r_{tunnel} - \delta^*)^2 \tag{20}$$

The method for obtaining displacement thickness is detailed later. With the amplification or attenuation of waves travelling up or downstream accounted for, the influence of the two families of waves are now examined.

2. Relaxation Waves - The Influence of the C_- Family

Returning to the first term of Equation 15, the C_- family of waves are the waves travelling upstream from the shock towards the slice, changing in magnitude as the streamtube narrows. Since Equation 15 relates the change in enthalpy of the slice from its original enthalpy at time t^0, Δp_{sh} becomes the change in pressure from the time when the slice was first processed by the shock:

$$\Delta psh = p_{sh}^{t^0} - p_{sh}^{t^-} \tag{21}$$

At any time level t, the slice is some finite distance from the shock, but its pressure contains a relaxation wave emitted by the shock at some earlier time t^-. In the frame of reference of the shock, this travelled from the shock towards the slice at speed $c + u$, where the local c and u change as the wave traverses the slug. However, assuming a quasi-steady state in which these conditions change only slowly across the time $t - t^-$, the time which the wave will take to reach the slice may be approximated by using the average values of $\bar{c}$ and $\bar{u}$ throughout the test slug, where u is taken in the shock-stationary frame of reference. Thus, the time in the past at which the shock produced the relaxation wave which currently influences the slice is obtained as:

$$t^- = t - \Delta t_{wave} = t - \frac{l}{\bar{c} + \bar{u}} \tag{22}$$

Here, l is the distance from the slice to the shock. Since the shock trajectory is known, at a given time of computation along the trajectory, the shock speed at the past time t^- is known, and so the value of the post-shock pressure at that time may simply be looked up. The resulting change in pressure Δp_{sh} is then modified by the amplification factor of Equation 19, leading to the form of Term 1 of Equation 15.

3. Upstream Waves - The Influence of the C_+ Family

Shifting focus to the second term of Equation 15, the strength of the wave $\Delta p_{sh}^{t^+}$ required to produce a change of shock Mach number $\Delta M_s^{t^+}$ at time t^+ from the current Mach at time t, $\frac{\partial p_{sh}^{t^+}}{\partial M_s^{t^+}} \Delta M_s$ is now examined. Although the change in shock speed between any two points in time is known, the actual size of the wave required to bring about that change has not yet been determined. This value may be obtained by examination of the eigenvalues of the matrix produced by the characteristic evaluation of Roe. Across a Riemann discontinuity, the speed of the right-going wave seen in Figure 7 is an eigenvalue of the Roe matrix [C26].

This speed is given by:

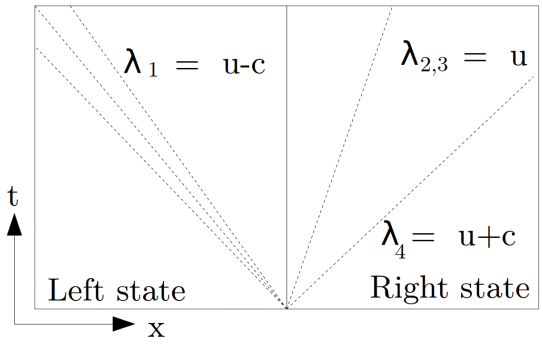

Fig. 7 Wave Speeds Across a Discontinuity

$$V_s = \lambda_4 = \tilde{u} + \tilde{c} \tag{23}$$

The Roe variables in one dimension are computed as:

$$\tilde{u} = \frac{u_L\sqrt{\rho_L} + u_R\sqrt{\rho_R}}{\sqrt{\rho_L} + \sqrt{\rho_R}} \tag{24}$$

$$\tilde{c} = \sqrt{(\gamma - 1)(\tilde{H} - \frac{1}{2}\tilde{u}^2)} \tag{25}$$

$$\tilde{H} = \frac{H_L\sqrt{\rho_L} + H_R\sqrt{\rho_R}}{\sqrt{\rho_L} + \sqrt{\rho_R}} \tag{26}$$

The change in shock speed with respect to a change in the left-state pressure may be obtained by taking the derivative of Equation 23 with respect to pressure.

$$\frac{\partial M_s^{t^+}}{\partial p_{sh}^{t^+}} = c_1^{-1}\left(\frac{\partial \tilde{u}}{\partial p_{sh}} + \frac{\partial \tilde{c}}{\partial p_{sh}}\right) \tag{27}$$

First examining the change in Roe velocity:

$$\frac{\partial \tilde{u}}{\partial p_L} = \frac{\partial \tilde{u}}{\partial \rho_L}\frac{\partial \rho_L}{\partial p_L} \tag{28}$$

$$\frac{\partial \tilde{u}}{\partial \rho} = \frac{\sqrt{\rho_R}(u_L - u_R)}{2(\sqrt{\rho_L} + \sqrt{\rho_R})^2\sqrt{\rho_L}} \tag{29}$$

In the case of a chemically reacting flow, a local derivative estimate of $\frac{\partial \rho_L}{\partial p_L}$ may again be found by multiple solutions of a constant entropy-pressure equilibrium problem.

Turning now to the Roe speed of sound:

$$\frac{\partial \tilde{c}}{\partial p_L} = \frac{\partial \tilde{c}}{\partial \tilde{H}} \frac{\partial \tilde{H}}{\partial p_L} + \frac{\partial \tilde{c}}{\partial \tilde{u}} \frac{\partial \tilde{u}}{\partial p_L} \tag{30}$$

$$\frac{\partial \tilde{c}}{\partial \tilde{H}} = \frac{\sqrt{\gamma - 1}}{2} \left(\tilde{H} - \frac{\tilde{u}^2}{2} \right)^{-\frac{1}{2}} \tag{31}$$

$$\frac{\partial \tilde{H}}{\partial p_L} = \frac{\partial \tilde{H}}{\partial H_L} \frac{\partial H_L}{\partial p_L} + \frac{\partial \tilde{H}}{\partial \rho_L} \frac{\partial \rho_L}{\partial p_L} \tag{32}$$

In the case of chemically reacting flows, the derivatives of H_L and ρ_L with p_L may again be approximated by use of a local derivative obtained from an equilibrium solver.

$$\frac{\partial \tilde{H}}{\partial H_L} = \frac{\sqrt{\rho_L}}{\sqrt{\rho_L} + \sqrt{\rho_R}} \tag{33}$$

$$\frac{\partial \tilde{H}}{\partial \rho_L} = \frac{\sqrt{\rho_R}(H_L - H_R)}{2(\sqrt{\rho_L} + \sqrt{\rho_R})^2 \sqrt{\rho_L}} \tag{34}$$

$$\frac{\partial \tilde{c}}{\partial \tilde{u}} = -\frac{(\gamma - 1)\tilde{u}}{2\sqrt{(\gamma - 1)(\tilde{H} - \frac{1}{2}\tilde{u}^2)}} \tag{35}$$

Plugging Equations 28-34 into Equation 27 with properties of the left state given as U^t_{sh} and properties of the right state as U_1, and inverting, the change in pressure required to bring about a given change in shock speed is found from:

$$\frac{\partial p^{t^+}_{sh}}{\partial M^{t^+}_s} = \frac{1}{\frac{\partial M^{t^+}_s}{\partial p^{t^+}_{sh}}} = c_1 \left(\frac{\partial \tilde{u}}{\partial p_{sh}} + \frac{\partial \tilde{c}}{\partial p_{sh}} \right)^{-1} \tag{36}$$

The change in Mach number ΔM_s is computed as the change in shock Mach number from the time t to t^+. As with the relaxation waves, the finite distance between shock and contact discontinuity causes a finite time of travel for the wave of interest. The wave presently influencing the slice at t will influence the shock at a future time t^+, and this time may be found from Equation 37.

$$t^+ = t + \Delta t_{wave} = t + \frac{l}{\bar{c} - \bar{u}} \tag{37}$$

Note that Equation 37 differs from Equation 22 by the sign of contribution of the local velocity, causing the upstream wave to traverse the test slug more slowly than the relaxation waves. Having found the time in the future t^+ at which the upstream wave will reach the shock, $\Delta M^{t^+}_s$ may then be determined. Near the end of the trajectory, the shock speed that

might be achieved at time t^+, absent disturbances at the end of the tube such as a dump tank, may not be known.

In circumstances where the shock trajectory beyond the test section are unknown, as is often the case in experimental setups, the shock trajectory may simply be extrapolated under an implicit assumption that no strong upstream waves such as a reflected expansion will influence the shock shortly past the known trajectory data. The presence of any strong waves in the test slug near the end of the tube would substantially influence the properties of the test slug, and so such a situation is typically avoided in experimental setups e.g. by piston tailoring in a free-piston shock tube facility. In the characterisation of flow properties in a completed experiment, readings from a pressure transducer located just prior to the test section may be used to minimize this limitation by modifying the extrapolated trajectory to match the measured static pressure. The potential errors introduced by this practice are discussed in-depth in the second paper.

Returning to Equation 15, the original strength of the upstream waves thus determined is now seen to be modified by the inverse of the characteristic modification term $\frac{\partial p_E}{\partial p_{sh}}$, since the upstream waves must travel down the nozzle in the opposite direction from the relaxation waves travelling up it:

$$\frac{\partial p_E}{\partial p_{sh}^{t^+}} = \frac{1}{\partial p_E / \partial p_{sh}} \tag{38}$$

Finally, the change in total enthalpy due to the moving frame of reference is given as:

$$\int_{us_1}^{us_2} u_E \partial u_s = u_E \left(u_s^t - u_s^{t^0} \right) \tag{39}$$

All terms in Equation 13 have been defined and the change in enthalpy of an isentropic slice resulting from variations in shock speed may now be computed.

With all parameters for Equation 12 now determined, the total enthalpy of the slice at the present time step t can be computed by use of Equation 12. Obtaining $h_E^t = H_E^t - \frac{1}{2}u_E^2$, the static enthalpy and entropy for the slice is known, and so the other thermodynamic properties may be computed. In the case of an equilibrium chemically reacting flow, the properties may be obtained from solving a constant enthalpy-entropy equilibrium problem.

The above analysis reflects the development of only a single slice of gas. However, repeating this process for a number of slices processed at different points along the tube, the properties and locations of each slice are known at the end of the tube. For example, a plot of temperature versus location for all the slices should be an accurate representation of the temperature throughout the test slug as might be measured by a stationary sensor in the test section. Simultaneously, the pressure and other properties of the entire test slug, along with the development history of each portion represented by a slice is also known.

E. Limiting the Variation of Pressure

In the above development, the conservation of mass and energy are coupled and solved for each individual slice by combining several simplified models for various aspects of the flow. However, the conservation of momentum is never ensured. Each slice is tracked individually and unable to communicate its momentum in exchange for pressure with the other slices in the test slug, despite its being a subsonic flow in the moving frame of reference. As a result, the absence of the momentum equation leads to an inability to capture the effect of momentum exchanged for pressure behind the shock as its post-shock velocity shifts. At a constant shock speed in an inviscid flow, the post-shock momentum will be constant. However, if the shock suddenly decelerates, it will produce a lower post-shock momentum, and the faster-moving, heavier gas from earlier in the trajectory will collide with the new slower, less compressed gas, producing a compression wave. In addition to its travel towards the shock as an extra source of upstream wave, this wave should travel to the rear of the test slug. As it does so, the wave should influence the pressures throughout. Furthermore, the rearmost slices will have been exposed to the most such waves throughout the trajectory and traded the most momentum, and so this effect is most pronounced at the rear of the test slug. It is important also to note that the effect of momentum exchange is isentropic in nature. Without inclusion of this effect, the detailed methodology under conditions of strong shock deceleration will show a non-physical drop in pressure towards the rear of the test slug.

Rather than obtaining an approximation or a more expensive full solution of the complex interchange of pressure and momentum throughout the test slug, the effects of the lack of momentum conservation may be accounted for indirectly. It may be observed in Satchell *et al.* [C9] that the static pressure traces behind both accelerating and decelerating shocks increase monotonically until the contact discontinuity, even for strongly decelerating shocks. Thus, by imposing upon the slices in the present methodology a constraint wherein the pressure must not decrease moving upstream from the shock, the influence of momentum exchange may be accommodated by enforcing its ultimate effect. At the end of each time step, if the pressure of a slice is found to drop below that of a slice immediately downstream of it, the upstream slice pressure is isentropically elevated to match that of the downstream slice, and its other thermodynamic variables accordingly recomputed. The result is a static pressure through the test slug which is, under all conditions, monotonically increasing or constant while maintaining the condition of isentropy for all slices.

IV. Implementation of Quasi One Dimensional Model

Development of the methodology described above, entitled for reference herein as the LAagrange Shock Tube Analysis (LASTA) methodology, centered around the tracking of an individual slice processed by the shock at some arbitrary time along the shock trajectory. However, by repeating the methodology across numerous individual slices distributed along the tube, the entire test slug may be reconstructed. The LASTA methodology was implemented in the Python programming language. The tube inputs to LASTA are the fill gas pressure, temperature and composition, the geometry of the shock tube (tube length and diameter), history extraction locations and the initial location of the

Lagrangian slices and time steps.

V. Validation

LASTA was validated against a series of numerical simulations by Satchell *et al.* [C9] as all data is known at fine time and spatial resolution. As these are perfect gas simulations, they allow direct validation of the wave processes without the complications of thermochemistry. Further application of LASTA for true experimental data, different geometries and equilibrium thermochemistry models is provided in the associated paper [C20].

A. Test case Setup

Three shock tube simulations of varying shock speed profiles are used as test cases produced using the FROSST code. These results are detailed in Satchell *et al.* [C9]. This assumed a perfect gas and a laminar boundary layer. The resulting shock trajectories may be seen in Figure 8, and may be seen to consist of a strongly decelerating case, a strongly accelerating case, and also a nearly flat shock trajectory. All three cases result in a shock speed of 2100 m/s at the end of the tube. Argon was used for the test gas, with a fill pressure of 66.7 Pa and fill temperature of 300 K. The tube geometry was 100 mm in diameter and a length of 8 m.

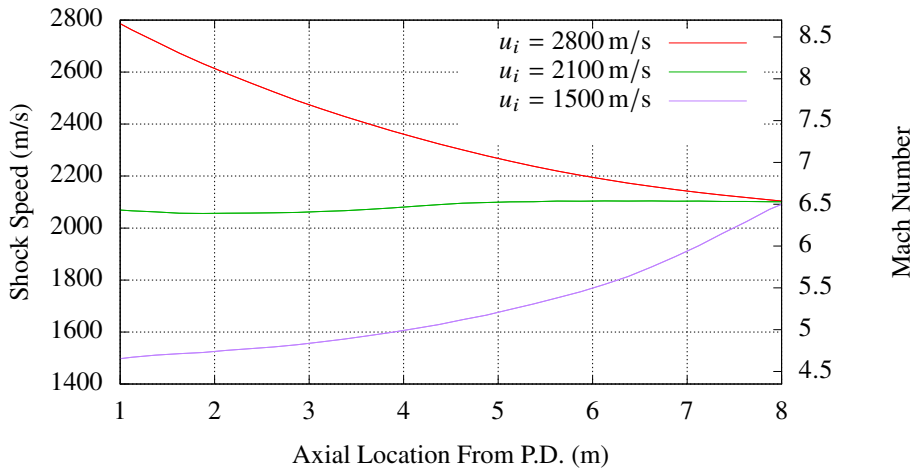

Fig. 8 Three shock trajectories arriving at the same shock Mach number at the end of the tube.

LASTA was run using 75 slices distributed evenly along the tube, and each was tracked with a time step of 3 μs for all shock trajectories. The last time step was computed when all slices on a given trajectory had reached an axial distance of 8 m from the start of the tube, and the slice conditions and timestamp when each slice crossed that location were recorded. This creates a property trace directly comparable against the centreline data measurements of FROSST [C9]. Each trajectory required an average of 3.76 s in order to run all 2000 time steps on a single Intel®Xeon(R) W-2155 CPU @ 3.30 GHz core with 31 GiB memory.

B. Overall Results

The resulting comparisons of pressure and temperature against the results of Satchell *et al.* [C9] are shown in Figure 9. The LASTA method is seen to reproduce all test slug temperatures to within 1% for the entire length of the test slugs in the multidimensional Navier-Stokes simulations. Pressure is also within 1% for pressures throughout all test slugs, except the very rear of the accelerating case. Here, a jet of driver gas is seen to arrive at 220 μs, at which point the LASTA pressure prediction agrees to within 3.5%. The source of this small discrepancy is believed to arise in the reflection from the contact discontinuity of compression waves produced by the accelerating shock within the FROSST simulation. Although the effect of such reflected waves upon shock trajectory would be captured in part by the upstream waves contribution in LASTA, their lingering and direct influence upon the slices themselves is not captured by the methodology. Since strong and monotonic acceleration is not common in actual shock tube experiments, this circumstance is considered to be an extreme.

Test time is overpredicted by the methodology in LASTA for the accelerating and decelerating cases. The overprediction of test time has two sources. The first is due to the inability of the one-dimensional code to predict a jet which emerges along the wall in the highly accelerating case to contaminate the rear 35% of multidimensional test slug. This jet is due to the elevating pressure in the test slug, which causes the contact discontinuity to lose containment of the driver gas through the boundary layer. The jet is observable in the two-dimensional Navier Stokes simulation results by the gradual decline in temperature in that case as opposed to the comparatively sharp declines seen in the other cases. Examination of the temperature profiles reveals that the LASTA method agrees strongly with the rearmost location of each contact discontinuity. This observation provides further evidence that the method accurately predicts the primary flow behaviours, but is hampered by the contamination. In agreement with the analysis of Hooker [C22], the presence of strong mixing at the contact discontinuity adds considerable uncertainties to any evaluation of the rear portions of the test slug in either the multidimensional simulation or even experiments, and so the overprediction at rear of the test slug is considered acceptable. The second source of disagreement in test time is the consumption of test gas by the boundary layer. Although LASTA is able to turn off slices whose boundary layer mass flow exceeds the core mass flow, additional test gas also slides down the contact discontinuity and out of the test slug [C9]. As a result, the oldest slice shown in Figure 9 originates near 1 m, whereas the gas at the rear of the test slug in FROSST originated around 3.5 m.

C. Sub Model Interrogation

Although the quasi one-dimensional methodology detailed in this paper has been shown to reproduce the core flow properties to reasonable accuracy, the individual components of the model each have their own assumptions and limitations. It is therefore necessary to investigate the accuracy of each of these models in the context of the unique challenges presented by each shock trajectory. The following discussion is presented for the purposes of illustration and analysis of the limiting assumptions in the methodology, with a focus on the foundational processes of individual packet

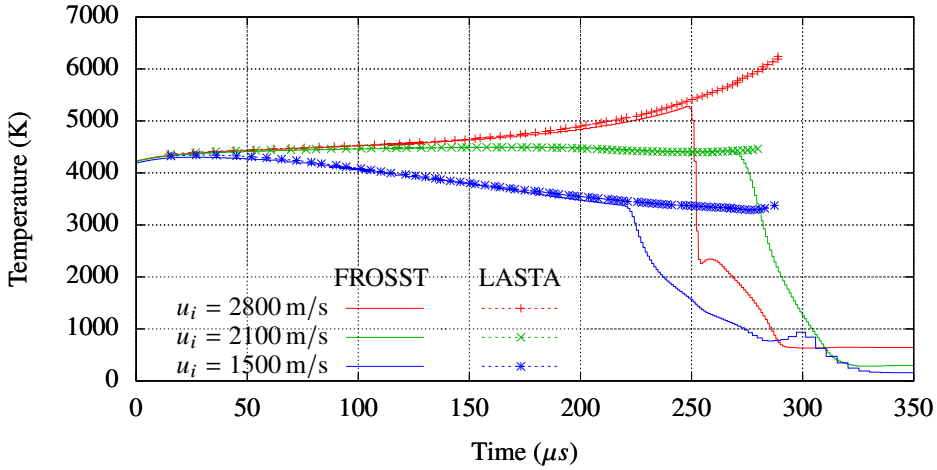

(a) Temperature Profiles for All Cases

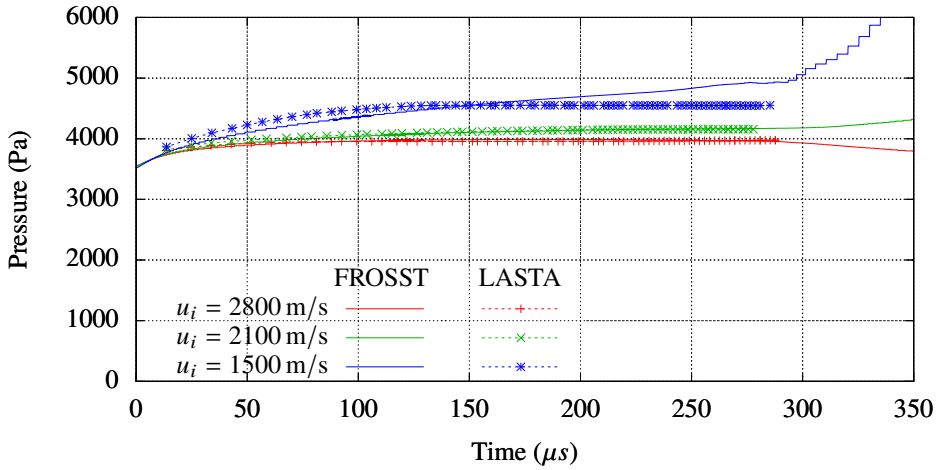

(b) Pressure Profiles for All Cases

Fig. 9 Test slug reconstructions for five shock trajectories, FROSST vs the LASTA method.

evolution. In particular, the boundary layer and mass loss model, and also the upstream and relaxation wave models are examined. Additionally, the use of a practical constraint of the pressure is examined.

A gas slice originating at $x = 4$ m from the diaphragm was interrogated for each of the cases. This originating location was selected because the final slice location should sit near the rear of the test slug under the present conditions, but remain well ahead of any jets or vortices which form around the contact discontinuity [C9]. The relatively long lifetime of these packets ensures maximal exposure to the relaxation effects described above, making them ideal for assessment of the methodology. The axial location and properties of this slice were then compared against a corresponding massless Lagrangian particle tracked in the FROSST simulations, originating along the centreline at the same axial location. The details of this implementation are given in [C9]

1. Modelling of the Boundary Layer and Mass Balance

Firstly, the nearly constant speed shock trajectory at 2100 m/s is examined. The axial velocity of the slice is a direct result of the mass balance from the mass flow thickness as predicted by Mirels. The axial velocity also determines the test slug length by establishing the location of each slice. Thus the accurate capture of velocity and location indicate an accurate representation of boundary layer properties. Coupled to the slice pressure by virtue of the wall density in Equation 5, accuracy of the axial velocity is also both highly sensitive to and broadly determines the accuracy of the total enthalpy balance. The comparison between the gas packets of FROSST and the slices of the LASTA methodology are seen in Figure 10 for the constant-speed shock.

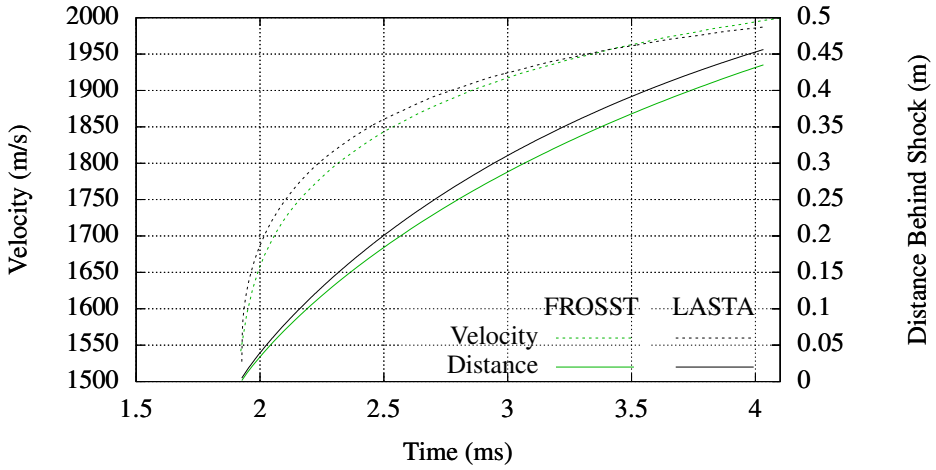

Fig. 10 Variation in velocity and position with time for a slice of gas originating at 4 m as processed by FROSST and LASTA for the constant-velocity shock case.

Slice axial velocity may be seen to match the FROSST gas packet velocity to within 1.1% at all times, integrating to a 1.1% difference in final position by the end of the tube, although this interestingly amounts to a 4% difference in distance behind the shock. This strong agreement indicates that the mass flow thickness, and resulting mass balance is accurately predicted by Mirels' estimates. The close matching is also a weaker but significant indication of static pressure agreement, since the boundary layer thickness is sensitive to the wall and core flow densities in Equations 2-4, which are in turn set by pressure in the isentropic slug. By matching the velocity and thereby location of each slice, the level of entropy at the final location of the slice within the test slug is also guaranteed to match. Consequentially, determination of the other properties at that location rests solely upon accurate capture of enthalpy variations due to wave effects.

2. Modelling of Upstream and Relaxation Waves

The accuracy of the speed and integrated position calculations demonstrates the accuracy of the boundary layer and mass balance formulations. The ability to capture the relaxation and upstream waves is now investigated. The total

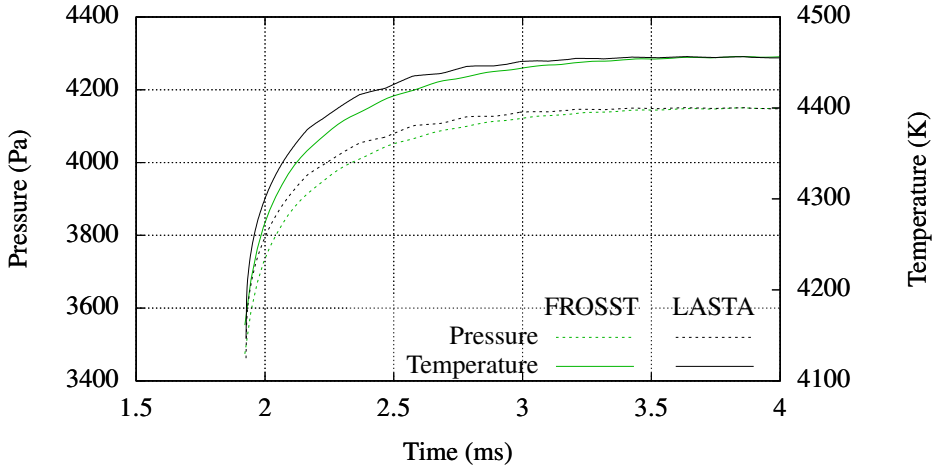

(a) Constant-velocity shock case.

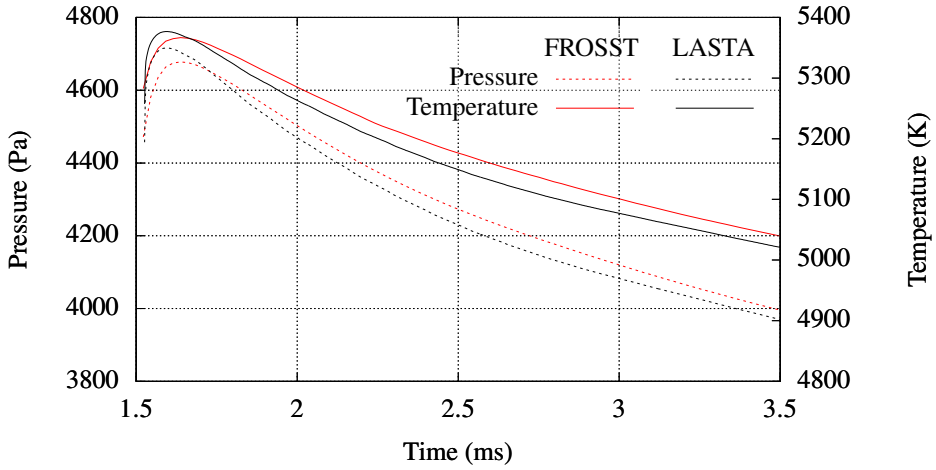

(b) Decelerating shock case.

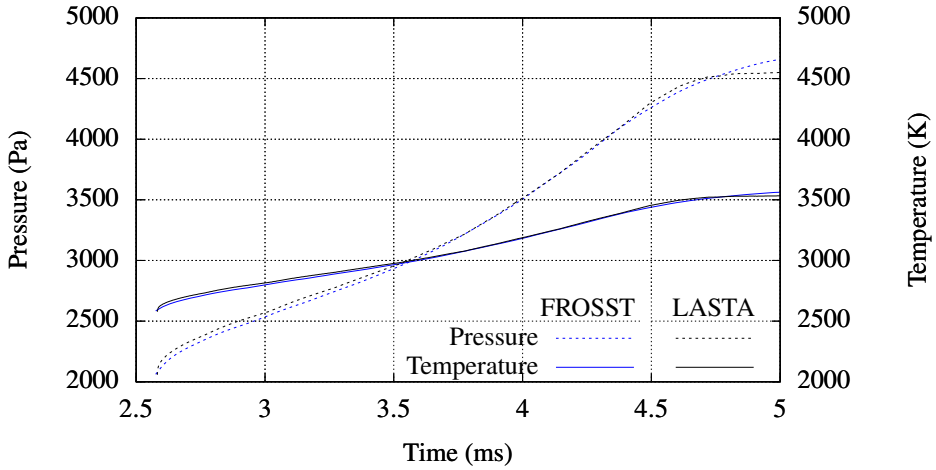

(c) Accelerating shock case.

Fig. 11 Variation in pressure and temperature with time for a slice of gas originating at 4 m as processed by FROSST and LASTA for the each of the three cases.

enthalpy balance for these ideal gas cases explicitly determines the temperature at each time step. In the constant shock speed case, the total enthalpy is spatially uniform across the shocked test gas, and so property variations arose only from shifts in velocity. However, in the presence of a variable shock speed, the relaxation waves combine with the upstream waves in Equation 15 to modify the static enthalpy of the slice. Thus, accurate capture of the unsteady temperature and pressure history of the slice reflects accurate modeling of the influence of these waves upon the total enthalpy of the slice.

Figure 11 compares the variation in slice pressure and temperature for each of the cases. In the constant speed case which is absent wave effects, 1.3% agreement is obtained for both pressure and temperature at all points in time, as seen in Figure 11a, with nearly identical matching by the end of the trajectory. The slight waviness in both data sets is due to small variations in shock speed near the end of the trajectory from the shock speed estimates of FROSST. Examining next the decelerating case, temperature in Figure 11b is seen to match to within 0.5% throughout the trajectory. The agreement in pressure for the decelerating case was also within 1%. Examining the accelerating case, Figure 11c shows that temperature is seen to match to within 0.5%, while agreement to 1.3% is seen in pressure throughout its trajectory, diverging from well within 1% only at the very end of the test. This divergence is considered due to the FROSST slice falling under the influence of contaminating driver gas.

This close agreement across all three case types suggests that the wave contributions to static enthalpy are accurately captured, within the restrictions of their limiting approximations. Although the wave calculations account for the time of travel of each wave contribution, the approximation of frozen properties through the test slug throughout the wave's travel would introduce a further degree of time lag error. Finally, both types of waves are subject to a small degree of amplitude error because of the same assumption of frozen test slug properties. As the speed of the shock increases, the length of the test slug shortens and so the time available for such errors to compound is reduced, and so this method is anticipated to remain accurate at higher shock Mach numbers.

3. Influence of the Pressure Constraint

The influence of the constraint which prevents the pressure from dropping along the test slug may be evaluated in the context of the decelerating case, for which the effects are most pronounced. Figure 12 shows that the slice pressure is elevated steadily by the influence of downstream slices as compared to the unconstrained case. As the shock slows, the post-shock pressure reduces, allowing the slice to lower in pressure as the expansion waves reach it. However, the presence of the pressure constraint reduces the degree to which the pressure would drop absent an accounting of momentum exchange.

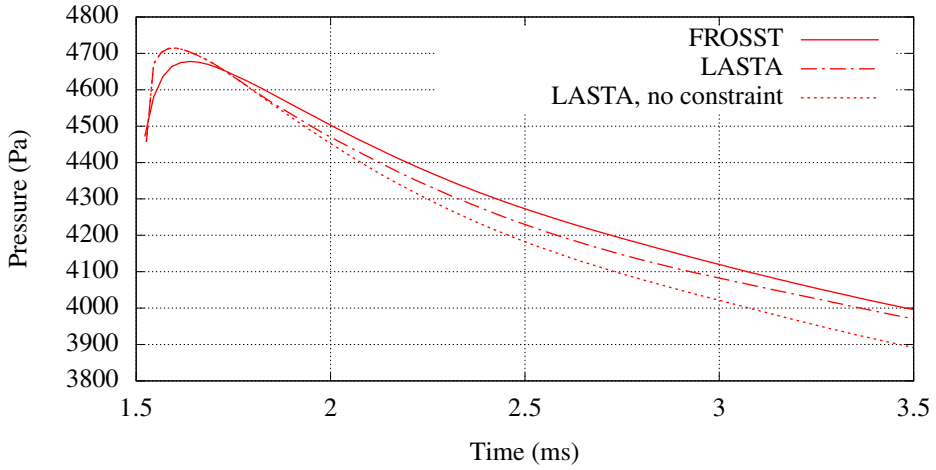

Fig. 12 Comparison of slice pressure history for the LASTA methodology with and without the pressure constraint, plotted against centreline gas packet of FROSST. All packets originated at $x = 4$ m in the decelerating shock case.

VI. Model performance in the presence of strong upstream waves

The cases thus far examined have deliberately limited the potential influence of upstream waves in order to focus on the effects of shock history alone. However, the LASTA method must be validated to show its proper function in the context of more complex upstream waves representative of real experiments. Similar simulations as described previously were performed in FROSST using the same facility geometry and fill conditions as the above discussion, varying driver section length and finite diaphragm opening times to produce different shock profiles. LASTA was then run against these shock profiles and the results compared, as shown in Figure 13. The specific driver conditions which produced these conditions have been deliberately omitted. Only the shock trajectory, fill conditions and tube geometry are required as inputs to LASTA, and indeed are the primary inputs available from experimental data. Finally, physical hypersonic shock tubes range in diameter from 50 cm or less through as wide as 300 mm, causing boundary layer effects to play more or less dominating roles on the dynamics of the test slug. The accuracy of LASTA in the context of a wider tube is shown in Appendix B.

Comparing Cases A and B, and consistent with the findings of [C9], it is evident that only a small amount of the gas from the period influenced by the slower initial shock speed remains present in the test slug. However, its presence causes a deviation in temperature for the rear 20% of the test slug. The agreement of these two cases almost identically with FROSST, offset by the small difference in end-tube shock speed, indicates that only the test gas which survives contributes meaningfully to the state of the test gas. Put differently, a LASTA simulation starting after 3 m, which is the originating location of the oldest surviving test gas, would contain all necessary information to match the full numerical simulation. This convenience was tested and confirmed to be true. LASTA agrees to within 1% for both pressure and temperature for these relatively simple cases.

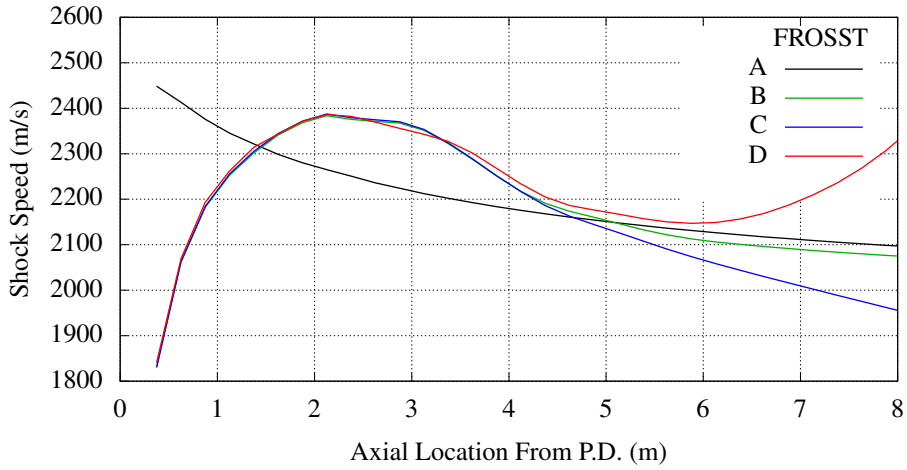

(a) Shock speed profiles for cases involving complex upstream waves.

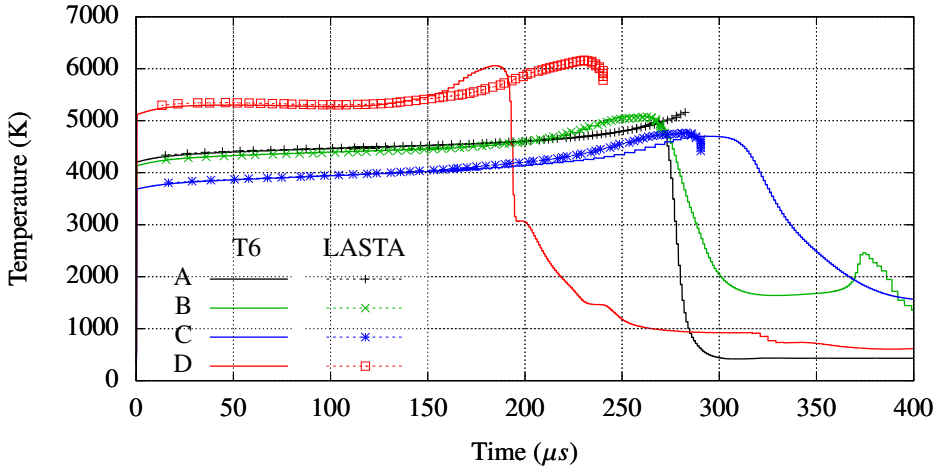

(b) Test gas temperature profiles.

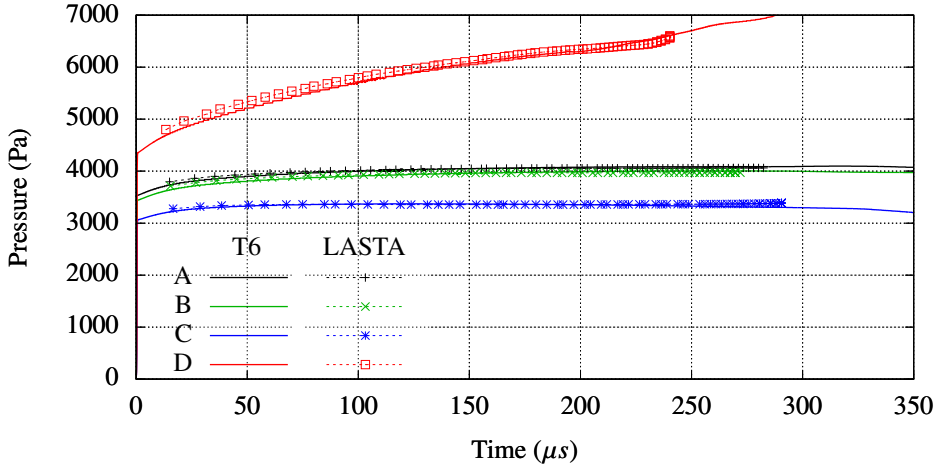

(c) Test gas pressure profiles.

Fig. 13 Shock trajectories and resulting test gas traces in the presence of complex upstream waves.

Case C likewise shows excellent agreement between FROSST and LASTA to within 1% for the entire test slug, with a 7% shorter test time predicted by LASTA. The longer test time predicted by FROSST is due to a strong reflected expansion wave pulling on the contact discontinuity, smearing it significantly and extending the test time. This effect may be observed by comparing the FROSST temperature profiles of Cases B and C, where Case C shows a more stretched contact discontinuity. LASTA does not possess a model to capture this, and so cannot match the test time perfectly, but the difference is considered to be acceptable.

Examining Case D, the influence of the acceleration is evident in the highly different trend in pressure and, more subtly, the bulk of the temperature trace which decreases, rather than increasing monotonically compared to the other cases. The overall trends and peak temperature are seen to agree to within 1.7%, and pressure to within 1%. However, the FROSST simulation is seen to predict a significantly shorter test time. Referring to the earlier description of the contaminating jets, the presence of the jet and its resulting vortex is clear in the FROSST results, as seen in Figure 14. The jet has the effect of pushing the test gas forward and also contaminating it, resulting in the shorter test time. As with the high acceleration case of Figure 11, however, the LASTA prediction can be seen to correctly locate the rear of the jet. This agreement gives further confidence in the proper function of the LASTA mass balance computations, although it cannot match the complex multidimensional influence of the jet along the wall. It may also be noted that, although variations in test slug temperature is similar to other cases, a large variation in pressure through the test slug is evident when compared to the other cases. This variation would have a pronounced effect on any thermochemical processes and radiative emissions. As such, the ability to match the pressure under this strong variation is highly important.

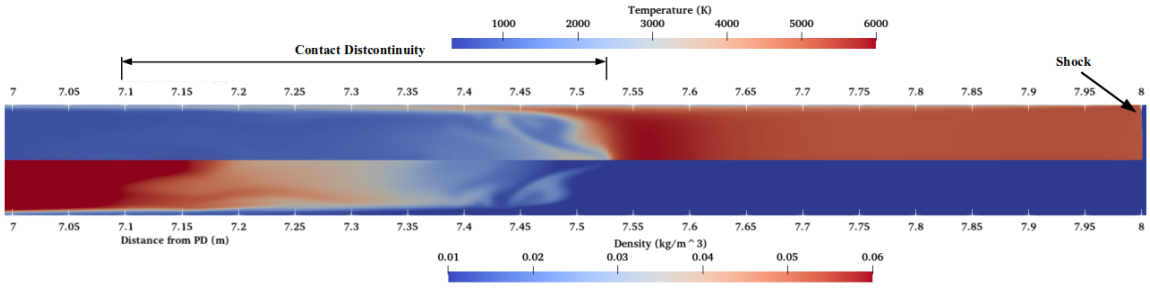

Fig. 14 Extended interface vortex caused by end-tube shock acceleration in Case D. Shock located at 8 m.

A final interesting facet of the above cases is the notable clustering of slices towards the rear of the test slug. This bunching is caused by the non-uniform acceleration of the various slices, with the rearmost slices accelerating the most due to boundary layer mass consumption. Although strictly qualitative in nature, the agreement in this behaviour with the descriptions of Hooker [C22] and Mirels [C8] lends confidence that the interaction between boundary layer and core flow is modelled correctly.

VII. Conclusions

An analytical framework to model shock tube experiments has been developed and presented. This accounts for the non-ideal effects from the driver/diaphragm rupturing and boundary layer growth on the resulting shock speed and thus flow properties and position of the shocked test gas at end of the tube. The method assumes the gas is in thermochemical equilibrium. This methodology takes as input the shock speed history along the tube, along with tube fill conditions, thus enabling the modelling of every experimental test individually. This methodology functions by examining the right- and left-going waves which interact with each isentropic slice of shock-processed test gas. These individual slices then combine to form the entire test slug. The functionality of individual portions of the method, particularly the evolution of individual shock-processed gas slices, was validated against Lagrangian gas packets tracked in the axisymmetric Navier-Stokes FROSST solver for the same cases. Individual slices were shown to agree to within 3% on temperature and pressure throughout the slice trajectory. Combining 75 such individual slices, the final temperature and pressure profiles in test slugs for three shock trajectories ending in the same end-tube Mach number were reproduced to within 1% for all cases but one, which agreed to within 1% until the rear of the test slug, which then stayed within 3% agreement. Cases involving complex non-deal facility waves were also simulated by both FROSST and LASTA, and also showed excellent agreement. Further validation and application of the tool is presented in a second paper.

Appendix A: Boundary Layer Equations for a Turbulent Flow

The LASTA methodology as described above assumes a laminar boundary layer. However, the boundary layer will transition to turbulence under many circumstances. In such cases, the mass flow consumed by the boundary layer will increase significantly, while simultaneously increasing core flow restriction. This reduction in inviscid flow area is accompanied by an elevation of the wave amplification factor $\frac{\partial p_E}{\partial p_{sh}}$, as well as a greater degree of clustering of the slices, thereby influencing the enthalpy recovery as well. As a result, both the test time and core flow thermodynamic properties may be anticipated to shift substantially from laminar predictions in the presence of a turbulent boundary layer. The following equations may be used in the LASTA methodology if a turbulent boundary layer is suspected. Either the entire test slug may be assumed turbulent, or some transition model such as the integrated Reynolds number proposed by Weilmunster [C27] may be used in order to cause the boundary layer predictions to switch between the laminar and turbulent equation sets.

Mirels published predictions for the test time of a shock tube with a turbulent boundary layer in the test slug based upon an analysis of boundary layer mass flow consumption [C28]. The same basic form of Equation 5 applies as with the laminar case, but the formulation of β changes substantially. It is instead given for turbulent flow as:

$$\beta = \beta_0 \left[\frac{W^2 + 1.25W - 0.8}{W(W - 1.0)} \right]^{0.8} \tag{A1}$$

Here, β_0 is the shape factor which would be predicted for uniform post-shock properties, and is given as:

$$\beta_0 = \frac{p_\infty}{p_0}\frac{W}{W-1}K_0 \tag{A2}$$

The factor K_0 is essentially a Karman-type shape factor which varies with shock strength and wall temperature:

$$K_0 = 0.0575\frac{\delta^*/\delta}{1-W}\frac{1-W^{0.8}}{\theta/\delta}(W-1)^{1.8}\left[\frac{\mu_m}{\mu_w}\frac{\rho_w}{\rho_{sh}}\left(\frac{\rho_m}{\rho_{sh}}\right)^3\right]^{0.2} \tag{A3}$$

The peculiar form of Equation A3 is driven by the need to find the terms $\frac{\delta^*/\delta}{1-W}$ and $\frac{1-W}{\theta/\delta}^{0.8}$ independently by numerical integration:

$$\frac{\delta^*/\delta}{1-W} = \frac{1}{W-1}\left\{7\frac{h_{sh}}{h_w}\int_0^1 \frac{\zeta^6[W-(W-1)z]}{D}d\zeta - 1\right\} \tag{A4}$$

$$\frac{\theta/\delta}{1-W} = 7\frac{h_{sh}}{h_w}\int_0^1 \frac{\zeta^6[W-(2W-1)z+(W-1)\zeta^2]}{D}d\zeta \tag{A5}$$

and

$$D = 1 + \left(\frac{h_r}{h_w} - 1\right)\zeta + \left(\frac{h_r}{h_w} - \frac{h_{sh}}{h_w}\right)\zeta^2 \tag{A6}$$

Equations A4-A5 must be integrated numerically using the shock speed at each time step. The recovery enthalpy h_r is taken as the post-shock recovery enthalpy in the absolute frame of reference. h_m is a reference enthalpy akin to the Eckert reference temperature [C29], which is designed to adjust the shape factor K_0 to account for the variation of temperature in the boundary layer due to a cold wall beneath a hot flow. It is given as:

$$h_m = 0.5h_{sh}\left(\frac{h_w}{h_{sh}} + 1\right) + 0.22h_{sh}\left(\frac{h_r}{h_{sh}} - 1\right) \tag{A7}$$

The associated density ρ_m at the reference enthalpy h_m is found by solving a pressure-enthalpy equilibrium problem for a gas in chemical equilibrium.

It must be noted also that the mass flow thickness is treated as the same as the displacement thickness in the formulation presented by Mirels for turbulent flow, although the two are held distinct in the laminar case. The Eckert coefficients were derived for air, but vary in sufficiently small magnitudes with changes in gas properties that they are typically accepted as accurate for other gases, as well [C30]. The coefficients in A1 are based on correlations from the integrated boundary layer equations, and Mirels notes that they are accurate for both air and argon to within 2% for w > 2 [C28].

Appendix B: Application of LASTA to a 200 mm Diameter Tube

Tube diameter was doubled to 0.2 m from the cases of Figure 13 in order to show the scalability of Mirels' estimates, as well as the resulting mass balance in LASTA. In the wider tube, the boundary layer comprises a much smaller percentage of the total flow area, and so viscous effects are greatly reduced. Figure B1 shows the much longer test time resulting from the wider tube, as well as the faster shock speed due to fewer viscous losses.

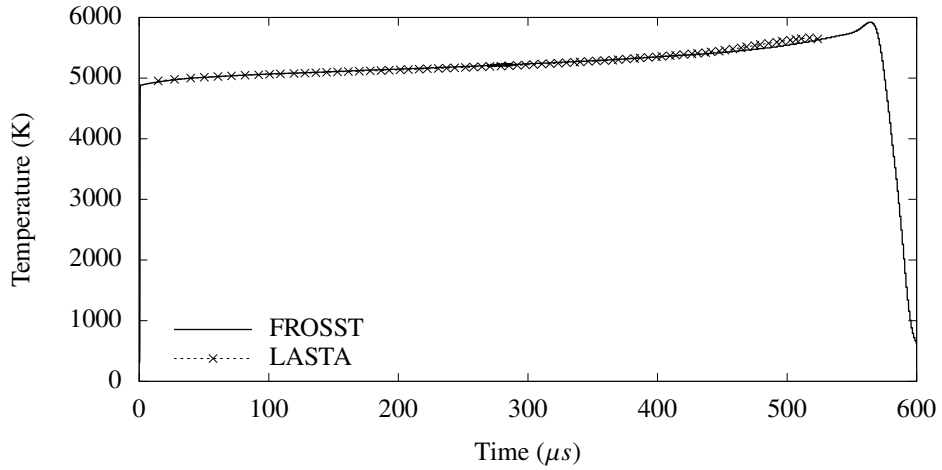

(a) Test gas temperature profiles.

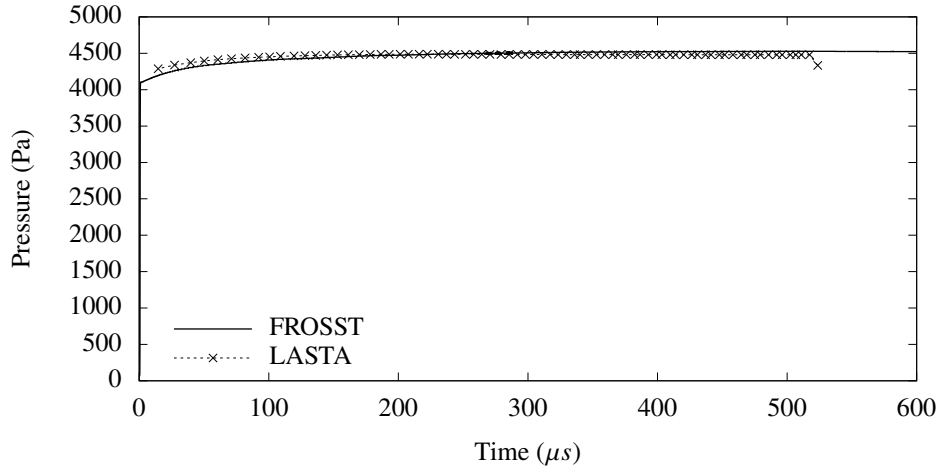

(b) Test gas pressure profiles.

Fig. B1 Shock trajectories and resulting test gas traces in the presence of complex upstream waves.

Pressure and temperature both agree to within 1% for the entire test slug, confirming that the mass balance scaled appropriately. With the wider tube, little test gas is lost to the boundary layer, and so the entire shock history is retained, as opposed to only the last 4 m as with the other cases. Since the first metre is dominated by unsteady viscous effects and the initial formation of the shock, some extent of disagreement is anticipated at the rear of the test slug, and so this small disagreement is not considered problematic.

VIII. Acknowledgements

The authors would like to thank the US Air Force for their support of this effort.

References

[C1] Mirels, H., "Test Time in Low-Pressure Shock Tubes," *Physics of Fluids*, Vol. 6, No. 9, 1963, pp. 1201–1214. https://doi.org/10.1063/1.1706887.

[C2] Morgan, R. G., and Gildfind, D. E., "Shock Tube Simulation of Low Mach Number Blast Waves," *29th International Symposium on Shock Waves 1*, Springer International Publishing, 2015, pp. 83–88. https://doi.org/10.1007/978-3-319-16835-7_11.

[C3] White, D. R., "Influence of Diaphragm Opening Time on Shock-Tube Flows," *Journal of Fluid Mechanics*, Vol. 4, No. 6, 1958, p. 585–599. https://doi.org/10.1017/S0022112058000677.

[C4] Satchell, M., Collen, P., McGilvray, M., and Mare, L. D., "Numerical Simulation of Shock Tubes Using Shock Tracking in an Overset Formulation," *AIAA Journal*, 2021, pp. 1–11. https://doi.org/10.2514/1.j059829.

[C5] Chandel, D., Nompelis, I., and Candler, G., "Computations of High Enthalpy Shock-waves in Electric Arc Shock-Tube (EAST) at NASA Ames," *2018 AIAA Aerospace Sciences Meeting*, American Institute of Aeronautics and Astronautics, 2018. https://doi.org/10.2514/6.2018-1722.

[C6] Kotov, D. V., Yee, H., Panesi, M., Prabhu, D. K., and Wray, A. A., "Computational Challenges for Simulations Related to the NASA Electric Arc Shock Tube (EAST) Experiments," *Journal of Computational Physics*, Vol. 269, 2014, pp. 215 – 233.

[C7] Brandis, A., Cruden, B., Prabhu, D., Bose, D., McGilvray, M., Morgan, R., and Morgan, R., "Analysis of Air Radiation Measurements Obtained in the EAST and X2 Shocktube Facilities," *10th AIAA/ASME Joint Thermophysics and Heat Transfer Conference*, American Institute of Aeronautics and Astronautics, 2010. https://doi.org/10.2514/6.2010-4510.

[C8] Mirels, H., "Flow Nonuniformity in Shock Tubes Operating at Maximum Test Times," *Physics of Fluids*, Vol. 9, No. 10, 1966, p. 1907. https://doi.org/10.1063/1.1761542.

[C9] Satchell, M., Mare, L. D., and McGilvray, M., "Flow Non-Uniformities Behind Accelerating Shockwaves in Shock Tubes," *AIAA Scitech 2021 Forum*, American Institute of Aeronautics and Astronautics, 2021. https://doi.org/10.2514/6.2021-0649, URL https://doi.org/10.2514/6.2021-0649.

[C10] James, C. M., Smith, D. R., McLean, C., Morgan, R. G., Lewis, S. W., Toniato, P., Wei, H., and McIntyre, T. J., "Using Optically Filtered High-Speed Imaging to Characterise Expansion Tube Operating Conditions," *Shock Waves*, Vol. 30, No. 5, 2020, pp. 523–544. https://doi.org/10.1007/s00193-020-00948-x.

[C11] Anderson, J., *Hypersonic and High Temperature Gas Dynamics*, American Institute of Aeronautics and Astronautics, Reston, VA, 2000.

[C12] Bensassi, K., Brandis, A. M., and Cruden, B. A., "Computational Modelling for Non-equilibrium Shock Tube Flows," *Proceedings of the 32nd International Symposium on Shock Waves (ISSW32 2019)*, Research Publishing Services, 2019. https://doi.org/10.3850/978-981-11-2730-4_0468-cd, URL https://doi.org/10.3850/978-981-11-2730-4_0468-cd.

[C13] Jacobs, P. A., "Quasi-One-Dimensional Modeling of a Free-Piston Shock Tunnel," *AIAA Journal*, Vol. 32, No. 1, 1994, pp. 137–145. https://doi.org/10.2514/3.11961.

[C14] James, C. M., Gildfind, D. E., Lewis, S. W., Morgan, R. G., and Zander, F., "Implementation of a State-to-State Analytical Framework for the Calculation of Expansion Tube Flow Properties," *Shock Waves*, Vol. 28, No. 2, 2018, pp. 349–377. https://doi.org/10.1007/s00193-017-0763-3.

[C15] Priyadarshini, M. S., Munafò, A., Brandis, A. M., Cruden, B. A., and Panesi, M., "One-Dimensional Modeling Methodology for Shock Tubes: Application to the EAST facility," *2018 Joint Thermophysics and Heat Transfer Conference*, American Institute of Aeronautics and Astronautics, 2018. https://doi.org/10.2514/6.2018-4181, URL https://doi.org/10.2514/6.2018-4181.

[C16] Gollan, R., and Jacobs, P., "About the Formulation, Verification and Validation of the Hypersonic Flow Solver Eilmer," *International Journal for Numerical Methods in Fluids*, Vol. 73, No. 1, 2013, pp. 19–57. https://doi.org/10.1002/fld.3790, URL https://doi.org/10.1002/fld.3790.

[C17] Bensassi, K., and Brandis, A. M., "Time Accurate Simulation of Nonequilibrium Flow Inside the NASA Ames Electric Arc Shock Tube," *AIAA Scitech 2019 Forum*, American Institute of Aeronautics and Astronautics, 2019. https://doi.org/10.2514/6.2019-0798.

[C18] Holbeche, T. A., and Spence, D. A., "A Theoretical and Experimental Investigation of Temperature Variation Behind Attenuating Shock Waves," *Proceedings of the Royal Society of London. Series A, Mathematical and Physical Sciences*, Vol. 279, No. 1376, 1964, pp. 111–128. URL http://www.jstor.org/stable/2414836.

[C19] Light, G. C., "Test Gas Properties Behind a Decelerating Shock Wave in a Shock Tube," *Physics of Fluids*, Vol. 16, No. 5, 1973, p. 624. https://doi.org/10.1063/1.1694397.

[C20] Satchell, M., Glenn, A., Collen, P., Penty-Garaets, R., McGilvray, M., and di Mare, L., "An Analytical Method of Evaluating Nonuniformities in Shock Tube Flows. Part 2: Application," , 2021. Submitted to AIAAJ.

[C21] Collen, P. L., Doherty, L., McGilvray, M., Naved, I., Geraets, R. T. P., Hermann, T. A., Morgan, R. G., and Gildfind, D., "Computations of High Enthalpy Shock-waves in Electric Arc Shock-Tube (EAST) at NASA Ames," *57th AIAA Aerospace Sciences Meeting*, American Institute of Aeronautics and Astronautics, 2019. https://doi.org/10.2514/6.2019-1941.

[C22] Hooker, W. J., "Testing Time and Contact-Zone Phenomena in Shock-Tube Flows," *Physics of Fluids*, Vol. 4, No. 12, 1961, p. 1451. https://doi.org/10.1063/1.1706243, URL https://doi.org/10.1063/1.1706243.

[C23] Mirels, H., "Laminar Boundary Layer Behind a Strong Shock Moving Into Air," *NACA Technical Note D-291*, 1961.

[C24] Mirels, H., "Boundary Layer Behind Shock or Thin Expansion Wave Moving Into Stationary Fluid," *NACA TN-3712*, 1956.

[C25] McBride, B., and Gordon, S., "Computer program for calculation of complex chemical equilibrium compositions and applications. I: Analysis," *NASA-RP-1311*, Vol. 19, 1996.

[C26] Roe, P., "Approximate Riemann solvers, Parameter Vectors, and Difference Schemes," *Journal of Computational Physics*, Vol. 43, No. 2, 1981, pp. 357 – 372. https://doi.org/https://doi.org/10.1016/0021-9991(81)90128-5.

[C27] Weilmuenster, K., "An Experimental Investigation of Wall Boundary Layer Transition Reynolds Numbers in an Expansion Tube," *NASA Technical Report NASA-NASA-TN-D-7541, L-9337*, 1974.

[C28] Mirels, H., "Shock Tube Test Time Limitation Due to Turbulent Wall Boundary Layer," *AIAA Journal*, Vol. 2, No. 1, 1964, pp. 84–93. https://doi.org/10.2514/3.2218.

[C29] Eckert, E. R., "Survey on Heat Transfer at High Speeds," *WADC TR 54-70*, 1962.

[C30] Simon, H., Liu, C., and Hartnett, J., "The Eckert Reference Formulation Applied to High-Speed Laminar Boundary Layers of Nitrogen and Carbon Dioxide," *International Journal of Heat and Mass Transfer*, Vol. 10, No. 3, 1967, pp. 406–409. https://doi.org/10.1016/0017-9310(67)90159-7, URL https://doi.org/10.1016/0017-9310(67)90159-7.

An Analytical Method of Evaluating Nonuniformities in Shock Tube Flows. Part 2: Application.

Matthew Satchell *, Alex Glenn †, Peter Collen ‡, Rowland Penty-Geraets §, Matthew McGilvray ¶, and Luca Di Mare ‖
Osney Thermofluids Institute, University of Oxford, United Kingdom

Shock tube experiments are a primary means of obtaining ground test data for the hypersonic regime. Accurate characterisation of the test gas is crucial to understanding experimental results. However, characterisation of the flows produced behind the shock wave has historically proven challenging. This paper applies a methodology to calculate the shocked test gas properties using the experimentally recovered shock speed profile. Static pressure, Pitot pressure and heat transfer predictions are found to closely match the experimental data for a range of shock trajectories with both Argon and Air test gases. Thermochemical variations in the test gases are found to depend strongly upon variations in shock speed along the tube. It is shown that characterisation of the test gases requires accommodating the influence of wave effects associated with the varying shock speed. Tube diameter is found to influence test time significantly in interaction with a variable shock speed, and also the magnitude of nonuniformities in the test gas. Location and number of shock timing stations in experimental facilities are found to play a vital role in the ability to accurately characterise the test gas of a given experiment.

I. Introduction

High speed vehicles generate non-equilibrium thermochemical effects which are directly coupled to the aerodynamics and heat transfer. Shock tubes have been a key ground test facility to explore thermochemistry by replicating the stagnation line flowfield. Although typically thought of as simple, (i.e. producing clean test flow behind a constant shock speed), most real experiments in these facilities are impacted by boundary layer growth and non-ideal driver and diaphragm rupturing effects. Thus, the shock speed varies as it propagates down the tube, leading to nonuniformities in the test gases of shock tubes [D1–6]. The use of only the final shock speed rather than the complete shock history along the tube leads to large discrepancies in the shocked test gas flow properties [D7]. As each experiment in a given facility will produce a different shock speed profile, a method of analysing the test gas properties for each experiment is needed.

In the preceding paper [D8], a theoretical basis by which the nonuniformities in the test gas produced by non-ideal

*DPhil Candidate, Department of Engineering Science, Oxford Thermofluids Institute, University of Oxford.
†DPhil Candidate, Department of Engineering Science, Oxford Thermofluids Institute, University of Oxford.
‡DPhil Candidate, Department of Engineering Science, Oxford Thermofluids Institute, University of Oxford.
§Research Associate, Department of Engineering Science, Oxford Thermofluids Institute, University of Oxford.
¶Associate Professor, Oxford Thermofluids Institute, Department of Engineering Science, University of Oxford.
‖Associate Professor, Oxford Thermofluids Institute, Department of Engineering Science, University of Oxford.

effects in shock tubes was detailed. The code thus developed was entitled the LAgrange Shock Tube Analysis (LASTA). The shocked test gas entropy distribution is directly related to the shock speed at which each slice is processed. The enthalpy distribution is affected by both effects caused by the growth of boundary layers and by influences arising from non-ideal processes in the driver and diaphragm rupturing. The test slug total length (distance between the shock and contact discontinuity) and the ultimate position of each gas slice is also dependent on the loss of mass to the boundary layer through the Mirels effects [D1]. LASTA simulates the shocked test gas as series of gas slices tracking along the tube in a Lagrangian frame of reference, assuming thermochemical equilibrium. It takes as input a prescribed shock history down the tube, which can be directly measured in a given experiment, as well as the initial test gas pressure, temperature and composition. The previous paper showed the accuracy of this approach with validation against Navier-Stokes simulations.

This paper applies the developed LASTA code to verify its suitability and practical application across a broad range of real experiments. Consideration is given to the effect of tube diameter, non-ideal driver/diaphragm waves, thermochemistry and shock speed measurement resolution. LASTA is applied to simulate real experiments from the Oxford T6 facility operated in Aluminium Shock Tube mode for both Air and Argon test gases at speeds where dissociation and ionization will be present. The results are compared to experimental measurements of the static pressure, Pitot pressure and stagnation point heat flux histories. This work clearly demonstrates that LASTA is capable of predicting test gas nonuniformities to a high degree of accuracy, allowing reliable investigation of equilibrium thermochemical variations. Furthermore, this paper uses the LASTA methodology to investigate the requisite resolution of shock speed measurements in experiments in order to accurately characterise test gas nonuniformities. Finally, this paper examines the role of tube diameter at a given set of conditions in contributing to test gas nonuniformities.

II. Shock Tube Experiments

The LASTA methodology was previously validated against a series of numerical simulations [D8]. However, these simulations were performed in the context of an ideal gas. Although they did include non-ideal facility effects such as unsteady diaphragm effects, such simulations necessarily involve less complex flows than actual experiments. As such, additional validation is desired involving real gases in experimental test flows. Along with validation, such a comparison allows examination of the influence of non-ideal facility effects upon thermochemical variations in experimental test gases. Experimental data for these investigations was obtained in the University of Oxford T6 Stalker tunnel.

A. T6 Stalker Tunnel

T6 [D9] is a multi-mode free piston driven shock tunnel performs hypervelocity and high temperature experiments. In the experiments detailed here, T6 was operated in aluminium shock tube mode, which has an optional secondary driver and an expansion from 96.3 mm to 225 mm for the shock tube (Figure 1). The length of the aluminium shock

tube is 6.1 m after the conical expansion. The test window is located at 6.5 m from the secondary diaphragm and the test section measurement rake is at 7.2 m from the secondary diaphragm. This rake is located in the outlet at the tube. All shock speed measurements used in the calculations presented in this paper are taken downstream of the nozzle expansion.

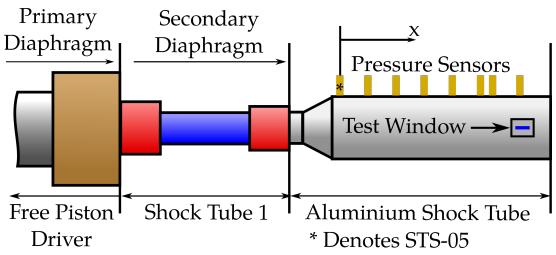

Fig. 1 Schematic of T6 in Aluminium Shock Tube mode.

Five experiments were performed with both pure Argon and synthetic Air (mass fractions of 0.233 O_2 and 0.767 N_2) as test gases, at a range of fill pressures as detailed in Table 2. All data was recorded on a National Instruments PCIe 6368 card with 2 MS/s/ch at 16 bits digitisation. Measurements of the shock progression along the tube are taken using wall mounted PCB Piezotonics 113B27/28, where the arrival is assumed to be the rising edge as detected using a canny edge filter [D10]. The locations of these are detailed in Table 1, as referenced from the first sensor after the expansion, STS-5, which is located at 1.46 m from the secondary diaphragm. The local shock speed is calculated using the distance between sensor locations and the time of flight between measurement locations. Shock speed calculations were performed only after STS-5. The position of the shock speed is assumed to be halfway between the sensor locations. As there is a variable sensor response and shock speed between the locations, as well as motion between the final static sensor and the Pitot sensor due to tunnel recoil, the overall uncertainty in shock speed is approximated to be 1.7% with individual uncertainties detailed in each figure. All pressure measurements have an uncertainty of ±7%, as per Hayne *et al* [D11].

Measurements of the Pitot pressure and heat flux were made in the core flow at the test section rake location. Pitot pressure was measured with PCB Piezotronics 113B24 series transducers, mounted in swirl caps for protection [D12]. These have a variable response time due to the period required to fill the internal cavity. Stagnation point heat flux measurements were made using a novel diamond calorimeter heat transfer gauge (DHTG) developed by Penty Geraets et al. (2020) [D13], flush-mounted in a cylindrical body of diameter 10.50 mm and corner radius 0.13 mm. Using the correction of Zoby [D14] these were found to have an effective spherical radius of 15.21 mm. This value is required for the formula of of Sutton and Graves [D15] which is used to generate the computational heat flux predictions. For these experiments, in-house HTA-3 signal conditioning units were employed; these have an effective bandwidth of 400 kHz. The gauges were characterised by measuring their resistance change with temperature in a high-uniformity calibration oven. The measured temperature is processed into heat flux using the Sequential Function Specification

Table 1 Pressure transducer locations in T6.

Descriptor	Measurement Type	Distance from STS-5 (m)
STS-5	Static Pressure	0.000
STS-7	Static Pressure	1.000
STS-9	Static Pressure	2.000
STS-10	Static Pressure	2.970
STS-12	Static Pressure	4.070
STS-13	Static Pressure	4.620
STS-15	Static Pressure	5.070
STS-17	Static Pressure	5.270
PP-01	Pitot Pressure	5.700
DHTG-1	Stagnation Heat Flux	5.700

Method [D13]. The overall uncertainty in the heat flux is 10%.

The temperature of the tube was 20° C ±0.5 C throughout the experiment as recorded via a thermocouple on the facility. The primary and secondary driver conditions were altered to achieve the resultant shock speed profiles. Table 2 summarizes these conditions, and shows also the maximum and final shock Mach numbers to highlight the variation of shock speed associated with each.

B. LASTA Setup

LASTA was used to simulate the T6 experiments by using the experimentally recorded shock trajectories as inputs. Experimental shock speed measurements were obtained along the full length of the facility, but only the shock timing stations downstream of the nozzle were used to construct the trajectories. No information regarding the driver gas or shock behaviour upstream of the nozzle exit was required. Each simulation used 1800 time steps on the order of 0.5 μs for the Air shots, and 1 μs for the Argon shots. Slices were distributed every 0.25 m along a tube of radius 112.5 mm for a total length of 5.7 m. Stagnation conditions were output at PP-01/DHTG-1. Static pressure traces were output at STS-15 for T6s215 and T6s218 to match the experimental wall pressure transducer there, as STS-17 experienced an error during those tests. Test T6s204 output at STS-17, allowing for a reading closer to the tube-end for that test. Fill temperature and pressure were input to match the experimental conditions. All simulations assumed a laminar boundary layer. The Argon shots used a three-species composition (Ar, Ar^+, e^-) equilibrium thermochemical model, whilst the Air tests used a 9-species equilibrium Air species set consisting of N_2, O_2, N, O, NO, NO^+, N^+, O^+ and e^-. Equilibrium compositions were computed using a Gibbs free energy minimization technique following the developments of Zeleznik [D16] and Huff and Morrell [D17]. The equilibrium code is being locally developed as an open source resource, but has yet to be published [D18]. Equilibrium wall conditions were assumed in calculation of the boundary layer properties.

Heat transfer was computed using the method of Sutton and Graves [D15], where the heat transfer $\dot{q}$ is found from:

$$\dot{q} = K\sqrt{\frac{p_p}{R}}(H_s - h_w) \tag{1}$$

Here, $K = 0.1113\,\mathrm{kg/s\text{-}m^{1.5}\text{-}atm^{0.5}}$ for Air and $K = 0.1495\,\mathrm{kg/s\text{-}m^{1.5}\text{-}atm^{0.5}}$ for Argon. R is the effective spherical radius, p_p is the Pitot pressure, H_s is the stagnation enthalpy, and h_w is the flow enthalpy at the cold wall.

The three-species Argon simulations consumed 6 seconds of wall clock time on a single core, whereas the 9-species Air simulations took 700 seconds on a single core. This growth in time is partly due to the use of smaller time steps with the higher speed Air tests, as well as the greater number of species. It may be noted that this methodology is highly parallizable and so simulation time may be substantially reduced.

Table 2 Summary of Experimental Conditions in T6

T6 Shot Number	Test Gas	Fill (Pa)
T6s214	Argon	66.6
T6s212	Argon	133.2
T6s218	Air	155.3
T6s204	Air	106.7
T6s215	Air	321.2

C. Argon Tests

The shock speed trajectories of each Argon test are shown in Figure 2a, with the final experimental shock speed taken at 5.5 m from STS-5, halfway between STS-17 and PP-01. Velocities shown beyond this location are the extrapolated conditions. Tests T6s214 and T6s212 contain 7% and 25% decelerations in shock speed, respectively. Figure 2b also shows the static and Pitot pressure traces from LASTA and the experiments. The LASTA simulation of the strong deceleration T6s212 is seen to match closely with experimental data, while a small error in measured final shock speed causes an increase in the Pitot pressure for shot 214 slightly above the experimental value. Although the post-shock Argon is initially only 0.1% ionized by mole fraction, under stagnation conditions at the probe faces, the Argon becomes 1.4% ionized for T6s214, influencing the Pitot and heat transfer measurements, particularly near the rear of the test slug. In T6s212, the ionization ranges to as high as 1.6% near the rear of the test slug, a variation seen in Figure 3. Despite these sources of error, the agreement between LASTA and experiment for the Argon cases is considered to be acceptable.

The comparison with the Argon experiments is further strengthened by the matching of heat transfer for both tests, as seen in Figure 2d. LASTA is able to predict the heat flux trend through the test slug. T6s212 shows a more substantial rise in heat transfer; this is associated with the elevated temperatures caused by the stronger deceleration of T6s212, as

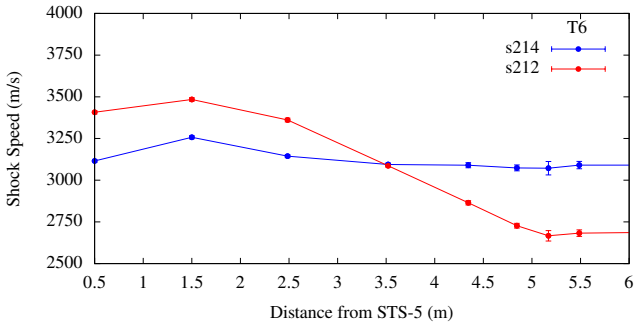

(a) Shock speed versus location for the Argon tests T6s214 and T6s212.

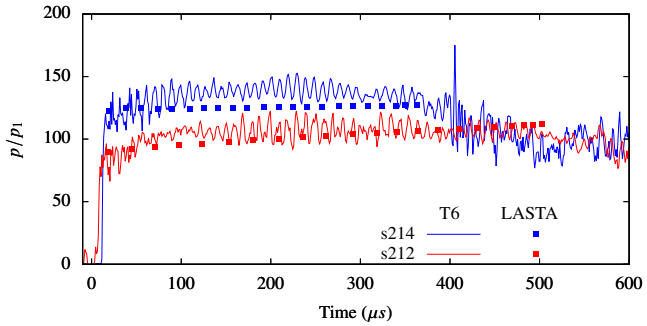

(b) Static pressure traces, normalised by fill pressure p_1 for each test at $x = 5.07$ m for T6s215 and T6s218, $x = 5.27$ m for T6s204.

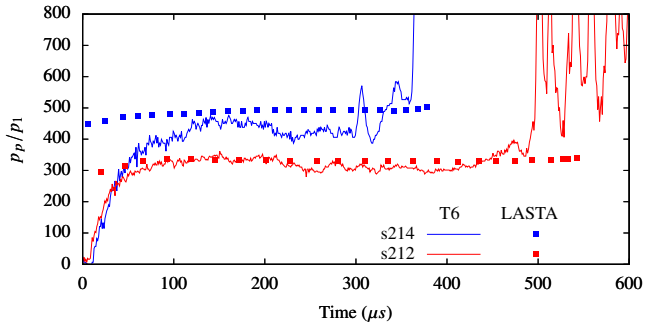

(c) Pitot pressure traces p_p, normalised by fill pressure p_1 for each test at $x = 5.70$ m.

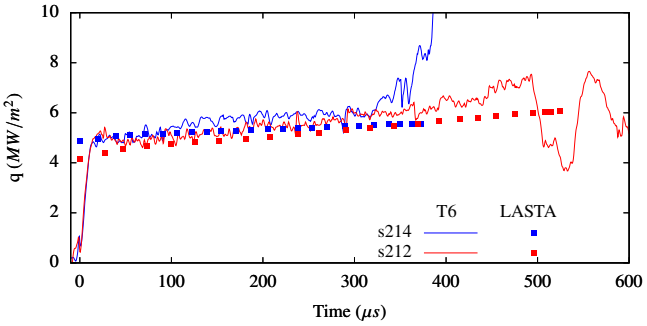

(d) Heat transfer data for each test at $x = 5.70$ m.

Fig. 2 LASTA comparison to experimental static and Pitot pressures, and heat transfer for the Argon tests.

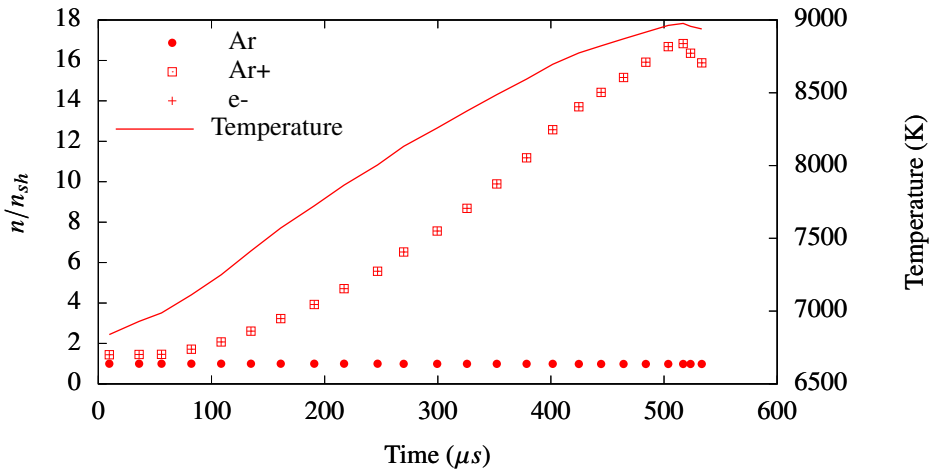

Fig. 3 Normalised variation of species' freestream number densities from post-shock values in T6s212. Post-shock moles of each species are: Ar: 9.8e-1 Ar^+: 1.5e-2 e^-: 1.5e-2 at x = 5.70 m

confirmed by the LASTA simulation.

D. Air Tests

A more complete investigation of thermochemical effects may be performed in the context of the Air tests. Figure 4 shows the Air tests' shock speed profiles and resulting test gas wall static pressure and centreline Pitot measurements, normalized by the fill pressure p_1. Note that test T6s204 had an extra sensor installed 300 mm from STS-5, which is visible in its shock profile. This normalization was performed in order to highlight the subtly different trends observable the Pitot traces of T6s218 and T6s204. The arrival of contaminating vortices is visible in T6s218 and T6s204 in the sudden presence of relatively large oscillations, denoting the end of the useful test time. For all three tests, LASTA is able to reproduce the test slug Pitot and static pressures to within experimental uncertainties. Additionally, heat flux measured experimentally for T6s215 is reproduced to within 3% as seen in Figure 4d. Static pressures are obtained 0.43 m upstream of the Pitot sensors, and the test gas added between these sensors accounts for the difference in test times observed between the two. It may be noted that, as temperature and pressure shift through the test slug, the equilibrium species must shift with them in order to produce an accurate density. The Pitot pressure and heat transfer scale with density, and so agreement between prediction and experimental data in these quantities indicates accurate capture of the thermochemical state of the test gas. Such an accurate capture of thermochemistry is suggested by the strong agreement between LASTA and T6 data.

The significance of the slightly different Pitot trends between tests T6s218 and T6s204 is now examined in the context of thermochemistry. Figure 5 shows the variation of chemical species through the test slug both tests. A comparison between the two reveals that the extent of species variation is strongly influenced by shock speed effects.

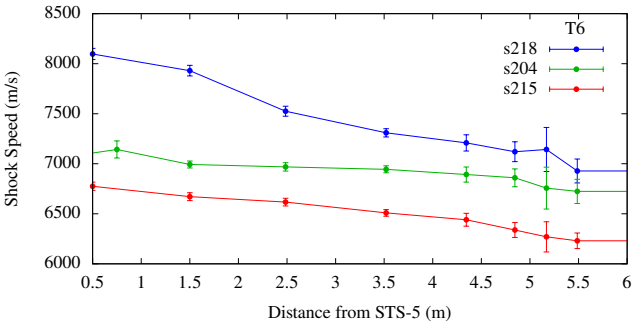

(a) Shock speed versus location for the Air tests.

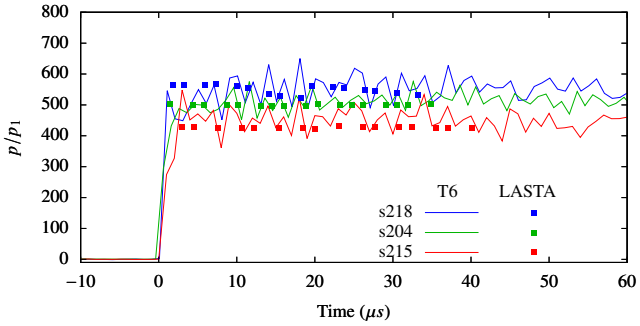

(b) Static pressure traces, normalised by fill pressure for each test at x = 5.27 m.

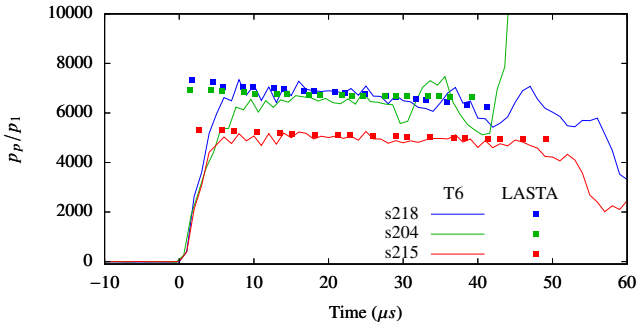

(c) Pitot pressure traces, normalised by fill pressure for each test at x = 5.70 m.

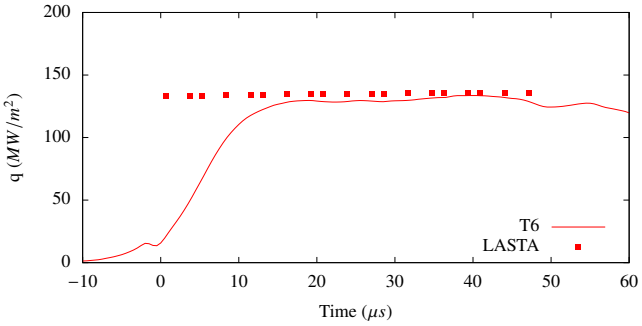

(d) Heat transfer for T6s215 at x = 5.70 m.

Fig. 4 LASTA comparison to experimental data for the Air tests.

Although the two shocks arrive at the test section at a speed within 3% of one-another, the higher deceleration test T6s218 shows more than twice the variation in ionized species and follows an entirely different trend. The qualitative trends observed in each are also notable. It is therefore evident that the different shock trajectories produced substantially different test gas thermochemical variations.

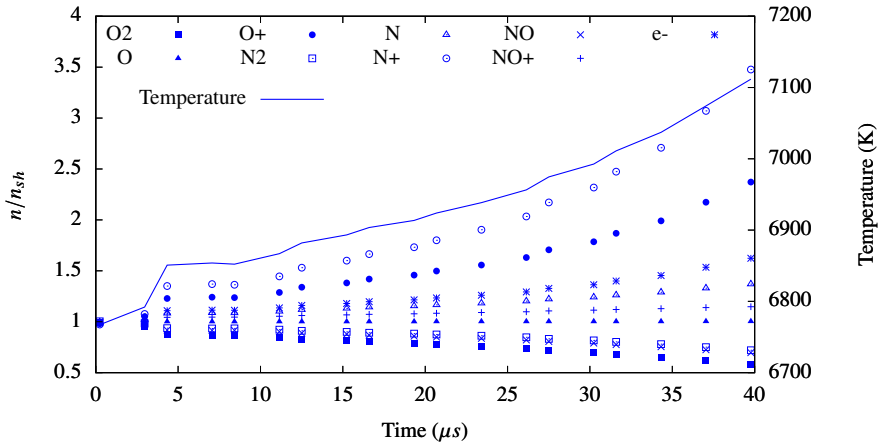

(a) Normalised variation of species' freestream number densities from post-shock values in T6s218. Post-shock moles of each species are: O2: 4.18e-5, O:4.2e-1, O+: 1.8e-4, N2: 3.2e-1, N: 9.3e-1, N+: 4.5e-4, NO: 3.4e-3, NO+ 7.2e-4, e-: 1.3e-3

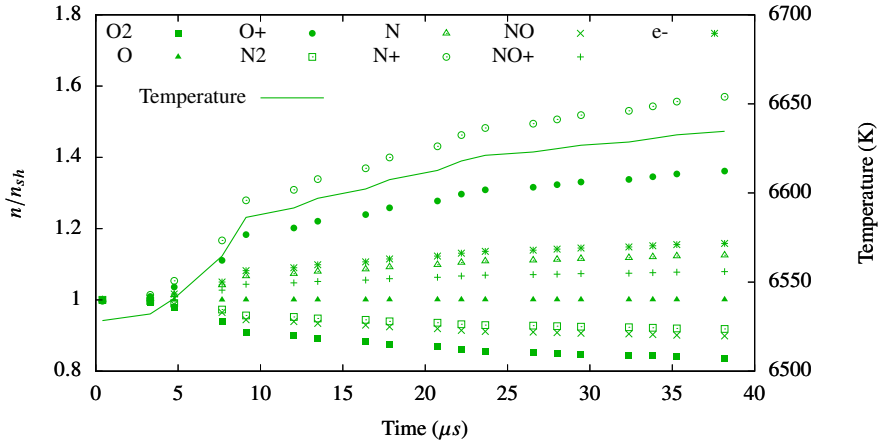

(b) Normalised variation of species' freestream number densities from post-shock values in T6s204. Post-shock moles of each species are: O2: 5.6e-5, O:4.2e-1, O+: 7.5e-5, N2: 4.4e-1, N: 7.0e-1, N+: 4.5e-4, NO: 4.1e-3, NO+ 5.9e-4, e-: 7.9e-4

Fig. 5 Comparison of thermochemical variations through the test slugs of tests T6s218 and T6s204.

III. Considerations in Characterising Shock Tube Experiments

The comparisons above demonstrate that LASTA can accurately characterise experimental test gases. In the broader application of the code, it is of interest to understand how its results differ from those of existing flow characterisation methodologies. Furthermore, many facility sizes and instrumentation configurations exist, and so the accuracy of the present analysis as applies to a range of instrumentation layouts must be examined. To perform these investigations, a

shock trajectory through Air typical of T6 experiments was selected using a relatively high resolution of sensors every 0.1 m, and LASTA was run against this trajectory as a baseline, as seen in Figure 6. The fill pressure was 100 Pa, and the tube diameter was 100 mm. LASTA was configured the same as for the experimental cases discussed above.

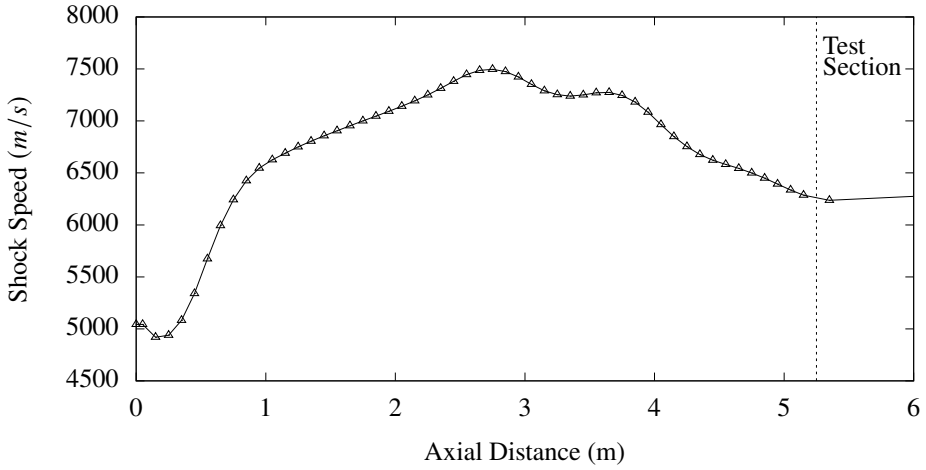

Fig. 6 High resolution shock speed profile representative of typical T6 experiments.

A. Comparison of LASTA to Alternative Methods

The property variations through the test slug as computed using the LASTA methodology were compared against four other predictions:

1) Variations from post-shock properties with boundary layer mass balance
2) Variations due to boundary layer effects only
3) Variations from post-shock properties only without boundary layer mass balance
4) No variations

The first alternative prediction was to account for entropy variations as well as boundary layer effects, but not allowing for the influence of wave effects, such as was proposed by Light [D3]. The second prediction was using boundary layer effects only, such as predicted by Mirels [D2] and versions of which are presently common practice. This methodology is also equivalent to a stagnation-line computation without the three-dimensional effects which are often accommodated in such computations. The third alternative simply takes the post-shock properties and holds them constsant for each slice, where the locations are defined as those obtained by the Mirels computation. This concept is similar to that depicted in Brandis et al. [D19], although it may be noted that use of constant post-shock velocities results in slices actually passing the decelerating shock. The final comparison is against a uniform test slug as predicted by the final shock speed, versions of which assumption are also common in shock tube studies. Figure 7 shows the resulting variations. Figures 7a and 7b show the temperature and pressure, respectively. The resulting variation in

electron number density is seen in Figure 7c. Finally, Figure 7d plots the entropy for each slice, colored by its original location in the shock tube so that it is evident from what portion of the shock trajectory each slice originated.

Removing wave effects from the LASTA methodology substantially changes both the magnitude of the nonuniformities and also the test time as the boundary layer mass balance responds to the higher pressures and temperatures. This is most apparent in the pressures, where relaxation effects produce a remarkably different pressure distribution than the full LASTA prediction. Examining the entropy-only case, it is clear that by decoupling the variable post-shock properties from the boundary layer mass balance, the post-shock properties are preserved while the test time is extended considerably. This is exacerbated in part because more slices persist until the end of the tube as their mass flow is sufficient to avoid being consumed entirely by the boundary layer. This is also seen in Figure 7d by comparing the entropy levels of each slice against its originating and final locations. The most significant effect of boundary layer mass consumption is to redistribute the entropy produced by shock speed variation by determining the distance between the slices, and it is evident that the coupling of wave effects plays a substantial role in the boundary layer mass balance. The enthalpy recovery of the Mirels' methodology is seen to produce, for this trajectory, minimal variation away from the uniform test slug. This is due to the comparatively thin boundary layer for this case, whereas a more narrow tube or a lower fill pressure would produce more significant Mirels-type variations.

B. Resolution of shock timing sensors

Experimental measurements of shock speed depend upon the use of fast-response sensors, typically measuring pressure, to determine the arrival of the shock at any given distance from the diaphragm. The difference in shock arrival times at consecutive sensors is used to obtain shock speed measurements along the tube. The number of sensor locations along the tube is limited, thus a finite number of shock speed measurements are possible. As a result, the resolution of short wavelength changes in shock speed may be severely limited, or missed altogether. Furthermore, a limited number of shock timing sensors can distort the computed shock trajectory in terms of the locations and magnitudes of local maxima or minima, and uncertainties exist in the shock-timing measurements themselves. Finally, each test facility has its own arrangement of shock timing sensors, and so the fundamental capacity to measure shock speed variations is different between many laboratories. Altogether, the influence of shock speed measurement resolution must be considered.

The removal or modification of any substantial portion of the trajectory such as a local maximum which occurred between two sensors will result in the removal of that entropy level from the test slug. Such an absence will also introduce a degree of uncertainty in the distribution of slices due to the loss of pressure variations influencing the boundary layer thickness during the missing maximum. Since the mass balance between core flow and boundary layer is highly sensitive to pressure variations, the absence of a given portion of the trajectory may cause gas slices either to persist longer than they should, or prematurely cause the boundary layer to consume all mass from a slice, eliminating it

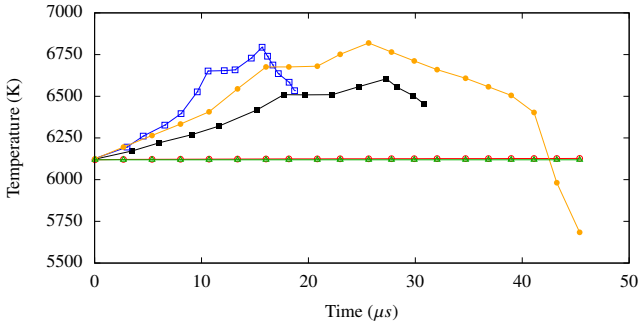

(a) Temperature profiles.

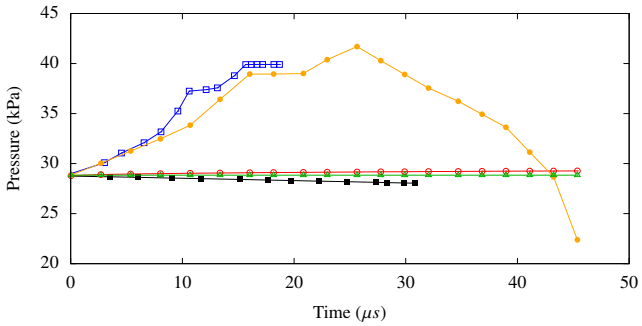

(b) Static pressure profiles.

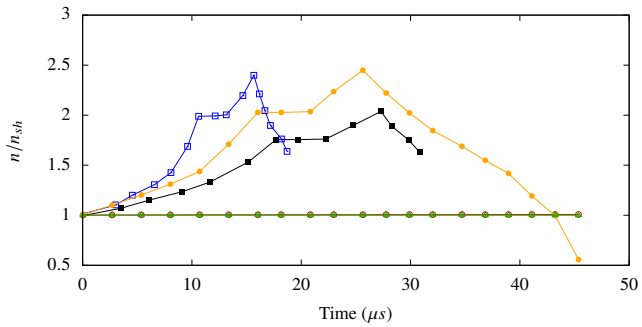

(c) Normalised electron number densities.

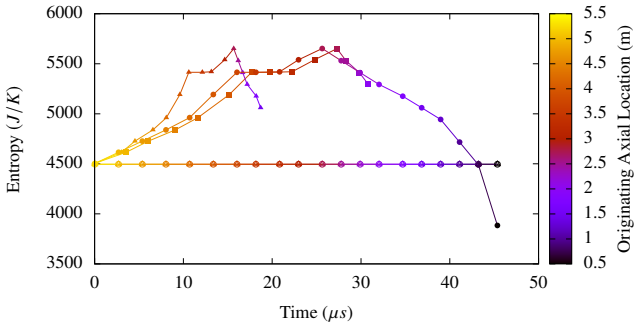

(d) Entropy profiles, colored by originating axial location.

Fig. 7 A comparison of test slug temperature nonuniformities from different analysis methodologies.

from the test slug and thereby advancing the contact discontinuity towards the shock.

Different trajectories were obtained by progressively removing sensors from the high resolution baseline trajectory of Figure 6. Each unique trajectory was determined by integrating the time of arrival between the remaining sensors. The sensor resolutions used were: 0.1 m, 1.0 m, 2.0 m, 5.0 m, and also a case where the shock speed is considered constsant. The evident dependence of observed shock trajectory upon measurement limitations is presented in Figure 8a.

Figure 8 shows the shock trajectories, temperature and pressure profiles through the test slug. Mirels' analysis, which assumes a constant shock speed and is outlined in Appendix A, was also applied to the full resolution case in order to predict the test time. It is clear that the variable shock speed leads to a significant decrease in test time. This is caused by the decelerating shock producing slower post-shock gas than the faster upstream gas. The faster upstream gas then pushes forward into the test slug, thereby shortening the test time.

It is evident that both the predicted test time and test gas properties are strongly influenced by the number and placement of shock timing sensors for shock speed integration. The 1 m resolution is able to largely capture the trajectory, but lacks the nuance of the full-resolution case, and so predicts slightly different trends and a peak temperature 1% lower. The difference in pressure is slightly more pronounced, showing a 2% maximum difference. The significance of these differences is seen in Figure 8d, which shows the variation of electron density through each test slug. The 1 m resolution generally obtains strong agreement, and the differences are generally qualitative in nature. However, the small differences in pressure and temperature lead to a 9% greater maximum electron density through the test slug, caused mostly by substantial variations in ionised Nitrogen and Oxygen. The other shock trajectories neither qualitatively nor quantitatively approach the variations observed in the full resolution case. It is thus clear that, in order to accurately characterise experimental test flows, the shock trajectory must be sufficiently resolved. In this case, a minimum resolution of 1 m was shown necessary to capture nearly all of the variation.

C. Tube Diameter

The influence of tube diameter upon test slug properties for a highly varying shock speed history is now examined. Four diameters were run: 25 mm, 50 mm, 100 mm, and 200 mm. Figure 9 shows that the larger diameter tubes asymptotically increase the test time, consistent with the predictions of Mirels, which assume a constant shock speed. Test time predictions according to the methodology of Mirels [D1] are shown in dotted lines. The varying shock speed shortens the test times considerably when compared to those predicted by Mirels' theory from the final shock speed. The narrowest tube is seen to most closely match Mirels' predictions, which is caused by the domination of the flow area by boundary layer effects. The increased boundary layer mass flow relative to the diminished core flow causes the case to approach the Mirels' limit in which the entire shock-processed mass flow is consumed by the boundary layer, thereby determining the length of the test slug.

As the test time changes, the trends in temperature are largely maintained, but 'stretched' or 'compressed' according

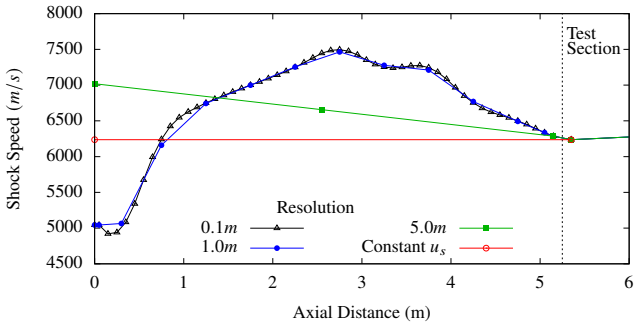

(a) Shock speed profiles derived from coarse speed measurements from the same baseline shock speed profile.

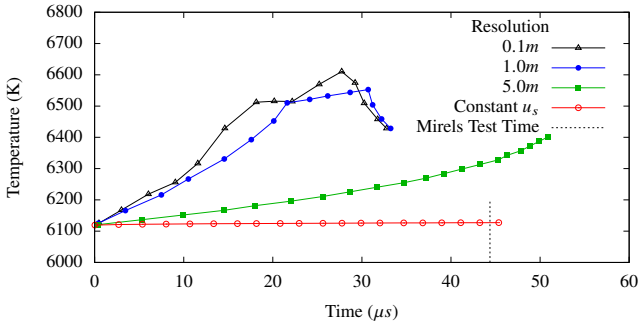

(b) Test gas temperature profiles.

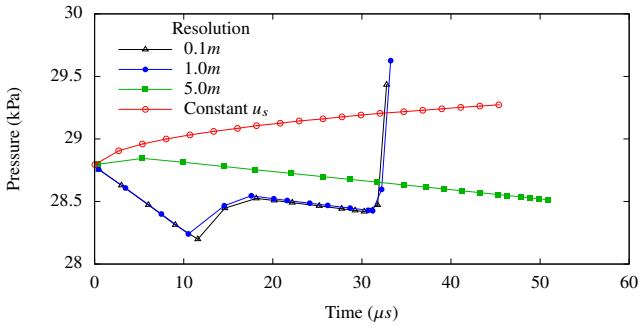

(c) Test gas static pressure profiles.

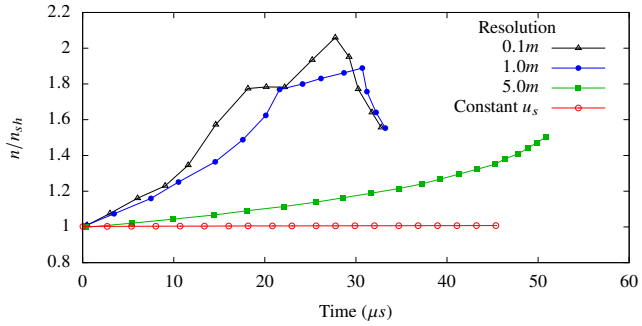

(d) Test gas ratio of slice electron number density to post-shock electron number density.

Fig. 8 The influence of limited experimental shock speed measurements. Measurement location was 5.25 m.

to the distribution produced by variations in speed. A small degree of variation in peak temperature is also noticeable with decreased tube diameter. This effect is due to the constriction of the stream tube by the boundary layer. Although minor under the present conditions, this effect would become more significant with a turbulent boundary layer or a lower fill pressure, either of which conditions result in thicker boundary layers.

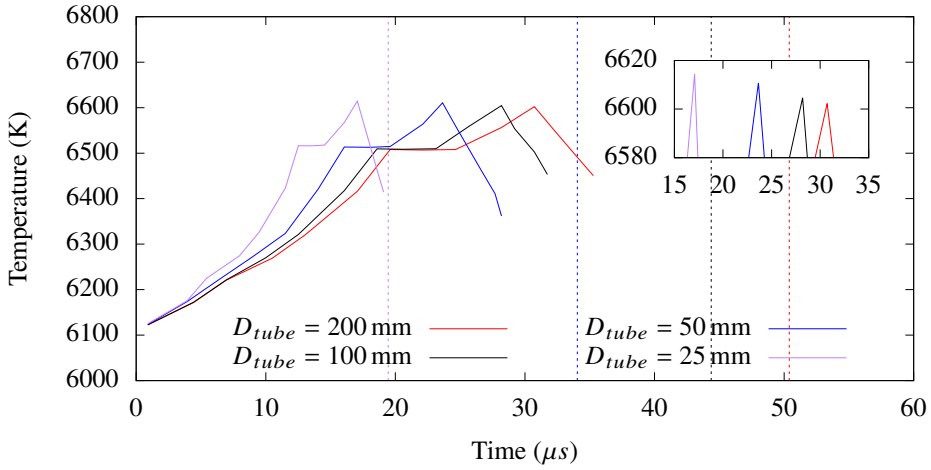

Fig. 9 Temperature profiles in the baseline shock trajectory when performed in tubes of varying diameters. Dotted lines are predictions of test time utilising Mirels' methodology [D 1].

IV. Conclusions

This paper applied a novel analytical methodology to characterise test gases in experimental shock tube flows where non-ideal effects were present. This work used the LASTA code to assess the sources of thermochemical variations through experimental test slugs, and demonstrated that shock history plays a dominant role in determining the observed thermochemical properties. Unsteady experimental test gas properties may be entirely derived from shock history alone. LASTA was compared against other common shock tube characterisation methodologies, and found to produce substantially different trends and maxima in test gas nonuniformities by capturing the complex interactions between wave effects and entropy distribution through the gas. Accurate measurement of the experimental shock speed profile requires of a sufficient number of shock-timing transducers along the length of the tube. Incomplete information about shock trajectory was found to influence anticipated test time and thermochemical variations through the test slug. Tube diameter was found to influence test slug nonuniformities both by changing the overall test time and also by altering the magnitude of wave and boundary layer effects associated with shock speed variation. This influence is expected to increase with a turbulent boundary layer. The results presented herein indicate that the LASTA methodology should lead to a meaningful improvement in the thermochemical and radiative analyses produced by shock tube experiments.

Appendix

Mirels [D1] developed a methodology for determining the test time in a shock tube experiment based upon laminar boundary layer theory. The analysis method assumes a shock of constant speed, and determines the distance behind the shock at which the boundary layer has consumed all mass flow processed by the shock. This distance necessarily demarks the location of the contact discontinuity, and so concludes the test slug. The test time is then determined by use of the approximation that the contact discontinuity is travelling at the same speed as the shock. Thus, the test time is found as the time it takes for a particle to travel the test slug length at the speed of the shock. The maximum test slug length takes some time to develop as the shock traverses the tube, and so Mirels' analysis included a means of computing the test time at any given distance down the tube after burst. The algorithm is detailed below:

The maximum test slug length l_m is given as:

$$l_m = \frac{d^2}{18\beta^2}\left(\frac{\rho_{e,0}}{\rho_{w,e0}}\right)^2 \frac{u_{e,0}}{u_w - u_{e,0}} \frac{u_{e,0}}{\nu_{w,0}} \tag{A1}$$

Here, subscript $_{e,0}$ denotes core flow properties behind the shock, u_w is the shock speed in the laboratory frame of reference, and $u_{e,0}$ is the post-shock flow speed in the shock frame of reference. Subscript $_w$ denotes wall properties, which assume a cold wall. β is found from the relation:

$$\beta = 1.59C^{0.37}\left(1 + \frac{1.796 + 0.802W}{W^2 - 1}\right) \tag{A2}$$

where

$$C = \left(\frac{\rho_e \mu_e}{\rho_w \mu_w}\right)_0 \tag{A3}$$

The term W is a measure of shock strength, given as the ratio of post-shock velocity in the shock frame of reference to shock speed $w = \frac{u_{e,0}}{u_w}$.

Knowing the maximum test slug length, the slug length l_t behind the shock when it is at any particular distance from the diaphragm is found at each shock location x_s by iterative solution of the relationship:

$$-\frac{1}{2}X = ln(1 - T^{0.5}) + T^{0.5} \tag{A4}$$

where $X = \frac{x_s}{W l_m}$ and $T = \frac{l_t}{l_m}$. The test time at each shock location down the tube is then found as $t_{test} = l_t/u_w$.

V. Acknowledgements

The authors would like to thank the US Air Force for their support of this effort.

References

[D1] Mirels, H., "Test Time in Low-Pressure Shock Tubes," *Physics of Fluids*, Vol. 6, No. 9, 1963, pp. 1201–1214. https://doi.org/10.1063/1.1706887.

[D2] Mirels, H., "Flow Nonuniformity in Shock Tubes Operating at Maximum Test Times," *Physics of Fluids*, Vol. 9, No. 10, 1966, p. 1907. https://doi.org/10.1063/1.1761542.

[D3] Light, G. C., "Test Gas Properties Behind a Decelerating Shock Wave in a Shock Tube," *Physics of Fluids*, Vol. 16, No. 5, 1973, p. 624. https://doi.org/10.1063/1.1694397.

[D4] Holbeche, T. A., and Spence, D. A., "A Theoretical and Experimental Investigation of Temperature Variation Behind Attenuating Shock Waves," *Proceedings of the Royal Society of London. Series A, Mathematical and Physical Sciences*, Vol. 279, No. 1376, 1964, pp. 111–128. URL http://www.jstor.org/stable/2414836.

[D5] Petersen, E. L., and Hanson, R. K., "Nonideal Effects Behind Reflected Shock Waves in a High-Pressure Shock Tube," *Shock Waves*, Vol. 10, No. 6, 2001, pp. 405–420.

[D6] Cruden, B. A., Brandis, A. M., and Prabhu, D. K., "Compositional Dependence of Radiance in CO2/N2/Ar Systems," *44th AIAA Thermophysics Conference*, American Institute of Aeronautics and Astronautics, 2013. https://doi.org/10.2514/6.2013-2502.

[D7] Satchell, M., Mare, L. D., and McGilvray, M., "Flow Non-Uniformities Behind Accelerating Shockwaves in Shock Tubes," *AIAA Scitech 2021 Forum*, American Institute of Aeronautics and Astronautics, 2021. https://doi.org/10.2514/6.2021-0649, URL https://doi.org/10.2514/6.2021-0649.

[D8] Satchell, M., , McGilvray, M., and di Mare, L., "An Analytical Method of Evaluating Nonuniformities in Shock Tube Flows. Part 1: Theory and Development," , 2021. Submitted to AIAAJ.

[D9] Collen, P. L., Doherty, L., McGilvray, M., Naved, I., Geraets, R. T. P., Hermann, T. A., Morgan, R. G., and Gildfind, D., "Computations of High Enthalpy Shock-waves in Electric Arc Shock-Tube (EAST) at NASA Ames," *57th AIAA Aerospace Sciences Meeting*, American Institute of Aeronautics and Astronautics, 2019. https://doi.org/10.2514/6.2019-1941.

[D10] James, C., "Using a Simplified Canny Edge Detector to Detect Shock Arrival in Expansion Tubes and Shock Tunnels," *Proceedings of the 32nd International Symposium on Shock Waves (ISSW32 2019)*, Research Publishing Services, 2019. https://doi.org/10.3850/978-981-11-2730-4_0031-cd, URL https://doi.org/10.3850/978-981-11-2730-4_0031-cd.

[D11] Hayne, M. J., Mee, D. J., Gai, S. L., Stewart, B. S., and Morgan, R. G., "Flow Establishment Over Rearward-Facing Steps in High Enthalpy Flows," *Shock Waves*, Springer Berlin Heidelberg, 2005, pp. 173–178. https://doi.org/10.1007/978-3-540-27009-6_23, URL https://doi.org/10.1007/978-3-540-27009-6_23.

[D12] McGilvray, M., Austin, J. M., Sharma, M., Jacobs, P. A., and Morgan, R. G., "Diagnostic modelling of an expansion tube operating condition," *Shock Waves*, Vol. 19, No. 1, 2009, pp. 59–66. https://doi.org/10.1007/s00193-009-0187-9, URL https://doi.org/10.1007/s00193-009-0187-9.

[D13] Penty Geraets, R. T., McGilvray, M., Doherty, L. J., Morgan, R. G., James, C. M., , and Buttsworth, D. R., "Development of a fast-response diamond calorimeter heat transfer gauge," *Journal of Thermophysics and Heat Transfer*, Vol. 34, 2020, pp. 193–202.

[D14] Zoby, E. V., and Sullivan, E. M., "Effects of Corner Radius on Stagnation-Point Velocity Gradients on Blunt Axisymmetric Bodies," *Journal of Spacecraft and Rockets*, Vol. 3, No. 10, 1966, pp. 1567–1567. https://doi.org/10.2514/3.59538, URL https://doi.org/10.2514/3.59538.

[D15] Sutton, K., and Graves, R., "A General Stagnation-Point Convective-Heating Equation for Arbitrary Gas Mixtures," *NASA TR R-376*, 1971.

[D16] Zeleznik, F. J., and Gordon, S., "Calculation of Complex Chemical Equilibria," *Industrial & Engineering Chemistry*, Vol. 60, No. 6, 1968, pp. 27–57. https://doi.org/10.1021/ie50702a006.

[D17] Huff, V., and Morrell, V., "General Method for Computation of Equilibrium Composition and Temperature of Chemical Reactions," *NASA-TN-2113*, 1950.

[D18] Clarke, J., Satchell, M., and di Mare, L., "Oxford Chemical and Thermodynamics Library," , 2021. Not yet submitted.

[D19] Brandis, A., Cruden, B., Prabhu, D., Bose, D., McGilvray, M., Morgan, R., and Morgan, R., "Analysis of Air Radiation Measurements Obtained in the EAST and X2 Shocktube Facilities," *10th AIAA/ASME Joint Thermophysics and Heat Transfer Conference*, American Institute of Aeronautics and Astronautics, 2010. https://doi.org/10.2514/6.2010-4510.

Chapter 6

CONCLUSIONS AND FUTURE WORK

6.1 REVIEW OF MAJOR FINDINGS

The stated objective of this DPhil was to answer the question: 'What are the primary sources of nonuniformities in the test gases of shock tube experiments, and how can they be efficiently modelled to enable a complete characterisation of experimental test gases?' Towards this end, three primary efforts were undertaken. These efforts, and the major findings achieved in their pursuit, are enumerated below:

1. *Develop and validate an axisymmetric Navier-Stokes solver capable of rapidly and accurately simulating the major sources of flow phenomena in shock tubes*
    - By using an overset formulation containing each of the primary discontinuities in shock tubes within its own moving domain, the computational cost of simulating shock tubes diminishes substantially
    - A solution of the Reimann problem across the shock provides the appropriate wave speed for the moving shock domain
2. *Identify and study the sources of nonuniformities behind the shock*
    - The trajectory of a shock in shock tube experiments:
        - plays a vital role in determining the end-tube test gas properties
        - contains nearly all information required to characterise the test gas
    - The primary contributors to test gas nonuniformities are:
        - Entropy variations due to the changing shock speed
        - Relaxation waves produced by the changing shock speed as the post-shock pressure equilibrates throughout the test slug
        - Total enthalpy recovery associated with acceleration of the core flow due to boundary layer effects

  - Waves originating upstream, such as waves from the driver or mass consumption from the boundary layer
  - The interplay of these factors with the boundary layer mass consumption rate and its associated effects

3. *Develop and validate an analytical model which captures the influence of each of the primary sources of nonuniformities in order to fully characterise the test slug*

   - The above contributors to test gas nonuniformities interact with and exacerbate thermochemical nonuniformities behind the shock
   - The test slug may be modelled as the summation of a number of slices which:
     - Have an entropy level set by the shock at their initial processing
     - Are isentropic after their initial processing
     - Have total enthalpy is influenced by these factors
   - Such a model is both highly computationally efficient and accurate
   - This model may be used to dramatically improve the present state of the art in shock tube experimental characterisation

6.2 FUTURE WORK

Although the LASTA and FROSST codes have yielded exciting results and answered several trenchant questions in the extant literature, much work remains both to improve the codes themselves, and then to apply them to an array of interesting problems. Discussion of future work shall be divided into three categories: improvements to FROSST, improvements to LASTA, and the application of either code to future investigations.

FROSST was written in a combination of the FORTRAN and C++ programming languages. The parallelisation scheme was not implemented in a way which took full advantage of the C++ language, and left much to be desired. Although the code in its current form completes full-facility simulations relatively quite rapidly, dramatic improvement could be obtained by a less naive implementation of the parallelism. Such speed improvements will become vital for the necessary inclusion of equilibrium thermochemistry and then, at a still later date, nonequilibrium thermochemistry.

Many improvements to LASTA are attainable. Perhaps the most obvious theoretical shortcoming of the methodology is the use of a pressure limiter in order to account for the effects of momentum exchange. It is also possible that this limitation accounts for other effects as well, such as the reflection of relaxation waves from the contact discontinuity. A more thorough investigation of the physical underpinnings which necessitate the pressure limiter is a natural first step towards improving the method.

As it stands, the methodology captures the unsteady time history of each slice in high resolution, but relies upon an equilibrium thermochemical formulation in order to determine the chemical state. However, the availability of the unsteady history provides an opportunity to include nonequilibrium thermochemistry instead, thus allowing LASTA to characterise the extent to which nonuniformities influence the nonequilibrium portion of test slugs, provided some initial post-shock nonequilibrium state. Since the entropy is not necessarily conserved through the nonequilibrium state, the first step along such a path would be to identify a means of accounting for its variation. Work is already progressing using LASTA to reconsider how much of a given test slug is actually in nonequilibrium, and what the impact of such findings might be on the extraction of chemical rate processes.

A recurring question in the literature is the interference with radiative measurements of the boundary layer. For example, Cruden *et al* [23] cite boundary layer thermochemistry as the source of measured radiative nonuniformities in experiments simulating conditions on Mars. LASTA presently uses Mirels' approximate models in order to obtain boundary layer properties. These are essentially one-size-fits-all boundary layer solutions which lack many important flow details such as property profiles within the boundary layer. The basic LASTA methodology could be extended to include a higher fidelity resolution of the boundary layer by in-situ solution of the boundary layer equations. Such work is already underway by Associate Professor Luca di Mare.

The LASTA methodology could also be extended to include more complex facility configurations such as expansion and reflected shock tubes. However, given the highly complex and entropy-producing flow phenomena which occur near the diaphragm, it is suspected that the ultimate application of LASTA to complex shock facilities will be akin to state-to-state methodologies such as the UQ Equilibrium Shock Tube Code junior (ESTCj) code [42], or a variant of the UQ PITOT code [46] which is able to supplement portions of its analysis using experimental outputs as inputs. Furthermore, hybrid methodologies such as using one-dimensional methods for upstream tube sections and more expensive multidimensional simulations for the final portions of the facility may be improved by use of LASTA as a more efficient and experimentally informed *a posteriori* substitution for an *a priori* one-dimensional solver such as L1d [44]. Given the many potential options for development and integration, the implications of the LASTA formulation upon facilities containing secondary diaphragms are manifest.

The results of this work also open the door to a number of interesting investigations. One of the many examples include examination of the influence upon thermochemical measurements of trance

contaminants in the fill gas, such as water or atmospheric air where conditions aside from Earth's atmosphere are desired. Another example might be to use unsteady LASTA outputs as an input to more complex simulations which seek to capture the influence of nonuniformities behind a secondary diaphragm or upon test articles such as flight models. The LASTA methodology also provides a testbed for investigating analytical models of shock tube flows such as turbulence transition models for the boundary layer.

Possibly the most influential opportunities for the future uses of LASTA include a revisitation of nonequilibrium and radiative emissions studies which have either had difficulty identifying equilibrium regions or been influenced by flow nonuniformities which were hitherto unexplained. Although LASTA cannot predict all nonuniformities, such as those originating with contamination from driver gas, it is possible that the use of LASTA against legacy data will help to reveal the sources of some of the many discrepancies in nonequilibrium rate data and radiative emissions. DPhil candidate Peter Collen, in collaboration with the author, has used LASTA to characterise experiments performed in T6 [16]. LASTA was run against the experimentally obtained shock trajectory, with an end-tube shock speed of $9.5\,\mathrm{km/s}$ in Air. The resulting test slug chemical composition and properties were input to the NASA NEQAIR code [79] to predict the radiance which would be produced by the equilibrium-only LASTA test slug. Figure 6.1 shows the resulting comparison to experimentally obtained atomic oxygen radiance integrated between 760 nm and 785 nm. The close agreement after the initial nonequilibrium peak suggests that nearly the entire test gas is actually in equilibrium, whereas it was previously assumed that much of the observed variation was due to nonequilibrium effects. Using these and other similar results with LASTA, Peter Collen has been able to make significant strides in the analysis of shock tube thermochemical phenomena.

6.3 FINAL THOUGHTS

The product of this pursuit has been a successful identification of the sources of nonuniformities which have materially degraded the results of hypersonic shock tube experiments around the world. Furthermore, an analytical model was developed which was demonstrated to accurately predict these nonuniformities, and applied to experimental results across a range of Mach numbers, test gases, and fill conditions. This analytical model was designed to be highly computationally efficient, allowing for real-time characterisation of experimental results and allowing a reproduction in 10 minutes on

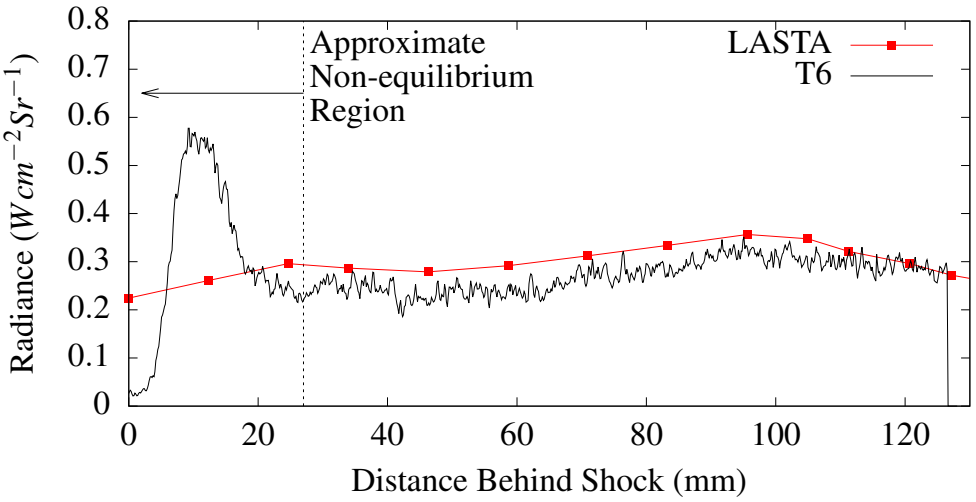

Fig. 6.1 LASTA-predicted atomic oxygen radiance compared against T6 experiment.

one computational core what presently requires weeks or even months of time on a high performance computational cluster. Perhaps the most significant long term result is that, by using the LASTA methodology to fully characterise the experimental test gas in shock tubes, the degree of uncertainty in thermochemical rates will diminish significantly. The resulting data will be fed into CFD solvers, enabling far more accurate, and confident, design of thermal protection systems and hypersonic flight vehicles for the exploration of our own world and the planets beyond.

References

[1] Alpher, R. A. and White, D. R. (1958). Flow in shock tubes with area change at the diaphragm section. *Journal of Fluid Mechanics*, 3(5):457–470.

[2] Anderson, J. (2000). *Hypersonic and High Temperature Gas Dynamics*. American Institute of Aeronautics and Astronautics, Reston, VA.

[3] Bensassi, K. and Brandis, A. M. (2019). Time accurate simulation of nonequilibrium flow inside the NASA ames electric arc shock tube. In *AIAA Scitech 2019 Forum*. American Institute of Aeronautics and Astronautics.

[4] Bensassi, K., Brandis, A. M., and Cruden, B. A. (2019). Computational modelling for non-equilibrium shock tube flows. In *Proceedings of the 32nd International Symposium on Shock Waves (ISSW32 2019)*. Research Publishing Services.

[5] Bensassi, K. and Brandis, A. (2019). Time accurate simulation of nonequilibrium flow inside the NASA ames electric arc shock tube. URL: https://ntrs.nasa.gov/api/citations/20190025143/downloads/20190025143.pdf.

[6] Brandis, A., Cruden, B., Prabhu, D., Bose, D., McGilvray, M., Morgan, R., and Morgan, R. (2010). Analysis of air radiation measurements obtained in the EAST and x2 shocktube facilities. In *10th AIAA/ASME Joint Thermophysics and Heat Transfer Conference*. American Institute of Aeronautics and Astronautics.

[7] Brandis, A. M. and Cruden, B. A. (2018). Shock tube radiation measurements in nitrogen. In *2018 Joint Thermophysics and Heat Transfer Conference*. American Institute of Aeronautics and Astronautics.

[8] Brandis, A. M., Johnston, C. O., Cruden, B. A., Prabhu, D., and Bose, D. (2015). Uncertainty analysis and validation of radiation measurements for earth reentry. *Journal of Thermophysics and Heat Transfer*, 29(2):209–221.

[9] Brouillette, M. (2003). Shock waves at microscales. *Shock Waves*, 13(1):3–12.

[10] Candler, G. V. and MacCormack, R. W. (1991). Computation of weakly ionized hypersonic flows in thermochemical nonequilibrium. *Journal of Thermophysics and Heat Transfer*, 5(3):266–273.

[11] Chandel, D. (2018). *Computations of Atmospheric Entry Gas Dynamics in Shock-tube Experiments*. Phd dissertation, University of Minnesota.

[12] Chandel, D., Nompelis, I., and Candler, G. (2018). Computations of high enthalpy shock-waves in electric arc shock-tube (EAST) at NASA Ames. In *2018 AIAA Aerospace Sciences Meeting*. American Institute of Aeronautics and Astronautics.

[13] Chandel, D., Nompelis, I., Candler, G., and Brandis, A. (2019). CFD predictions of high enthalpy shocks in nitrogen. In *AIAA Aviation 2019 Forum*. American Institute of Aeronautics and Astronautics.

[14] Chue, R. S. M. and Eitelberg, G. (1998). Studies of the transient flows in high enthalpy shock tunnels. *Experiments in Fluids*, 25(5):474–486.

[15] Clarke, J., Satchell, M., and di Mare, L. (2021). Oxford chemical and thermodynamics library. Not yet submitted.

[16] Collen, P., Satchell, M., Glenn, A., Di Mare, L., and McGilvray, M. (2021). On the impact of shock speed variation in high-enthalpy shock tube radiation experiments for atmospheric entry. In Preparation.

[17] Collen, P. L., Doherty, L., McGilvray, M., Naved, I., Geraets, R. T. P., Hermann, T. A., Morgan, R. G., and Gildfind, D. (2019a). Commissioning of the t6 stalker tunnel. In *AIAA Scitech 2019 Forum*. American Institute of Aeronautics and Astronautics.

[18] Collen, P. L., Doherty, L., McGilvray, M., Naved, I., Geraets, R. T. P., Hermann, T. A., Morgan, R. G., and Gildfind, D. (2019b). Computations of high enthalpy shock-waves in electric arc shock-tube (EAST) at NASA Ames. In *57th AIAA Aerospace Sciences Meeting*. American Institute of Aeronautics and Astronautics.

[19] Cruden, B. A. (2011). Absolute radiation measurement during planetary entry in the NASA ames electric arc shock tube facility. AIP.

[20] Cruden, B. A. and Brandis, A. M. (2020). Measurement of radiative nonequilibrium for air shocks between 7 and 9 km/s. *Journal of Thermophysics and Heat Transfer*, 34(1):154–180.

[21] Cruden, B. A., Brandis, A. M., and Johnston, C. O. (2018). Development of a radiative heating margin policy for lunar return missions. *Journal of Thermophysics and Heat Transfer*, 32(2):303–315.

[22] Cruden, B. A., Brandis, A. M., and Prabhu, D. K. (2013). Compositional dependence of radiance in CO2/n2/ar systems. In *44th AIAA Thermophysics Conference*. American Institute of Aeronautics and Astronautics.

[23] Cruden, B. A., Prabhu, D., and Martinez, R. (2012). Absolute radiation measurement in venus and mars entry conditions. *Journal of Spacecraft and Rockets*, 49(6):1069–1079.

[24] Daru, V. and Tenaud, C. (2009). Numerical simulation of the viscous shock tube problem by using a high resolution monotonicity-preserving scheme. *Computers and Fluids*, 38(3):664 – 676.

[25] Duff, R. E. (1959). Shock-tube performance at low initial pressure. *Physics of Fluids*, 2(2):207.

[26] Fujii, N., Koshi, M., Ando, H., and Asaba, T. (1979). Evaluation of boundary-layer effects in shock-tube studies of chemical kinetics. *International Journal of Chemical Kinetics*, 11(3):285–304.

[27] Geraets, R. T. P. and McGilvray, M. (2019). Stagnation point heat flux measurements in a plasma wind tunnel using a diamond heat transfer gauge. In *AIAA Scitech 2019 Forum*. American Institute of Aeronautics and Astronautics.

[28] Gildfind, D. E. (2019). A procedure to compute influence of experimental shot-to-shot variation on expansion tube test flow properties. *Shock Waves*, 29(7):985–1006.

[29] Gildfind, D. E., Jacobs, P. A., Morgan, R. G., Chan, W. Y. K., and Gollan, R. J. (2017a). Scramjet test flow reconstruction for a large-scale expansion tube, part 1: Quasi-one-dimensional modelling. *Shock Waves*, 28(4):877–897.

[30] Gildfind, D. E., Jacobs, P. A., Morgan, R. G., Chan, W. Y. K., and Gollan, R. J. (2017b). Scramjet test flow reconstruction for a large-scale expansion tube, part 2: Axisymmetric CFD analysis. *Shock Waves*, 28(4):899–918.

[31] Glass and Patterson (1955). A theoretical and experimental study of shock-tube flows. *Journal of the Aeronautical Sciences*, 22(2):73–100.

[32] Gollan, R. (2007). Computing post-shock thermochemically relaxing flow behind a steady normal shock. *University of Queensland Division of Mechanical Engineering Report 2007/09*.

[33] Gollan, R. (2008). *The Computational Modelling of High-Temperature Gas Effects with Application to Hypersonic Flows*. Phd dissertation, University of Queensland.

[34] Gollan, R., Jacobs, C., Jacobs, P., Morgan, R., McIntyre, T., Macrossan, M., Buttsworth, D., Eichmann, T., and Potter, D. (2009). A simulation technique for radiating shock tube flows. In *Shock Waves*, pages 465–470. Springer Berlin Heidelberg.

[35] Gollan, R. and Jacobs, P. (2013). About the formulation, verification and validation of the hypersonic flow solver eilmer. *International Journal for Numerical Methods in Fluids*, 73(1):19–57.

[36] Goozée, R. J., Jacobs, P. A., and Buttsworth, D. R. (2006). Simulation of a complete reflected shock tunnel showing a vortex mechanism for flow contamination. *Shock Waves*, 15(3):165–176.

[37] Gu, S. and Olivier, H. (2020). Capabilities and limitations of existing hypersonic facilities. *Progress in Aerospace Sciences*, 113:100607.

[38] Hartunian, R. A., Russo, A. L., and Marrone, P. V. (1960). Boundary-layer transition and heat transfer in shock tubes. *Journal of the Aerospace Sciences*, 27(8):587–594.

[39] Heppenheimer, T. A. (2006). *Facing the Heat Barrier: A History of Hypersonics*. NASA.

[40] Holbeche, T. A. and Spence, D. A. (1964). A theoretical and experimental investigation of temperature variation behind attenuating shock waves. *Proceedings of the Royal Society of London. Series A, Mathematical and Physical Sciences*, 279(1376):111–128.

[41] Hooker, W. J. (1961). Testing time and contact-zone phenomena in shock-tube flows. *Physics of Fluids*, 4(12):1451.

[42] Jacobs, P., Gollan, R., Potter, D., Zander, F., Gildfind, D.and Blyton, P., Chan, W., and Doherty, L. (2014). Estimation of high-enthalpy flow conditions for simple shock and expansion processes using the estcj program and library. *University of Queensland, Mechanical Engineering, Research Report*.

[43] Jacobs, P., Silvester, T., Morgan, R., Scott, M., Gollan, R., and McIntyre, T. (2005). Superorbital expansion tube operation: Estimates of flow conditions via numerical simulation. In *43rd AIAA Aerospace Sciences Meeting and Exhibit*. American Institute of Aeronautics and Astronautics.

[44] Jacobs, P. A. (1994). Quasi-one-dimensional modeling of a free-piston shock tunnel. *AIAA Journal*, 32(1):137–145.

[45] Jacobs, P. A. (1998). Shock tube modelling with l1d. *The University of Queensland Report 13/98*.

[46] James, C. M., Gildfind, D. E., Lewis, S. W., Morgan, R. G., and Zander, F. (2018). Implementation of a state-to-state analytical framework for the calculation of expansion tube flow properties. *Shock Waves*, 28(2):349–377.

[47] Johnston, C. O. and Kleb, B. (2012). Uncertainty analysis of air radiation for lunar-return shock layers. *Journal of Spacecraft and Rockets*, 49(3):425–434.

[48] Kendall, M., Morgan, R., and Jacobs, P. (1997). A compact shock-assisted free-piston driver for impulse facilities. *Shock Waves*, 7(4):219–230.

[49] Kotov, D. V., Yee, H., Panesi, M., Prabhu, D. K., and Wray, A. A. (2014). Computational challenges for simulations related to the NASA Electric Arc Shock Tube (EAST) experiments. *Journal of Computational Physics*, 269:215 – 233.

[50] Lemal, A., Bando, K., Nomura, S., Takayanagi, H., and Fujita, K. (2018). Prediction of nonequilibrium peak radiation during earth's atmosphere suborbital reentry. *Journal of Thermophysics and Heat Transfer*, 32(1):256–261.

[51] Lemal, A., Jacobs, C. M., Perrin, M.-Y., Laux, C. O., Tran, P., and Raynaud, E. (2016). Prediction of nonequilibrium air plasma radiation behind a shock wave. *Journal of Thermophysics and Heat Transfer*, 30(1):197–210.

[52] Light, G. C. (1973). Test gas properties behind a decelerating shock wave in a shock tube. *Physics of Fluids*, 16(5):624.

[53] McBride, B. and Gordon, S. (1996). Computer program for calculation of complex chemical equilibrium compositions and applications. I: Analysis. *NASA-RP-1311*, 19.

[54] McGilvray, M., Austin, J. M., Sharma, M., Jacobs, P. A., and Morgan, R. G. (2009). Diagnostic modelling of an expansion tube operating condition. *Shock Waves*, 19(1):59–66.

[55] McGilvray, M., Dann, A. G., and Jacobs, P. A. (2013). Modelling the complete operation of a free-piston shock tunnel for a low enthalpy condition. *Shock Waves*, 23(4):399–406.

[56] McGilvray, M., Doherty, L. J., Morgan, R. G., Gildfind, D., Jacobs, P., and Ireland, P. (2015). T6: The Oxford University Stalker Tunnel. In *20th AIAA International Space Planes and Hypersonic Systems and Technologies Conference*. American Institute of Aeronautics and Astronautics.

[57] Mirels, H. (1957). Attenuation in a shock tube due to unsteady-boundary-layer action. *NACA Report 1333*.

[58] Mirels, H. (1963). Test time in low-pressure shock tubes. *Physics of Fluids*, 6(9):1201–1214.

[59] Mirels, H. (1964). Shock tube test time limitation due to turbulent wall boundary layer. *AIAA Journal*, 2(1):84–93.

[60] Mirels, H. (1966). Flow nonuniformity in shock tubes operating at maximum test times. *Physics of Fluids*, 9(10):1907.

[61] Olivier, H., Zonglin, J., Hongru, R., and Lu, F. (2002). Detonation-driven shock tubes and tunnels. In *Advanced Hypersonic Test Facilities*, pages 135–203. American Institute of Aeronautics and Astronautics.

[62] Palmer, G., Prabhu, D., Brandis, A., Eichmann, T., Potter, D., and McIntyre, T. (2011). Numerical simulation of radiation measurements taken in the x2 facility for mars and titan gas mixtures. In *42nd AIAA Thermophysics Conference*. American Institute of Aeronautics and Astronautics.

[63] Park, C. (1989). *Nonequilibrium Hypersonic Aerothermodynamics*. AIAA Education Series.

[64] Petersen, E. L. and Hanson, R. K. (2001). Nonideal effects behind reflected shock waves in a high-pressure shock tube. *Shock Waves*, 10(6):405–420.

[65] Petrie-Repar, P. and Jacobs, P. (1998). A computational study of shock speeds in high-performance shock tubes. *Shock Waves*, 8(2):79–91.

[66] Priyadarshini, M. S., Munafò, A., Brandis, A. M., Cruden, B. A., and Panesi, M. (2018). One-dimensional modeling methodology for shock tubes: Application to the EAST facility. In *2018 Joint Thermophysics and Heat Transfer Conference*. American Institute of Aeronautics and Astronautics.

[67] Resler, E. L., Lin, S.-C., and Kantrowitz, A. (1952). The production of high temperature gases in shock tubes. *Journal of Applied Physics*, 23(12):1390–1399.

[68] Roshko, A. (1960). On flow duration in low-pressure shock tubes. *Physics of Fluids*, 3(6):835.

[69] Rothkopf, E. M. and Low, W. (1974). Diaphragm opening process in shock tubes. *The Physics of Fluids*, 17(6):1169–1173.

[70] Rudinger, G. (1961). Effect of boundary-layer growth in a shock tube on shock reflection from a closed end. *Physics of Fluids*, 4(12):1463.

[71] Simpson, C. J. S. M., Chandler, T. R. D., and Bridgman, K. B. (1967). Effect on shock trajectory of the opening time of diaphragms in a shock tube. *The Physics of Fluids*, 10(9):1894–1896.

[72] Spence, D. (1961). Unsteady shock propagation in a relaxing gas. *Proceedings of the Royal Society of London. Series A. Mathematical and Physical Sciences*, 264(1317):221–234.

[73] Spurk, J. H., Gerber, N., and Sedney, R. (1966). Characteristic calculation of flowfields with chemical reactions. *AIAA Journal*, 4(1):30–37.

[74] Warshay, M. (1968). Effects of boundary layer buildup in shock tubes upon chemical rate measurements. *NACA TN-D-4795*.

[75] Weber, Y. S., Oran, E. S., Boris, J. P., and Anderson, J. D. (1995). The numerical simulation of shock bifurcation near the end wall of a shock tube. *Physics of Fluids*, 7(10):2475–2488.

[76] Weilmuenster, K. (1974). An experimental investigation of wall boundary layer transition reynolds numbers in an expansion tube. *NASA Technical Report NASA-NASA-TN-D-7541, L-9337*.

[77] West, T. K., Johnston, C. O., and Hosder, S. (2017). Uncertainty and sensitivity analysis of afterbody radiative heating predictions for earth entry. *Journal of Thermophysics and Heat Transfer*, 31(2):294–306.

[78] White, D. R. (1958). Influence of diaphragm opening time on shock-tube flows. *Journal of Fluid Mechanics*, 4(6):585–599.

[79] Whiting, E., Park, C., Yen, L., Arnold, J., and Paterson, J. (1996). NEQAIR96, nonequlibrium and equilibrium radiative transport and spectra program: User's manual. *NASA Technical Report NASA-RP-1389*.

[80] Wilson, G. J., Sussman, M. A., and Bakos, R. J. (1995). Numerical simulations of the flow in the hypulse expansion tube. *NASA Technical Report NASA-TM-110357*.

[81] Yee, H., Kotov, D., Wang, W., and Shu, C.-W. (2013). Spurious behavior of shock-capturing methods by the fractional step approach: Problems containing stiff source terms and discontinuities. *Journal of Computational Physics*, 241:266 – 291.

[82] Zeitoun, D. and Imbert, M. (1979). Interaction between the unsteady boundary layer and inviscid hot flow in a shock tube. *AIAA Journal*, 17(8):821–827.

[83] Zeleznik, F. J. and Gordon, S. (1968). Calculation of complex chemical equilibria. *Industrial & Engineering Chemistry*, 60(6):27–57.

Appendix A: LASTA Operating Instructions

This section describes running instructions and best practices for using the LASTA code. Specific formatting and variable names are referenced in the actual README files available with the code; this section is intended as an overview and general guide to using the code. Several sample cases are distributed with the code which provide additional tutorial into the appropriate settings for a given set of conditions. LASTA is divided into four main components: *input.py, lgclcass.py, slug.py*, and the OCEAN library. There are also a number of supporting classes and functions, but this document is focused upon the use and interplay of these primary features. As an overview, *input.py* is a customisable input script which defines the case and run conditions. *slug.py* is the overall architecture which processes the inputs and outputs, performs time steps, and calls *lgclass.py*, which actually computes the mathematical operations as outlined in Chapter 5 for each slice. *slug.py* also manages the outputs. OCEAN is a FORTRAN library which computes equilibrium thermochemical properties, akin to CEA [53]. The library is distributed with LASTA, and must be compiled and installed so that LASTA can call it at need. Compilation and installation instructions are included in the README files.

A1 input.py

Input into LASTA is achieved in the form of a Python script, akin to the structure utilised in the L1d code [43]. Myriad inputs and flags are possible here, and are fully explained within the class *lginputclass.py* which processes the input script, but the primary inputs are now described.

1. Input shock trajectory file name
    - Format: distance (m), time (s) space-delimited file
2. Fill gas properties for use in OCEAN

- Species chemical symbols, including those desired for consideration even if not present in the fill gas (e.g. ionised species)
- Species mole fraction (moles of species/kg mixture)
- Flag for turbulence modelling
- Transition integrated Reynolds number for switching between laminar and turbulent models
- Fill temperature (K)
- Fill pressure (Pa)
- Prandtl number
- Transport properties file*

3. Tube geometry

- Tube radius (m)
- Output locations (distance (m) from start of trajectory). Two are presently possible, intended to match the locations of the Pitot probe and the final wall pressure transducer prior to the test section.

4. Resolution parameters

- Slice resolution (m)
- Distance of first slice from start of trajectory (m). This is used to save from modeling slices which are ultimately consumed by the boundary layer and therefore not present in the test slug.
- Number of time steps into which the trajectory is divided. The user must ensure that these are sufficiently small to maintain accuracy.

The sample cases distributed with the code cover a range of thermochemical inputs, fill conditions and flags for using different models. These may be studied for further insight, and are intended as baselines from which new users may construct input decks for new conditions.

*: OCEAN cannot presently compute transport properties for ionised mixtures, as this capability is still under development. Viscosity is the only transport property which is presently used, as Mirels' formulas assume a constant Prandtl number. Thus, viscosity for the relevant range of temperature and

pressure conditions must be tabulated from, for example, CEA, into a format which LASTA may call. Formatting instructions are provided for this file, and such a file has been constructed for Air across a very broad range of conditions. A flag is also present in *input.py* to use a Sutherland formulation instead, and options are available to input the Sutherland constants rather than a transport properties file.

A2 Calling LASTA

Calling LASTA is as simple as executing *input.py*. The script contains a call to the function *slug*, which comprises the bulk of the *slug.py* file. *slug* processes the inputs, and defines each slice as a class with its own properties such as location, temperature, etc. *slug* iterates through time, calling at each time step the update function of each slice, which performs the mathematical operations of Chapter 5 of this document, and are contained in *lgclass.py*. *lgclass.py* is conveniently commented so that it is clear what portion of the process is being performed at each section of code, and commands may be uncommented which enable the user to turn off different influences (e.g. upstream waves) in order to study how they affect the solution.

When LASTA is run and slices are processed at each time step by *lgclass.py*, many slices will be eliminated either by the boundary layer or as a result of obtaining a velocity which exceeds that of the shock. The code outputs a warning when a slice has thereby been eliminated, indicating where the slice originated (e.g. it was initially positioned at 4 m). As each slice reaches the specified output locations, the code prints the originating location of the slice, and the time at which it crossed the output location. Time steps cease when all surviving slices have crossed the downstream output location. When *slug.py* has finished time step computations, it begins processing outputs.

A3 Outputs

Python makes determining outputs easily customisable, and the options for outputs are well-documented in this portion of the code. However, most users will likely find the pre-defined outputs to contain whatever information is desired. Three primary output files are produced, as well as several auxiliary output files which the user may find convenient for debugging. These auxiliary files are described in the README, as well as the particular formatting of all of the files. The primary output

files are: *pslugrun.out, pslugrun.2.out, and chempslugrun.out*. It may be noted that the input file also demands a run name character string, which is appended to each of these filenames so as to allow easy distinction between outputs from different runs.

A3.1 *pslugrun.out* and *pslugrun.2.out*

pslugrun.out and *pslugrun.2.out* are formatted identically, and consist of the time-stamped properties of each slice when it crossed the output locations, where *pslugrun.2.out* is the downstream output location. As each slice crosses the output location during time steps, the time at which it crosses, and its chemical composition, thermochemical properties, integrated Reynolds number, stagnation and Pitot properties for that slice, and other information is denoted. The *pslugrun* files contain this data, minus the chemical composition, and may be plotted directly against the included time stamps to obtain centreline property traces for comparison against experimental measurements.

A3.2 *chempslug.out*

chempslug.out is developed by the same process as the *pslugrun* files, but explicitly contains the thermochemical composition data for each slice as it crossed the downstream output location. This file is more lightweight than the *pslugrun* files, and contains along with chemical species only the timestamp, temperature and pressure. This output file was developed primarily to enable an easy reference file for coupling with codes such as NEQAIR [79], which may be applied to the thermochemical traces of LASTA in order to predict the radiative intensity associated with the test gas.

A4 Best Practices

As a general note, experienced CFD users are likely familiar with the best practices for limiting the stability and discretisation errors associated with typical numerical solutions of the Navier-Stokes equations. However, this code is not a solution of the Navier-Stokes, or even of some derivative set of equations; rather, LASTA is the sum of a number of models, none of which are subject to the same types of limitations typically associated with numerical methods. Thus, when considering best practices in operating the code, it is important to remember that the limitations of LASTA lay primarily in the applicability and interactions of the models used by LASTA.

When performing computations for a new set of operating conditions, the extent of shock-processed gas which remains in the test slug is not easily obtained prior to running. As a result, the location of the most upstream slice which will survive until the end of the run cannot be known a-priori. It is also important to note that adding spatial resolution (more slices) in no way influences the accuracy of the methodology, since the slices do not interact; the number of slices serves only to provide sufficient resolution for variations in the final property traces. Since adding too many time steps or slices can easily slow the code to an expensive state, it is best to start a new set of conditions with a relatively coarse spatial and temporal resolution (e.g. 1 m and 400 time steps, respectively). Having observed which portion of shock-processed gas remains in the test slug, the starting location of the simulation may be adjusted, and an appropriate spatial resolution applied. The test cases distributed with the code contain examples of appropriate spatial resolutions.

Time discretisation error arises primarily from the interplay of slice pressure and the mass flow balance. Too large a time step can cause an out-of-date pressure at the slice location to yield an erroneous mass flow computation, and thus slice speed and associated variations. This is sometimes manifested as a premature consumption of a slice by the boundary layer. The appropriate number of time steps, and thus time step size, is not known *a priori*. Start with a coarse time step during the initial spatial probing run described previously. The number of time steps may be doubled after an appropriate spatial resolution is obtained, and the run repeated. The time resolution may be determined as sufficient when the distribution of properties in the final trace ceases to change with increased time steps. The test cases distributed with the code contain appropriate time step numbers for reference.

Although determining the appropriate resolution can be somewhat tedious for new conditions outside of the user's built-up intuition from experience with LASTA, the entire process takes roughly one hour of wall time, and successive runs at similar conditions are then much faster (e.g. 10-15 minutes for an 11 species simulation). After repeated uses of the code, the author was able to acquire a rapid intuition about the appropriate resolutions to use under different conditions, and the process for new cases was accelerated considerably.